Structural Analysis and its Implications for Oxide Ion Conductivity of Lanthanide Zirconate Pyrochlores

by

Ali Shehu

Submitted in partial fulfilment of the requirements of the Degree of Doctor of Philosophy

18th April 2018

School of Biological and Chemical Sciences
Queen Mary University of London
United Kingdom

Statement of Originality

I, Ali Shehu, confirm that the research included within this thesis is my own work or that where it has been carried out in collaboration with, or supported by others, that this is duly acknowledged below and my contribution indicated. Previously published material is also acknowledged below.

I attest that I have exercised reasonable care to ensure that the work is original, and does not to the best of my knowledge break any UK law, infringe any third party's copyright or other Intellectual Property Right, or contain any confidential material.

I accept that the College has the right to use plagiarism detection software to check the electronic version of the thesis.

I confirm that this thesis has not been previously submitted for the award of a degree by this or any other university.

Signature: 

Date: 18th April 2018

Acknowledgements

I enjoyed my PhD, I loved my PhD; it was such a unique and special part of my life. Therein I gained new skills, I gained new knowledge, I elevated my dreams, my ambitions, and my love for science to new heights. During the course of my PhD, there were many of those who supported me, the most special of whom entered my heart, never to come out, and thus I will briefly mention those here.

I will start with my wife, Jetmira, who exceeded all bounds of kindness to me, who means immensely to me. Jetmira offered me peace of heart and mind, thus allowing me the much-needed freedom for one to delve deeply and widely into the realms of physics, chemistry, mathematics, and science as a whole. Jeta has been the best companion I could have possibly had in discussing matters of science, which is what would so enjoyably fill our evenings on a daily basis. Furthermore, Jetmira supported financially both, our daughters (Urtesa & Mesonia) and I, for over a year, and continues to do so, while always comforting me. Raising a family whilst doing my PhD, meant that I needed all the help I could get, and with such regard, my beloved cousin and good friend Fatjon Domi and my dear friend Abdul Karim have always been there for me with their generosity and willingness to help, for which I am very grateful to.

I am very grateful to my primary supervisor, Dr Isaac Abrahams, who made the PhD experience easy for me, despite the hardships and the stress that the PhD research entails. I enjoyed my trips with Isaac to ISIS, Rutherford Appleton Laboratory for neutron beam time; where it was my honour and pleasure to sit with Isaac, to work together, to eat together, and to have free discussions of all kinds. I am also very grateful to my other two supervisors, Prof Martin T. Dove, and Dr Stephen Hull for their continuous support and advice. I am grateful to Dr Rory Wilson, who ran the X-ray diffractometer, for all his hard work and the advice he offered me. I am especially grateful to Prof Franciszek Krok, Dr Marcin Malys, and their research group, over at Warsaw University of Technology, Poland, for their guidance and assistance in carrying out and interpreting the electrical measurements. I enjoyed their extraordinary hospitality in my trip of two weeks to Warsaw, the pleasure of which I can never forget.

I am very grateful to Dr Nicholas Cheval from France, who was a postdoc at the time, and who's tips on literature finding continue to be invaluable to me. I appreciate and I will miss Dr Tippu Sheriff, for the very warm friendship he offered me, for the coffees and the conversations we had together, which I enjoyed greatly. I will miss my fellow PhD student, Lei Wang, who would always cheer me up, make me laugh and enlighten my mood. I enjoyed the afternoon Americano-coffees I would have from Starbucks, served mostly by Camillo or Richard, whom I will miss dearly for their kindness and the laughs we had together.

I am very grateful to the Science and Technology Facilities Council (STFC) and Queen Mary University of London for jointly funding my PhD, and thus enlightening my life. Finally, all praise and thanks be to the Lord of the worlds, who enabled me to get to here, for out of my own accord, I would have been unable to even take a single step.

Abstract

The local structure evolution as a function of composition and temperature, and the resulting electrical conductivities were studied in samples with general composition $(Yb_{1-x}Nd_x)_2Zr_2O_7$, using Reverse Monte Carlo (RMC) modelling of total neutron scattering data and Impedance Spectroscopy. At low neodymium content ($0.00 \leq x \leq 0.50$), this system crystallizes in the fluorite structure with space group $Fm\bar{3}m$, where-as at high neodymium content ($0.75 \leq x \leq 1.00$), a pyrochlore structure with space group $Fd\bar{3}m$ is observed. For compositions with high neodymium content prepared at lower temperatures, a fluorite structure is seen, which shows gradual evolution of pyrochlore ordering with increasing calcination temperature. Cation anti-site disorder was present throughout the compositional range. Total conductivity increases with increasing Nd content, up to a maximum at $x = 0.75$ and then decreases. The conductivity of these oxides is of the order of 10^{-4} S cm^{-1} at 700 °C.

Variable temperature neutron powder diffraction experiments were carried out on the $(Nd_{1-x}Ca_x)_2Zr_2O_{7-x}$ ($0.10 \leq x \leq 0.50$) system, to investigate the local structural evolution as a function of composition and temperature. The entire compositional range studied exhibits a single phase with a pyrochlore-type structure. The variable temperature study showed that the pyrochlore structure is maintained throughout the temperature range studied. No cation anti-site disorder was present in any of the compositions, over the temperature range studied. Total conductivity increases with increasing Ca content, up to a maximum at $x = 0.30$ and then decreases. The conductivity of these oxides is of the order of 10^{-3} S cm^{-1} at 700 °C.

Structural evolution in oxidising and reducing atmospheres was investigated in cerium zirconate, $Ce_2Zr_2O_{7+\delta}$. A number of transformations were revealed, depending on the atmosphere (O_2 vs CO) and temperature. Upon heating the pyrochlore phase in flowing O_2, three distinct phases were observed, with transitions at *ca*. 140 °C and 410 °C. At around 140 °C, a previously un-identified phase formed, which was fitted with a triclinic model that contained 10 Ce and 10 Zr sites, each with a distorted cubic coordination. Above 410 °C, the triclinic phase transformed to a cubic phase, corresponding to the κ-phase (space group $P2_13$). RMC modelling of the local structure of the κ-phase, revealed an ordered, pyrochlore-like cation sub-lattice, with a disordered anion sub-lattice. Upon re-heating the κ-phase in CO, the pyrochlore phase re-appeared at around 260 °C. At 290 °C, the pyrochlore phase was phase pure.

Table of Contents

Chapter 1 – Introduction

1.1 Energy and fuel cells

The full development of clean and sustainable energy technologies is crucial for the world's current wellbeing and its future development. Amongst all the various technologies studied to date, fuel cells play an especially important role.[1] Fuel cells allow for direct conversion of chemical energy into electrical energy and consists of an electrolyte, a cathode, and an anode, as shown in **Fig. 1.1**. A fuel, such as hydrogen is fed into the anode, and an oxidant such as oxygen is fed into the cathode.[2] The anode and cathode catalyse the respective chemical reactions, whereas the electrolyte acts as a barrier to fuel and/or oxidant diffusion, thus preventing direct chemical combustion. Half-cell reactions take place at the anode and cathode, producing ions which then traverse the electrolyte. The flow of ionic charge then induces a flow of electronic charge through an outside circuit, thus producing electrical power.[3]

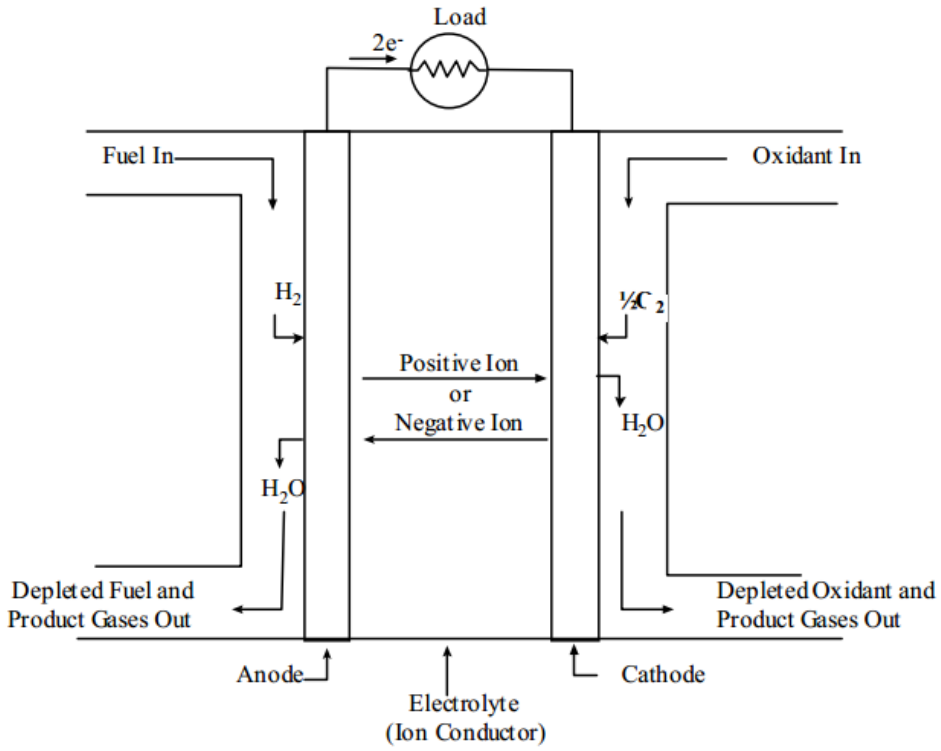

Fig. 1.1 Schematic of an individual fuel cell.[4]

Fuel cells offer several advantages over conventional power generation technologies, such as: higher conversion efficiency, lower production of pollutants, zero noise pollution, and the ability for co-generation.[5] However, it has proved difficult to develop fuel cells into competitive technological products. Problems have mainly been associated with the synthesis of materials with the appropriate properties that would allow for a competitive cost of electricity over existing technologies.[6,7] Though progress has been made in the development of these technologies, there is still a great need for novel materials and an understanding of their structural and mechanistic features.[8,9,10] These issues have been the driving force in the search for alternative materials.

Amongst all the fuel cell types investigated to date, solid oxide fuel cells (SOFCs) are especially promising, mainly due to their fuel flexibility. SOFCs use hydrocarbon fuels, and thus have the potential to act as a bridging technology between current and future hydrogen-based technologies.[11] However, the widespread use of SOFCs has been hindered by their high operating temperatures (800 to 1000 °C). High operating temperatures preclude the use of materials with cheaper fabrication costs such as metals, instead of ceramics, for the non-electrochemical parts of the fuel cell. High operating temperatures also increase the likelihood of cracks in the material developing upon thermal cycling. Therefore, it has become a major research challenge to reduce the operating temperature of SOFCs (T_{op}) to < 800 °C.[12,13]

The lower operating temperatures would then allow for the use of cheaper materials in interconnects and heat exchangers, thus significantly reducing the overall cost.[14,15] The lower operating temperature would also result in an increase in the durability of component materials, due to reduced problems with thermal cycling. However, the lower operating temperature results in some new disadvantages, such as an increased electrolyte resistance and a decrease in the rates of the electro-catalytic reactions.[12] This ultimately results in a reduction of the cell voltage and hence power output.

Thus, finding new combinations of electrolyte and electrode materials that minimise these losses while allowing for fast ion transport and high rates of electrochemical reactions remains a significant materials challenge.[10] Several areas of interest have emerged with regard to solid oxide fuel cells, such as the discovery of new compounds through in-situ characterization techniques and theoretical methods for predicting ion migration mechanisms and the associated activation energies.[16]

1.2 Oxide-ion conductors and electrolytes

Oxide ion conductors are materials in which oxide ions are able to migrate in the oxide lattice via oxide ion vacancies or interstitials.[17] This is a diffusive process, where the oxide ions occupy partially an array of crystallographically equivalent sites. Ionic conductivity (σ) can be expressed as the product of the charge carrier concentration, ionic charge and mobility, equation 1.1:

$$\sigma = \sum_i n_i e_i \mu_i \tag{1.1}$$

where n_i is the number of charge carriers of species i (oxide ions), e_i is the charge of the ions (1.6×10^{-19} C for monovalent ions) and μ_i is the mobility of the ions defined as the proportionality constant between the velocity of the charge carriers and their driving force, where the driving force is the gradient in electrochemical potential of the charge carriers of species i. The temperature dependence of the conductivity is then expressed by the Arrhenius equation, as:

$$\sigma T = A_T \exp\left(-\frac{E}{RT}\right) \tag{1.2}$$

where A is the pre-exponential factor, E is the activation energy, R is the gas constant (8.314 J K^{-1} mol^{-1}) and T is the absolute temperature (in K). The activation energy is an indication of the difficulty of ion hopping.

The magnitude of ion conduction varies considerably between materials, and thus the type of the electrolyte determines the operation temperature of the fuel cell. Therefore, the performance of the electrolyte is crucial to the development of intermediate temperature SOFCs (IT-SOFCs).[6,18] Several oxide-ion conducting electrolytes have been investigated to date, however, none is entirely satisfactory for application in IT-SOFCs with an operating temperature, T_{op}, less than 800 °C. Despite continued research efforts into alternative oxide-ion conducting materials, it is difficult to synthesise electrolyte materials with appropriate properties for one to displace the conventional fluorite structured compounds based on ZrO_2 and CeO_2. Nevertheless, the search for new electrolyte materials with improved properties continues.[19]

Research efforts have been dedicated to the optimization of both new and conventional electrolyte materials, primarily via chemical doping and novel synthesis routes. Chemical doping induces mobile oxygen vacancies into the host compound, resulting in increased ionic conductivity up to some maximum value. Many oxide ion conducting materials display order-disorder phase transitions and exhibit high oxide ion conductivities only above the transition into the more disordered phase. Chemical doping encourages the order-disorder phase transition, leading to increased ionic conductivities at lower temperatures.[8]

1.3 Electrolyte materials

The electrolyte materials studied to date can be grouped into three main structure type categories: (i) fluorite-based materials (zirconia, ceria, doped bismuth oxide, pyrochlore); (ii) perovskites and related intergrowth structures (lanthanum gallate, brownmillerites, BiMeVOX), (iii) LaMOX and apatites.[20] While the various structure types offer their advantages and disadvantages, their practical use and operation temperatures that may be achieved depend crucially on the minimum film thickness that may be successfully manufactured.

1.3.1 Fluorite-structured oxides

The majority of materials that have shown a suitable combination of properties for electrolytic applications are of the fluorite-type crystal structure, **Fig. 1.2**. In particular, these material types have been shown to possess adequate oxide-ion conductivities, accompanied with high structural stabilities in both oxidising and reducing atmospheres. Oxide ions are conducted via the oxygen hopping mechanism along oxygen ion vacancies, the concentrations of which can be further increased via doping with cations of lower valency.

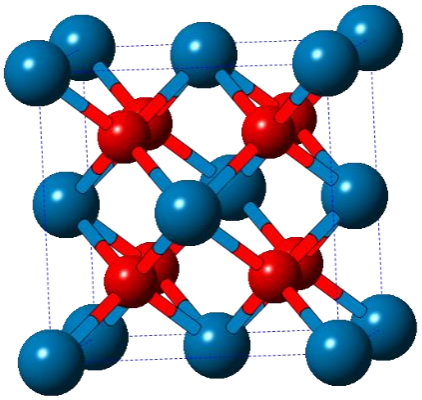

Fig. 1.2 Unit cell contents of the ideal fluorite structure, consisting of cubic close packed cations (blue atoms) with the anions (red atoms) occupying all the tetrahedral sites.

1.3.1.1 Zirconia-based solid electrolytes

The high conductivity phase with the fluorite structure of pure zirconia is achieved at temperatures above 2300 °C,[21] however, acceptor dopants can be added into the material which stabilise the high temperature phase and also increase the concentration of oxygen vacancies.[22] Typical acceptor dopants include Y^{3+} and Sc^{3+}, producing yttria-stabilized zirconia (YSZ) and scandium-stabilized zirconia (ScSZ) respectively. Indeed, the material of choice for commercial SOFCs is YSZ with 8 mol % Y_2O_3. This is mainly due to YSZ possessing reasonable levels of ionic conductivities accompanied with high structural stability under operating conditions. Stabilised zirconias show high levels of compatibility with the most common electrode materials, and a high chemical stability with regard to the reactant media. The conductivity of stabilised zirconias is mainly ionic with minimal electronic contribution, as compared to other electrolytes materials.

On the other hand, ScSZ exhibits a higher ionic conductivity, and as such has received considerable research interest, however its practical use has been hampered by the high cost of scandium.[23] The small size mismatch between Zr^{4+} and Sc^{3+} results in low activation energies for defect formation, leading to high ion mobility and conductivity. The highest conductivity of all zirconium oxides is shown by ScSZ with 8-12 mol % Sc.[23] However, the activation energy for conductivity in this system is high and

therefore conductivity drops rapidly with decreasing temperature, until at 500 °C the conductivity of ScSZ is lower than that of YSZ. At higher Sc contents (10–15 mol %) the conductivity diminishes more rapidly with decreasing temperature, due to the cubic phase transforming to a rhombohedral phase which possesses a lower ionic conductivity.[23] Nevertheless, the cubic phase of ScSZ can be stabilised by the addition of small amounts of other dopants such as Y^{3+}.[22]

Compatibility issues are indeed of huge concern for electrolyte materials in SOFCs, since the electrolyte is located at the centre-point of the fuel cell assembly and is thus in contact with the electrodes, the sealants, and the interconnects. For YSZ, chemical instability in relation to the cathode material is generally of greatest concern. This is because at high temperatures, YSZ reacts with the perovskite electrode materials, resulting in a pyrochlore phase that blocks oxide ion migration across the electrode/electrolyte interface.[7] Furthermore, aging of both the YSZ and ScSZ is of great concern as it leads to diminished conductivities during operation. In ScSZ, aging has been attributed to the formation of a distorted fluorite phase.[24]

1.3.1.2 Doped ceria electrolytes

Doped ceria and doped lanthanum gallate possess a high ionic conductivity, and form the most viable alternatives to stabilised zirconias as electrolyte materials for IT-SOFCs. Additionally, these materials have been shown to have a satisfactory compatibility with electrode materials containing perovskite oxides.

The two most widely used alternatives to YSZ as electrolytes in IT-SOFCs are doped ceria and doped lanthanum gallate, both because of the high ionic conductivity and compatibility with high-performance electrode materials, such as cobalt-containing perovskite oxide cathodes. At lower temperatures (500–700 °C), doped ceria materials have been shown to possess higher conductivities than stabilised zirconias. This has been attributed to the larger ionic radius of Ce^{4+} (0.87 Å in 6-fold coordination) than Zr^{4+} (0.72 Å),[25] which leads to a more open structure through which oxide ions migrate. Total conductivities are of greater ionic character with decreasing temperatures, until at 500 °C electronic conductivity is negligible. Furthermore, doped ceria compounds have a high chemical stability with respect to the electrode materials.

Aliovalent substitution has been used to increase the number of oxygen vacancies in the crystal lattice, via a charge compensation mechanism.[26] The dopant species also tend to act as nucleating centres for vacancy clusters. The conductivity increases with dopant concentration up to a maximum and then decreases, as was seen in zirconia.[27] Gadolinium and samarium, used as dopants, offer the highest conductivity in ceria based materials, due to their lowest size mismatch.[28,29] As with zirconia, co-doping has been used to further improve the conductivity of ceria based materials.[30] Other dopants used in ceria based materials include lanthanum, yttrium, ytterbium, and neodymium.[31] However, there is still a great need for a better understanding between the dopant species and the resulting conductivity in these materials.

The main drawback of doped ceria compounds is the reduction of Ce^{4+} to Ce^{3+}, at temperatures above *ca*. 600 °C, which gives rise to electronic conductivity and an expansion of the lattice, which induces mechanical failure.[32,33,34]

1.3.1.3 Bi_2O_3- based electrolytes

Bismuth oxide undergoes a phase transition at ~730 °C, which is accompanied with almost two orders of magnitude increase in conductivity.[35,36] This high temperature phase has a face centred cubic array of Bi^{3+} cations, with the oxide ions randomly spread over three quarters of the tetrahedral interstices. The oxygen sub-lattice contains a high concentration of vacancies, which is the reason for its high oxide ion conductivity. This phase (δ-Bi_2O_3) shows the highest conductivity ($\sigma \approx 2.3$ S cm^{-1} at 800 °C) amongst all the oxide ion conductors.[5,37] However, this phase has a narrow temperature range of stability between 730 °C and its melting point at approximately 830 °C.[38] At temperatures below 730 °C, depending on cooling conditions, this phase transforms to either the monoclinic α-phase, the cubic γ-phase or the tetragonal β-phase, all of which have lower ionic conductivity.[39]

Solid solution formation with other oxides has been used extensively, in attempts to stabilise the high temperature phase at lower temperatures.[40,41,42] It was thus shown that the optimum conductivity can be achieved for the lowest concentration of the substituent cations necessary to stabilize the high temperature δ-phase at lower temperatures.[43,44] Bi_2O_3-based materials possess several disadvantages, such as low stability in reducing atmospheres and low mechanical strength.[45,46]

1.3.2 Perovskite and related intergrowth structures

The ABO_3 perovskite structure, **Fig. 1.3**, allows for a large choice of doping with cations of lower valence either on the A or the B sites. The lattice, therefore contains a large concentration of mobile oxygen vacancies, leading to high oxide ion conductivities.[8] These materials are therefore most promising for electrolytic applications.[16]

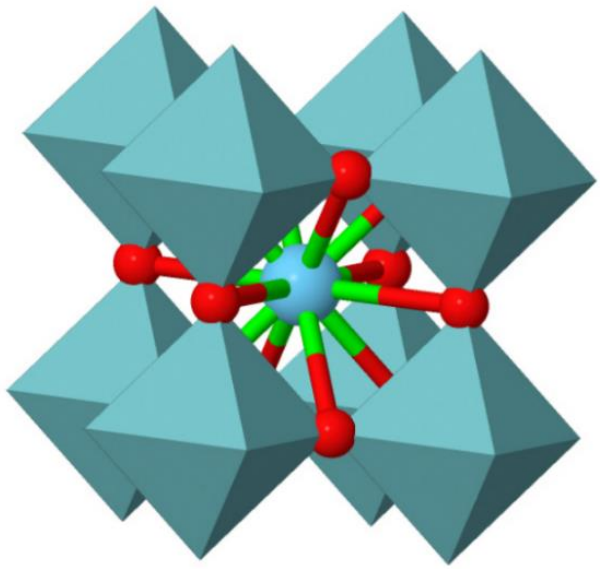

Fig. 1.3 Crystal structure of cubic perovskite, ABO_3, showing the corner-shared AO_6 octahedra with the B cations (large cyan atom) centred on 12-coordinate sites. The small red spheres are O atoms.

1.3.2.1 $LaGaO_3$-based electrolytes

Goodenough & co-workers and Ishihara & co-workers first reported the high ionic conductivity of $La_{0.9}Sr_{0.1}Ga_{0.8}Mg_{0.2}O_{2.85}$ (LSGM).[47,48] This material was shown to possess higher conductivities than YSZ at intermediate temperatures, with ionic conductivity over a wide range of oxygen partial pressure ($10^{-20} < pO_2 < 1$).[49,50] Computational studies have revealed that ionic conductivity proceeds via a vacancy hopping mechanism, along the GaO_6 octahedron edge.[51] Transition metals, such as cobalt and iron have been used as dopant to further improve on the conductivity of LSGM.[52,53] Achieving processing conditions for fabricating single phase microstructures of LSGM remains a challenge. Additionally, volatility of gallium at high temperatures and its chemical instability under oxidising and/or reducing conditions have further hindered the use of LSGM in electrolytic applications.[30,54,55,56]

1.3.2.2 Brownmillerite-like phases derived from $Ba_2In_2O_5$

The brownmillerite-type structure, $A_2B_2O_5$, consists of corner-shared BO_6 octahedra alternating with layers of corner-shared BO_4 tetrahedra. The brownmillerite-type crystal structure is only possible for B cations that are able to form both octahedral and tetrahedral coordination geometries, as is the case for Al^{3+}, Ga^{3+}, In^{3+}, and Ge^{4+}. This structure type is a derivative of the perovskite structure, where the oxygen vacancies are ordered into alternate BO_2 sheets.[57 58]

Partial substitution of $Ba_2In_2O_5$ has been shown to lead to high conductivity materials.[59] The highly-conductive, disordered cubic, perovskite structure can be stabilised at intermediate temperatures via the substitution of In with cations such as Zr^{4+}, Ce^{4+}, Sn^{4+} or Hf^{4+}.[60,61] Thus, at intermediate temperatures, doped $Ba_2In_2O_5$ shows an ionic conductivity that is higher than stabilized zirconia.[62] Nevertheless, there are significant challenges to be overcome in the practical use of $Ba_2In_2O_5$-based materials, due to their low stability in humid atmospheres and in the presence of CO_2.[63,64]

1.3.2.3 BIMEVOXes

The crystal structure of the BIMEVOXes is derived from the parent oxide $Bi_4V_2O_{11}$. Its lattice consists of $(Bi_2O_2)_n^{2n+}$ layers alternating with perovskite-like $(VO_{3.5})_n^{2n-}$ layers, **Fig. 1.4**. These materials contain a large concentration of oxygen vacancies, with the potential for high ionic conductivity.[20,65]

Complex polymorphism is seen in these materials, derived from three main phases, α, β and γ.[66] The highly conductive γ-phase can be stabilised at room temperature via the substitution of V with a range of iso- and aliovalent cations, such as Cu^{2+}, Ni^{2+}, Co^{2+}, and Mg^{2+}. Total conductivities have been shown to be almost purely ionic in nature, at temperatures above 630 °C.[8] However, BIMEVOXes do possess some crucial disadvantages, such as low stability in reducing atmospheres and low mechanical strength.

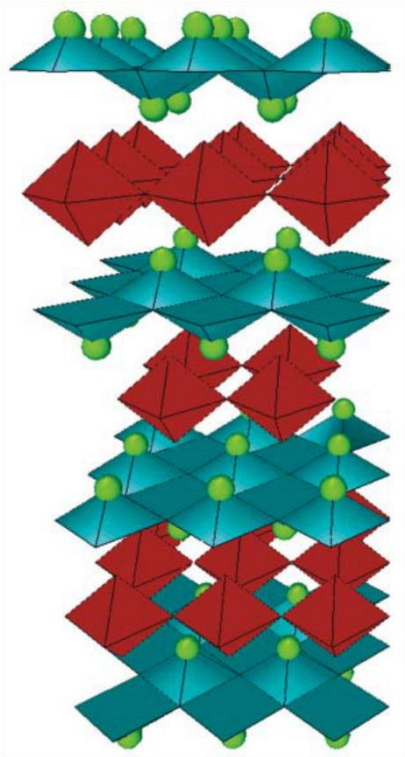

Fig. 1.4 Idealized γ-$Bi_4V_2O_{11-\delta}$ structure. Red octahedra represent VO_6, blue pyramids represent BiO_4, and green spheres represent Bi atoms.[66]

1.3.3 New oxide-ion conductors

As described above, many conventional materials with high ionic conductivity are known, with some already in practical use. However, their widespread application is still limited by several drawbacks, such as high operating temperatures, partial electronic conductivity and/or poor chemical stability. These issues have hinted on the need to develop new materials with improved properties. In this section, the most recent advances in the development of novel oxide-ion conducting materials are highlighted.

1.3.3.1 $La_2Mo_2O_9$ (LAMOX)

First reported by Lacorre *et al*. in 2000, $La_2Mo_2O_9$ (LAMOX) is a fast oxide ion conductor, with a conductivity surpassing that of YSZ.[67] The crystal structure of LAMOX shows a first order phase transition at approximately 580 °C, where it transforms from the non-conductive α-phase to the highly-conductive β-phase, which shows a maximum conductivity of 6×10^{-2} S cm^{-1} at 800 °C.[68] The β-phase may be stabilised at room temperature by doping with group one (e.g., K^+ and Rb^+) or group two (e.g., Ca^{2+} and Ba^{2+}) cations onto the La site.[69,70,71]

LAMOX materials do, however, possess low chemical stability under reducing conditions, leading to reactivity with the electrode materials. Additionally, the total conductivity of these materials tends to have a considerable electronic contribution at low oxygen partial pressures. These disadvantages of LAMOX materials rather limit their use in electrolytic applications.[69]

1.3.3.2 Apatites

Apatite type oxides are a very interesting class of new materials being considered as alternative materials for SOFC electrolyte applications.[72] The apatite structure, **Fig. 1.5,** with general formula $M_{10}(XO_4)_6O_{2\pm y}$ where M stands for a lanthanide cation and X is a *p*-block element, allows for a large variety of dopants on both the M and X sites. The crystal structure of these materials is thus very flexible to local distortion and volume changes.[73]

The conductivity of these materials depends crucially on non-stoichiometry; the stoichiometric compositions in terms of cations and anions have very low conductivities. In these material types, the mechanism of conductivity is of interstitial-type transport, which is enabled by the high concentration of defects such as interstitial oxide ions. This is in contrast to the mechanism of ionic conductivity found in fluorite and perovskite materials, where conductivity occurs via a vacancy hopping mechanism.[74] Additionally, the conductivity in the apatite structure is anisotropic and shows an optimum value in the direction of the *c*-axis. Of particular interest amongst the apatite type materials, are apatite silicates and germanates, which have been shown to have high ionic conductivities at intermediate temperatures.[75] [76]

As would be expected from a new material under study, there are several disadvantages associated with these material types. In particular, they are difficult to synthesise, as very high temperatures (>1600 °C) are required. Therefore, finding new, more efficient, methods of synthesis has become a research challenge.[77] The ionic conductivity of these materials has been shown to improve with extra addition of oxygen, however, the non-stoichiometry range supported by the apatite crystal structure is very narrow.[8]

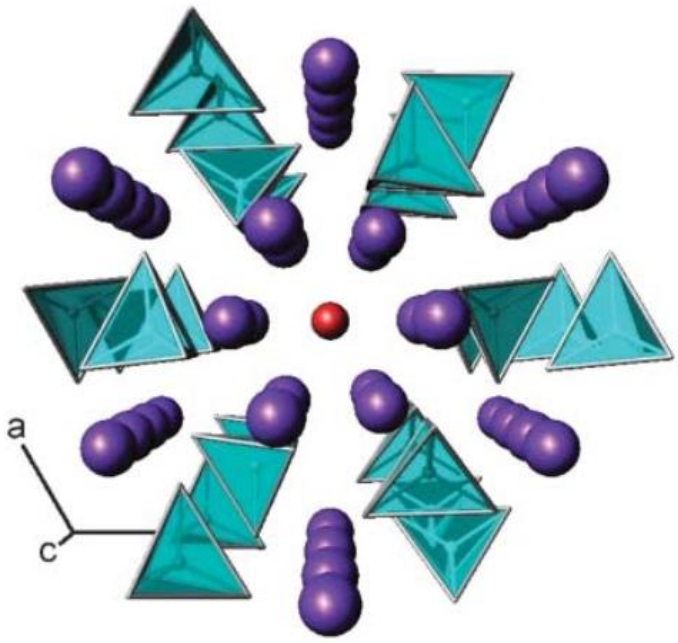

Fig. 1.5 The apatite structure, $M_{10}(XO_4)_6O_{2\pm x}$, (tetrahedra = XO_4, purple spheres = M, red spheres = O).[72]

1.4 Pyrochlore oxides

1.4.1 Crystallography

The pyrochlore crystal structure ($A_2B_2X_6Y$) is a 2 ×2 × 2 superstructure derivative of the fluorite type structure (AX_2), where both cation and anion vacancies are ordered.[78,79] The fully ordered pyrochlore structure crystallizes in the cubic space group $Fd\bar{3}m$ (i.e. *F* $4_1/d$, $\bar{3}$, 2/*m*, No. 227, where *F* stands for face centred cubic centring, 4_1, is a four-fold screw axis with a translational component of ¼, *d* is a 'diamond' glide plane, $\bar{3}$ is a 3-fold inversion axis, 2 is a two-fold rotational axis and *m* is a mirror plane), with eight formula units per unit cell. This space group contains two possible origin choices, with origin choice two being the most commonly used. Origin choice two places the smaller B-site cations at the 16*c* (0, 0, 0) site and the larger A-site cations at the 16*d* (1/2, 1/2, 1/2) site. The structure consists of three distinct tetrahedral anion sites (8*a*, 8*b*, and 48*f*), with one of the anion sites (site 8*b*) being vacant in the fully ordered structure. The A-site cations are the larger trivalent lanthanide cations, and the B-site cations are the smaller tetravalent transition-metal or main group cations (e.g., Ti^{4+}, Zr^{4+}, Hf^{4+}). X and Y are typically oxygen anions, but can include OH^- and F^- anions. The A-site cation is 8-coordinate within a distorted cubic polyhedron, while the B cation is 6-coordinate within a distorted octahedral environment, **Fig. 1.6**. [80]

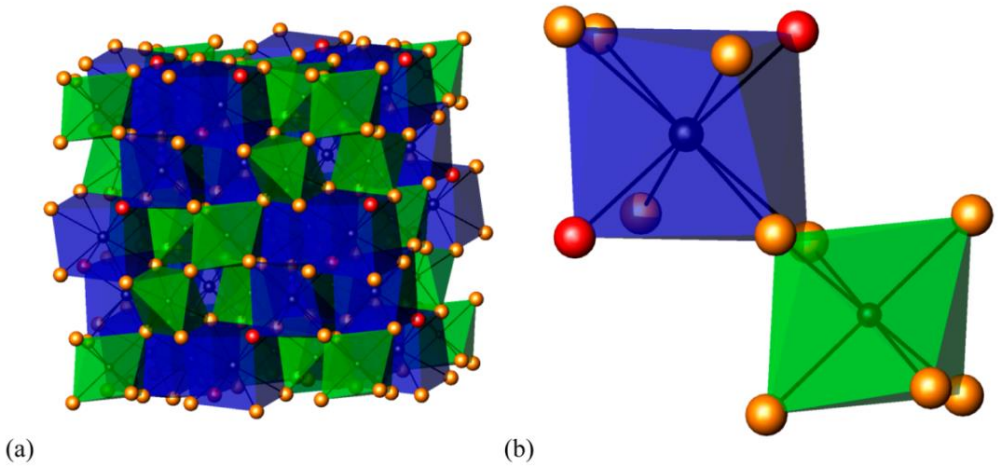

Figure 1.6 (a) The pyrochlore structure, $A_2B_2O_7$, showing the A-site (blue) and B-site (green) polyhedra, and (b) the local coordination environment around the A- and B-site cations. The O(1) and O(2) oxygen atoms located at the 48*f* and 8*b* sites are shown as gold and red balls, respectively.[81]

The phase stability of the pyrochlore structure is determined by the relative ionic radii i.e the ionic radius ratio, r_A/r_B, and the 48*f* oxygen positional parameter *x*.[82,83,84] The r_A/r_B for stable pyrochlore compounds has been shown to lie between 1.46 ($Gd_2Zr_2O_7$) and 1.78 ($Sm_2Ti_2O_7$) under ambient conditions, however, this may be increased to the range of 1.29–2.30 by high-pressure, high-temperature, synthesis.[79,85] The pyrochlore structure may contain considerable amounts of cation anti-site disorder, depending on composition and the synthesis route of the material.[78,86,87] The crystal structure allows for a large degree of substitutional and/or displacive disorder on the A-site, as result of the weak interactions between the B_2O_6 and A_2O' sub-lattices.[84,88,89] Order-disorder transformations, **Fig. 1.7**, are commonly seen in compounds with the pyrochlore structure. The order–disorder transformation occurs simultaneously on both the cation and the sub-lattice. However, the cation and anion disordering may occur to different degrees and at different rates.[90,91,92]

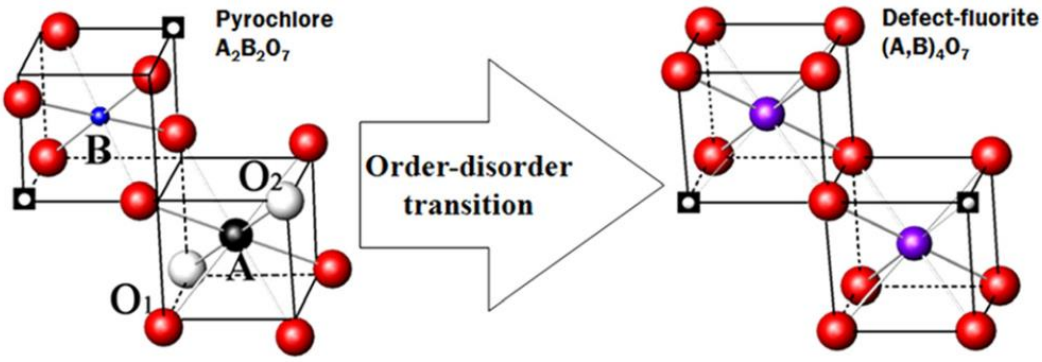

Figure 1.7 Order-disorder transition between the ordered pyrochlore structure, $A_2B_2O_7$, and the disordered defect-fluorite $(A/B)_4O_7$ structure. Red balls represent oxygen atoms and the squares with holes represent anion vacancies.[93]

1.4.2 Ionic conductivity

Pyrochlore oxide materials have been shown to possess high ionic conductivities and thus are promising electrolytes materials for SOFC applications.[30,88,94,95,96] What is especially interesting about pyrochlore oxides, is the fact that their electrical behaviour spans from those of insulators through semiconductors and onto fast ionic conductors. This is as a result of the ability of the pyrochlore structure to accommodate a wide range of cations and both the A- and B-sites. At high temperatures, pyrochlore oxide materials are intrinsic ionic conductors, with their conductivity being comparable to that of YSZ.[97,98,99] However, these compounds have relatively low oxide ion conductivity at intermediate temperatures (700–800 °C) and thus, need further improvement in conductivity, in order to meet the requirements of IT-SOFCs.

In order to achieve high levels of oxide ion conductivity, the pyrochlore structure must contain a high concentration of mobile oxygen vacancies coupled with a low activation energy for ion migration. The vacancy concentration is in turn determined by the presence of Frenkel defects, which is substantially encouraged by the presence of disorder in the cation sub-lattice.[86,95,100,101,102] Cation disordering can be further enhanced by either increasing the average size of the cations at the B-site or by decreasing the average size of the cations at the A-site.[94,103,104,105] Alternatively, structural disorder can be thermally induced in a system with a fixed composition.[102,106,107,108] Nevertheless, compounds showing high degrees of disorder also display higher activation energies for ion migration.[109,107,110] Thus, optimum ionic conductivities are obtained in partially ordered systems.[78,111,112]

Static lattice energy minimization calculations[86] and molecular dynamics simulations[113] indicate that oxygen ion transport in pyrochlore oxide materials occurs via an oxygen vacancy hopping mechanism between the 48*f* sites.[89,110,114] Yamamura *et al*. systematically investigated the relationship between crystal structure and oxide-ion conductivity for various pyrochlore oxides and found that oxide-ion conductivity is strongly dependent on crystal phase, cation radius ratio, and the degree of ordering of oxygen vacancies.[112,115,116] Similarly, Shlyakhtina and Shcherbakova carried out a comprehensive structural and electrical study of $Ln_2M_2O_7$-based (*Ln* = La–Lu, Y, Sc; *M* = Ti, Zr, Hf, Sn) oxides and showed that the M─O bond covalency also plays a significant

role in determining oxide-ion conductivities.[99,117] Furthermore, moving away from stoichiometry diminishes ionic conductivity, as was found in rare earth zirconates,[118] as well as in rare earth titanates.[119]

Conductivity in pyrochlore oxide materials can be further improved via doping at either the A-site,[120,121,122] the B-site,[123,124] or both.[125,126] The effectiveness of the dopant species in enhancing oxide-ion conductivity is crucially dependant on dopant site location ("A" or "B" cation sub-lattice) and on dopant concentration.[127] Ionic conductivity increases initially with dopant concentration, due to the increasing concentration of oxygen vacancies, however, it reaches a maximum after which it declines. The decline in conductivity can be understood in terms of the formation of defect clusters, which act to trap mobile oxygen vacancies.

1.4.2.1 Titanate pyrochlore oxides

Rare earth titanate pyrochlore oxides have been shown to possess high oxide ion conductivities, with some surpassing that of YSZ.[128,129,130] The conductivity of un-doped $Gd_2Ti_2O_7$ is low, due to low levels of intrinsic anion disorder and therefore low concentration of mobile oxygen vacancies. On the other hand, pyrochlore-type $Gd_2Zr_2O_7$ demonstrates substantial structural disorder which induces ionic conductivity as high as 0.01 S cm^{-1} at 900 °C.[131] Therefore, the $Gd_2(Zr_xTi_{1-x})_2O_7$ pyrochlore is an extrinsic ionic conductor at low Zr concentrations, however it becomes an intrinsic fast-ion conductor at large Zr concentrations.[107,127,]

Substitution of Gd^{3+} by Ca^{2+} was found to be very effective in enhancing ionic conductivity in $(Gd_{1-x}Ca_x)_2Ti_2O_{7-\delta}$ (x = 0.05–0.10), where conductivities as high as 0.02–0.03 S cm^{-1} at 900 °C were achieved.[104,132] However, the solubility of calcium in the gadolinium sub-lattice is limited to no more than 7 atomic%.[127] Mo-doped $Gd_2Ti_2O_7$, on the other hand, has been shown to be a mixed ionic and electronic conductor.[133]

Incorporation of calcium cations into the ytterbium sub-lattice in $Yb_2Ti_2O_7$ increases the ionic conductivity from 1×10^{-2} S cm^{-1} to ~0.2 S cm^{-1} at 1000 °C in $(Yb_{0.9}Ca_{0.1})_2Ti_2O_{6.9}$, which, to the best of my knowledge, is the maximum value observed for all rare earth pyrochlore oxides.[134] Further A-site doping in the $(Yb_{0.9-x}Tb_xCa_{0.1})_2Ti_2O_{7-\delta}$ (x = 0.1, 0.2, 0.3, 0.4) pyrochlores was shown to have no significant effect on the bulk component of their oxide-ion conductivity.[135]

Other pyrochlore-type titanate compounds include systems of the form $Ln_{2+x}Ti_{2-x}O_{7-x/2}$, which consist of a disordered pyrochlore structure with significant amounts of cation anti-site defects. These systems have been shown to possess a maximum ionic conductivity of 10^{-3} S cm^{-1} at 740 °C.[136]

1.4.2.2 Zirconate pyrochlore oxides

In rare earth zirconate pyrochlore oxide materials, the highest oxide ion conductivity is seen in the stoichiometric zirconates of the intermediate lanthanide systems (*Ln* = Sm–Gd), which are always intrinsically disordered.[97,106,109] Yamamura *et al*. reported the oxide-ion conductivity of the fluorite and pyrochlore phases in the $Ln_2Zr_2O_7$ systems.[112] It was thus shown that oxide-ion conductivity increases with increasing ionic radius ratio in the fluorite phase range, up to a maximum (8.3×10^{-3} S cm^{-1} at 800 °C) in the vicinity of the phase boundary in the pyrochlore phase range, after which it decreases.

$Gd_2Zr_2O_7$ has the highest intrinsic ionic conductivity (~10^{-2} S cm^{-1} at 700 °C) amongst the un-doped pyrochlore compounds.[78,137] However, in order to further improve the ionic conductivity of these materials, various dopants have been incorporated at the Gd^{3+} site.[138,139,140] For example, replacement of Gd^{3+} by Nd^{3+} in $Gd_2Zr_2O_7$ was shown to progressively increase oxygen vacancy ordering, which resulted in an order of magnitude increase in ionic conductivity at an Nd concentration of 50 mol%.[138] The relationship between structural disorder and the resulting enhancement of ionic conductivity was also observed in the $Gd_2(Sn_{1-x}Zr_x)_2O_7$ (GSZ) system.[141]

Yamamura *et al*. reported pyrochlore-type $La_2Zr_2O_7$ materials with a conductivity of 4.2×10^{-4} S cm^{-1} at 800 °C,[112] which is much lower than that of YSZ (~2.5×10^{-2} S cm^{-1} at the same temperature).[19] On the other hand, Ou *et al*. reported $La_2Zr_2O_7$ nanofibers possessed a maximum conductivity of 0.016 S cm^{-1} at 500 °C, which is ~400 times higher than that of the previously reported bulk $La_2Zr_2O_7$.[142] Yang *et al*. carried out a systematic study into the system $(La_{1-x}Y_x)_2Zr_2O_7$ ($0 \leq x \leq 1$).[143] They found that conductivity increased consistently with increasing Y concentration up to the pyrochlore/fluorite phase boundary (x = 0.5), due to increased concentrations of mobile oxygen vacancies. However, once the system had transformed to the fluorite structure, further increase in Y concentration decreased conductivity, due to increased activation energy for migration. Thus, optimum conductivity was obtained near the pyrochlore-to-fluorite phase boundary.

1.4.2.3 Hafnate and ruthenate pyrochlore oxides

The ionic conductivity of hafnate pyrochlore oxides was found to be lower than that of the zirconate analogues. This was attributed to the higher degree of covalency in the Hf–O bonds, which leads to an increase in the bond strength and hence the activation energy for migration increases.[144] On the other hand, the total conductivities of ruthenate pyrochlores ($Bi_2Ru_2O_7$ or $Pb_2Ru_2O_{6.5}$) are dominated by a high electronic contribution (10-1000 S cm^{-1} at room temperature).[145,146] Electrical characterization of R_2MnRuO_7 (R = Tb, Dy, Ho, Er, Tm, Yb, Lu and Y) showed these systems to exhibit semiconducting behaviour, with the highest conductivity possessed by the Er_2MnRuO_7 system, reaching a maximum value of 8.9 S cm^{-1} at 900 °C.[147]

1.5 Aims and objectives

In this thesis, attempts have been made to synthesise a range of pyrochlore type oxides that exhibit significant oxide ion conductivity. The co-precipitation method was used to prepare the materials studied. Unlike traditional solid-state synthesis, co-precipitation allows the cations to be homogeneously distributed, and thus significantly reduces the sintering temperature and time, to produce ceramics with densities close to the theoretical values.

X-ray and neutron diffraction techniques have been used to experimentally determine the extent to which substitutional changes affect the crystal structure and the local environment of pyrochlore oxides, particularly with respect to the fluorite/pyrochlore phase boundary. Upon substitution into the system, the cations become disordered, making positional determination of the oxygen atoms especially difficult. Neutron scattering can provide insight to a material that would otherwise be unattainable through X-ray diffraction. A qualitative interpretation of the neutron diffraction data is given via Reverse Monte Carlo (RMC) modelling.

The electrical conductivity of the sintered specimens was measured by a dc two-probe method, in the temperature range 150 - 800 °C. Based on the results, the trend of bonding with the chemical valence and coordination number is analysed, and the relationship between bonding and the conductivity properties is discussed. A mechanistic understanding of the disordering processes and the resulting electrical conductivity properties in these materials has been constructed by matching the structural predictions (both average and local) with electrical conductivity observations.

Chapter 2 details the experimental techniques and programs used to produce the atomistic configurations. Chapter 3 details the structural and electrical study into the $(Yb_{1-x}Nd_x)_2Zr_2O_7$ with $0.00 \leq x \leq 1.00$ system, which is known to undergo the fluorite/pyrochlore transition.[148] Chapter 4 details the study of the effects of aliovalent doping in the system $(Nd_{1-x}Ca_x)_2Zr_2O_{7-x}$ with $0.00 \leq x \leq 0.50$, where particular emphasis is paid to the increased vacancy concentration and the resulting electrical conductivity. Finally, in chapter 5 the effect of cation ordering in cerium zirconate oxides is investigated. A number of fluorite/pyrochlore related phases are identified.

Chapter 2 – Methods

2.1 Chapter overview

A number of methods have been used to characterise the materials synthesised in this thesis, including X-ray and neutron diffraction, and alternating current (AC) impedance spectroscopy. In this chapter, the background and justifications of the use of these methods are introduced. Details of the samples synthesised, as well as the general synthetic methods, are given along with instrumental and operational parameters for the characterisation methods. Specific details of the studied systems are given in the subsequent chapters.

2.2 Materials synthesis

The conventional solid-state reaction technique is commonly implemented, due to its ease and simplicity of set up. The method does, however, possess some major disadvantages such as high calcination temperature, uneven particle size distribution, and poor sintering of the products. Alternative synthesis methods have been sought in the literature, which aim to achieve an atomic-scale mixture of the reactants that would lead to enhanced materials' diffusion and homogeneity. To mention but a few of these techniques: solution combustion synthesis, co-precipitation, sol–gel, and hydrothermal methods.[149]

The compounds investigated in this thesis, **Table 2.1**, were synthesised via the co-precipitation method. Stoichiometric amounts of the zirconium ($ZrOCl_2 \cdot 8H_2O$) and lanthanide (Ln_2O_3) cation precursors were dissolved in distilled water and hydrochloric acid (2 M) respectively. The solutions were warmed gently, to aid dissolution, when necessary. Ammonia solution (2 M) was added to the mixed solution, until it reached a pH of 11. The resulting precipitate was filtered and washed several times with water and then ethanol. The precipitate was then dried at 80 °C in an oven. The hydrate powder decomposed to a polycrystalline oxide upon heating to 900 – 1500 °C for 12 h.

Table 2.1 Compounds studied in this thesis

Ytterbium/neodymium zirconate (Chapter 3)		Neodymium/calcium zirconate (Chapter 4)		Cerium zirconate* (Chapter 5)
$(Yb_{1-x}Nd_x)_2Zr_2O_7$		$(Nd_{1-x}Ca_x)_2Zr_2O_{7-\delta}$		$Ce_2Zr_2O_{7+\delta}$
Composition	Annealing temperature / °C	Composition	Annealing temperature / °C	Annealing temperature / °C
$x = 0.00$	1150	$x = 0.10$	1350	500
$x = 0.25$	1150	$x = 0.20$	1350	1000
$x = 0.50$	1150	$x = 0.30$	1350	1500
$x = 0.75$	950	$x = 0.40$	1350	
	1150	$x = 0.50$	1350	
	1350			
$x = 1.00$	950			
	1150			
	1350			

*original samples for neutron diffraction were synthesised by the group of Dr S. Hull, ISIS Facility, Rutherford Appleton Laboratory, UK.

2.3 Powder diffraction

2.3.1 The crystalline state

The crystalline state of solid materials is characterised by long range-internal order of its atomic constituents, manifested by symmetry operations such as translational, rotational, reflection, and inversion symmetry.[150] On the other hand, amorphous materials are those that lack this internal long-range ordering, although they may show well defined short-range ordering of atoms. Having said that, a real crystalline material is far from perfect, as it always contains a number of defects, such as interstitial atoms, vacancies or atoms replaced by another chemical species.[151] Defects will be spread randomly when found in small concentrations such as in the form of impurities, however they will tend to influence each other at higher concentrations. This influence may result from a small

charge imbalance or a slight geometrical distortion of the local environment. This can result in clustering of individual point defects. While changes in the random distribution of defects can result from this, in many cases the clusters themselves may be randomly distributed, making the identification of defect clustering over random distributions of point defects difficult. Many of the physical and chemical properties of crystals depend on the presence of defects, and a thorough understanding of these defects is necessary to understand these physical properties.[152]

2.3.2 Structural characterisation of crystalline materials

Diffraction techniques are the methods of choice for structural elucidation of crystalline materials.[153] Diffraction is the process of scattering of incident radiation by a material with internal periodic order, involving constructive and destructive interference of the scattered radiation. The patterns of diffraction reflect the arrangement and distribution of the scattering constituents making up the material under study.[154] For diffraction to occur, the wavelength of the incident radiation must be of the same order of magnitude as the distance between the scattering objects. This ensures that each consecutive beam of the scattered radiation travels a distance equal to an integral multiple of the wavelength, λ, which is necessary for the scattered beams to interfere constructively.[155] These conditions may be summarised using geometry, **Fig. 2.1**, and calculated via Bragg's law, equation 2.1:

$$\lambda = 2d_{hkl} \sin \theta_{hkl} \qquad (2.1)$$

where λ is the wavelength of the incident radiation, the indices h, k and l are three integers (the Miller indices) that uniquely label each lattice plane and hence each intensity maximum ('peak') in the diffraction pattern and d_{hkl} is the interplanar spacing of a specific set of lattice planes, defined by the Miller indices. It thus follows, for diffraction of monochromatic radiation to occur from a particular set of lattice planes, they must be orientated at the correct angle θ_{hkl}, called the Bragg angle, with respect to the incident radiation. In the powder diffraction method, a monochromatic beam of radiation bombards a finely powdered sample, which consists of vast numbers of randomly

orientated crystallites. Thus, at any one time, a number of the crystallites will be correctly orientated with respect to the incident beam, so as to satisfy Bragg's law for every set of lattice planes.

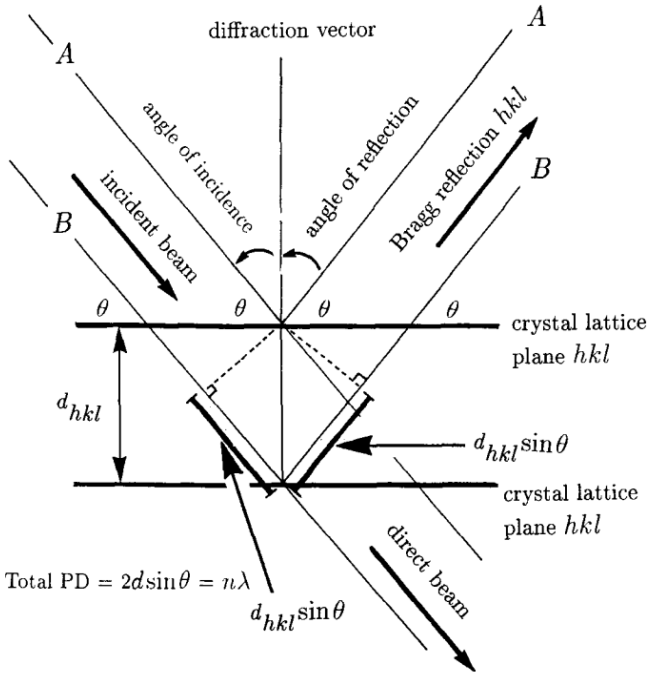

Fig. 2.1 Geometry of diffraction and its relationship to Bragg's Law. Note the definition of θ.[156]

The occurrence of diffraction was first demonstrated by von Laue, Friedrich and Knipping in 1912, who showed that incident X-rays could be diffracted by crystalline solids.[157] The first practical use of the newly discovered phenomenon was then made by the Bragg father-and-son team, who in 1913, successfully determined the crystal structure of sodium chloride. X-rays have wavelengths from ~0.1 to ~100 Å, which are located between γ-radiation and ultraviolet rays in the electromagnetic spectrum, **Fig. 2.2**. X-rays are the simplest, most accessible, and by far the most commonly used radiation in powder diffraction.

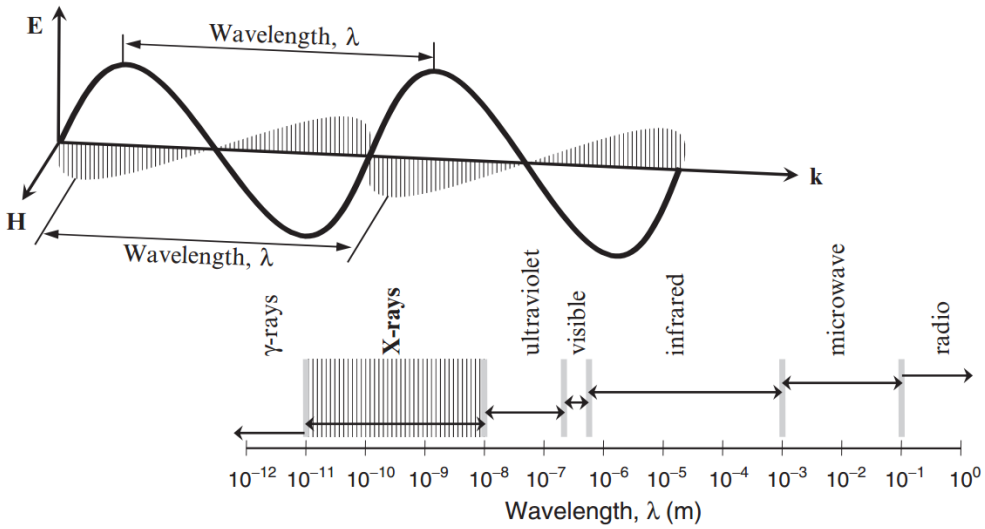

Fig. 2.2 *Top* – schematic of the transverse electromagnetic wave in which electric (**E**) and magnetic (**H**) vectors are mutually perpendicular, and both are perpendicular to the direction of the propagation vector of the wave, **k**. *Bottom* – the electromagnetic spectrum.[158]

A widely used alternative to X-rays in diffraction experiments, are beams of neutrons.[159,160] Neutrons are subatomic particles with no charge and a mass similar to that of the protons (1.675×10^{-27} kg). Neutrons also have a magnetic moment, which arises from the combination of their constituent quarks. Following on from quantum mechanics, fast moving neutrons behave like waves, with wavelength, λ, determined by the de Broglie relation:

$$\lambda = \frac{h}{mv} \tag{2.2}$$

where h is Planck's constant ($h = 6.626 \times 10^{-34}$ Js), m is the particle's rest mass, and v is the particle's velocity ($mv = p$, particle momentum).[161] As with X-rays, scattered neutron beams can therefore reveal the distribution of the internal constituents of crystal structures in reciprocal space. Nevertheless, whereas electrons are scattered almost entirely by electron shells of the atoms, neutrons are scattered mainly by the atomic nuclei. This leads to major practical implications, giving each technique its associated advantages and disadvantages.

In diffraction experiments, the measured intensity of each Bragg peak is directly proportional to the square of the structure factors, F(*hkl*) (*i.e* |F(*hkl*)|^2). Therefore, while the magnitude of the structure factor, |F(*hkl*)|, can be directly obtained, its phase is unknown. This is known as the phase problem of crystallography.[162] Techniques that provide estimated values of the phase of the structure factor (e.g. the Patterson method or direct methods) are employed to determine the structure. Alternatively, as is often used in Rietveld analysis of powder diffraction data, where peak overlap represents an additional complication in structure determination, starting models based on structural analogues are used to provide initial phasing of the structure factors. In both cases, subsequent structure refinement ensures that the crystal structure is consistent with the diffraction data.[163] Techniques such as difference Fourier analysis can be used to locate additional atoms in the model.

2.3.3 Complementarity of X-ray and neutron diffraction

X-ray and neutron diffraction techniques possess strengths and weaknesses that are often complementary to each other, and so the choice of one radiation type over the other, or indeed the use of both radiation types in a single study, is of importance.[164] The X-ray scattering power of each atom in the periodic table increases monotonically with atomic number, **Fig. 2.3**, since X-rays are scattered by electrons and thus the scattering power follows the number of electrons that the atoms possess. This means that elements with similar atomic number will be difficult to distinguish in the crystal structure using X-ray data, since they possess similar X-ray scattering powers. Furthermore, it is difficult to determine the positions of small atoms (i.e. low atomic number) in the presence of large atoms (i.e. high atomic number), due to the relatively small scattering power of the smaller atoms being eclipsed by the larger scattering power of the larger atoms. Interference effects cause the X-ray scattering power of an atom to diminish with increasing wave vector, $\boldsymbol{Q}$, **Fig. 2.4,** which is determined by the inverse of the size of the atom, where the absolute value of $\boldsymbol{Q}$ follows from **Fig. 2.5** as:

$$Q = |\boldsymbol{Q}| = \frac{4\pi}{\lambda}\sin\theta \qquad (2.3)$$

Q determines the length scale that is probed by the diffraction experiment, with small Q corresponding to large distances and large Q corresponding to small distances.

Neutrons can penetrate into matter much further than X-rays, **Fig. 2.6**, due to their relatively weak interaction with matter. This is especially important in the study of bulk phenomena such as phase transitions. The greater penetration depth of neutrons also results in better grain statistics, due to the signal of the incident beam averaging over larger sample volumes. The use of complex equipment for control of sample environments is more readily available with neutron beams. However, this has the disadvantage that long counting times (of the order of minutes and hours) are needed and relatively large samples (1–10 cm^3) are typically required.

The neutron scattering power, or cross-section, σ,[165] of an atomic nucleus defined as:

$$\sigma = 4\pi b^2 \tag{2.4}$$

is independent of atomic number and varies in an irregular manner on moving across the periodic table, **Fig. 2.3**. This means that a lighter element can be a stronger neutron scatterer than a heavier element, and two elements with similar atomic number can have strikingly different scattering powers. When the material under study contains a mixture of light and heavy elements, structural elucidation might only be possible with neutron data.[92, 166]

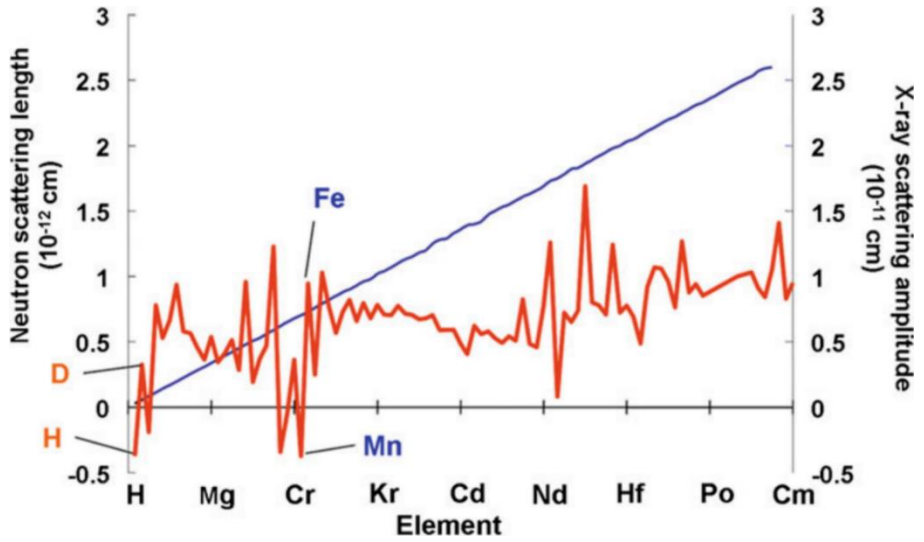

Fig. 2.3 Neutron-scattering lengths, *b*, (red line) and X-ray scattering amplitudes (blue line) for various isotopes (neutrons based on naturally-abundant isotopes unless specifically identified) and elements (X-rays).[167]

Even though with neutrons, elements with similar atomic numbers can be distinguished, there can be other pairs of atoms with very different atomic numbers, but with similar neutron scattering cross-sections (e.g. Cl and Br), which would be better distinguished with X-ray data. None of the elements of the periodic table possesses exceptionally large neutron scattering cross-sections, and so it is never the case where the scattering of one atom is swamped by that of another atom. Furthermore, isotopes of the same element have different scattering powers, which differ not only in magnitude, but also in 'sign', since the scattering process may or may not give a change of phase of π to the wave of the neutron beam. With neutron data, one may use the technique of isotopic substitution, where the neutron scattering cross-section for a chemical species can be altered by changing the isotopic composition.[168]

Due to the very small size of nuclei as compared to the wavelength of the neutron beam, they are considered as 'point' scatterers. Thus the nucleus- neutron scattering power is independent of scattering angle, **Fig. 2.4**. As a result, the diffraction intensities are stronger at higher angles, as compared to those obtained with X-rays. Therefore, a powder neutron diffraction pattern contains considerably more intensity information at high θ values than a powder XRD pattern of the same material. Furthermore, the range of momentum transfer, $\boldsymbol{Q}$, available with neutrons is greater than that with X-rays, because of the $\boldsymbol{Q}$ dependence of the X-ray form factor.

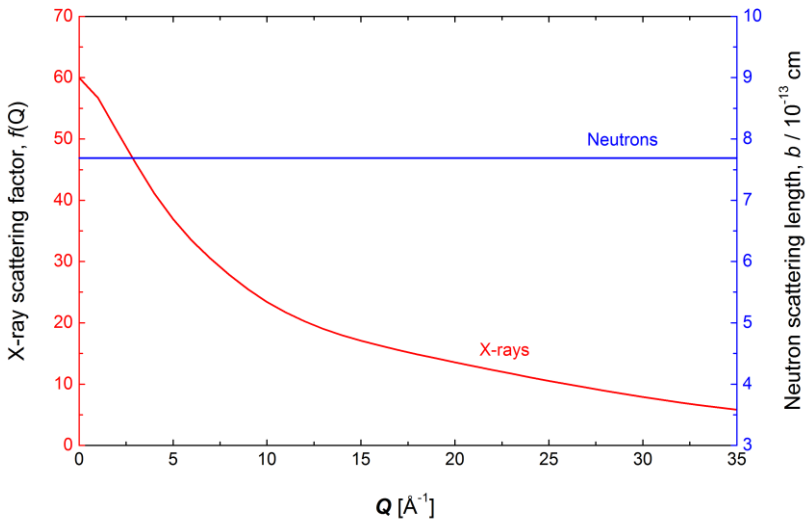

Fig. 2.4 Variation in X-ray scattering factor f (red line) and neutron scattering length b (blue line) for a neutral neodymium atom with wave vector Q.

Neutron diffraction data at high angles pinpoint the location of the atomic nuclei, whereas X-ray data provide information on the distribution of the electron density. This difference is especially important, since it cannot always be assumed that the nuclei reside at the centre of the electron cloud, due to valence effects. Therefore, when high accuracy information needs to be established on the material under study, then neutron diffraction is the technique of choice.

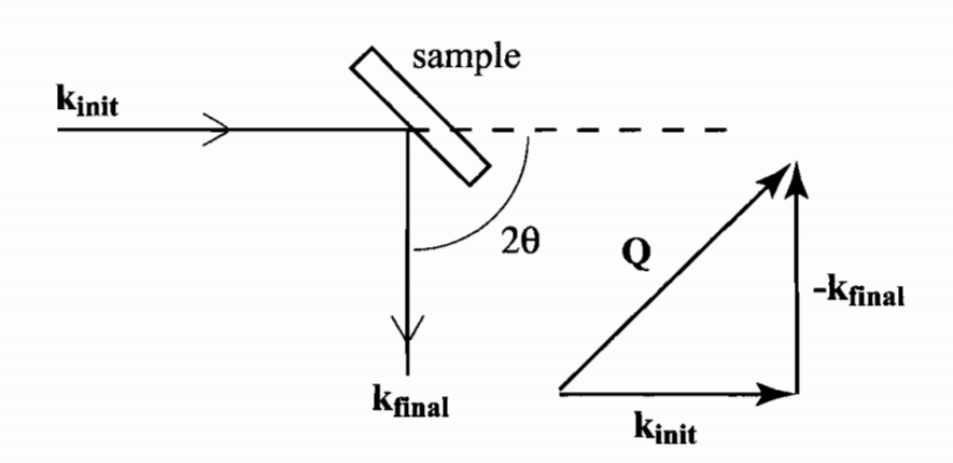

Fig. 2.5 Geometry of the powder diffraction measurement and definition of the scattering vector, ***Q***. [169]

Although neutrons interact mainly with the atomic nuclei, neutrons also have a magnetic moment, which interacts with the magnetic moment of atoms that possess unpaired electrons. Thus, in materials with magnetic atoms (e.g., Mn, Fe), peaks may occur in the diffraction pattern that are solely due to magnetic scattering, from which, magnetic pole figures may be measured. However, if no magnetic super-structures are present in the material under study, the magnetic contribution to scattering is very difficult to separate from nuclear scattering.

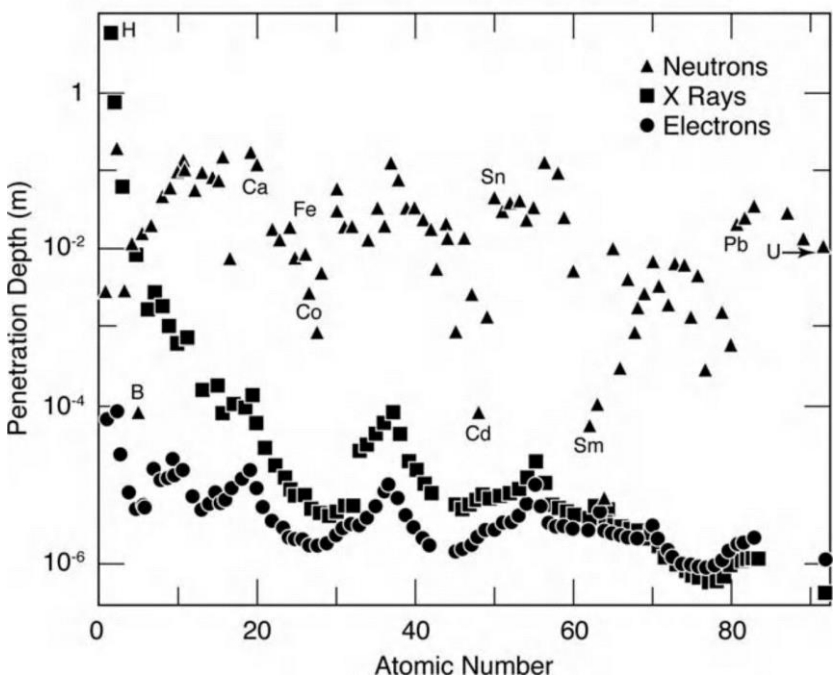

Fig. 2.6 Plot showing how deeply a beam of electrons, X-rays, or thermal neutrons penetrates a particular element in its solid or liquid form before the beam intensity has been reduced by a factor 1/*e*, which is about 37% of its original intensity. The neutron data are for neutrons having a wavelength of 0.14 nm.[170]

The combined use of XRD and neutron powder diffraction data is advantageous over the use of powder XRD data alone or powder neutron diffraction data alone, due to the complementary characteristics of each technique, as described above. However, as the opportunity to record powder neutron diffraction data is much less routine due to the need for central facilities, it is common practice to first determine the structure of the material under study using powder XRD data and then to plan powder neutron diffraction experiments, if various structural aspects cannot be adequately determined from the analysis of the powder XRD data.

Both, XRD and neutron powder diffraction data were used for the structural characterisation of the materials investigated in this thesis. The use of neutron diffraction data was essential for the study of these materials, in order to pinpoint the locations of the oxygen atoms and their vacancies. This is because oxygen atoms display appreciable neutron scattering amongst the much heavier cations.

2.3.4 Data collection and normalization

The depth and breadth of structural information that may be extracted from a powder diffraction pattern is inherent in several factors, such as the nature and energy of the incident radiation and the chemical/physical properties of the specimen. Thus, the choice of instrument and type of radiation is of paramount importance, for a successful outcome of an experiment, especially if the material under study has very subtle details such as a light/heavy atom mixture, etc.

2.3.4.1 X-ray data collection

X-rays are commonly produced, in a laboratory setting, through impacts of high energy electrons with a metal target, in the so-called 'X-ray tube'. Experiments are performed using a fixed wavelength, while treating the scattering angle as the variable quantity, **Fig. 2.7.** The sample and detector are rotated by θ and 2θ, respectively, where the reflected beams form a 'cone' of angle 2θ about the incident beam. Intensities are lower at high angles, thus data are sometimes collected for longer at high angles.

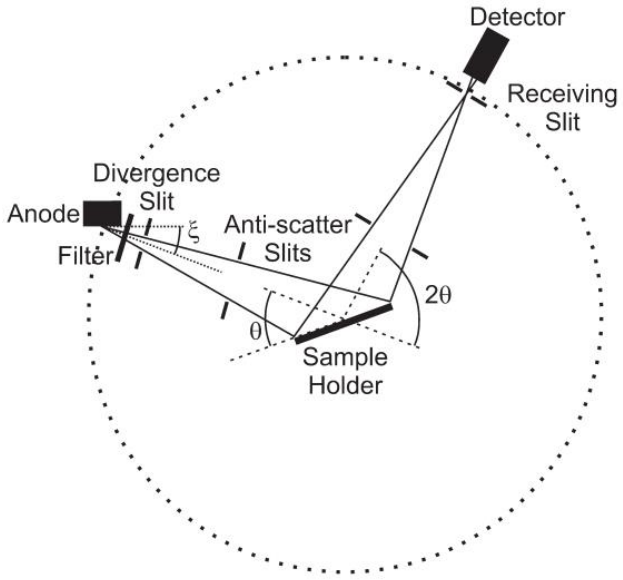

Fig. 2.7 Basic Bragg Brentano geometry. The dotted circle centred on the sample position represents the goniometer circle on which the image of the divergent source of X rays is focussed by diffraction from the flat plate sample. [171]

All the powder samples studied in this thesis, were characterised via X-ray powder diffraction (XRD), using instruments such as a PANalytical X'Pert-Pro or a Siemens D5000. Data were collected using Ni filtered Cu-Kα radiation (λ = 1.5418 Å) at room temperature, in flat plate θ/θ or $\theta/2\theta$ geometry respectively. Data were typically collected over the 2θ range 5 to 120°. For elevated temperature studies an Anton Paar HTK-16 or an Anton Paar HTK-1200 furnace was used over the temperature range 25 to 800 °C in steps of 50 °C. Samples were mounted on a Pt strip inside the camera (HTK-16) or on a Pt coated ceramic disk (HTK-1200).

2.3.4.2 Neutron data collection

Neutron diffraction experiments are performed either with constant wavelength neutron beams at nuclear reactors or with multiple wavelength neutron beams at spallation sources, **Fig. 2.8**, both of which are only available at large-scale, central facilities. In a spallation neutron source, **Fig. 2.9**, highly intense neutron beams are produced via bombardment of a heavy metal target such as tungsten with high energy pulses of protons, **Fig. 2.10**. To obtain wavelengths suitable for diffraction experiments, the neutron pulses are moderated, i.e. slowed down, **Fig. 2.11**, followed by collimation, to produce finely narrowed beams.

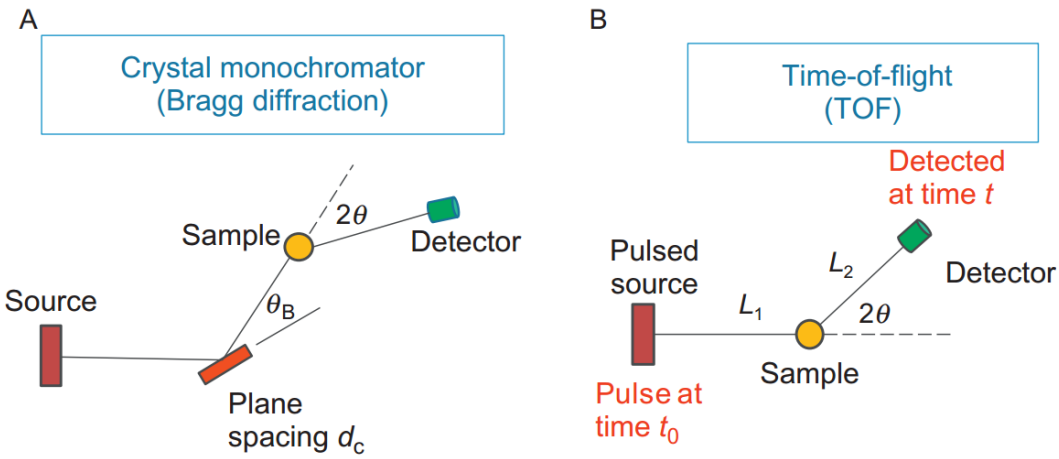

Fig. 2.8 Diffraction techniques: (**A**) crystal-monochromator diffraction and (**B**) time-of-flight diffraction.[172]

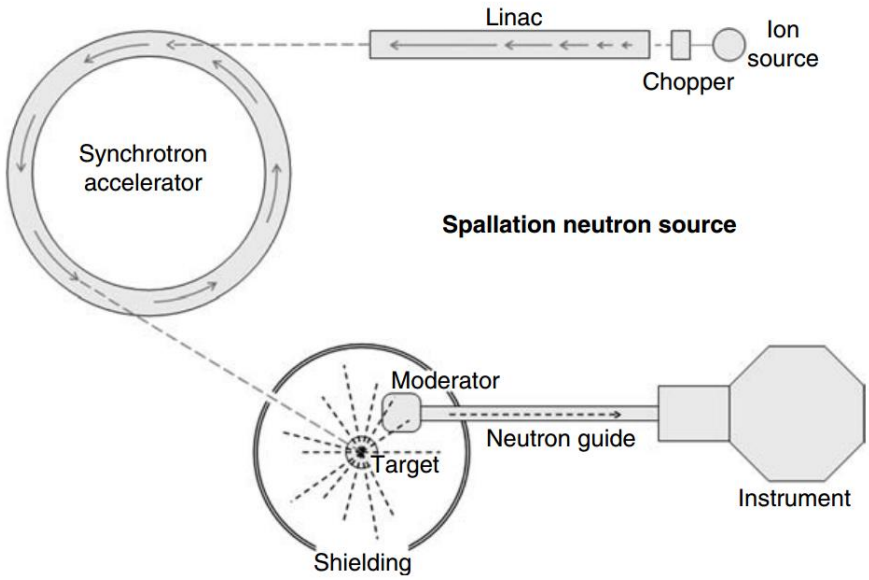

Fig. 2.9 Overview of a spallation neutron source. [173]

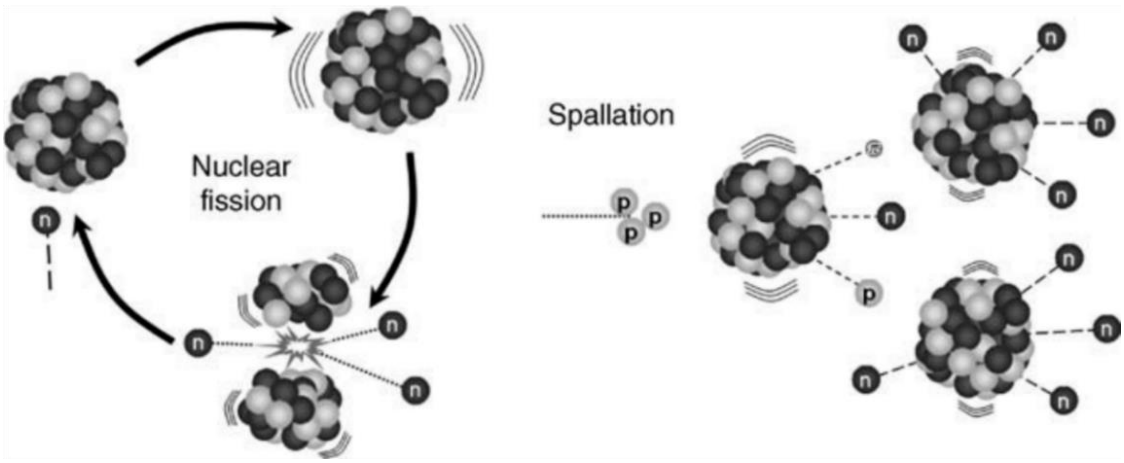

Fig. 2.10 Nuclear reactions: fission and spallation.[173]

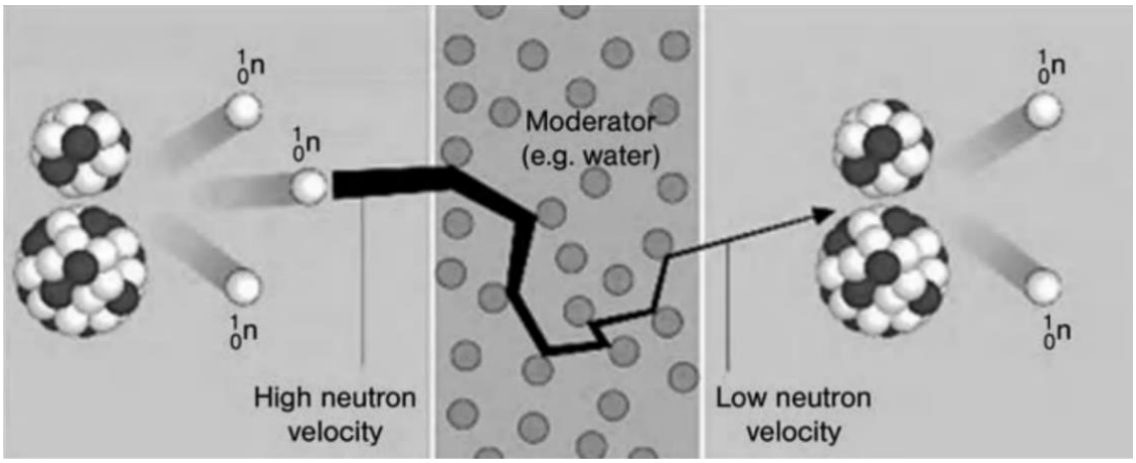

Fig. 2.11 Moderation of neutrons. [174]

Unlike X-rays and other electromagnetic radiation, for which velocity in a vacuum is constant, fast-moving neutrons have an associated velocity that is inversely proportional to their wavelength, through the de Broglie relationship. Therefore, a pulse of neutrons with a range of wavelengths becomes spatially extended along its flight path. The time it takes for neutrons in a single pulse to travel from the source, through the sample, and into the final detector (time-of-flight, TOF) is measured with very high accuracy, **Fig. 2.8 B**, which is equal to the distance divided by its velocity. Given that the distance is also known to high accuracy, the velocity is determined to a similarly high accuracy. The relationship to the wavelength of the neutron beam is:

$$\lambda = \frac{h}{mv} = \frac{ht}{mL} \tag{2.5}$$

From Bragg's law

$$\lambda = 2d \sin\theta = \frac{ht}{mL} \quad \Rightarrow \quad d = \frac{ht}{2mL \sin\theta} \tag{2.6}$$

The total flight time is given by Eqn. 2.7, assuming there is no energy transfer during the scattering process. *L* is, therefore, the total flight path

$$t = \frac{m}{\hbar}(L_1 + L_2)\lambda = \frac{m}{\hbar}\frac{L}{k} \tag{2.7}$$

As the scattering vector value $Q = 2\,k \sin\theta$, Q can be expressed as:

$$Q = \frac{2m}{\hbar}\left(\frac{L \sin\Theta}{t}\right) \tag{2.8}$$

The overall resolution is defined as equation 2.9, in which there are three independent variables: time, flight path, and scattering angle.

$$R = \frac{\Delta Q}{Q}\left[\left(\frac{\Delta t}{t}\right)^2 + \left(\frac{\Delta L}{L}\right)^2 + (cot\Theta\Delta\Theta)^2\right]^{\frac{1}{2}} \tag{2.9}$$

For a properly designed time-of-flight diffractometer, the three variables contribute equally to the resolution. This simplifies equation 2.9 to:

$$R = \sqrt{3}\,\frac{\Delta\lambda}{\lambda} = \sqrt{3}\,\frac{\Delta L}{L} = \sqrt{3}cot\Theta\Delta\Theta \tag{2.10}$$

All the neutron diffraction data presented in this thesis were collected on the Polaris diffractometer at ISIS,[175,176] **Fig. 2.12**. Polaris is a powder neutron diffractometer with medium resolution and high intensity. Its resolution is around 0.33% as the sample position is 14.0 m from the moderator. There are five groups of detectors as in **Fig. 2.13**; the back-scattering detectors have the highest resolution. The sample containers are typically made of vanadium, because this element has little coherent scattering (i.e. no strong Bragg peaks), but it does have appreciable incoherent scattering which contributes to the background. The data were collected over a wide ***Q*** range (between 0.3 to 31.4 $Å^{-1}$), suitable for total scattering analysis.

Fig. 2.12 Aerial view of ISIS and TS2 (the *box-shaped* building in foreground *right*) at the Rutherford Appleton Laboratory, UK. Part of the synchrotron ring Diamond is visible on the *upper right side*. *Photo courtesy of* RAL.

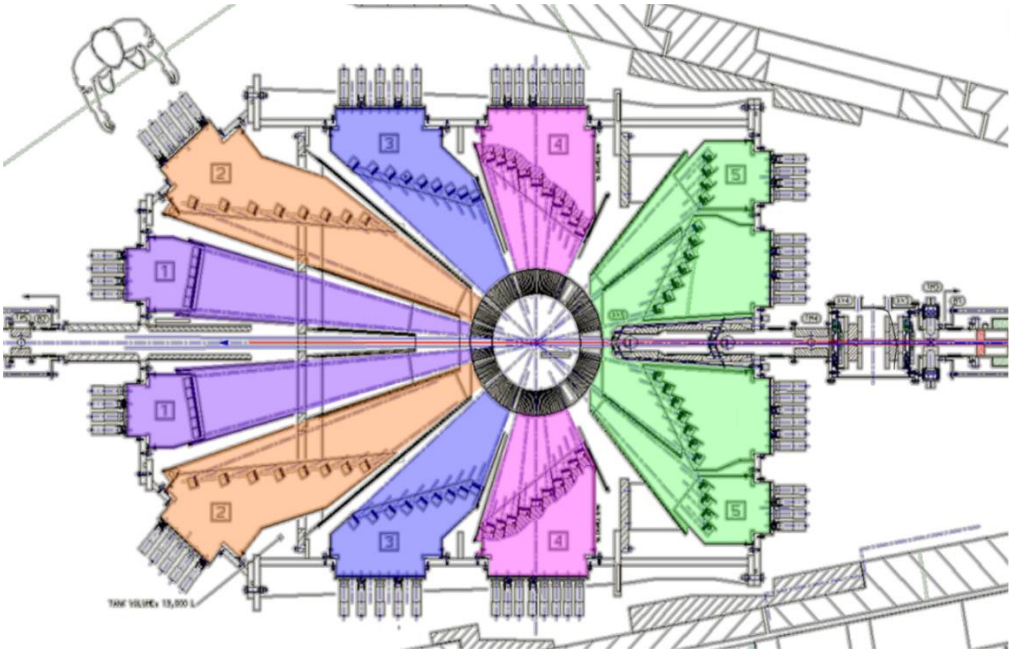

Fig. 2.13 Schematic view of POLARIS with detector banks 1–5 shaded with different colours.[177]

2.3.4.3 Gudrun corrections

The aim of the data corrections is to take the neutron counts as received by the instrument detectors and convert them to the appropriate scattering functions that can be interpreted in terms of the structure of the material. For total neutron scattering analysis, the data should be collected over as wide a range of scattering vectors as possible, and extending to high-*Q*. Therefore, the data need to be collected for longer, in order to measure the weaker, broader diffuse scattering with sufficient statistics. The data are then normalised accurately and placed on an absolute scale; this is done using vanadium, which, for neutrons, has a small coherent scattering length.

The data presented in this thesis were corrected using the program Gudrun, which is the ISIS data correction and normalisation toolkit for total scattering data.[178] Gudrun treats the experimental data for background, absorption, multiple-scattering etc. and produces normalised total scattering data. There are two separate processes that are run, in order to analyse diffraction data collected at a spallation source using Gudrun, namely Purge and Gudrun itself. The Purge portion of the program checks for non-functioning or noisy detectors, thereby eliminating them from the analysis in the subsequent summing of the groups. The Gudrun portion of the program then calculates the differential cross section (DCS) from the TOF diffraction data in the following steps:

(i) Subtract background
(ii) Normalize to calibration
(iii) Subtract multiple scattering
(iv) Apply absorption corrections
(v) Divide by number of atoms in sample

Scattering functions in both reciprocal space, S(*Q*), and real space, G(*r*) and D(*r*), are produced as output files.

2.3.5 Data analysis

2.3.5.1 Diffuse scattering

The diffraction patterns of crystalline materials with considerable amounts of disorder consist of sharp Bragg peaks, as well as diffuse peaks observed as broad undulations in the background scattering, **Fig. 2.14**. Diffuse scattering is associated with short-range atomic order and/or short-range magnetic order.[179,180] As the extent of disorder increases, the Bragg intensities decrease, but diffuse scattering increases, until for highly disordered crystals only a few Bragg peaks are observed.[181]

Bragg diffraction contains information about the distribution of atoms on an absolute scale, whereas diffuse scattering contains information about the arrangements of atoms relative to each other. Thus, for a full structural elucidation of disordered crystalline materials, information from both, Bragg and diffuse scattering, is required.[182,183] For the purposes of the work carried out in this thesis, only the short-range atomic order, as opposed to magnetic order is of interest.

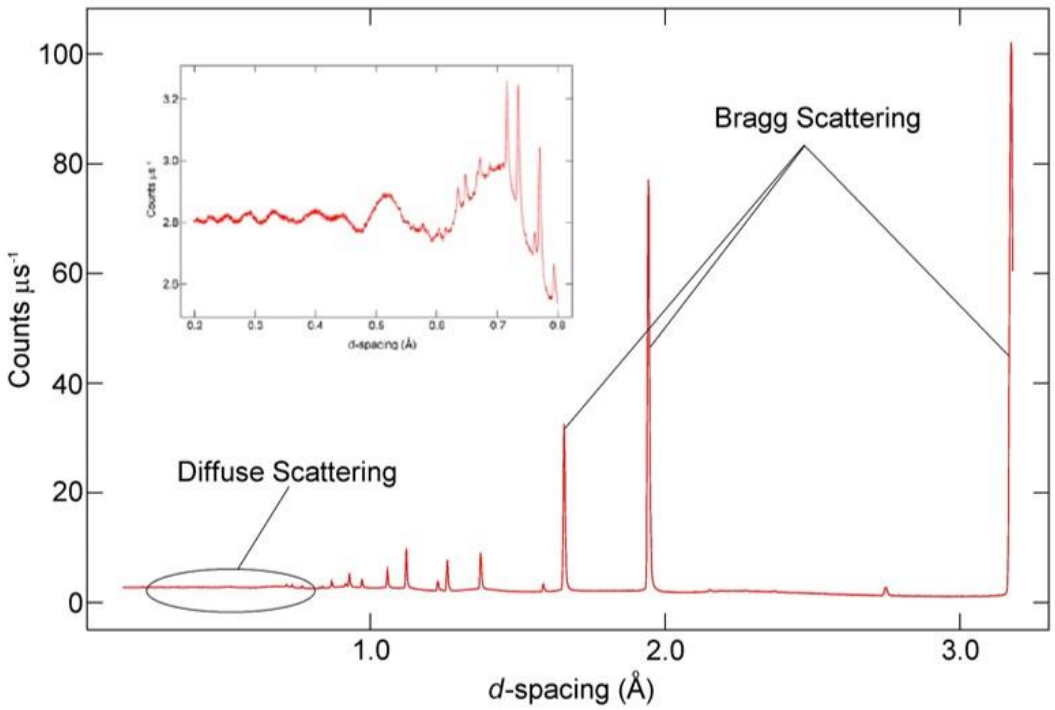

Fig. 2.14 Comparison of the features of Bragg diffraction and diffuse scattering

2.3.5.2 The structure factor

In diffraction theory, the sample being studied can be described as an assembly of atoms, whose positions can be approximated by a Dirac delta function (mathematical representation of a point):

$$\delta(x) = \lim_{\alpha \to 0} \frac{\sqrt{\pi}}{\alpha} e^{-x^2/\alpha^2} \qquad 2.11$$

defined by the following properties: $\delta\,(x \neq 0) = 0$, $\delta\,(x = 0) = \infty$, and $\int \delta\,(x)\,\mathrm{d}x = 1$.

For a monoatomic material, the sample's weighted density, ρ(r), over all space is given by:

$$\rho(\mathbf{r}) = \sum_j b_j \delta(\mathbf{r}_j - \mathbf{r}) \qquad 2.12$$

Application of the standard Fourier transform to the sample density:

$$\int \delta(\boldsymbol{r}_j - \boldsymbol{r}) \exp(i\mathbf{Q} \cdot \boldsymbol{r})\, dr = \exp(i\mathbf{Q} \cdot \boldsymbol{r}_j) \qquad 2.13$$

gives the scattering function $F(\mathbf{Q})$:

$$F(\mathbf{Q}) = \int \rho(\mathbf{r}) \exp(i\mathbf{Q} \cdot \mathbf{r})\, d\mathbf{r} = \sum_j b_j \exp(i\mathbf{Q} \cdot \mathbf{r}_j) \qquad 2.14$$

where $\mathbf{Q}$ is the scattering vector equal to the change in wave vector of the neutron beam through the scattering process, and the integral is taken over all space.

Neutron or X-ray diffraction experiments give the scattered intensity per unit atom $|F(\mathbf{Q})|^2$, the so-called structure factor S($\mathbf{Q}$):

$$
\begin{aligned}
S(\mathbf{Q}) &= \frac{1}{N}|F(\mathbf{Q})|^2 \\
&= \frac{1}{N}\left|\sum_j b_j \exp\left(i\mathbf{Q}\cdot\mathbf{r}_j\right)\right|^2 \\
&= \frac{1}{N}\sum_{i,j} b_i b_j \exp\left[i\mathbf{Q}\cdot\left(\mathbf{r}_i-\mathbf{r}_j\right)\right] \\
&= \frac{1}{N}\sum_{i,j} b_i b_j \exp\left(i\mathbf{Q}\cdot\mathbf{r}_{ij}\right) \qquad (2.15)
\end{aligned}
$$

where $\mathbf{r}_{ij}$ is the separation between pairs of atoms, and N is the total number of atoms in the sample.

The scattering data are averaged over all orientations of $\mathbf{Q}$ and $\mathbf{r}_{ij}$, to account for the fact that the scattering experiments were carried out with polycrystalline samples, as:

$$\langle \exp\left(i\mathbf{Q}\cdot\mathbf{r}_{ij}\right)\rangle = \frac{1}{4\pi}\int_0^{2\pi} \mathrm{d}\phi \int_0^{\pi} \exp\left(iQr_{ij}\cos\theta\right)\sin\theta\,\mathrm{d}\theta \qquad (2.16)$$

where $Q = |\mathbf{Q}|$ and $r_{jk} = \left|\mathbf{r}_j - \mathbf{r}_k\right|$, and θ and ϕ are angles in spherical coordinates such that θ is the polar angle between $\mathbf{Q}$ and $\mathbf{r}_{jk}$, and ϕ is the azimuthal angle ranging from 0 to 2π.

$$\langle \exp\left(i\mathbf{Q}\cdot\mathbf{r}_{ij}\right)\rangle = \frac{1}{2}\int_{-1}^{+1} \exp\left(iQr_{ij}x\right)\mathrm{d}x = \frac{\sin\left(Qr_{ij}\right)}{Qr_{ij}} \qquad (2.17)$$

Hence, the experimentally observed structure factor, $S(Q)$, averaged over all orientations, from an atomic configuration is given as:

$$S\,(Q) = \frac{1}{N}\sum_{i,j} b_i b_j \frac{\sin\left(Qr_{ij}\right)}{Qr_{ij}} \qquad (2.18)$$

2.3.5.3 The pair distribution function (PDF)

The PDF is a histogram of all interatomic distances within a given material, **Fig. 2.15**, which is calculated via the Fourier transform of both the Bragg reflections as well as diffuse scattering.[184] Thus, the partial PDF can be defined as the number of atoms of type

j, lying within a shell of radius *r* and thickness d*r*, centred on an atom of type *i*. The overall PDF can then be constructed via a summation of all the partial PDFs with appropriate weighting, consistent with the relative concentration and neutron scattering power of each atom.

The PDF reflects both the long-range structural order, as well as the local structural disorder. PDF analysis has been widely used for studying materials without long-range structural order, such as glasses and liquids. The advent of high power X-ray and neutron sources allowed PDF analysis to be applied to the study of crystalline materials.[185] As PDF has several roots in different scientific communities, the terminology varies across the literature. The work carried out in this thesis follows the nomenclature outlined by Keen.[186]

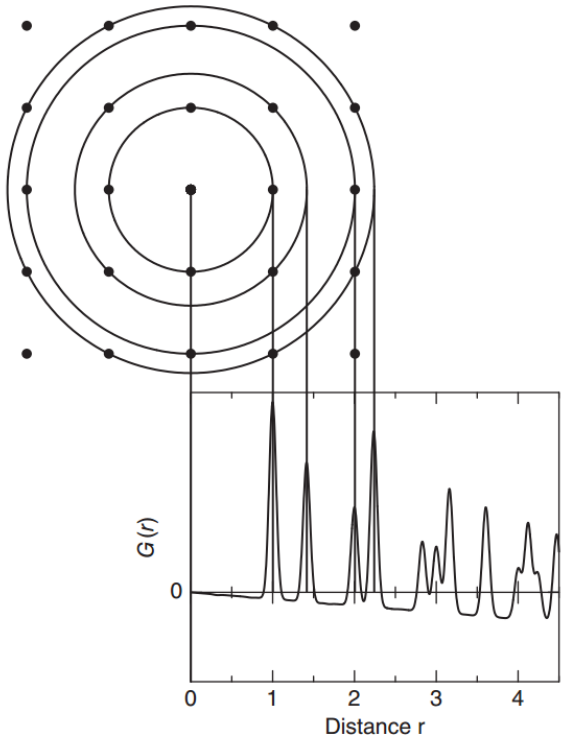

Fig. 2.15 Schematic sketch to illustrate the relationship between the structure and the PDF. The circles represent the first four interatomic distances in a simple 2D lattice. The projection of these distances onto a 1D graph corresponds to the positions of the peaks in the PDF. Maxima in the PDF are in addition weighted by the average coordination number and the product of the scattering lengths of the respective atom pairs.[187]

The PDF theory follows on from Equation 2.18 above, which can be broken down into two parts, one involving scattering from the same atom types ($i = j$), and the other involving scattering between atom pairs where $i \neq j$:

$$S\,(Q) = \frac{1}{N}\sum_{i} b_i^2 + \frac{1}{N}\sum_{i \neq j} b_i b_j \frac{\sin(Qr_{ij})}{Qr_{ij}} \tag{2.19}$$

Assuming a known sample concentration of species i, $\frac{1}{N}\sum_i b_i^2$ can be expressed as $\sum_i c_i b_i^2$, where c_i is the concentration of species i. The second part of equation 2.19, may be expressed as the number of particles of type j between distances r and $r + \mathrm{d}r$ from a particle of type i and $\rho_j = c_j\rho_0$, as:

$$n_{ij}(r) = 4\pi r^2 \rho_j g_{ij}(r)\mathrm{d}r \tag{2.20}$$

where $g_{ij}(r)$ is the pair distribution function.

The second part of equation 2.19 can thus be defined as:

$$\frac{1}{N}\sum_{i \neq j} b_i b_j \frac{\sin(Qr_{ij})}{Qr_{ij}} = 4\pi\rho \int \sum_{i \neq j} c_i c_j b_i b_j r^2 g_{ij}(r) \frac{\sin(Qr)}{Qr}\,\mathrm{d}r \tag{2.21}$$

Therefore, the scattering function $S(Q)$, can be re-defined as:

$$S(Q) = \sum_{i} b_i^2 + 4\pi\rho \int \sum_{i \neq j} c_i c_j b_i b_j r^2 g_{ij}(r) \frac{\sin(Qr)}{Qr}\,\mathrm{d}r \tag{2.22}$$

The integral diverges at $Q = 0$, since $g_{ij}(r) \rightarrow 1$ as $r \rightarrow \infty$. Thus, this is subtracted from the data, since all it does is to add a constant which, when Fourier transformed, gives a delta function. Therefore, a new function $i(Q)$, is defined as:

$$i(Q) = 4\pi\rho \int \sum_{i \neq j} c_i c_j b_i b_j r^2 (g_{ij}(r) - 1) \frac{\sin(Qr)}{Qr}\,\mathrm{d}r \tag{2.23}$$

which can be expressed in terms of the scattering function $S(Q)$ as:

$$i(Q) = S(Q) - \sum_{i} c_i b_i^2 - 4\pi\rho \int \sum_{i \neq j} c_i c_j b_i b_j r^2 g_{ij}(r) \frac{\sin(Qr)}{Qr}\,\mathrm{d}r \tag{2.24}$$

The real-space pair distribution function D(r) is defined as:

$$D(r) = 4\pi\rho r \sum_{i,j} c_i c_j b_i b_j \big(g_{ij}(r) - 1\big) \tag{2.25}$$

which can be expressed in terms of $i(Q)$ as:

$$i(Q) = 4\pi\rho \int \sum_{i \neq j} c_i c_j b_i b_j r^2 (g_{ij}(r) - 1) \frac{\sin(Qr)}{Qr} \mathrm{d}r \tag{2.26}$$

$$\begin{aligned} Qi(Q) &= 4\pi\rho \int \sum_{i \neq j} c_i c_j b_i b_j r (g_{ij}(r) - 1) \sin(Qr)\, \mathrm{d}r \\ &= \int D(r) \sin(Qr)\, \mathrm{d}r \end{aligned} \tag{2.27}$$

with the corresponding reverse Fourier transform giving:

$$D(r) = \frac{1}{(2\pi)^3} \int Qi(Q) \sin(Qr)\, \mathrm{d}r \tag{2.28}$$

and therefore

$$G(r) = D(r) - 4\pi\rho r \tag{2.29}$$

Coordination numbers are then obtained from integrating the pair distribution functions $g_{ij}(r)$ over r, as:

$$CN = \int_{r_1}^{r_2} 4\pi r^2 c_j \rho_0 g_{ij}(r) \mathrm{d}r \tag{2.30}$$

This determines the number of atoms of type j between distances r_1 and r_2 from an atom of type i.

It results from the definition of the PDF as the atom pair correlation function, that some structural information of the material under study can be extracted directly from the PDF, in a model-independent way. Bond lengths can be extracted from peak positions, coordination numbers can be extracted from peak integrated intensities, and finally, information about static or thermal disorder can be calculated from the peak widths.[188] Nevertheless, modelling the PDF data, reveals much more information than model-independent analysis.

A number of approaches have been developed to model PDFs. One approach is the so-called 'large-box refinement', as implemented in the RMCprofile program.[189, 190] The Reverse Monte Carlo (RMC) algorithm is used in the refinement strategy, which performs random structural modifications, in order to minimise the difference between the observed and calculated data sets. RMCprofile can simultaneously refine a model against both, PDF and Bragg diffraction data; through Bragg diffraction, the RMC algorithm maintains the average crystal structure close to that determined from a prior Rietveld refinement. All the RMC modelling work presented in this thesis was carried out using the RMCProfile program. This was especially useful in the investigation of local cation disorder and oxygen vacancy distribution.

Another approach, which is commonly implemented using the program PDFgui,[191] is the so-called 'small-box refinement'. The main difference from the 'large-box refinement' approach lies in the availability of the parameters and the choice of the refinement strategy. Whereas in large-box methods, the only parameters are atomic coordinates, small-box methods also include additional parameters, such as atomic ADPs, etc. Thus, the two methods, model disorder in very distinct ways.

In PDFgui, the user initially expands the asymmetric unit of a starting structure to a single unit cell or a supercell. Atom coordinates and instrumental parameters are then refined, using a standard least-squares algorithm, as opposed to performing random modifications of the structure, as implemented in the RMC algorithm. A particular strength of PDFgui, is the ability to refine the structure to a limited distance range, instead of the full PDF. This allows e.g. differentiation between a truly local structure and the average structure.

Yet another approach, as used in the DISCUS program,[192] allows the user to expand an initial structure to either a small or a large box, and to refine the local structure with respect to PDF or powder diffraction data. The main strength of this approach lies in its toolboxes that allow a wide variety of small and extended defects to be introduced into the structure. The DISCUS approach does, however, require prior knowledge of the types of defects present. As the refinement algorithm is based on a population-based evolutionary algorithm, it is computationally more expensive than PDFgui.

2.4 Rietveld refinement

2.4.1 Introduction to the method

Structure determination from diffraction data involves three main stages, i.e.: (i) unit cell determination and space group assignment, (ii) structure solution and (iii) structure refinement.[154] In structure solution, the aim is to construct an approximate description of the structure of the material, making use of the space group and unit cell as determined in the first stage, but having no knowledge of the atom arrangements in the unit cell. Provided the structure solution represents a close approximation to the actual structure, structure refinement can then produce a thorough description of the structure of the material under study.

In structure refinement, the various numerical parameters that describe the model structure are adjusted, until the best fit is achieved between the observed and calculated data sets. The Rietveld refinement method is the default technique of structure refinement from powder XRD and neutron diffraction data.[193,194] The method was introduced by Hugo Rietveld in 1969, for analysing complex diffraction patterns via a curve-fitting procedure.[195] The underlying concept of Rietveld refinement is that the entire diffraction pattern, given in step-scanned intensity data, is subjected to refinement at once, via a least-squares procedure.

2.4.2 Strengths of the method

It is inevitable that some information is lost in the diffraction process, due to overlapping peaks resulting from the 'projection' of the three-dimensional reciprocal lattice to a one-dimensional diagram. This difficulty can be overcome considerably via the use of step scanned profile intensities, instead of integrated intensities in the refinement procedure. In this way, the experimental data are used directly as measured, and it also allows for the extraction of maximum information content. Besides the refinement of the crystal structure, the Rietveld technique also provides a wealth of other interesting non-structural information, such as the peak width and shape, which can be related to crystallite size and strain. Furthermore, multiple phases can be refined simultaneously, where the scale factor is related to the amount of each of the phases present.

2.4.3 Limitations of the method

Like all methods based on least squares, the Rietveld refinement technique has a small radius of convergence of the parameters subjected to refinement. Therefore, for a successful refinement, the starting structural model must be a close representation of the actual crystal structure. This is especially necessary for the atomic parameters, where small deviations away from the true positions can result in drastically different peak intensities. The refinement requires constant monitoring, due to the global minimum of the least-squares residual function being relatively shallow, which can easily lead to false minima. Furthermore, the refinement algorithm will allow many more parameters to be refined than the data can actually support, and it frequently happens that two or more models lead to refinements that give very similar fits to the data, thus the user has to guide the refinement sensibly.

On the basis of counting statistics, the profile R-index rarely falls to the expected value, which is primarily caused by errors in the background estimation and the deficiencies of the assumed peak shapes. As a consequence, it is often difficult to know when the refinement procedure is actually complete. Thus, it is recommended to calculate difference Fourier maps and to take deviations seriously.[196] A difference Fourier map is produced by subtracting the scattering density calculated for the model from that calculated from observed reflection intensities.

$$C_{diffmap} = (m|F_{obs}| - D|F_{calc}|)^{(2\pi i\phi_{calc})} \tag{2.31}$$

where *m* is an estimate of the phase error, and *D* is a scale factor.

The difference map, thus, highlights the electron density not accounted for in the model. Additionally, difference maps allow for the user to see if further parameters need to be added, which is especially important since the algorithm cannot in itself introduce new parameters to the refinement.

2.4.4 Practical guide to the method

The basis for the Rietveld refinement is that the entire digitised experimental powder XRD/NPD pattern is used directly as measured, without any further manipulation. A digitised powder pattern is then calculated from the structural model, in order to compare it to the experimental pattern. The calculated structure factors along with the peak shape, background and instrumental parameters are used to calculate the intensity of a given point y_i in the diffraction profile, which for constant wavelength diffraction data is given by:

$$y(calc)_i = s\sum_{hkl} L_{hkl}|F_{hkl}|^2 \phi(x_i - x_{hkl})P_{hkl}A + y(back)_i \quad (2.32)$$

where s is a scale factor; L_{hkl} is a function containing Lorentz, polarisation and multiplicity factors; ϕ is the value of the profile peak shape function at position x_i for a peak whose calculated position is x_{hkl} and may be 2θ values for constant wavelength experiments or time-of-flight; P_{hkl} is the preferred orientation function; $y(back)_i$ is the background intensity at point I and A is an absorption correction factor.

With a structural model and reasonable values for the starting parameters, the Rietveld refinement can begin. The main refinement parameters can be divided into three overarching groups,[197] i.e.: (i) basic experimental parameters, such as profile parameters, half-widths, etc, (ii) unit cell parameters and crystallographic symmetry, and (iii) the structural parameters. The parameters are adjusted, i.e. refined, by least squares methods, in order to obtain the optimal fit, between the entire experimental and the entire calculated powder XRD/NPD patterns. The background is typically dealt with via the use of orthogonal Chebyshev polynomials of higher order (typically 15–20).

Numerical criteria of fit are used for assessment of the fit in quantitative detail, while graphical criteria allow for a global view, noting the ways in which the model might be at error. Of the several R-factors used to check on the quality of the refinement, R_{wp}, defined as:

$$R_{wp} = \left\{ \frac{\sum_i w_i \left[y_{i(\text{obs})} - y_{i(\text{calc})} \right]^2}{\sum_i w_i \left[y_{i(\text{obs})} \right]^2} \right\}^{\frac{1}{2}} \quad (2.33)$$

is statistically the most meaningful indicator, since the numerator is the residual that is minimized in the least squares procedure. The scaling of the calculated pattern to the observed one must be correct, in order to obtain a reasonable difference map. To check this, plots of the observed and calculated patterns should always be examined by eye. The structure should be refined to convergence, that is, the maximum shift/e.s.d. in the final cycle of refinement should be no more than 0.10. All parameters (profile and structural) should be refined simultaneously to obtain correct estimated standard deviations.

The GSAS suite of programs was used to carry out the Rietveld whole profile fitting, for the analysis of the Bragg reflection data, for the work presented in this thesis.[198,199] All the thermal parameters in the models presented in this thesis were refined isotropically. Typically, the thermal parameters (U_{iso}) of the cation sites were tied to the same value, whilst being refined. The thermal parameters of all the oxide ions were also typically tied to the same value, although the sites were crystallographically independent.

2.5 Reverse Monte Carlo (RMC) modelling

2.5.1 Introduction to RMC modelling

RMC modelling and neutron diffraction make a powerful combination of techniques for studying crystalline materials with significant amounts of structural disorder.[168,200,201,202] Through RMC modelling, three-dimensional models of the material under study are produced, which agree quantitatively with the experimental data, within their errors and subject to a set of constraints.[203,204] Thus, RMC modelling differs from the conventional computer simulation techniques, in that it is driven by experimental data, rather than by parameterised equations.[205]

The starting configuration typically consists of a supercell of the crystal unit cell, as determined by a prior Rietveld refinement. The supercell is as large as is practically feasible (~10^4 atoms) in order to minimise finite-size effects. Periodic boundary conditions are used, in order to avoid edge effects. In equilibrium, configurations are considered to be statistically independent, if separated by at least N accepted moves.[181] Some moves that increase χ^2 are accepted, so that the final result can, in principle, be independent of the initial configuration.[203] If the fit is consistent with all the data available, then the output configuration will be a true structural representation of the sample being studied.[206]

2.5.2 Strengths of RMC modelling

The RMC algorithm requires as input only the density and chemical composition of the sample, thus, no other assumptions about the sample need to be made.[207] The application of the closest-approach constraints allows simple systematic errors, such as incorrect normalization, to be readily corrected for. The explicit inclusion of Bragg scattering, gives more weight to the distribution of the atomic positions on an absolute scale, thus allowing the analysis to focus more on the correlation of the atomic positions.[189,208] Furthermore, fitting both total scattering factors as well as pair distribution functions is beneficial, since each function emphasises different aspects of the structure.

The inclusion of the bond valence sum (BVS) formalism avoids the formation of regions containing chemically unreasonable local configurations, which is especially important in the early stages of refinement.[209] Furthermore, the BVS constraints provide the fitting procedure with additional chemical information, in order to better differentiate between cation species that possess similar neutron scattering powers. The RMC algorithm can model the atomic and magnetic structures simultaneously, thus there is no need for an experimental separation of the nuclear and magnetic scattering components. The spins are rotated randomly on the atomic positions and the atom positions are also moved randomly, in order to minimize χ^2.

The output configuration contains a three-dimensional atomic structure and a three-dimensional spin structure, which are consistent with the experimental total structure factor(s), within experimental error.[179,181] The output configuration can be averaged onto a single unit cell, which can then be used to generate atom density maps or iso-surfaces. Programs such as 'atomeye' are available for viewing both the full configuration and the averaged unit cell distributions.[210] By examining the distribution in detail, considerable information can be extracted on the nature and extent of disorder in the material under study. The density distribution can also give an insight into the mechanism of ionic conduction, since the pathways along which ions move will have a higher ion density than other non-conducting pathways.

2.5.3 Limitations of RMC modelling

RMC models will always contain errors, which are often intrinsic to errors in the data and thus attempting to remove them, may result in other errors. Nevertheless, a small number of errors does not necessarily invalidate the usefulness of a model.[203] Additionally, there may often be a range of configurations with different degrees of disorder that match the data equally well, however, by maximising the range of experimental data, this problem can be minimised. In principle, the result of the RMC modelling is independent of the starting configuration, subject to the constraints applied, however, in practice this condition takes too long to achieve.[203] RMC also has the obvious disadvantage in comparison with MD or MC simulations in that it provides only static structural information and gives no details about the dynamics and the thermodynamics of the system.

2.5.4 Practical guide to RMC modelling

The starting point for RMCProfile is to generate an initial configuration of atoms, which is defined by a box with periodic boundary conditions and a given size, along with a list of constituent atoms and their positions within the box. The reciprocal space function $S(Q)$ and a real space correlation function, usually $G(r)$ or $D(r)$, as well as the Bragg profile data are calculated from the atom positions in the configuration. The Bragg data are included, to act as a constraint to preserve the long-range order in the structure. In order to reflect the finite size of the simulation box, the observed $S(Q)$ is convolved with a box function with size $L/2$, where L is the shortest length in the RMC configuration:

$$S_{conv}(Q) = \frac{1}{\pi}\int_{-\infty}^{+\infty} S_{\exp}(Q')\frac{\sin\left(\frac{L(Q-Q')}{2}\right)}{Q-Q'}\mathrm{d}Q' \qquad (2.34)$$

During an RMC simulation, atoms are chosen at random and their positions varied in a random manner, in order to improve the agreement with the experimental data. The overall comparison between the calculated functions and experimental data is then obtained by summing the individual χ^2 functions, as:

$$\chi^2 = w_1 \sum_i \frac{\left(S_{\text{calc}}(Q_i) - S_{\text{exp}}(Q_i)\right)^2}{\sigma_{Q_i}^2} + w_2 \sum_i \frac{\left(G_{\text{calc}}(r_i) - G_{\text{exp}}(r_i)\right)^2}{\sigma_{r_i}^2} + w_3 \sum_{hkl} \frac{\left(I_{\text{calc}}(hkl) - I_{\text{exp}}(hkl)\right)^2}{\sigma_{hkl}^2} + w_4 \sum_j^J \frac{\left(f_{j,\text{RMC}} - f_{j,\text{exp}}\right)^2}{\sigma_j^2} \quad (2.35)$$

where w_m is the χ^2 weighting of component m, I_{calc} (hkl) is the calculated Bragg intensity, I_{exp} (hkl) is the experimental Bragg intensity, f_j are constraints applied to the RMC calculation, and σ_i is the error that can be adjusted to modify the weighting for a particular constraint. By adjusting the weights of each component, the fit can be optimised so as not to unduly weight a particular component.

If the move improves the agreement within the applied constraints, then the move is accepted; if it worsens the agreement, then the move is still accepted if it lies within a certain probability P given by:

$$P = \exp\left(\frac{-\Delta\chi^2}{2}\right) \quad (2.36)$$

where $\Delta\chi^2$ is the increase in χ^2 caused by the move. If rejected the atom is returned to its original position. Atoms continue to be moved in this manner, until the agreement with the data is maximised and subsequent moves only cause the agreement factor to deviate by small amounts about the minimum. The resulting configuration of atoms may then be considered as consistent with the experimental structural data.

2.6 Impedance spectroscopy (IS)

2.6.1 Introduction to IS

IS is a powerful technique of elucidating electrical properties of materials and their interfaces.[211] The method typically involves investigating the alternating current (AC) response of the material under study, through direct measurement of impedance, in the frequency domain. The conventional definition of impedance is:

$$Z(\omega) = \frac{\nu(t)}{i(t)} \tag{2.37}$$

where $\nu(t) = V_0 \sin(\omega t)$ is a monochromatic signal at frequency of $\omega/2\pi$ applied to the system, and $i(t) = I_m \sin(\omega t + \theta)$ is the measured resulting steady state current. θ is therefore the phase difference between the voltage and the current. Assuming a linear response to the applied voltage, the waveforms can be considered to be sinusoidal and can be described by vector quantities, as:

$$V(t,\omega) = V_0\big(\cos(\omega t) - i\sin(\omega t)\big) = V_{0e^{i\omega t}} \tag{2.38}$$

$$I(t,\omega) = I_0\big(\cos(\omega t + \theta) - i\sin(\omega t + \theta)\big) = I_0 e^{i\omega t + \theta} \tag{2.39}$$

For handling simplicity of the impedance of an a.c. circuit with multiple components, the complex form is generally used:

$$Z(\varpi) = \frac{U(\omega)}{I(\omega)} = |Z|e^{j\theta} = Z' + jZ'' \tag{2.40}$$

where Z' = |Z| cos θ and Z" = |Z| sin θ.

Impedance measurements are made over a wide range of frequencies, by applying an AC potential to an electrochemical cell, and then measuring the current through the cell. The current is shifted in phase from the voltage by angle θ, **Fig. 2.16**, which is attributed to the delay in the electrical response of the sample to the applied voltage.[212] Both the magnitude (resistive) and phase shift (reactive) parts of impedance are frequency dependent.

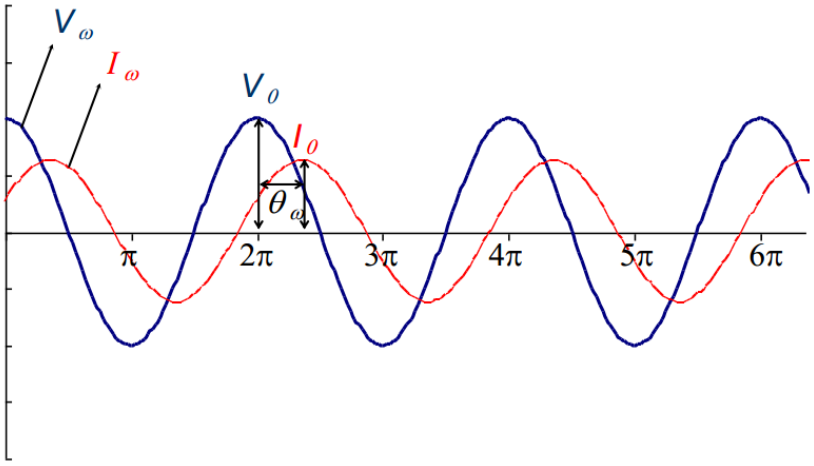

Fig. 2.16 Schematic diagram showing the waveforms of alternating voltage (V_ω) and current (I_ω) in AC impedance measurements. V_0 and I_0 are the amplitudes of voltage and current wave functions.

From the impedance spectrum, it is possible to identify different RC elements, based on the capacitance values, and assign them to the appropriate regions of the measured system. The values of the individual R and C components may then be quantified. Small capacitance values, e.g. 10^{-12} F cm^{-1}, are associated with large volume fractions, i.e. bulk material, whereas larger capacitances, e.g. 10^{-9} F cm^{-1}, are associated with progressively smaller volume fractions (grain boundaries, assuming a brickwork model for the ceramic microstructure). Typical capacitance values and their possible interpretations are listed in **Table 2.2**.

Table 2.2 Capacitance values and their possible interpretation.[211]

Capacitance, Fcm^{-1}	Phenomenon Responsible
10^{-12}	bulk
10^{-11}	minor, second phase
$10^{-11} – 10^{-8}$	grain boundary
$10^{-10} – 10^{-9}$	bulk ferroelectric near T_C (Curie Temperature)
$10^{-9} – 10^{-7}$	surface layer
$10^{-7} – 10^{-5}$	sample-electrode interface
10^{-4}	electrochemical reactions

The impedance spectrum can also be modelled via an equivalent electrical circuit, which contains resistive (R) and reactive (L inductance and/or C capacitance) components, both of which can be determined. For example, an equivalent circuit commonly used to represent electrical properties of a polycrystalline material contains two RC sections connected in series. These sections refer to electrically distinct regions within the material, e.g. bulk and grain boundary components, as shown in **Fig. 2.17**.

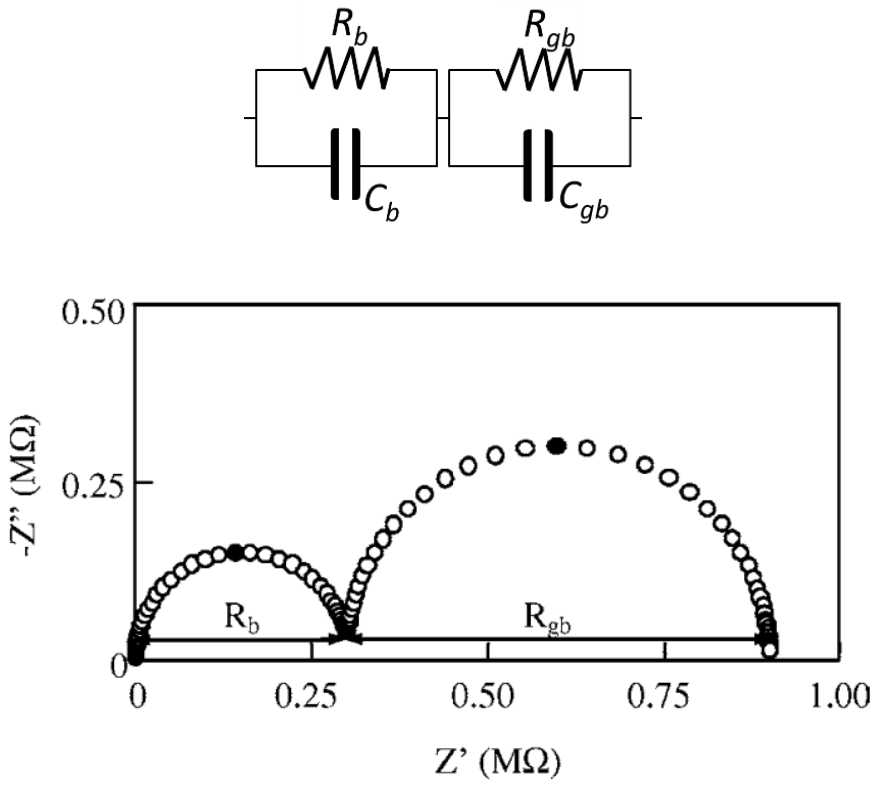

Fig. 2.17 Complex impedance spectrum for an ionic conductor.[213,214] R_b represents the bulk contribution resistance, R_{gb} represents the grain boundary contribution, and R_b + R_{gb} is the total resistance.

The equivalent circuit model can also be filled by other RC elements, corresponding to other physical properties and processes, such as dielectric relaxation of the bulk, sample-electrode interface, and electrochemical reactions at the interface. As such, the AC impedance electrical response of the measured system is quite complex; fitting to the equivalent circuit model should therefore be performed via sophisticated numerical analysis. The difficulty over the interpretation of IS data, is that it is often possible to fit a number of plausible equivalent circuits to a given data set, thus a critical assessment is required in deciding the appropriateness of a particular circuit.

2.6.2 IS procedure

IS measurements to characterise the ionic/electronic conducting behaviour of the compounds investigated in this thesis were made using the standard two-probe experiment, **Fig. 2.18**, with cells of regular shape (rectangular blocks, with approximate dimensions of 5 mm × 2 mm × 8.5 mm), where two identical platinum electrodes were applied to parallel sides of the sample. The electrodes were prepared by plasma sputtering, using a BAL-TEC (Leica) SCD 500 plasma sputter coater.

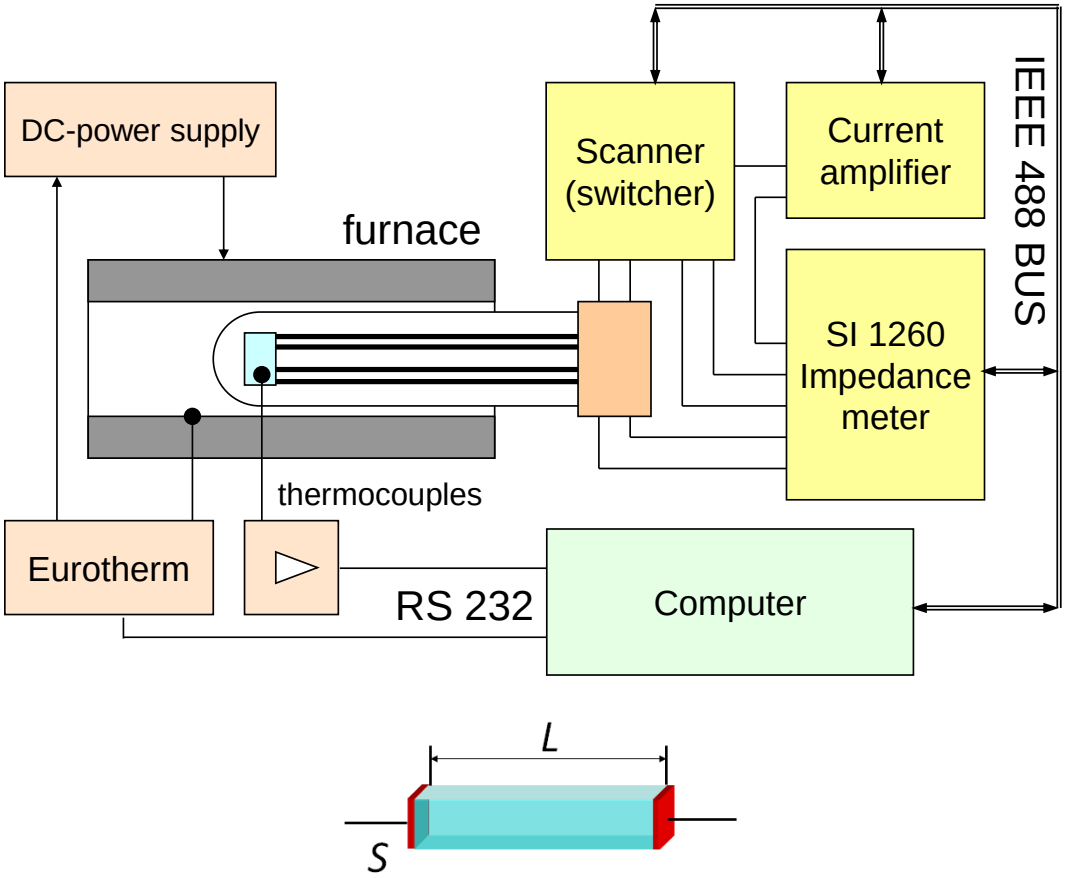

Fig. 2.18 Schematic of high temperature AC impedance set-up.

The impedance spectra for the work presented in this thesis, were recorded with an automated setup (available at the Faculty of Physics, Warsaw University of Technology, Poland), suitable for measurements of large absolute values of impedance, which combined a Solartron 1260 Impedance/Gain Phase Analyser (or Novocontrol Alpha AN impedance analyser) and a Keithley 428 Current Amplifier, as previously demonstrated.[215] Impedance was measured in the frequency range from 10 MHz to 0.01 Hz (between 16 and 8 frequency points per decade), with an applied AC signal of 50 mV rms. Measurements were made in air, at constant temperatures from approximately 100 °C to 850 °C, in two heating and cooling cycles (20 °C temperature steps, 10 min stabilisation time before each measurement). For a set of test frequencies, the impedance was measured before and after acquisition of each spectrum. When the summed relative difference in measured impedance exceeded the assumed tolerance of 1%, the measurement was repeated, as described elsewhere.[216]

Chapter 3 – Structure and Conductivity in Neodymium Ytterbium Zirconate

3.1 Introduction

Lanthanide zirconium oxides have been widely studied for many of their chemical and physical properties. Potential technological applications include, thermal barrier coatings (TBCs),[217,218] nuclear waste storage materials,[219,220] photocatalysis,[221,222] and electrolyte materials for solid oxide fuel cells.[223,99,224] These compounds exhibit either a defect-fluorite or a pyrochlore type structure, depending on stoichiometry, the relative cationic radii, the synthesis method, and the thermal treatment history.[225,166] Generally, the pyrochlore structure is favoured for lanthanides with an ionic radius larger than that of Gd^{3+} (r = 1.053 Å for eight coordinate geometry)[25] and the defect fluorite structure is favoured for smaller lanthanides. The properties of greatest technological interest in these materials are found near the fluorite-pyrochlore phase boundary.

The potential of lanthanide zirconium oxides to possess significant ionic and/or electronic conductivity was first shown in 1983 by Van Dijk *et al.*[109] Shlyakhtina and Shcherbakova reported conductivities in the range of 10^{-2} S cm^{-1} for $Ln_2Zr_2O_7$ (*Ln* = Gd, Eu, Sm) at 800 °C;[99] these conductivities are up to five orders of magnitude higher than those of most of the lanthanide (Er, Ho, Dy) titanates they studied, with $Yb_2Ti_2O_7$ being the exception, as shown in **Fig. 3.1**. Amongst the zirconates, conductivity is highest for $Gd_2Zr_2O_7$, which then decreases linearly with increasing radius of the lanthanide cation. The higher conductivity in $Gd_2Zr_2O_7$ is attributed to the smaller size mismatch between Gd^{3+} (1.05 Å) and Zr^{4+} (0.72 Å) cations.[25] With increasing size mismatch between the lanthanide and Zr^{4+} cations, the structure becomes more ordered, which results in a decrease in ionic conductivity.

The local structure in lanthanide zirconium oxides can be different from the long-range structure, which may affect the disordering mechanisms and the phase transformations that occur in these materials. Furthermore, when large concentrations of defects such as anion vacancies are present, they can aggregate into extended defects such as clusters, which leads to structural changes with remarkable effects on electrical properties.[86,226] Computational calculations have shown that the most stable intrinsic defect in these compounds are oxygen Frenkel pairs, consisting of a vacant 48f position and an interstitial ion located in the 8a site, of the $Fd\bar{3}m$ space-group. The order/disorder

transformation involves anti-site defects and anion Frenkel pairs, with the randomization of the cations between the 16*c* and 16*d* sites, and the oxygen anion/vacancies over the 48*f*, 8*b*, and 8*a* sites.

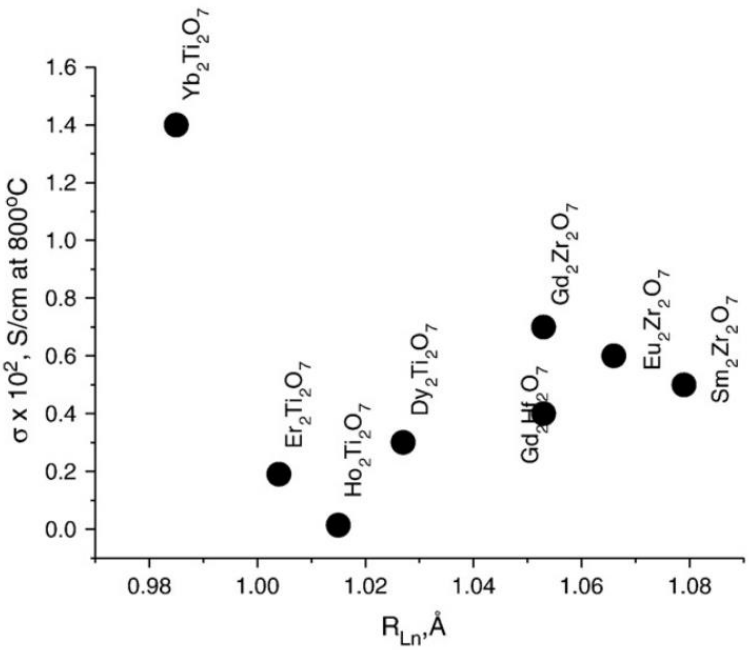

Fig. 3.1 Ionic conductivity vs. lanthanide ionic radius for some of the $Ln_2M_2O_7$ (Ln = Sm─Yb; *M* = Ti, Zr, Hf) pyrochlores.[99]

Migration of oxide ions takes place via thermally activated hopping to adjacent oxygen vacancies; as such, the oxide ion conductivity depends on the energy of formation of Frenkel defects, which is significantly lowered by increased cation disordering.[227,110] However, the activation energy needed for oxide ion migration increases with increased disorder, and thus optimum conductivities are found in partially ordered systems. Furthermore, ionic conductivity has been found to improve significantly by modifying the compositions through incorporation of appropriate aliovalent dopants to optimum doping concentrations, which acts not only by changing the vacancy concentration (see Chapter 4), but also by increasing the amount of disorder in the system.[228,225]

Given the impact of disorder and the local environment on the properties of lanthanide zirconium oxides, the simultaneous use of multiple techniques to achieve a complete understanding of the structure is crucial in explaining observed behaviour; this is particularly important for compositions near the pyrochlore/defect-fluorite phase boundary. However, few comprehensive studies of these materials, involving techniques

such as neutron diffraction, have been reported. Various studies have been carried out on the binary $Nd_2Zr_2O_7$ and $Yb_2Zr_2O_7$ systems; Fabrichnaya *et al.*[229] and Stolyarova *et al.*[230] established the phase equilibrium diagrams of $Nd_2Zr_2O_7$ and $Yb_2Zr_2O_7$ respectively, **Fig. 3.2**. However, to the best of my knowledge, no neutron diffraction study has been carried out on the ternary system $(Yb_{1-x}Nd_x)_2Zr_2O_7$.

(a)

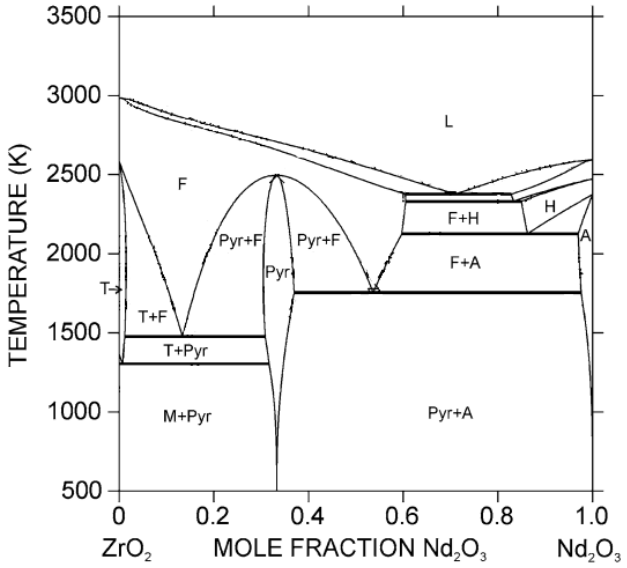

(b)

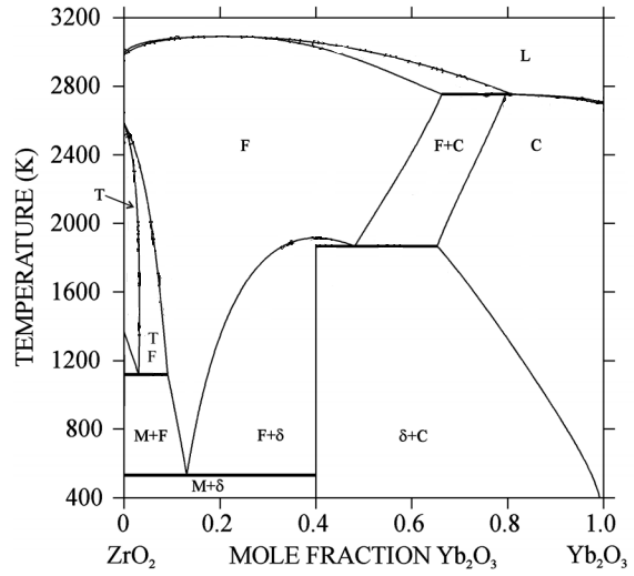

Fig. 3.2 Binary phase diagrams for (a) Nd_2O_3-ZrO_2 [229] and (b) Yb_2O_3-ZrO_2 [230] systems. Phase abbreviations are: Fluorite (F), Tetragonal (T), Monoclinic (M), Pyrochlore (Pyr), Liquid (L), cubic Yb_2O_3 solid solution (C), and $Yb_4Zr_3O_{12}$ phase with rhombohedral structure (δ).

Based on the cationic radius ratio rule (chapter 1.4.1) with the ionic radii from Shannon,[25] these systems are predicted to show the fluorite structure for Yb-rich compositions, which gradually transform to pyrochlore structure with increasing Nd content, **Fig. 3.3**.

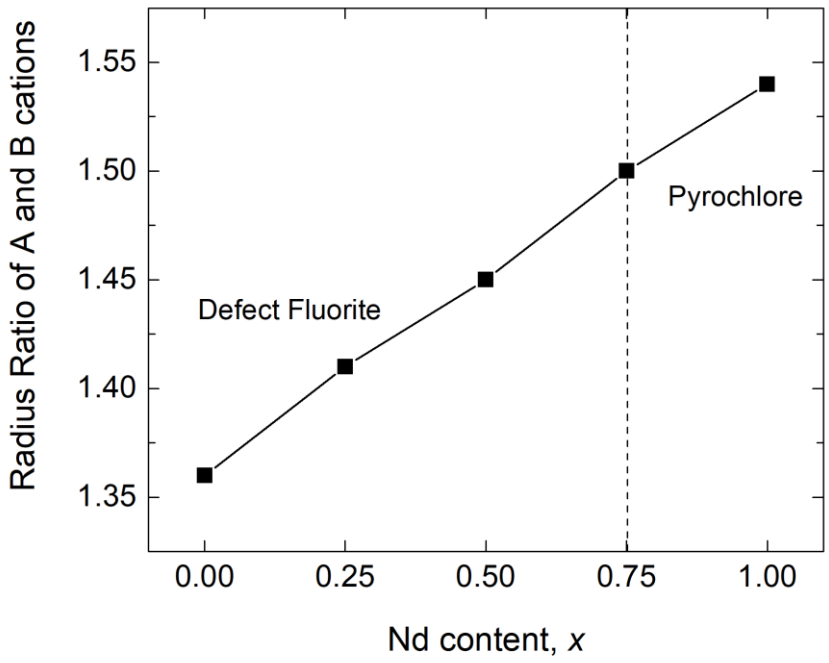

Fig. 3.3 Plot of radius ratio (r_A/r_B) as a function of composition, in $(Yb_{1-x}Nd_x)_2Zr_2O_7$, with ionic radii of 0.985, 1.109, and 0.72 Å for Yb^{3+}, Nd^{3+}, and Zr^{4+} respectively.[25]

Liu *et al*. studied structure evolution in $(Yb_{1-x}Nd_x)_2Zr_2O_7$, using X-ray diffrasction.[148] In the compositional range $0.00 \leq x \leq 0.55$, the samples exhibited a single phase fluorite structure; the compositions in the range $0.60 \leq x \leq 0.70$ exhibited a mixture of pyrochlore and fluorite structures; while the compositional range $0.75 \leq x \leq 1.00$ exhibited a single phase pyrochlore structure. These authors also studied the electrical properties of this system, using impedance spectroscopy.[231] Conductivity depended heavily on composition at all studied temperatures, and was shown to have an optimum value (9.32×10^{-3} S cm^{-1} at 900 °C) at the composition $Nd_{1.8}Yb_{0.2}Zr_2O_7$.

3.2 Experimental

3.2.1 Synthesis

Sample powders of general composition $(Yb_{1-x}Nd_x)_2Zr_2O_7$ were synthesised via a co-precipitation method, with an aqueous mixture of zirconyl chloride ($ZrOCl_2 \cdot 8H_2O$, 99.9%, Sigma Aldrich) and the appropriate rare-earth nitrates, followed by a subsequent high-temperature treatment. The synthesis from solution has the advantage of yielding a highly homogeneous cation distribution at relatively low temperatures.[149]

Stoichiometric amounts of neodymium (Nd_2O_3, 99.9%, Sigma Aldrich) and ytterbium (Yb_2O_3, 99.9%, Sigma Aldrich) oxides were dissolved in warm (80 °C) 2 M nitric acid. The solutions were then mixed together, along with the zirconyl chloride solution and stirred for 60 min. The mixed solution was slowly added under stirring to an excess of dilute ammonia solution with a pH value of 13, to obtain a gel-like precipitate. The gel was filtered, washed with distilled water several times to a pH value of 7, and then washed twice with industrial methylated spirit (IMS). The washed precipitate was dried at 80 °C for 24 h, then ground, and calcined at the required temperature in the range 800 - 1350 °C for 24 h, in air. **Table 3.1** summarises the quantities of precursors used for the compositions prepared in this study.

Table 3.1 Masses of reactants and volume of solvents used in the synthesis of the compositions of $(Yb_{1-x}Nd_x)_2Zr_2O_7$ studied in this chapter

x	Yb_2O_3 Mass (g)	Nd_2O_3 Mass (g)	2 M nitric acid volume (ml)	$ZrOCl_2 \cdot 8H_2O$ Mass (g)	H_2O Volume (ml)	2 M Ammonia Solution Volume (ml)
0.00	11.07	0	150	18.11	150	300
0.25	8.50	2.42	150	18.53	150	300
0.50	5.80	4.95	150	18.96	150	300
0.75	2.97	7.60	150	19.42	150	300
1.00	0.00	10.39	150	19.90	150	300

Sample composition was confirmed via Energy Dispersive X-ray Spectroscopy (EDS), using a Scanning Electron Microscope (FEI Inspect F) at the NanoVision Centre, Queen Mary University of London. The EDS detector used was the 'Inca X-act' from Oxford Instruments. Measurements were carried out at 5 different sample positions; the average of which and the corresponding standard deviations are shown in **Table 3.2**.

Table 3.2 Compositional confirmation via EDS. Standard deviations are given in parentheses.

x	Chemical Formula	Cation Ratio from EDS / Nd : Yb : Zr
0.00	$Yb_2Zr_2O_7$	0.0 : 2.0(4) : 2.0(8)
0.25	$Nd_{0.5}Yb_{1.5}Zr_2O_7$	0.5(1) : 1.6(4) : 2.0(6)
0.50	$NdYbZr_2O_7$	1.0(3) : 1.1(3) : 2.3(8)
0.75	$Nd_{1.5}Yb_{0.5}Zr_2O_7$	1.4(5) : 0.5(2) : 2.1(11)
1.00	$Nd_2Zr_2O_7$	2.0(1) : 0.0 : 2.2(1)

3.2.2 Diffraction

X-ray powder diffraction data were collected on either a PANalytical X'Pert Pro diffractometer fitted with an X'Celerator detector, or a Siemens D5000, using Ni filtered Cu-Kα radiation (λ = 1.5418 Å). Data were collected in flat plate θ/θ geometry over the 2θ range 5 to 120° in steps of 0.0167°, with an effective scan time of 200 s per step for the X'Pert Pro or steps of 0.02° with a scan time of 10 s per step for the D5000. Calibration was carried out with an external LaB_6 standard. For elevated temperature measurements, data were collected on the X'Pert Pro diffractometer using an Anton Paar HTK-16 camera. Measurements were performed at 50 °C intervals from, 100 to 1300 °C. For these measurements, data were collected in the 2θ range 5 to 120°, in steps of 0.0167°, with an effective scan time of 50 s per step.

Room-temperature total neutron scattering data were obtained at the ISIS facility, using the POLARIS diffractometer.[177] Data were collected on back-scattering (average

angle 146.72°), 90° (average angle 92.5°), intermediate-angle (average angle 52.21°), low-angle (average angle 33.5°) and very low angle (average angle 24.75°) detectors, corresponding to the approximate *d*-spacing ranges 0.04-2.6 Å, 0.05-4.1 Å, 0.73-7.0 Å. 0.3-48 Å and 0.13-13.8 Å, respectively. In each case, the sample was loaded into a thin walled 11mm diameter vanadium can, which was placed in front of the backscattering detectors, using an automatic sample changer. Data collections corresponding to total proton beam charge values of 1000 μA h to 1200 μA h were collected. Data collections of *ca*. 600 μA h were performed on an empty vanadium can, on the empty sample changer, and on a vanadium rod, for subsequent data correction purposes.

Long-range structure was analysed by the Rietveld method [195] using the General Structure Analysis System (GSAS) set of programs,[199] and the EXPGUI interface.[198] X-ray and neutron diffraction data were used simultaneously. Neutron diffraction data were corrected for instrument background and divided by a vanadium spectrum, which normalised the data to the energy distribution of the incident neutron flux, taking into account the variation in detector efficiency with neutron energy. Neutron data from the back-scattering and 90° banks were used in the Rietveld analyses. The background for each data set was modelled using a multi-term shifted Chebyshev polynomial. Neutron peak profiles were fitted using the time of flight GSAS type 2 profile function, while X-ray data were fitted using a pseudo-Voigt function (constant wavelength GSAS type 2). Initial models for structure refinement were based either on the ideal fluorite (space group $Fm\bar{3}m$, No. 225) or the pyrochlore (space group $Fd\bar{3}m$, No. 227) structures. Least squares refinement was carried out by varying the parameters in the following order: cell parameters, diffractometer constant (DIFA), peak-shape parameters, atomic coordinates, thermal parameters and finally site occupancies. DIFA introduces small corrections to account for peak shifts due to neutron absorption in the sample.

For total neutron scattering analysis, the background scattering and beam attenuation were corrected for using the program Gudrun,[178] and the resulting normalised total scattering structure factors, S(*Q*), were used to obtain the corresponding total radial distribution function, G(*r*), via a Fourier transform, as described in Chapter 2. It is *Q* which determines the length scale that is probed by the diffraction experiment, with small *Q* corresponding to large distances and large *Q* corresponding to small distances. A *Q* maximum of 25 Å^{-1} was chosen. The graphical user interface (GUI), provided with the

Gudrun distribution, was used as a guided editor for file input and to also provide graphics capabilities for looking at the outputs.

The analysis of the total neutron scattering data (Bragg peaks plus diffuse scattering components) was carried out using the RMCProfile software.[232] Reverse Monte Carlo (RMC) simulations used configuration boxes of 10 × 10 × 10 unit cells for the fluorite structures and 5 × 5 × 5 unit cells for the pyrochlore structures, both with approximate dimensions of approximately 50 Å × 50 Å × 50 Å, and containing approximately 11000 atoms. Initial configurations were generated from supercells of the refined crystal structure, with atoms randomly distributed over sites in the supercell corresponding to the regular 4*a* and 8*c* crystallographic sites in the $Fm\bar{3}m$ space group for the fluorite structure and 16*c*, 16*d*, 48*f*, 8*a*, 8*b* sites in the $Fd\bar{3}m$ space group for the pyrochlore structure.

Fitting was carried out against the reciprocal space data, S(*Q*), the real space data, G(*r*), and the Bragg profile data to provide a constraint for the long-range crystallinity. The G(*r*) profile was chosen rather than the often used D(*r*) for ease of visualization and direct comparison with calculated individual pair correlations $g_{ij}(r)$. S(*Q*) was broadened by convolution with a box function (Chapter 2, equation 2.38), in order to reflect the finite size of the simulation box. Calculations were performed using bond valence summation (BVS) constraints.[209] M-O and O-O minimum distance constraints were used, to avoid unrealistically short M-O and O-O contact distances. Additionally, a loose O-O constraint in the form of a Morse potential,[190] was needed to satisfactorily model the first $g_{OO}(r)$ correlation centred around 2.6 Å, due to the extent of disorder in the oxide ion distribution, particularly in the fluorite structures. The potential consisted of a stretch value of 1.29 eV, a stretch search of 25 %, and a temperature of 1500 K.

The maximum displacement for all moves was set to 0.04 Å for cations and 0.08 Å for anions. Atom swapping was found to have no significant effect on the fit. A set of ten parallel runs on different random configurations were used to produce average $g_{ij}(r)$ plots and to calculate standard deviations on derived parameters. The low standard deviations (~ 0.5 %) provided for adequate statistics. To ensure convergence of calculations, the values of χ^2 for the fits to the Bragg, the S(*Q*), and the G(*r*) data were plotted as a function of run time. For compositions near the fluorite/pyrochlore phase boundary, the same conclusions were reached whether a disordered fluorite or an ordered pyrochlore supercell was used as a starting configuration.

3.2.3 Electrical measurements

For electrical measurements, the calcined powders were finely ground in a mortar and pestle, pressed uniaxially into cylindrical pellets, by applying a pressure of 180 MPa, and then sintered in air at 1600 °C. Sintered pellets had densities of ~ 93 % of the theoretical value, **Table 3.3a**, as determined by the Archimedes method, with water as the displaced fluid. Electrical measurements were carried out via a.c. impedance spectroscopy up to *ca*. 850 °C, using a fully automated Solatron 1255/1286 system, in the frequency range 1 Hz to 5×10^5 Hz. Measurements were carried out at the Institute of Physics, Warsaw University of Technology, Poland. The pellets were cut as rectangular blocks, **Table 3.3b**, using a diamond saw. Platinum electrodes were sputtered by cathodic discharge on the two smallest faces. Impedance spectra were acquired over two cycles of heating and cooling at stabilized temperatures.

Table 3.3. Parameters for pellets of $(Yb_{1-x}Nd_x)_2Zr_2O_7$ used in electrical measurements

(a) Measured pellet densities (± 0.05), theoretical powder densities and relative densities

Composition	Measured density (g cm^{-3})	Theoretical density (g cm^{-3})	Relative Density (%)
$x = 0.00$	7.12	7.708	92.3
$x = 0.25$	7.00	7.375	95.0
$x = 0.50$	6.51	7.040	92.5
$x = 0.75$	6.14	6.701	91.6
$x = 1.00$	5.79	6.371	90.9

(b) Pellet dimensions (± 0.02)

Composition	Length (mm)	Height (mm)	Width (mm)	[a]L/A (cm^{-1})
$x = 0.00$	5.57	4.23	1.38	9.54
$x = 0.25$	6.89	4.21	1.55	10.56
$x = 0.50$	8.32	5.29	1.80	8.74
$x = 0.75$	7.16	4.50	1.56	10.20
$x = 1.00$	8.32	5.11	1.64	9.95

[a]A = (height × width)

3.3 Results and discussion

3.3.1 Phase behaviour

Attempts were initially made to prepare compositions in the series $(Yb_{1-x}Nd_x)_2Zr_2O_7$ ($0.00 \leq x \leq 1.00$) through solid state reaction of the parent oxides Yb_2O_3, Nd_2O_3 and ZrO_2, at various temperatures. **Fig. 3.4** shows the X-ray diffraction patterns of samples prepared at 1500 °C. Only in the case of the $x = 1.00$ composition is a single phase observed, corresponding to the pyrochlore structured phase $Nd_2Zr_2O_7$. The results suggested that cation diffusion was too slow at these temperatures and that better mixing of the precursors was required.

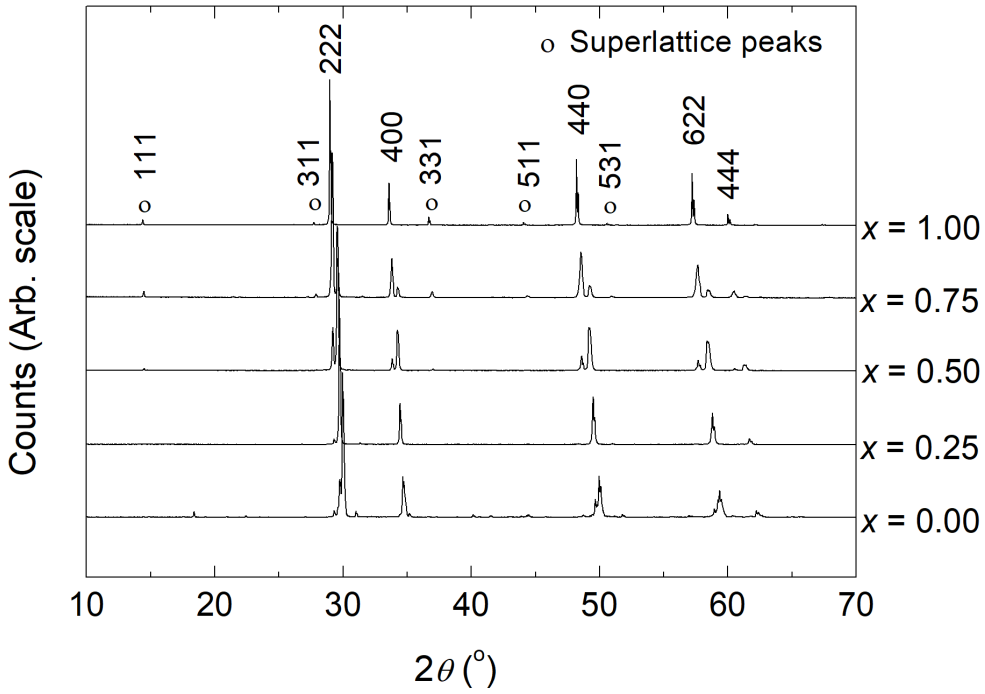

Fig. 3.4. Room temperature X-ray powder diffraction patterns of compositions in the series $(Yb_{1-x}Nd_x)_2Zr_2O_7$ ($0.00 \leq x \leq 1.00$), prepared by solid state methods at 1500 °C.

In order to improve precursor mixing, a co-precipitation route for synthesis was adopted following the work of Liu *et al.*[148] **Fig. 3.5** shows the X-ray diffraction patterns of co-precipitated samples of composition $(Yb_{1-x}Nd_x)_2Zr_2O_7$ ($0.00 \leq x \leq 1.00$) after annealing at 800 °C for 5 h. Each of the samples shows broad peaks characteristic of the fluorite structure.

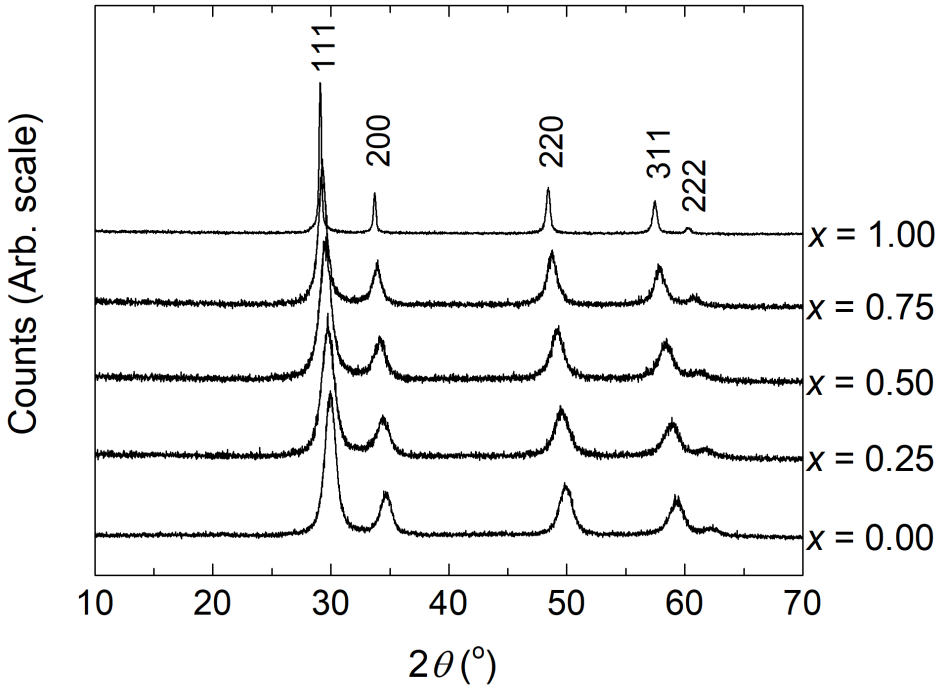

Fig. 3.5. Room temperature X-ray diffraction patterns of co-precipitated samples of composition $(Yb_{1-x}Nd_x)_2Zr_2O_7$ ($0.00 \leq x \leq 1.00$), after annealing at 800 °C for 5 h. Note peaks at *ca*. 39, 46 and 67° 2θ are due to the Pt sample holder.

In each case, the samples appear to be phase pure, within the detection limits (2-3 wt%) of the technique, thus indicating the total solubility of Nd in the $Yb_2Zr_2O_7$ fluorite structure. As described above, lanthanide zirconates display the fluorite structure for cations smaller than Gd^{3+}, and the pyrochlore structure for cations larger than Gd^{3+}. As such, ytterbium zirconate is known to exhibit the fluorite structure,[233] whereas neodymium zirconate exhibits the pyrochlore structure, as seen in **Fig. 3.4** above.[234,235] However, in the present case, pyrochlore ordering is not evident in samples annealed at 800 °C and is consistent with previous studies.[148]

Fig. 3.6 shows X-ray diffraction patterns of a representative sample, as a function of temperature, following co-precipitation and annealing at 800 °C. The X-ray diffraction patterns of other compositions are given in the Appendix. In each case, the Bragg peaks are seen to narrow as a result of sintering. The diffraction patterns at 1300 °C are plotted separately in **Fig. 3.7**. It is evident that at this temperature, a pure fluorite phase is seen for compositions x = 0.00 to x = 0.50, while at x = 1.00 a pure pyrochlore phase is formed. Close inspection of the pattern for the x = 0.75 composition (**Fig. 3.7 inset**) shows weak pyrochlore ordering peaks, confirming this composition to exhibit an intermediate type structure at this temperature.

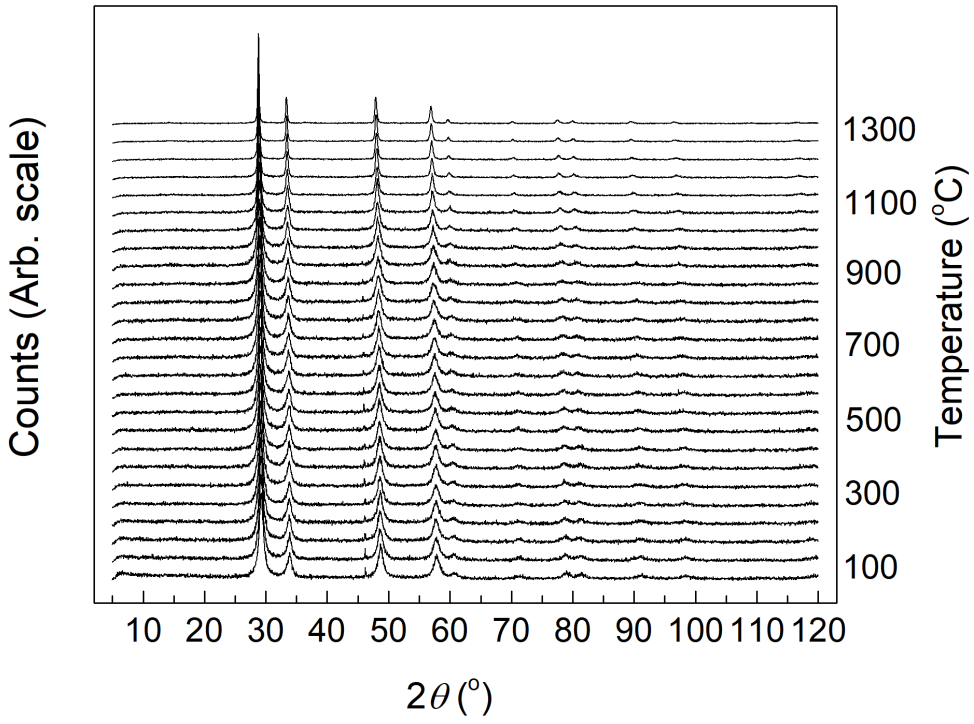

Fig. 3.6. Representative variable temperature X-ray diffraction data for $(Yb_{1-x}Nd_x)_2Zr_2O_7$; x = 0.75.

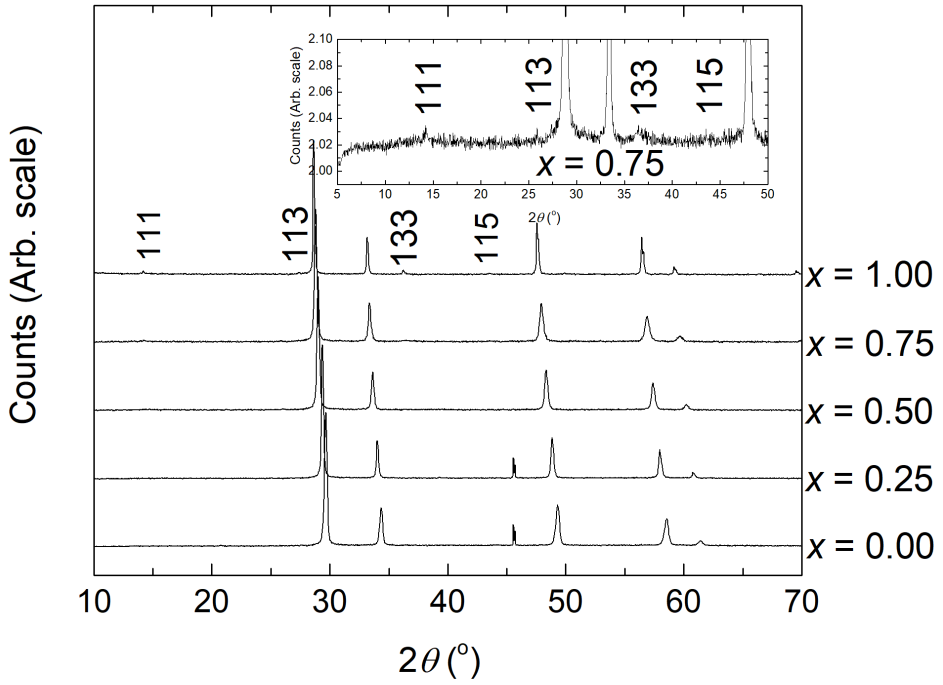

Fig. 3.7. X-ray diffraction patterns at 1300 °C of co-precipitated samples of composition $(Yb_{1-x}Nd_x)_2Zr_2O_7$ ($0.00 \leq x \leq 1.00$), after annealing at 800 °C for 5 h. Detail of the pattern for the x = 0.75 composition are inset. Note peak at *ca*. 46° 2θ is due to the Pt sample holder.

In order to directly compare the fluorite and pyrochlore structures, it is helpful to define an equivalent fluorite lattice parameter a_f:

$$a_{\mathrm{f}} = \frac{a_{\mathrm{p}}}{2} \tag{3.1}$$

where a_{p} is the pyrochlore lattice parameter. **Fig. 3.8** shows the thermal variation of a_{f}, derived from Rietveld analysis of the data, for each of the studied compositions. Thermal hysteresis is observed in the plots. On heating up to 1300 °C, curvature is seen in the plots, while on cooling, all samples show a linear plot for the lattice parameter. The extent of the hysteresis increases with increasing x-value, with the most hysteretic samples (x = 0.75 and 1.00) showing the fluorite structure before heating and the pyrochlore structure after heating. This suggests, that the observed curvature on heating may not only be associated with sintering, but also with ordering phenomena, which are most obvious in the samples that exhibit the pyrochlore structure after heating. If indeed this curvature is

associated with ordering, then the observed low levels of hysteresis in the other compositions might indicate that a degree of local ordering occurs, even in compositions that maintain the fluorite structure after heating.

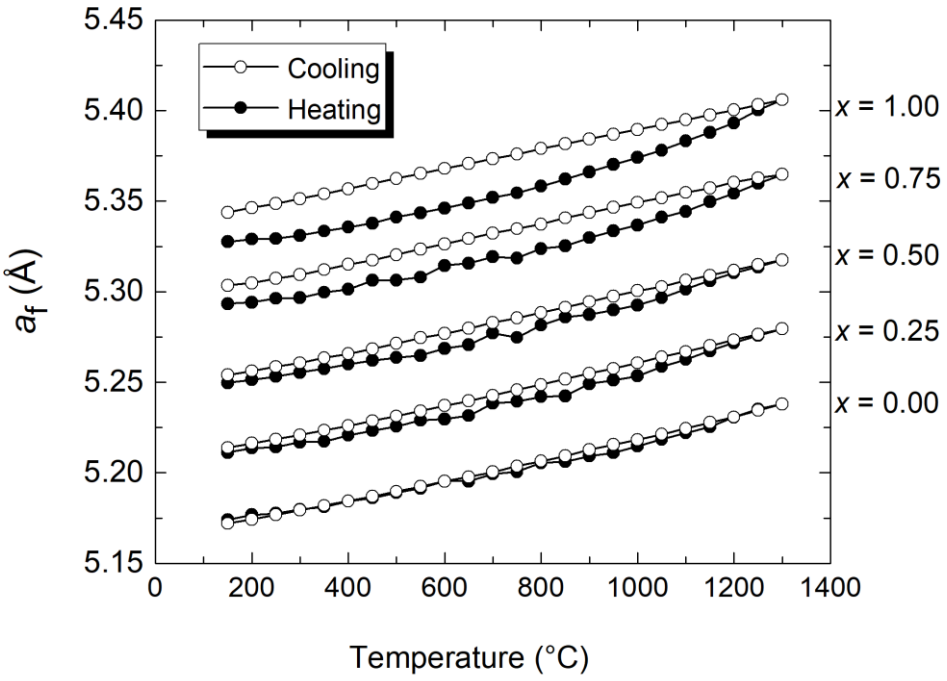

Fig. 3.8. Thermal variation of equivalent fluorite lattice parameter, a_f, derived from variable temperature X-ray diffraction data for co-precipitated samples of composition $(Yb_{1-x}Nd_x)_2Zr_2O_7$ ($0.00 \leq x \leq 1.00$), after annealing at 800 °C for 5 h.

Fig. 3.9 shows the room temperature X-ray powder diffraction patterns for a set of samples calcined at 1150 °C. As seen with the data at 1300 °C (**Fig. 3.7**) above, with increase in Nd^{3+} content, the structure transforms gradually from fluorite to pyrochlore. The pyrochlore ordering reflections (since the pyrochlore is a fluorite derivative), *i.e.* (111), (113), (133), and (115) are evident in two samples, $x = 0.75$ and $x = 1.00$. Thus, a decrease in the intensity of these reflections in the powder X-ray diffraction patterns is generally indicative of anti-site disorder in compounds adopting the pyrochlore-type structure.[225] In the case of the $x = 0.75$ composition, the intensity of the pyrochlore ordering peaks is relatively low, suggesting that the amount of anti-site disorder is relatively high. Similar behaviour has also been observed in other systems, such as in $(Nd_{1-x}Gd_x)_2Zr_2O_7$[87] and $(Nd_{1-x}Y_x)_2Zr_2O_7$.[236]

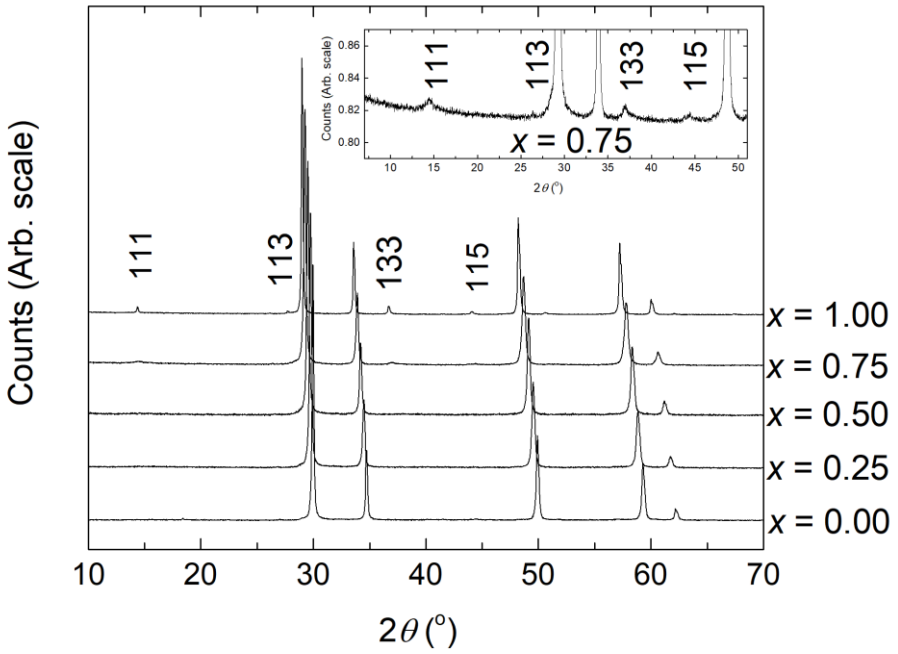

Fig. 3.9. Room temperature X-ray diffraction patterns of co-precipitated samples of composition $(Yb_{1-x}Nd_x)_2Zr_2O_7$ ($0.00 \leq x \leq 1.00$), after calcination at 1100 °C for 5 h. Indices of the pyrochlore super-lattice reflections are shown.

In the present study, no pyrochlore ordering peaks are evident in the diffraction data for the $x \leq 0.50$ compositions, and the samples appear more fluoritic in nature, at least in terms of long-range order. However, bearing in mind the small hysteresis seen in the thermal expansion of the lattice parameter seen in **Fig. 3.8** above, one cannot exclude the possibility of local pyrochlore type ordering for both the $x = 0.50$ and $x = 0.25$ compositions. As discussed above in section 3.1, lanthanide zirconates where the lanthanide cation has an ionic radius larger than that of Gd^{3+}, tend to adopt the pyrochlore structure, while those with ionic radii below that of Gd^{3+} generally exhibit a defect fluorite structure. Therefore, assuming the ionic radius of Gd^{3+} (1.053 Å)[25] to be the limiting value, the theoretical phase boundary composition, x_c, is easily calculated from the ionic radii of Yb^{3+} and Nd^{3+} (0.985 Å and 1.109 Å, respectively)[25] as follows:

$$1.053 = (1 - x_c)0.985 + 1.109x_c \qquad (3.2)$$

This gives a value for x_c of 0.548, *i.e.* entirely consistent with the observed phase behaviour in the present study.

Fig. 3.10. shows the compositional variation of a_f. The unit cell parameter is seen to increase linearly with increasing *x*-value in accordance with Vegard's law, up to x = 0.50, reflecting the substitution of the smaller Yb^{3+} cations by larger Nd^{3+} cations. A slight positive deviation is seen above x = 0.50, reflecting the larger volume of the more ordered pyrochlore phases. The value of the pyrochlore lattice parameter of ~10.67 Å for $Nd_2Zr_2O_7$ is in fairly reasonable agreement with the value reported by Subramanian *et al.*[79]

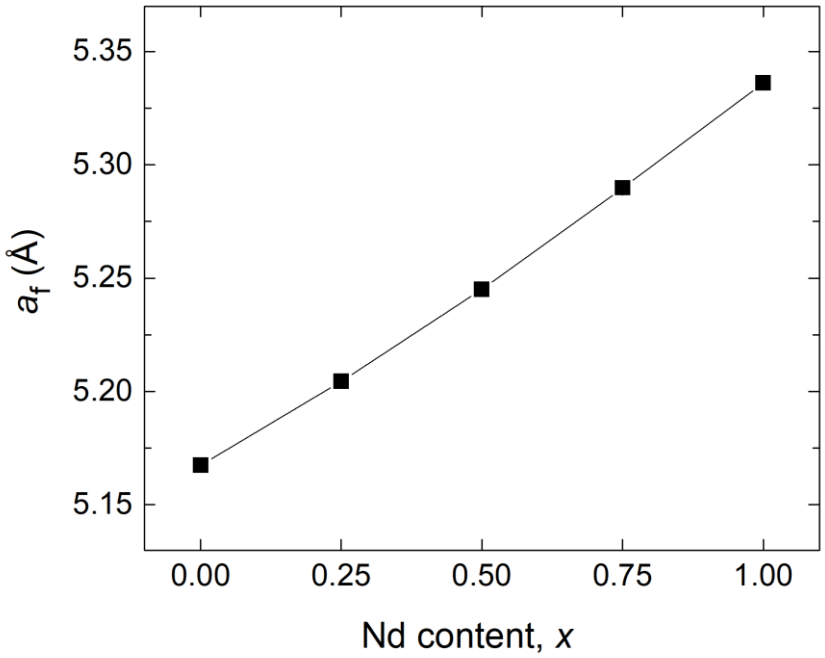

Fig. 3.10. Compositional variation of equivalent fluorite lattice parameter, a_f, for co-precipitated samples of composition $(Yb_{1-x}Nd_x)_2Zr_2O_7$ ($0.00 \leq x \leq 1.00$), after calcination at 1150 °C for 5 h. Error bars are smaller than the symbols used.

Compositions between x = 0.75 and x = 1.00 were examined to reveal the evolution of the pyrochlore super-structure, using neutron diffraction, **Fig. 3.11**. The pyrochlore superstructure peaks at x = 0.75 are considerably broader than those from the fluorite sub-structure, indicative of poor long-range ordering of the pyrochlore super-structure. The super-structure peaks are seen to become sharper with increasing *x*-value, consistent with increasing long-range order. Thus, compositions below x = 1.0, may be thought of as partially ordered, similar to what was observed in the $Gd_{2-x}Tb_xZr_2O_7$ system by Reynolds *et al.*[237]

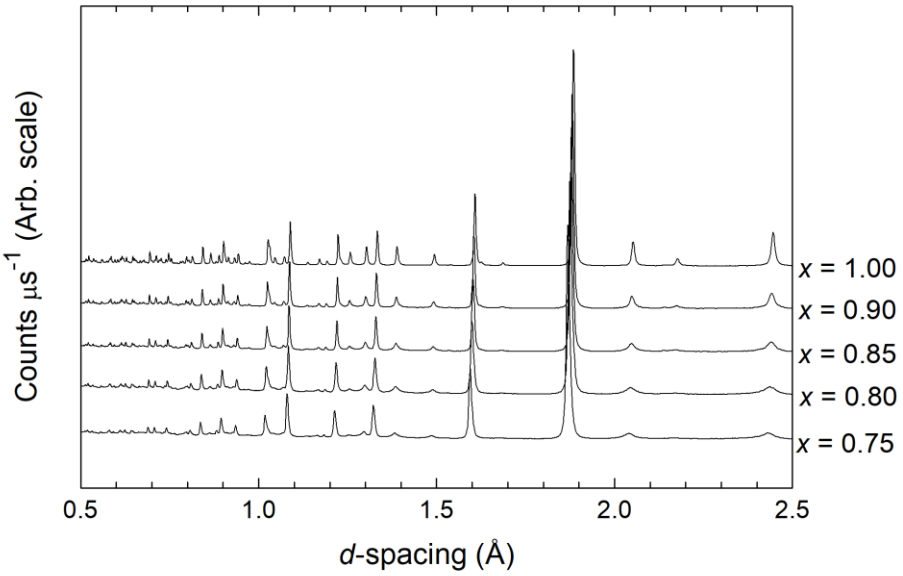

Fig. 3.11. Neutron diffraction profiles (back-scattered data) for samples of composition $(Yb_{1-x}Nd_x)_2Zr_2O_7$ ($0.75 \leq x \leq 1.00$), calcined at 1150 °C.

Fig. 3.12 shows the neutron diffraction profiles for the x = 0.75 and 1.00 compositions, calcined at various temperatures. In both cases, for samples calcined at 950 °C, only peaks corresponding to the fluorite structure are seen, but the peak widths are very broad, indicative of poor crystallinity. Increasing the calcination temperature to 1150 °C results in a narrowing of peaks, indicative of improved crystallinity. However, for the x = 0.75 composition, the pyrochlore super-structure peaks are very broad, suggesting only limited long-range order and significant anti-site cation disorder. After calcination at 1350 °C, the super-structure peaks for the x = 0.75 composition are sharper, but are still broader than the sub-structure peaks and the corresponding super-structure peaks for the x = 1.00 composition. Similar behaviour has been observed in lanthanide titanates[238] and hafnates.[239] These results indicate that even at a calcination temperature of 1350 °C, some fluorite like disorder persists in the x = 0.75 composition.

The variation of equivalent fluorite lattice parameter with calcination temperature is shown in **Fig. 3.13** for compositions x = 0.75 and x = 1.00. In both cases, a_f is seen to increase with increasing calcination temperature, with changes between 950 °C and 1350 °C of *ca*. 0.38% and 0.28% for the x = 0.75 and x = 1.00 compositions, respectively.These very small changes are likely associated with ordering and the removal of lattice strain.

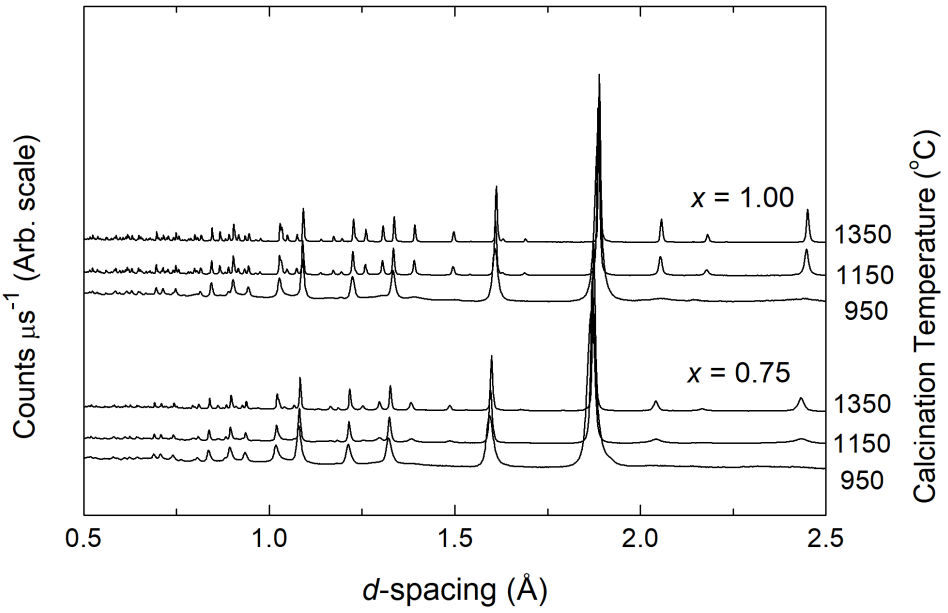

Fig. 3.12. Neutron diffraction patterns for $(Yb_{1-x}Nd_x)_2Zr_2O_7$ (x = 0.75 and 1.00), calcined at different temperatures.

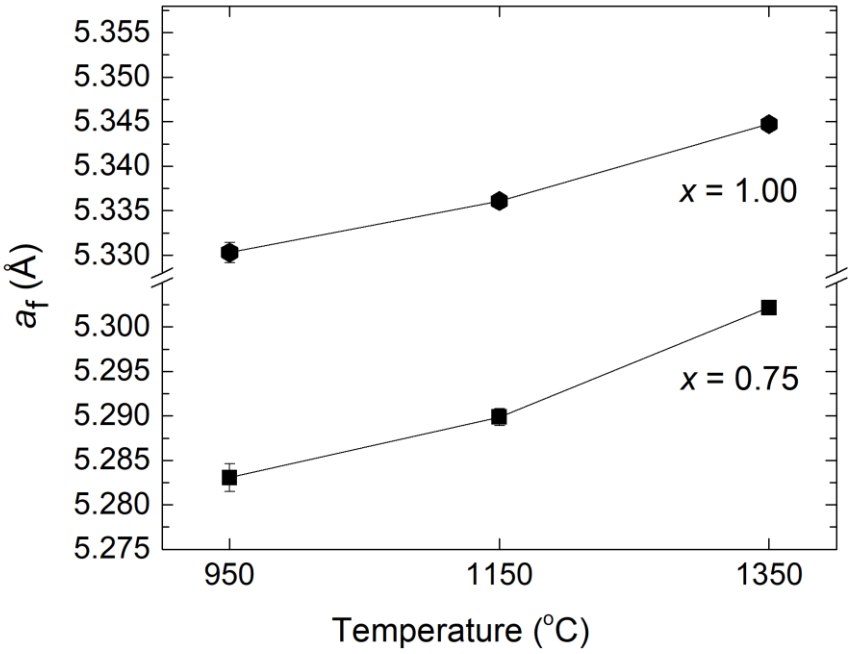

Fig. 3.13. Equivalent fluorite lattice parameter a_f as a function of calcination temperature for $(Yb_{1-x}Nd_x)_2Zr_2O_7$ (x = 0.75 and 1.00). Some of the error bars are smaller than the symbols used.

Average crystallite sizes were determined from the peak widths in the X-ray powder diffraction data of the studied compositions using Eqn 3.3. These are summarised in **Table 3.4**.

$$\Delta\beta = \frac{K\lambda}{\Delta\theta\cos\theta} \quad \Rightarrow \quad \beta = \frac{18000K\lambda}{\pi \mathrm{Lx}} \tag{3.3}$$

where β is the mean size of the crystallites, λ is the X-ray wavelength, K is a dimensionless shape factor with a value close to unity, θ is the Bragg angle and Lx is the Lorentzian mixing parameter obtained from GSAS. Unsurprisingly, crystallite sizes are seen to increase significantly with increasing calcination temperature.

Table 3.4. Average crystallite size as a function of composition and calcination temperature, in $(Yb_{1-x}Nd_x)_2Zr_2O_7$.

Composition	Annealing Temperature (°C)	Lx	Crystallite Size (Å)
x = 0.00	1150	11.1(4)	716
x = 0.25	1150	12.6(2)	631
x = 0.50	1150	14.7(9)	540
x = 0.75	1350	8.8(2)	909
	1150	12.5(3)	636
	950	41.5(8)	192
x = 1.00	1350	4.7(1)	1692
	1150	9.2(2)	869
	950	27.4(6)	291

3.3.2 Long-range structure

As mentioned above, the pyrochlore structure can be described as a cation and anion/vacancy ordered derivative of the fluorite structure. Therefore, X-ray diffraction patterns of the pyrochlore phase contain weak super-lattice reflections, in addition to the main reflections observed from the defect-fluorite phase. On the basis of the presence or absence of these super-lattice reflections, patterns corresponding to samples with x below

0.75 were refined in the defect-fluorite structure (space group $Fm\bar{3}m$), and those obtained from samples with x = 0.75 and 1.00, that exhibited the super-lattice reflections, were refined in the pyrochlore structure (space group $Fd\bar{3}m$) or a combination of both fluorite and pyrochlore structures.

3.3.2.1 Fluorite structured samples

Initial refinements of the fluorite structured compositions were carried out with oxygen atoms located on the ideal fluorite 8*c* site (0.25, 0.25, 0.25). This gave satisfactory fits in all cases. Nevertheless, further attempts to improve the fit were made, by considering positional disorder, the presence of which was indicated by the thermal parameters for anions (0.0489 $Å^2$ in the case of $Yb_2Zr_2O_7$). To model this disorder, the oxygen scattering was allowed to refine away from the ideal site in the 32*f* position *ca*. 0.27, 0.27 0.27. In all cases, this improved the fit. The significance of the improvement was checked using the F-Test described by Hamilton.[240] For example in the case of $Yb_2Zr_2O_7$, the total R_{wp} improved from 0.0316 to 0.0306, for the 8*c* and 32*f* site models respectively, at the expense of one additional variable. The total number of data points was 9697 with 114 variables. Using the Hamilton method, to represent a significantly better model the R-factor ratio needs to be higher than 1.0004 for these numbers of observables and variables. The observed R-factor ratio of 1.032 confirms the improvement to be significant. Attempts to refine simultaneous occupation of 8*c* and 32*f* sites, as seen for example in δ-Bi_2O_3,[241] failed to show any improvement over the single 32*f* site model. This was echoed for all compositions studied. Therefore, the results presented here correspond to the 32*f* single site model.

The fitted diffraction profiles for a representative fluorite structured composition, x = 0.25 calcined at 1150 °C are given in **Fig. 3.14** (the rest of the fits are given in Appendix B), with the corresponding crystal and refinement parameters given in **Table 3.5** and the refined structural parameters and significant contact distances given in **Table 3.6** (note symmetry related equivalent positions in Table 3.6 are denoted by the prime symbol, i.e. O(1)').

(a)

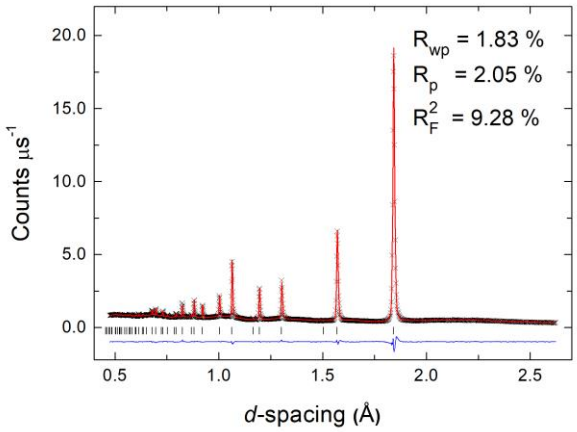

(b)

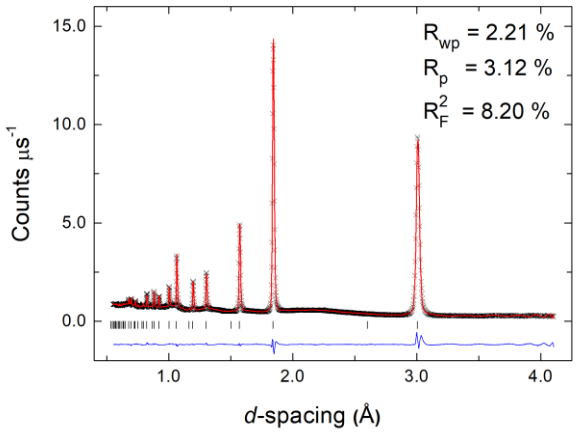

(c)

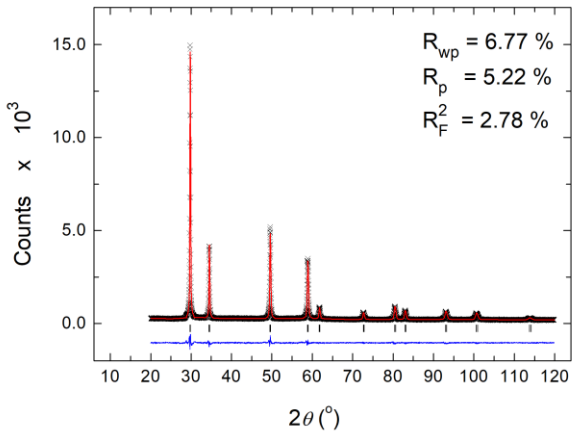

Fig. 3.14. Fitted diffraction profiles for a representative fluorite structured sample in the system $(Yb_{1-x}Nd_x)_2Zr_2O_7$, calcined at 1150 °C; x = 0.25, fits to (a) neutron backscattering; (b) neutron 90°, and (c) X-ray data are shown. Observed (crosses), calculated (solid line), and difference (lower) profiles of are shown. Reflection positions are indicated by markers.

Table 3.5. Crystal and refinement parameters for fluorite structured compositions in the system $(Yb_{1-x}Nd_x)_2Zr_2O_7$ ($0.00 \leq x \leq 0.50$) calcined at 1150 °C

Composition	$x = 0.00$	$x = 0.25$	$x = 0.50$
Calcination temp. (°C)	1150	1150	1150
Formula	$Yb_2Zr_2O_7$	$Yb_{1.5}Nd_{0.5}Zr_2O_7$	$YbNdZr_2O_7$
M_r (g mol^{-1})	640.52	626.14	611.74
Crystal system	Cubic	Cubic	Cubic
Space group	$Fm\bar{3}m$	$Fm\bar{3}m$	$Fm\bar{3}m$
Lattice parameter (Å)	5.1676(3)	5.2046(3)	5.2450(5)
Volume (Å^3)	137.99(2)	140.98(2)	144.29(4)
Z	1	1	1
D_{calc} (g cm^{-3})	7.708	7.375	7.040
R-factors:			
Neutron back scattering	$R_{wp} = 0.0285$	$R_{wp} = 0.0183$	$R_{wp} = 0.0228$
	$R_p = 0.0339$	$R_p = 0.0205$	$R_p = 0.0247$
	$R_{ex} = 0.0037$	$R_{ex} = 0.0038$	$R_{ex} = 0.0028$
	$R_F2 = 0.1344$	$R_F2 = 0.0928$	$R_F2 = 0.0976$
Neutron 90°	$R_{wp} = 0.0313$	$R_{wp} = 0.0221$	$R_{wp} = 0.0283$
	$R_p = 0.0462$	$R_p = 0.0312$	$R_p = 0.0314$
	$R_{ex} = 0.0034$	$R_{ex} = 0.0035$	$R_{ex} = 0.0026$
	$R_F2 = 0.1115$	$R_F2 = 0.0820$	$R_F2 = 0.0708$
X-ray	$R_{wp} = 0.0685$	$R_{wp} = 0.0677$	$R_{wp} = 0.0745$
	$R_p = 0.0517$	$R_p = 0.0522$	$R_p = 0.0593$
	$R_{ex} = 0.0496$	$R_{ex} = 0.0546$	$R_{ex} = 0.0600$
	$R_F2 = 0.0241$	$R_F2 = 0.0278$	$R_F2 = 0.0712$
Totals	$R_{wp} = 0.0306$	$R_{wp} = 0.0213$	$R_{wp} = 0.0264$
	$R_p = 0.0516$	$R_p = 0.0519$	$R_p = 0.0588$
χ^2	29.15	13.19	38.18
Total no. of variables	114	114	114
No. of profile points:			
Neutron back scattering	1713	1713	1713
Neutron 90°	2007	2007	2007
X-ray	5977	5977	5977
Total	9697	9697	9697
No. of reflections:			
Neutron back scattering	57	61	63
Neutron 90°	40	41	41
X-ray	24	24	26

Table 3.6. Refined atomic parameters and significant contact distances for fluorite structured compositions in the system $(Yb_{1-x}Nd_x)_2Zr_2O_7$ ($0.00 \leq x \leq 0.50$), calcined at 1150 °C

Composition	$x = 0.00$	$x = 0.25$	$x = 0.50$
Yb/Nd/Zr site	4*a*	4*a*	4*a*
Yb/Nd/Zr *x*,*y*,*z*	0	0	0
Yb/Nd/Zr Occ.	0.5/0/0.5	0.375/0.125/0.5	0.25/0.25/0.5
Yb/Nd/Zr U_{iso} (Å^2)	0.0246(2)	0.0242(1)	0.0220(2)
O(1) site	32*f*	32*f*	32*f*
O(1) *x*,*y*,*z*	0.2728(3)	0.2725(2)	0.2726(3)
O(1) Occ.	0.21875	0.21875	0.21875
O(1) U_{iso} (Å^2)	0.0338(5)	0.0379(4)	0.0440(5)
Yb/Nd/Zr-O(1) (Å)	2.1781(6)	2.1945(5)	2.2113(8)
Yb/Nd/Zr-O(1)′ (Å)	2.442(3)	2.456(2)	2.476(3)

where ′ indicates a symmetry related atom.

As seen in **Fig. 3.10** above, the lattice parameter increases with increasing Nd^{3+} content. The isotropic thermal parameter for O(1) is also seen to increase with increasing *x*-value, reflecting increasing disorder on the site.

For compositions $x = 0.75$ and $x = 1.00$, broadened diffraction patterns with no pyrochlore ordering peaks are seen for samples calcined at 950 °C, and therefore, these were modelled on the fluorite structure. As seen above in the lower *x*-value compositions, the single 32*f* site model gave a slightly better fit than the single 8*c* site model. **Fig. 3.15** shows the fitted diffraction profiles for the $x = 1.00$ composition calcined at 950 °C (fitted diffraction profiles for the $x = 0.75$ composition calcined at 950 °C are given in Appendix B), with the corresponding refinement and crystal parameters in **Table 3.7** and the refined structural parameters and significant contact distances in **Table 3.8**.

(a)

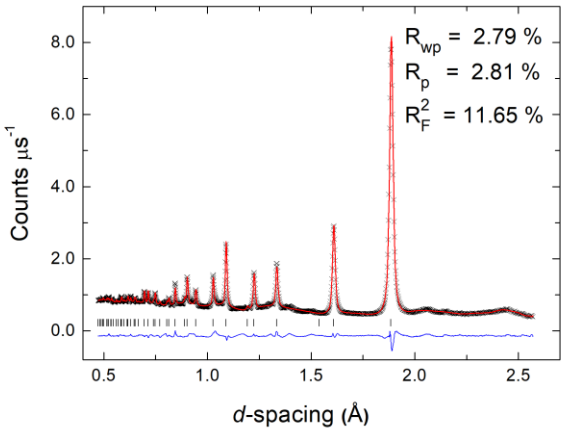

(b)

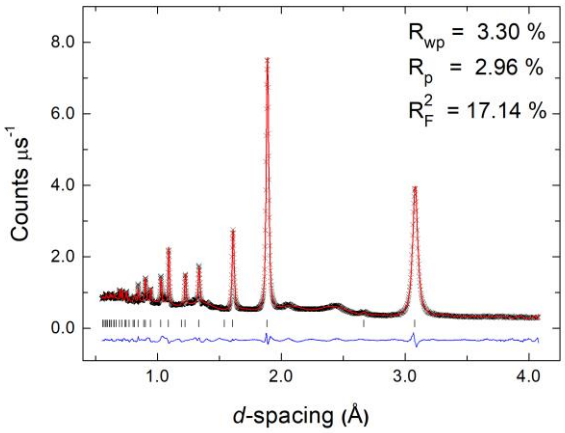

(c)

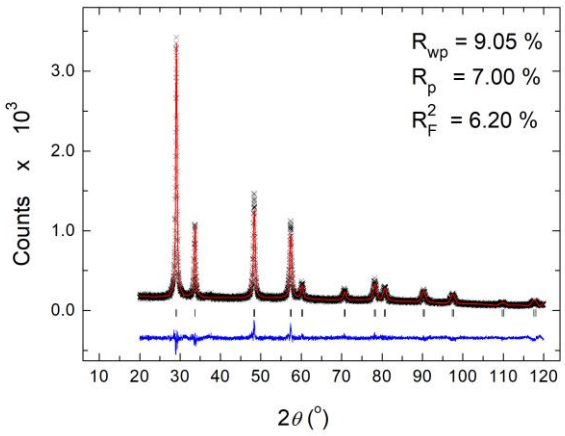

Fig. 3.15. Fitted diffraction profiles for a representative fluorite structured sample (x = 1.00) in the system $(Yb_{1-x}Nd_x)_2Zr_2O_7$, calcined at 950 °C. Fits to (a) neutron back scattering, (b) neutron 90°, and (c) X-ray data are shown. Observed (crosses), calculated (solid line), and difference (lower) profiles of are shown. Reflection positions are indicated by markers.

Table 3.7. Crystal and refinement parameters for fluorite structured compositions in the system $(Yb_{1-x}Nd_x)_2Zr_2O_7$ ($0.75 \leq x \leq 1.00$), calcined at 950 °C

Composition	$x = 0.75$	$x = 1.00$
Calcination temp. (°C)	950	950
Formula	$Yb_{0.5}Nd_{1.5}Zr_2O_7$	$Nd_2Zr_2O_7$
M_r (g mol^{-1})	597.33	582.92
Crystal system	Cubic	Cubic
Space group	$Fm\bar{3}m$	$Fm\bar{3}m$
Lattice parameter (Å)	5.2831(16)	5.3301(21)
Volume (Å^3)	147.45(13)	151.43(18)
Z	1	1
D_{calc} (g cm^{-3})	6.727	6.392
R-factors:		
Neutron back scattering	$R_{wp} = 0.0190$	$R_{wp} = 0.0279$
	$R_p = 0.0259$	$R_p = 0.0281$
	$R_{ex} = 0.0029$	$R_{ex} = 0.0039$
	$R_F2 = 0.1089$	$R_F2 = 0.1165$
Neutron 90°	$R_{wp} = 0.0246$	$R_{wp} = 0.0330$
	$R_p = 0.0328$	$R_p = 0.0296$
	$R_{ex} = 0.0025$	$R_{ex} = 0.0036$
	$R_F2 = 0.1373$	$R_F2 = 0.1714$
X-ray	$R_{wp} = 0.0750$	$R_{wp} = 0.0905$
	$R_p = 0.0599$	$R_p = 0.0700$
	$R_{ex} = 0.0641$	$R_{ex} = 0.0751$
	$R_F2 = 0.0600$	$R_F2 = 0.0620$
Totals	$R_{wp} = 0.0229$	$R_{wp} = 0.0314$
	$R_p = 0.0594$	$R_p = 0.0839$
χ^2	28.21	33.84
Total no. of variables	114	114
No. of profile points:		
Neutron back scattering	1868	1815
Neutron 90°	2325	2399
X-ray	6879	4999
Total	11072	9213
No. of reflections:		
Neutron back scattering	110	97
Neutron 90°	108	131
X-ray	30	30

Table 3.8. Refined atomic parameters and significant contact distances for fluorite structured compositions in the system $(Yb_{1-x}Nd_x)_2Zr_2O_7$ ($0.75 \leq x \leq 1.00$), calcined at 950 °C

Composition	$x = 0.75$	$x = 1.00$
Yb/Nd/Zr site	4*a*	4*a*
Yb/Nd/Zr *x*,*y*,*z*	0	0
Yb/Nd/Zr Occ.	0.125/0.375/0.5	0/0.5/0.5
Yb/Nd/Zr U_{iso} ($Å^2$)	0.0184(2)	0.0135(2)
O(1) site	32*f*	32*f*
O(1) *x*,*y*,*z*	0.2734(4)	0.2754(4)
O(1) Occ.	0.21875	0.21875
O(1) U_{iso} ($Å^{2)}$	0.0426(7)	0.0441(8)
Yb/Nd/Zr-O(1) (Å)	2.2254(10)	2.2408(11)
Yb/Nd/Zr-O(1)′ (Å)	2.502(4)	2.542(4)

Despite being calcined at 950 °C, the unit cell parameters for the $x = 0.75$ and 1.00 fluorite structures are very close to the equivalent fluorite lattice parameter values for the same compositions calcined at 1150 °C, that exhibited the pyrochlore structure (**Fig. 3.10** above). Therefore, despite the difference in calcination temperature and crystallite size, it is useful to compare fluorite structural parameters across the whole compositional range. **Fig. 3.16** shows the compositional variation of M-O(1) distances for the fluorite structured compositions. Both M-O(1) and M-O(1)′ increase with increasing *x*-value, reflecting the increasing unit cell volume.

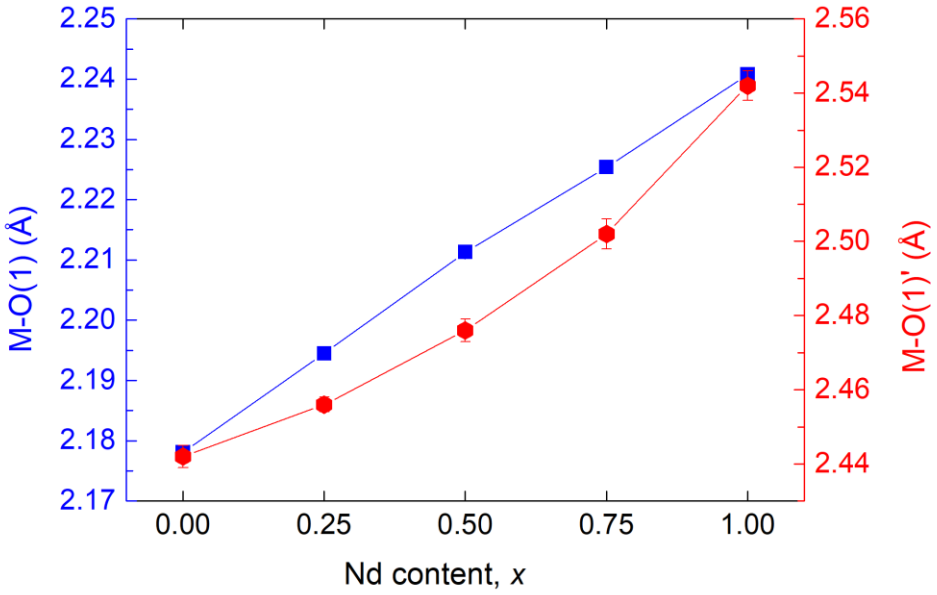

Fig. 3.16. Compositional variation of M-O distances, M-O(1) (blue) and (M-O(1)′ (red), in fluorite structured samples of composition $(Yb_{1-x}Nd_x)_2Zr_2O_7$. Some of the error bars are smaller than the symbols used.

To account for the effect of chemical expansion of the unit cell, the M-O(1) bond distances can be normalised to the lattice parameter as follows:

$$(\mathrm{M-O})_{norm} = a_0 \frac{(\mathrm{M-O})}{a} \tag{3.4}$$

where a_0 is the lattice parameter of the x = 0.00 composition. The resulting plots of normalised bond distances show a maximum in M-O(1) and a minimum in M-O(1)′ at x = 0.25 (**Fig. 3.17**).

These variations reflect the extent of distortion of the cation coordination environment, as the oxygen atoms shift away from the ideal 8*c* site towards the apices of the tetrahedral site in the <1 1 1> direction. This is easily seen in the O(1)-8*c* distance (**Fig. 3.18**), which reflects the normalized M-O(1) plot. The extent of distortion in the cation coordination environment rises sharply from x = 0.50 to 1.00, the compositional region where the critical cation ratio is reached, and the thermodynamically stable phase is of pyrochlore structure.

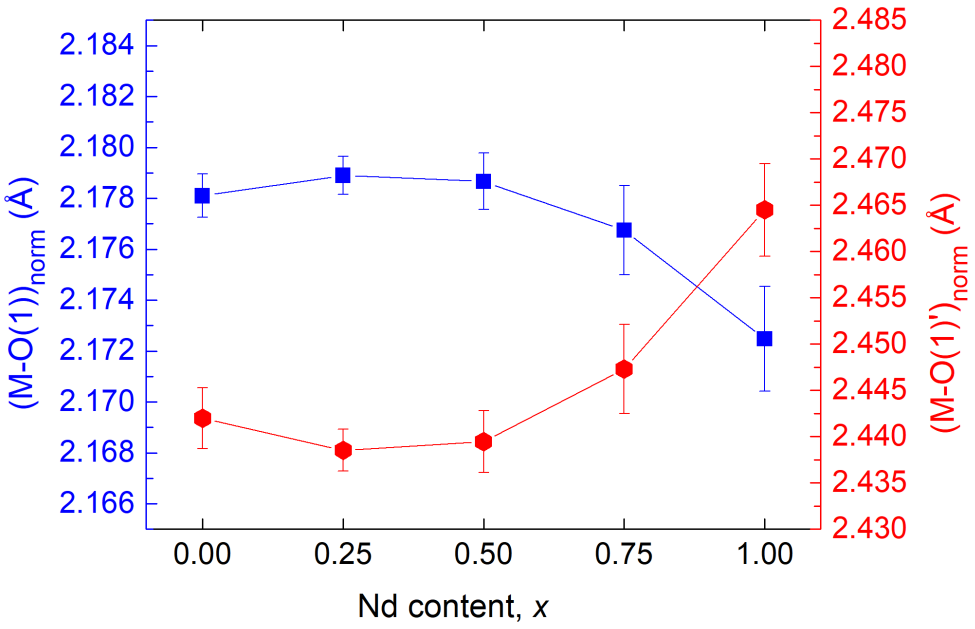

Fig. 3.17. Compositional variation in normalised bond distances, $(M\text{-}O(1))_{norm}$ (blue) and $(M\text{-}O(1)')_{norm}$ (red), in fluorite structured samples of composition $(Yb_{1-x}Nd_x)_2Zr_2O_7$

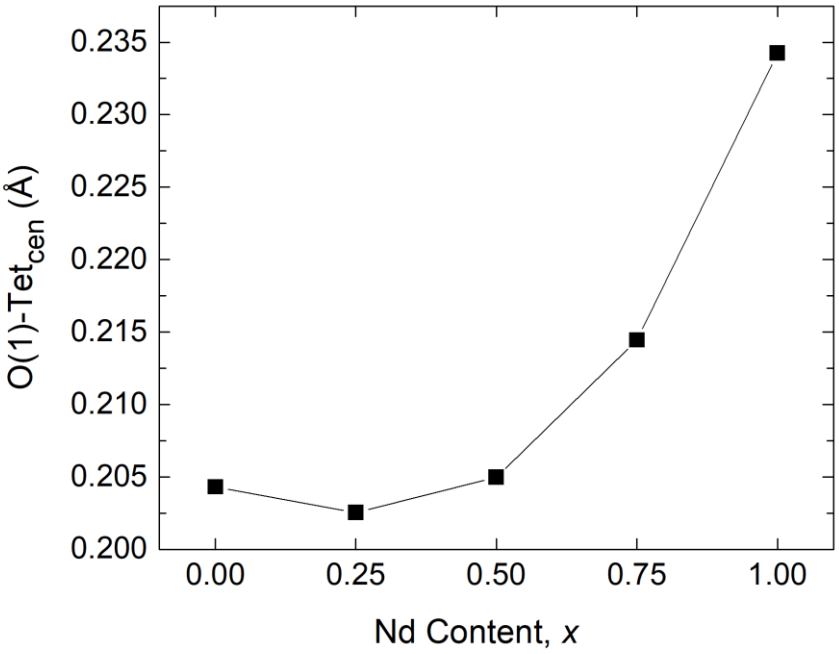

Fig. 3.18. Compositional variation of O(1)-8*c* distance in fluorite structured samples of composition $(Yb_{1-x}Nd_x)_2Zr_2O_7$. Error bars are smaller than the symbols used.

From the data in **Table 3.6** and **Table 3.8** above, it is possible to construct models for the local cation environments in this system. Since short inter-site contact distances preclude the simultaneous occupancy of more than one 32*f* site per tetrahedral cavity in the cubic close packed lattice, and bearing in mind the preferred coordination number of six for the small Zr^{4+} cation in oxide systems, it is likely that zirconium achieves this coordination through six shorter contacts to O(1), while the larger Nd^{3+} cation is likely to exhibit longer bond distances for example to the O(1)′ site, which is slightly further away. If all the Zr^{4+} cations exhibit six coordination, then the remaining oxygen atoms must be coordinated to Ln^{3+} in eight coordination geometry. In conjunction with the data in **Table 3.8**, two proposed coordination geometries are shown in **Fig. 3.19**, with Zr^{4+} in a distorted octahedral geometry and Ln^{3+} in cubic coordination geometry. These models are consistent with the average coordination numbers and bond lengths/angles as well as the known stereochemistry of these cations, but local deviations cannot be excluded.

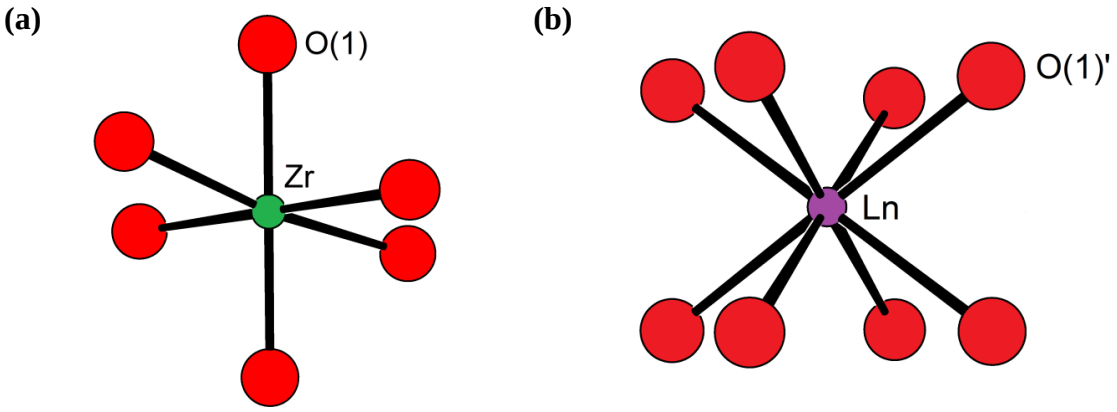

Fig. 3.19. Proposed coordination geometries for **(a)** zirconium and **(b)** Yb/Nd in fluorite structured compositions of general formula $(Yb_{1-x}Nd_x)_2Zr_2O_7$. Figures generated from the refined parameters for $Nd_2Zr_2O_7$.

3.3.2.2 Pyrochlore structured samples

For samples of composition $0.75 \leq x \leq 1.00$ annealed at 1150 °C, a number of models were tried to accurately fit the data. All compositions could be fitted with disordered fluorite model, but this failed to take into account the pyrochlore ordering peaks. Fits using a simple ordered pyrochlore model accounted for these super-lattice peaks, but there was difficulty in accurately modelling the peak shape, since the super-lattice peaks were broader than those arising from the fluorite sub-lattice (see **Fig. 3.11** above). This broadening suggests that the coherence length of the pyrochlore ordering was small.

Fits were improved by the use of a two-phase pyrochlore plus defect fluorite model, for example the total R_{wp} for the $x = 0.75$ composition improved from 0.0436 to 0.0321, for the single phase and two-phase models, respectively. This model can be interpreted as ordered pyrochlore regions within a disordered fluorite matrix, reflecting the transition from the fluorite to pyrochlore structures proceeding via the intermediate emergence and progressive growth of pyrochlore-type domains in a fluorite matrix.[239] However, despite the quality of the two-phase fit, the exact composition of the two phases in this model remains uncertain.

A more useful approach is to try to account for the preferred *hkl* dependent broadening in the peak shape parameters and treat the sample as a single pyrochlore phase with some disorder. Disorder on the anion sub-lattice was modelled first. Three oxygen atom sites were included in the model, viz.: O(1), the 48*f* site at *ca*. 0.375, 0.125, 0.125, O(2) the 8*b* site at 0.375, 0.375, 0.375 and O(3) the 8*a* site at 0.125, 0.125, 0.125, with respective starting occupancies of 1.0, 1.0 and 0.0. Initially, unconstrained refinement of site occupancies on these sites was carried out. These invariably led to partial occupancy of O(1) and O(3) and full occupancy of O(2). Therefore, in further refinements the occupancies of the O(1) and O(3) sites were allowed to vary within a total occupancy constraint and the occupancy of O(2) was fixed at unity.

The extent of anti-site cation ordering was also investigated in the refinements, with three different cations distributed over two sites. Therefore anti-site disorder was refined assuming an equal preference for Yb^{3+} and Nd^{3+} to substitute for Zr^{4+} and *vice versa, i.e.*:

$$Zr_{Zr}^{X} + xNd_{Nd}^{X} + (1-x)Yb_{Yb}^{X} \rightarrow Zr_{Nd/Yb}^{\bullet} + xNd_{Zr}^{'} + (1-x)Yb_{Zr}^{'} \quad (3.5)$$

Attempts to refine preferential substitution for a single lanthanide cation type always resulted in higher R-factors. To facilitate the refinement, isotropic thermal parameters for the A and B cation sites were tied to a single variable.

Fig. 3.20 shows the fitted diffraction profiles for a representative sample (x = 0.75), calcined at 1150 °C in the compositional range $0.75 \leq x \leq 1.00$. The corresponding crystal and refinement parameters are given in **Table 3.9**, refined structural parameters and significant contact distances given in **Table 3.10**.

(a)

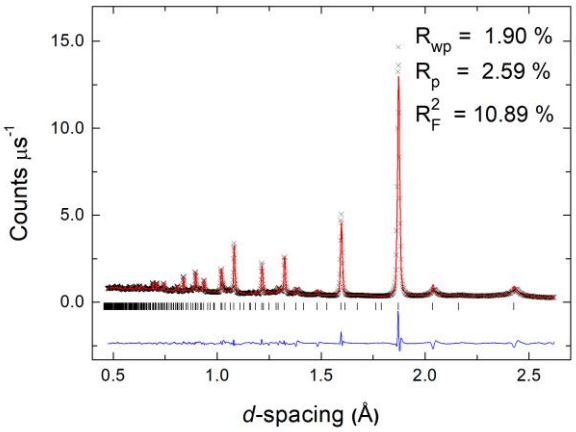

(b)

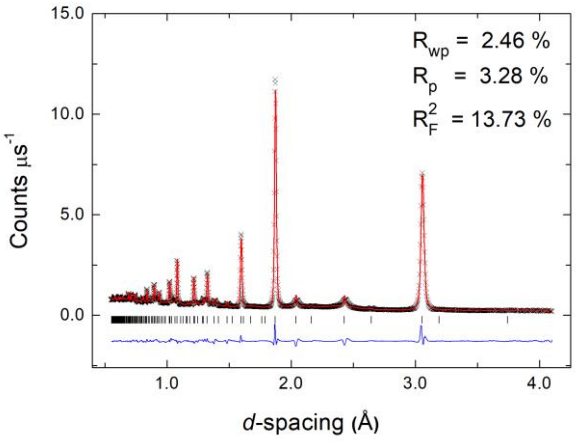

(c)

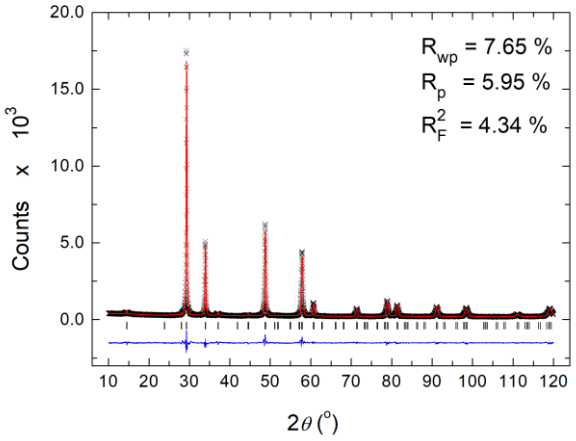

Fig. 3.20. Fitted diffraction profiles for a representative pyrochlore structured sample in the system $(Yb_{1-x}Nd_x)_2Zr_2O_7$, calcined at 1150 °C; x = 0.75, fits to (a) neutron backscattering; (b) neutron 90°, and (c) X-ray data are shown. Observed (crosses), calculated (solid line), and difference (lower) profiles of are shown. Reflection positions are indicated by markers.

Table 3.9. Crystal and refinement parameters for pyrochlore structured compositions in the system $(Yb_{1-x}Nd_x)_2Zr_2O_7$ ($0.75 \leq x \leq 1.00$), calcined at 1150 °C

Composition	$x = 0.75$	$x = 0.80$	$x = 0.85$
Calcination temp. (°C)	1150	1150	1150
Formula	$Yb_{0.5}Nd_{1.5}Zr_2O_7$	$Yb_{0.4}Nd_{1.6}Zr_2O_7$	$Yb_{0.3}Nd_{1.7}Zr_2O_7$
M_r (g mol^{-1})	597.32	594.44	591.56
Crystal system	Cubic	Cubic	Cubic
Space group	$Fd\bar{3}m$	$Fd\bar{3}m$	$Fd\bar{3}m$
Lattice parameter (Å)	10.5798(9)	10.6144 (29)	10.6326(21)
Volume (Å^3)	1184.2(3)	1195.9 (1.0)	1202.0(7)
Z	8	8	8
D_{calc} (g cm^{-3})	6.701	6.603	6.538
R-factors:			
Neutron back scattering	$R_{wp} = 0.0389$	$R_{wp} = 0.0369$	$R_{wp} = 0.0403$
	$R_p = 0.0532$	$R_p = 0.0528$	$R_p = 0.0604$
	$R_{ex} = 0.0037$	$R_{ex} = 0.0050$	$R_{ex} = 0.0051$
	$R_F2 = 0.1545$	$R_F2 = 0.1368$	$R_F2 = 0.1464$
Neutron 90°	$R_{wp} = 0.0487$	$R_{wp} = 0.0463$	$R_{wp} = 0.0474$
	$R_p = 0.0486$	$R_p = 0.0502$	$R_p = 0.0562$
	$R_{ex} = 0.0035$	$R_{ex} = 0.0049$	$R_{ex} = 0.0049$
	$R_F2 = 0.1504$	$R_F2 = 0.1336$	$R_F2 = 0.1143$
X-ray	$R_{wp} = 0.0765$	$R_{wp} = 0.0696$	$R_{wp} = 0.0755$
	$R_p = 0.0595$	$R_p = 0.0536$	$R_p = 0.0565$
	$R_{ex} = 0.0517$	$R_{ex} = 0.0506$	$R_{ex} = 0.0509$
	$R_F2 = 0.0434$	$R_F2 = 0.0340$	$R_F2 = 0.0444$
Totals	$R_{wp} = 0.0447$	$R_{wp} = 0.0425$	$R_{wp} = 0.0446$
	$R_p = 0.0594$	$R_p = 0.1115$	$R_p = 0.1169$
χ^2	59.99	32.24	34.41
Total no. of variables	119	121	120
No. of profile points:			
Neutron back scattering	1986	1986	1986
Neutron 90°	2117	2117	2118
X-ray	6581	6581	6581
Total	10684	10684	10685
No. of reflections:			
Neutron back scattering	724	727	745
Neutron 90°	326	330	326
X-ray	126	126	126

Table 3.9. Continued

Composition	$x = 0.90$	$x = 0.95$	$x = 1.00$
Calcination temp. (°C)	1150	1150	1150
Formula	$Yb_{0.2}Nd_{1.8}Zr_2O_7$	$Yb_{0.1}Nd_{1.9}Zr_2O_7$	$Nd_2Zr_2O_7$
M_r (g mol^{-1})	588.68	585.80	582.92
Crystal system	Cubic	Cubic	Cubic
Space group	$Fd\bar{3}m$	$Fd\bar{3}m$	$Fd\bar{3}m$
Lattice parameter (Å)	10.6488(18)	10.6677(13)	10.6722(3)
Volume (Å^3)	1207.6(6)	1214.0(5)	1215.5(1)
Z	8	8	8
D_{calc} (g cm^{-3})	6.476	6.410	6.371
R-factors:			
Neutron back scattering	$R_{wp} = 0.0389$	$R_{wp} = 0.0321$	$R_{wp} = 0.0306$
	$R_p = 0.0582$	$R_p = 0.0475$	$R_p = 0.0490$
	$R_{ex} = 0.0050$	$R_{ex} = 0.0051$	$R_{ex} = 0.0040$
	$R_F2 = 0.1231$	$R_F2 = 0.0839$	$R_F2 = 0.0562$
Neutron 90°	$R_{wp} = 0.0409$	$R_{wp} = 0.0336$	$R_{wp} = 0.0292$
	$R_p = 0.0544$	$R_p = 0.0484$	$R_p = 0.0475$
	$R_{ex} = 0.0048$	$R_{ex} = 0.0048$	$R_{ex} = 0.0036$
	$R_F2 = 0.1144$	$R_F2 = 0.0815$	$R_F2 = 0.0624$
X-ray	$R_{wp} = 0.0799$	$R_{wp} = 0.0823$	$R_{wp} = 0.0887$
	$R_p = 0.0598$	$R_p = 0.0626$	$R_p = 0.0660$
	$R_{ex} = 0.0524$	$R_{ex} = 0.0534$	$R_{ex} = 0.0543$
	$R_F2 = 0.0408$	$R_F2 = 0.0576$	$R_F2 = 0.0517$
Totals	$R_{wp} = 0.0405$	$R_{wp} = 0.0335$	$R_{wp} = 0.0307$
	$R_p = 0.1156$	$R_p = 0.1164$	$R_p = 0.0658$
χ^2	30.61	20.19	26.08
Total no. of variables	118	118	116
No. of profile points:			
Neutron back scattering	1985	1985	1985
Neutron 90°	2325	2325	2431
X-ray	6581	6581	6880
Total	10891	10891	11296
No. of reflections:			
Neutron back scattering	753	769	769
Neutron 90°	562	572	772
X-ray	126	126	126

Table 3.10a. Refined atomic parameters and significant contact distances for pyrochlore structured compositions in the system $(Yb_{1-x}Nd_x)_2Zr_2O_7$ ($0.75 \leq x \leq 0.85$), calcined at 1150 °C

Composition	$x = 0.75$	$x = 0.80$	$x = 0.85$
Yb(1)/Nd(1)/Zr(1) site	16*d*	16*d*	16*d*
Yb(1)/Nd(1)/Zr(1) *x*,*y*,*z*	0.5	0.5	0.5
Yb(1) Occ.	0.198(4)	0.161(5)	0.130(3)
Nd(1) Occ.	0.593(11)	0.643(18)	0.738(19)
Zr(1) Occ.	0.210(15)	0.196(23)	0.132(22)
Yb(2)/Nd(2)/Zr(2) site	16*c*	16*c*	16*c*
Yb(2)/Nd(2)/Zr(2) *x*,*y*,*z*	0.0	0.0	0.0
Yb(2) Occ.	0.052(4)	0.039(5)	0.020(3)
Nd(2) Occ.	0.157(11)	0.157(18)	0.112(19)
Zr(2) Occ.	0.790(15)	0.804(23)	0.868(22)
Yb/Nd/Zr U_{iso} ($Å^2$)	0.0153(1)	0.0123(2)	0.0108(2)
O(1) site	48*f*	48*f*	48*f*
O(1) *x*	0.3496(2)	0.3438(1)	0.3415(1)
O(1) y,z	0.125	0.125	0.125
O(1) Occ.	0.867(4)	0.889(3)	0.912(2)
O(1) U_{iso} ($Å^{2)}$	0.0299(4)	0.0251(4)	0.0217(3)
O(2) site	8*b*	8*b*	8*b*
O(2) *x*,*y*,*z*	0.375	0.375	0.375
O(2) Occ.	1.0	1.0	1.0
O(2) U_{iso} ($Å^{2)}$	0.074(2)	0.0379(9)	0.0284(6)
O(3) site	8*a*	8*a*	8*a*
O(3) *x*,*y*,*z*	0.125	0.125	0.125
O(3) Occ.	0.799(24)	0.666(16)	0.527(12)
O(3) U_{iso} ($Å^{2)}$	0.074(2)	0.0379(9)	0.0284(6)
Yb(1)/Nd(1)/Zr(1)-O(1) (Å)	2.4556(13)	2.5036(10)	2.5243(8)
Yb(1)/Nd(1)/Zr(1)-O(2) (Å)	2.2906(2)	2.2981(5)	2.3020(3)
Yb(2)/Nd(2)/Zr(2)-O(1) (Å)	2.1466(10)	2.1244(7)	2.1166(6)
Yb(2)/Nd(2)/Zr(2)-O(3) (Å)	2.2906(2)	2.2981(5)	2.3020(3)
M-O weighted average (Å)	2.298	2.310	2.316

Table 3.10b. Refined atomic parameters and significant contact distances for pyrochlore structured compositions in the system $(Yb_{1-x}Nd_x)_2Zr_2O_7$ ($0.90 \leq x \leq 1.00$), calcined at 1150 °C

Composition	$x = 0.90$	$x = 0.95$	$x = 1.00$
Yb(1)/Nd(1)/Zr(1) site	16*d*	16*d*	16*d*
Yb(1)/Nd(1)/Zr(1) *x*,*y*,*z*	0.5	0.5	0.5
Yb(1) Occ.	0.093(2)	0.048(1)	
Nd(1) Occ.	0.838(18)	0.903(17)	0.909(3)
Zr(1) Occ.	0.069(20)	0.050(18)	0.091(3)
Yb(2)/Nd(2)/Zr(2) site	16*c*	16*c*	16*c*
Yb(2)/Nd(2)/Zr(2) *x*,*y*,*z*	0.0	0.0	0.0
Yb(2) Occ.	0.007(2)	0.002(1)	
Nd(2) Occ.	0.062(18)	0.047(15)	0.091(3)
Zr(2) Occ.	0.944(1)	0.950(18)	0.909(3)
Yb/Nd/Zr U_{iso} ($Å^2$)	0.0172(2)	0.00711(8)	0.0059(1)
O(1) site	48*f*	48*f*	48*f*
O(1) *x*	0.33907(7)	0.33719(5)	0.33582(3)
O(1) y,z	0.125	0.125	0.125
O(1) Occ.	0.944(1)	0.968(1)	0.985(1)
O(1) U_{iso} ($Å^2$)	0.0172(2)	0.0133(1)	0.00986(7)
O(2) site	8*b*	8*b*	8*b*
O(2) *x*,*y*,*z*	0.375	0.375	0.375
O(2) Occ.	1.0	1.0	1.0
O(2) U_{iso} ($Å^2$)	0.0171(4)	0.0101(2)	0.0059(1)
O(3) site	8*a*	8*a*	8*a*
O(3) *x*,*y*,*z*	0.125	0.125	0.125
O(3) Occ.	0.335(8)	0.190(5)	0.091(3)
O(3) U_{iso} ($Å^{2)}$	0.0171(4)	0.0101(2)	0.0059(1)
Yb(1)/Nd(1)/Zr(1)-O(1) (Å)	2.5457(6)	2.5637(4)	2.5748(2)
Yb(1)/Nd(1)/Zr(1)-O(2) (Å)	2.3055(3)	2.3096(2)	2.31060(5)
Yb(2)/Nd(2)/Zr(2)-O(1) (Å)	2.1079(4)	2.1027(3)	2.0972(2)
Yb(2)/Nd(1)/Zr(2)-O(3) (Å)	2.3055(3)	2.3096(2)	2.31060(5)
M-O weighted average (Å)	2.323	2.329	2.332

Fig. 3.21 shows the variation in the pyrochlore lattice parameter as a function of composition from $x = 0.75$ to $x = 1.0$. The lattice parameter shows the expected expansion with increasing x-value, as the larger Nd^{3+} cation replaces the smaller Yb^{3+} cation. The plot shows slight deviation from linearity at $x = 0.75$ and $x = 1.00$. This is due to small differences in calibration between X-ray data collected on the D5000 diffractometer ($x = 0.80$ to 0.95) and those collected on the X'Pert Pro diffractometer ($x = 0.75$ and 1.00). This is also reflected in higher R-factors for the fits to the D5000 data.

Anti-site cation disorder is evident across the compositional range, but decreases with increasing x-value (**Fig. 3.22**). At $x = 0.75$ the system contains around 20% anti-site cation disorder, decreasing to less than 10% at $x = 1.00$.

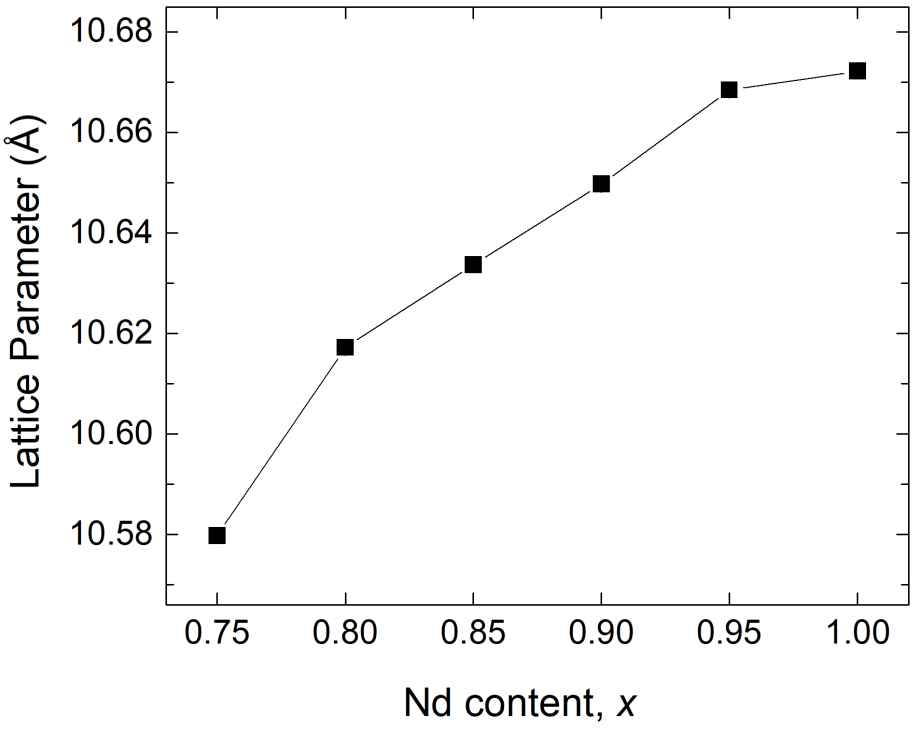

Fig. 3.21. Compositional variation of pyrochlore lattice parameter in $(Yb_{1-x}Nd_x)_2Zr_2O_7$ ($0.75 \leq x \leq 0.10$) compositions calcined at 1150 °C. Error bars are smaller than the symbols used.

(a)

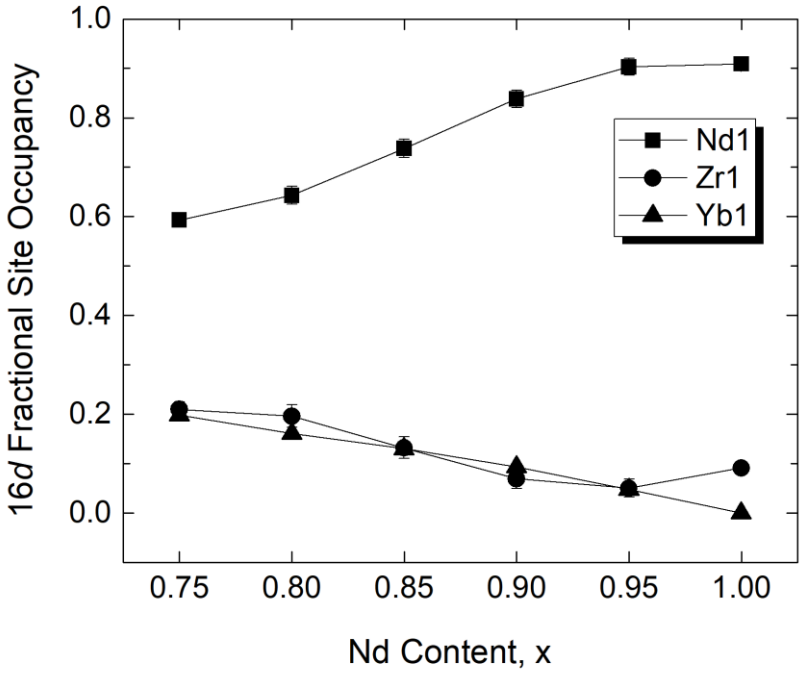

(b)

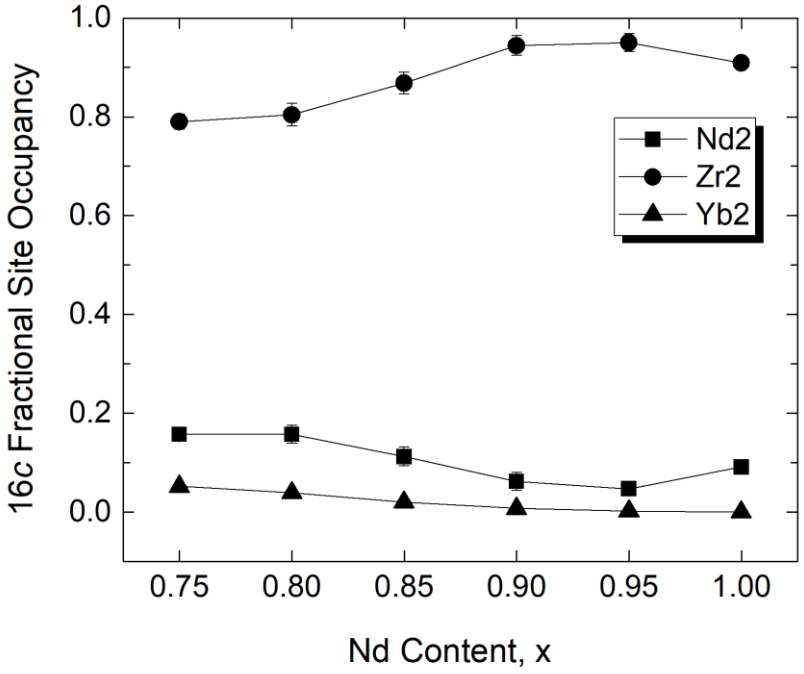

Fig. 3.22. Compositional variation of (a) 16*d* and (b) 16*c* fractional site occupation by Yb, Nd and Zr in $(Yb_{1-x}Nd_x)_2Zr_2O_7$ ($0.75 \leq x \leq 0.10$) compositions, calcined at 1150 °C. Some of the error bars are smaller than the symbols used.

The main defect in the oxide ion sub-lattice is the oxygen Frenkel defect:

$$O_O^X \rightarrow O_i^{''} + V_O^{\bullet\bullet} \quad (3.6)$$

Occupancy of the 8*a* site requires displacement of anions from either the 48*f* or 8*b* sites.[110,237] In the present case, the 8*b* (O(2)) site was always found to be fully occupied and the Frenkel vacancies are entirely located on the 48*f* site (O(1)).

The concentration of Frenkel defects decreases with increasing *x*-value as seen in **Fig. 3.23**, which shows the oxygen site occupancies presented as a fraction of total oxygen content. At $x = 0.75$, around 10% of the total oxide sub-lattice is displaced into the O(3) site.

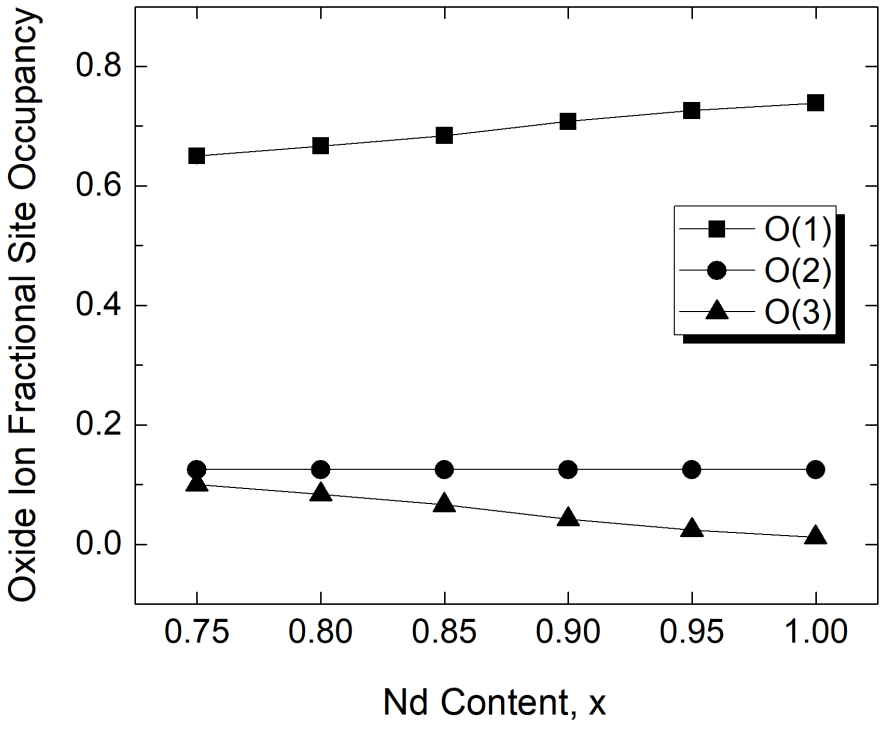

Fig. 3.23. Compositional variation of oxide ion site occupancies presented as a fraction of total oxide ion content in $(Yb_{1-x}Nd_x)_2Zr_2O_7$ ($0.75 \leq x \leq 0.10$) compositions calcined at 1150 °C. Error bars are smaller than the symbols used.

The presence of oxygen Frenkel defects is correlated with the anti-site cation disorder. In an ideal pyrochlore structure, the larger lanthanide cations would be located exclusively in the 16*d* site and the smaller Zr^{4+} cations in the 16*c* site. Cations on the 16*d* site coordinate to six O(1) (48*f* site) atoms and two O(2) (8*b* site) atoms (**Fig. 3.24a**), while those on the 16*c* site adopt a lower coordination number of six made up of six contacts to O(1) (48*f* site) atoms (**Fig. 3.24b**). As seen in **Table 3.10** above, it is cations on the 16*c* site that coordinate to the interstitial O(3) oxide ions in the 8*a* site. The anti-site cation disorder means that some Zr^{4+} is present on the 16*d* site and prefers a lower coordination geometry, which is achieved through the Frenkel vacancies on the O(1) site (**Fig.3.24c**) . Similarly, the lanthanide cations present on the 16*c* site can achieve a higher coordination number by coordinating to two additional O(3) atoms (8*a* site) as seen in **Fig. 3.24d**. Indeed, the ratio of the number of Yb^{3+} and Nd^{3+} cations located on the 16*c* site to the number of oxide ions on the O(3) site is approximately 1:2 for all but the x = 1.00 composition, where there is only a small concentration of cation anti-site defects (**Table 3.11**).

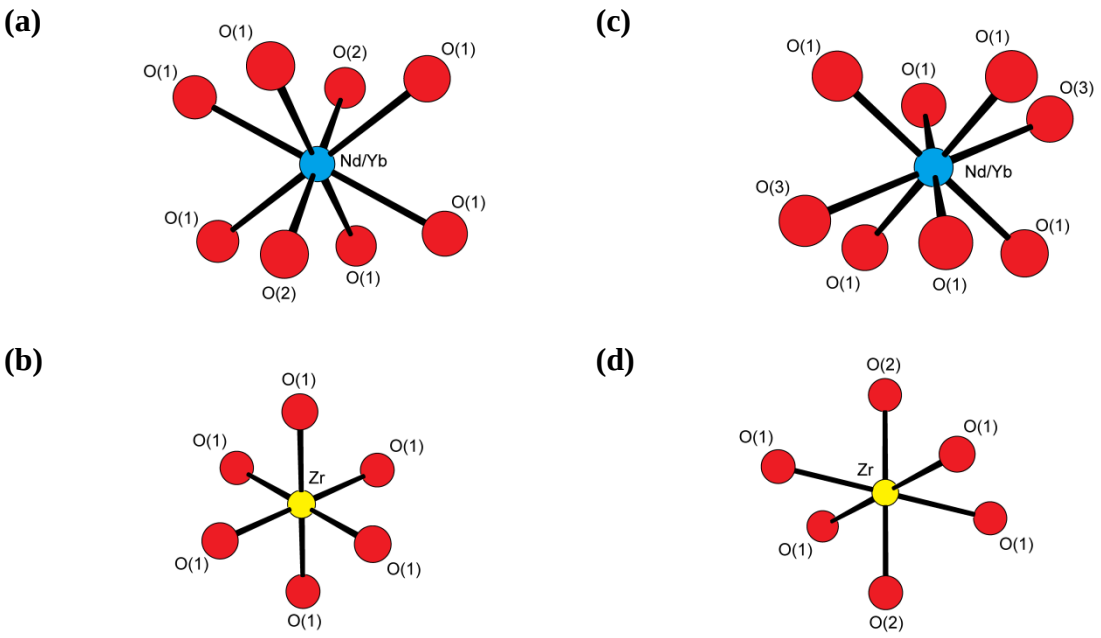

Fig. 3.24. Cation coordination geometries in $(Yb_{1-x}Nd_x)_2Zr_2O_7$, showing (a) lanthanide cation on 16*d* site, (b) zirconium cation on 16*c* site, (c) lanthanide cation on 16*c* site and (d) zirconium cation on 16*d* site. Figures generated from the x = 0.75 composition, calcined at 1350 °C.

Table 3.11 Compositional variation in anion:cation ratios in $(Yb_{1-x}Nd_x)_2Zr_2O_7$ ($0.75 \leq x \leq 0.10$) compositions, calcined at 1150 °C.

Composition (x)	Yb(2) + Nd(2) per cell	O(3) per cell	O3:[Yb(2) + Nd(2)]
0.75	3.3(2)	6.4(2)	1.9
0.80	3.1(3)	5.3(1)	1.7
0.85	2.1(3)	4.2(1)	2.0
0.90	1.1(3)	2.68(6)	2.4
0.95	0.78(8)	1.52(4)	1.9
1.00	1.46(5)	0.73(2)	0.5

As for the fluorite structured samples, it is helpful to examine the extent of displacement of the oxygen atoms within the tetrahedral site, as a measure of the distortion of the cation coordination polyhedron. Only the O(1) position has a refineable coordinate (x) and its distance to the centre of the site at 0.375, 0.125 0.125 is plotted as a function of composition in **Fig. 3.25**. As seen for the fluorite systems, there is a general increase in this distance from $x = 0.75$ to $x = 1.0$, indicating increasing distortion in the cation coordination polyhedron, with increasing Nd^{3+} content.

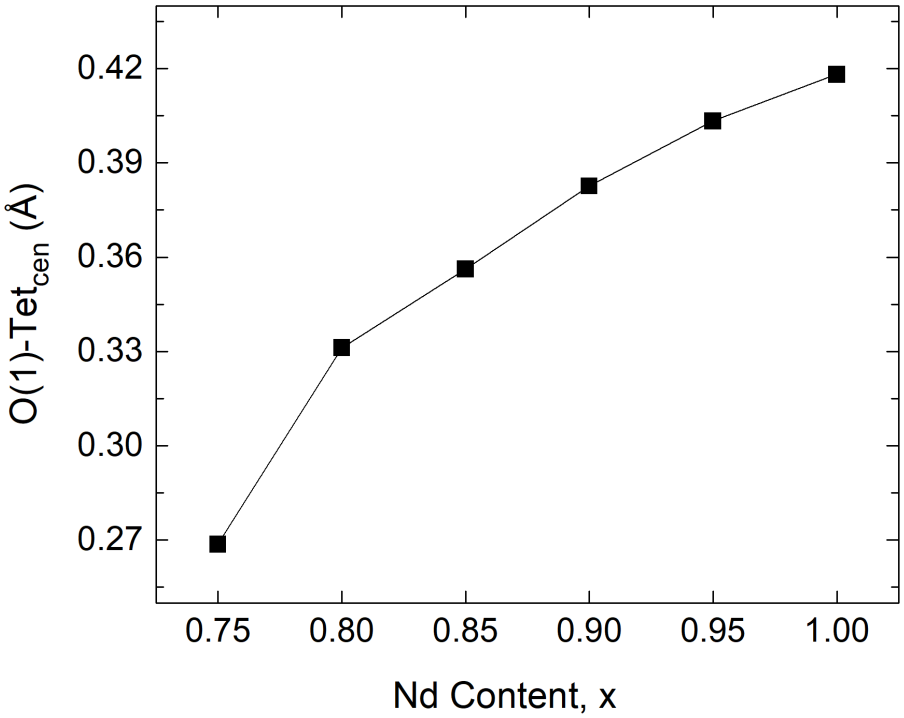

Fig. 3.25. Compositional variation of the distance from O(1) the centre of the tetrahedral site (Tet_{cen}) in the ccp lattice of pyrochlore structured compositions of $(Yb_{1-x}Nd_x)_2Zr_2O_7$, calcined at 1150 °C. Error bars are smaller than the symbols used.

Fig. 3.26 shows the fitted diffraction profiles for the pyrochlore sample of the x = 1.00 composition, calcined at 1350 °C (the fitted diffraction profiles for the other pyrochlore sample calcined at 1350 °C, i.e. the x = 0.75 composition, are given in Appendix B). The crystal and refinement parameters are given in **Table 3.12**, with the refined structural parameters and significant contact distances, given in **Table 3.13**.

The percentage changes in refined parameters between the samples calcined at 1150 and 1350 °C are summarised graphically in **Fig. 3.27**. The lattice parameter shows a very small but measurable increase of around 0.2% for samples calcined at 1350 °C, compared to those calcined at 1150 °C. This shift in the lattice parameter is probably associated with the relief of crystallographic strain. The higher temperature allows for better sintering of the material and grain growth, as evidenced in the increase in crystallite size in **Table 3.4** above.

(a)

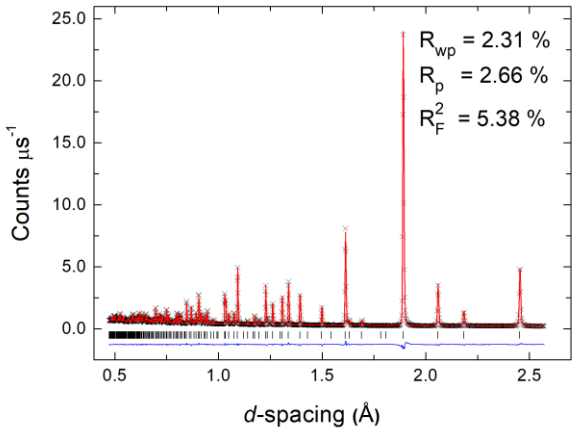

(b)

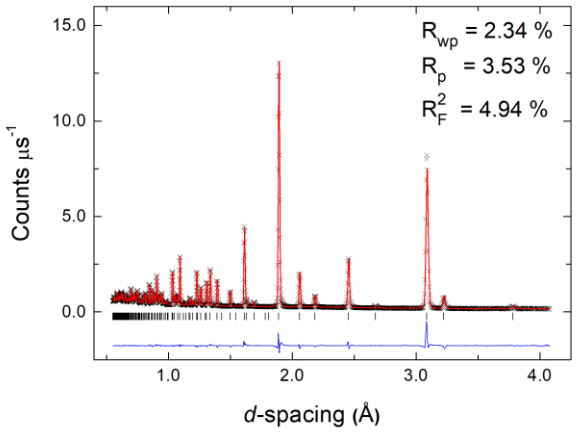

(c)

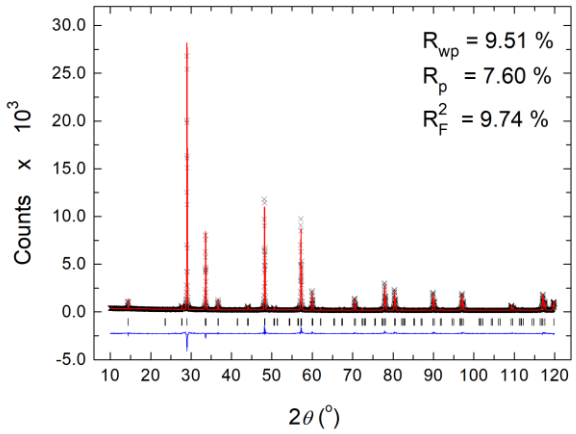

Fig. 3.26. Fitted diffraction profiles for a representative pyrochlore structured sample in the system $(Yb_{1-x}Nd_x)_2Zr_2O_7$, x = 1.00, calcined at 1350 °C; fits to (a) and (d) neutron back scattering, (b) and (e) neutron 90° and (c) and (f) X-ray data are shown. Observed (crosses), calculated (solid line), and difference (lower) profiles of are shown. Reflection positions are indicated by markers.

Table 3.12. Crystal and refinement parameters for pyrochlore structured compositions in the system $(Yb_{1-x}Nd_x)_2Zr_2O_7$ ($0.75 \leq x \leq 1.00$), calcined at 1350 °C

Composition	$x = 0.75$	$x = 1.00$
Calcination temp. (°C)	1350	1350
Formula	$Yb_{0.5}Nd_{1.5}Zr_2O_7$	$Nd_2Zr_2O_7$
M_r (g mol^{-1})	597.32	582.92
Crystal system	Cubic	Cubic
Space group	$Fd\bar{3}m$	$Fd\bar{3}m$
Lattice parameter (Å)	10.6043(4)	10.68948(7)
Volume (Å^3)	1192.5(1)	1221.43(3)
Z	8	8
D_{calc} (g cm^{-3})	6.654	6.340
R-factors:		
Neutron back scattering	$R_{wp} = 0.0287$	$R_{wp} = 0.0231$
	$R_p = 0.0467$	$R_p = 0.0266$
	$R_{ex} = 0.0040$	$R_{ex} = 0.0040$
	$R_F2 = 0.1124$	$R_F2 = 0.0538$
Neutron 90°	$R_{wp} = 0.0292$	$R_{wp} = 0.0234$
	$R_p = 0.0434$	$R_p = 0.0353$
	$R_{ex} = 0.0036$	$R_{ex} = 0.0037$
	$R_F2 = 0.1150$	$R_F2 = 0.0494$
X-ray	$R_{wp} = 0.0830$	$R_{wp} = 0.0951$
	$R_p = 0.0634$	$R_p = 0.0760$
	$R_{ex} = 0.0543$	$R_{ex} = 0.0553$
	$R_F2 = 0.0570$	$R_F2 = 0.0974$
Totals	$R_{wp} = 0.0297$	$R_{wp} = 0.0247$
	$R_p = 0.0633$	$R_p = 0.0756$
χ^2	26.97	15.82
Total no. of variables	119	88
No. of profile points:		
Neutron back scattering	1985	1861
Neutron 90°	2325	2321
X-ray	6581	6880
Total	10891	11062
No. of reflections:		
Neutron back scattering	724	559
Neutron 90°	560	562
X-ray	124	126

Table 3.13. Refined atomic parameters and significant contact distances for fluorite structured compositions in the system $(Yb_{1-x}Nd_x)_2Zr_2O_7$ ($0.75 \leq x \leq 1.00$), calcined at 1350 °C.

Composition	$x = 0.75$	$x = 1.00$
Yb(1)/Nd(1)/Zr(1) site	16*d*	16*d*
Yb(1)/Nd(1)/Zr(1) *x*,*y*,*z*	0.5	0.5
Yb(1) Occ.	0.226(2)	
Nd(1) Occ.	0.677(5)	0.934 (7)
Zr(1) Occ.	0.097(7)	0.066(6)
Yb(2)/Nd(2)/Zr(2) site	16*c*	16*c*
Yb(2)/Nd(2)/Zr(2) *x*,*y*,*z*	0.0	0.0
Yb(2) Occ.	0.024(2)	
Nd(2) Occ.	0.073(5)	0.066(7)
Zr(2) Occ.	0.903(7)	0.934(7)
Yb/Nd/Zr U_{iso} ($Å^2$)	0.01263(6)	0.00567(4)
O(1) site	48*f*	48*f*
O(1) *x*	0.34080(5)	0.33509(2)
O(1) y,z	0.125	0.125
O(1) Occ.	0.955(1)	0.992(1)
O(1) U_{iso} ($Å^2$)	0.0204(1)	0.00940(5)
O(2) site	8*b*	8*b*
O(2) *x*,*y*,*z*	0.375	0.375
O(2) Occ.	1.0	1.0
O(2) U_{iso} ($Å^2$)	0.0164(3)	0.00462(9)
O(3) site	8*a*	8*a*
O(3) *x*,*y*,*z*	0.125	0.125
O(3) Occ.	0.270(5)	0.045(2)
O(3) U_{iso} ($Å^{2)}$	0.0164(3)	0.00462(9)
Yb(1)/Nd(1)/Zr(1)-O(1) (Å)	2.5227(4)	2.5842(2)
Yb(1)/Nd(1)/Zr(1)-O(2) (Å)	2.29590(6)	2.31434(1)
Yb(2)/Nd(2)/Zr(2)-O(1) (Å)	2.1074(3)	2.0972(1)
Yb(1)/Nd(1)/Zr(1)-O(3) (Å)	2.29590(6)	2.31434(1)

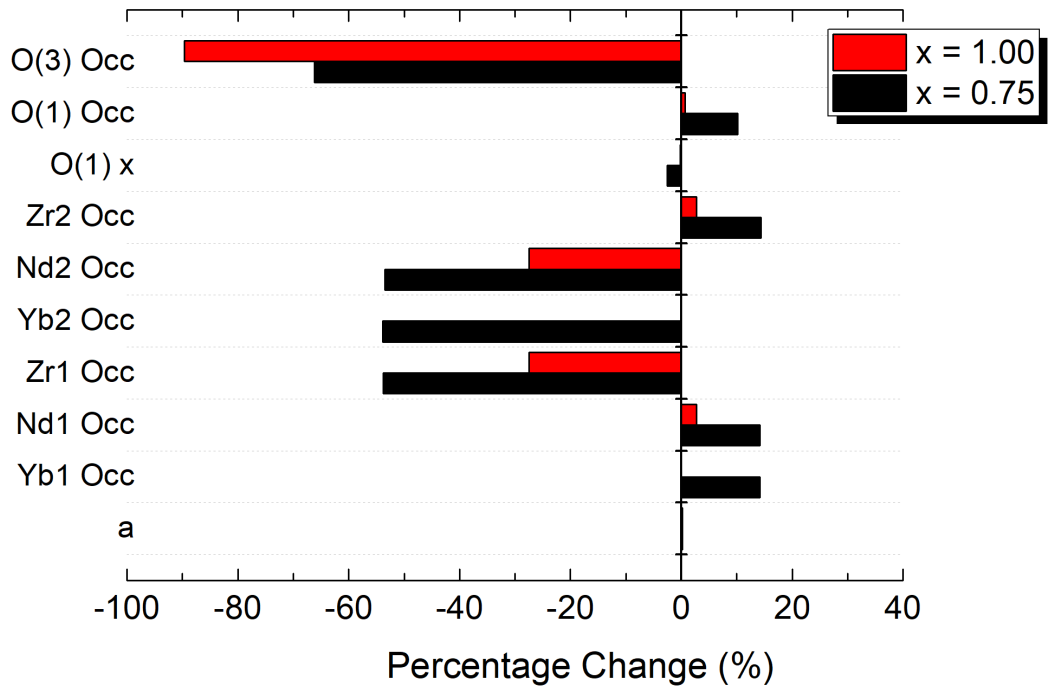

Fig. 3.27. Percentage change in refined structural parameters between samples calcined at 1150 °C and 1350 °C for x = 0.75 and x = 1.00 compositions.

The most significant changes are the reduction of cation anti-site disorder and the concentration of oxide ion Frenkel defects; the latter is illustrated graphically in **Fig. 3.28a**. While the samples calcined at the higher temperature still show measureable amounts of both types of defects, their concentration is much lower than at 1150 °C. For both compositions, the O3:[Yb(2)+Nb(2)] ratio decreases (**Fig. 3.28b**), suggesting the correlation between oxygen Frenkel interstitials and cation anti-site disorder is weaker at higher temperatures. For the x = 0.75 composition, there is a 35% increase in the distance between O(1) and the tetrahedral site centre, suggesting more positional disorder within the tetrahedral site at the higher calcination temperature. However, for the x = 1.00 composition, this change is negligible.

(a)

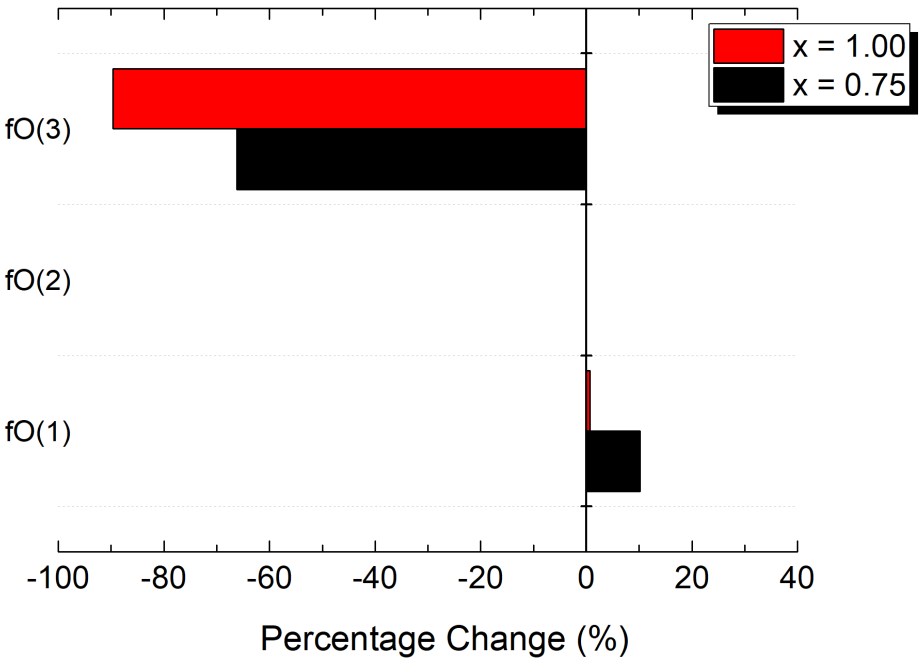

(b)

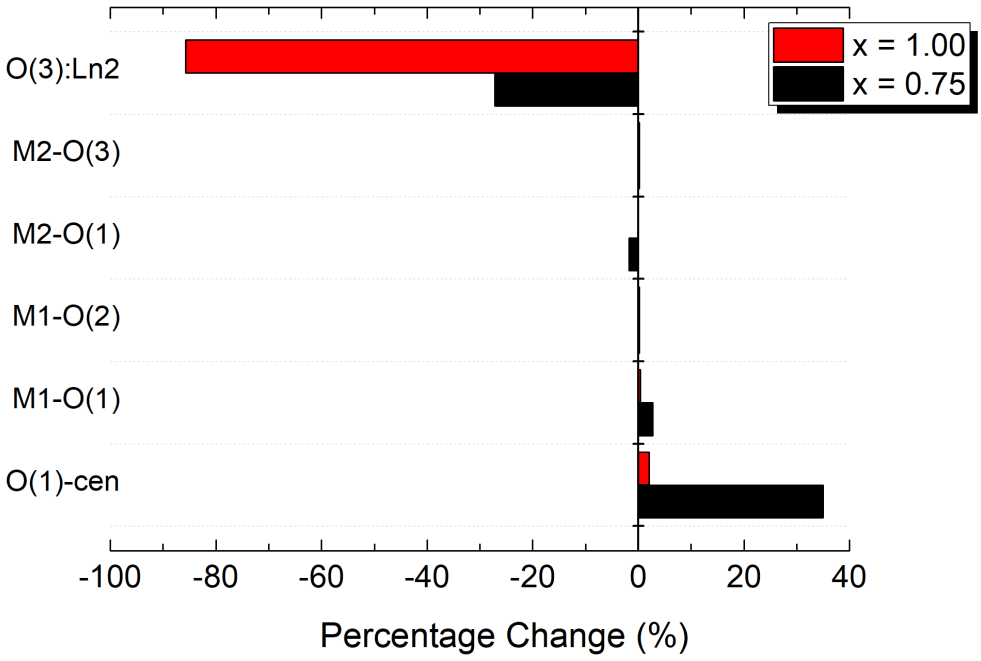

Fig. 3.28. Percentage change in (a) oxide ion fractions of total oxide ion content and (b) oxygen distances and O(3):Ln(2) ratio between samples calcined at 1150 °C and 1350 °C for x = 0.75 (black) and x = 1.00 (red) compositions.

The degree of cation order, Ø, can be expressed as a function of the occupancy, σ, of *Ln* (Nd and Yb) on the larger A site as: Ø = 2σ - 1. For the fully disordered fluorite structure, σ = 0.5 and Ø = 0. In the ideally ordered pyrochlore structure, *Ln* only occupies the A-site (σ = 1.0) and Ø is 1 (100%).[93] As shown in **Table 3.14**, the Rietveld refinement results suggest that the degree of cation ordering for compositions $0.00 \leq x \leq 0.50$ are close to 0.5. Similarly, the degree of cation ordering for compositions $0.75 \leq x \leq 1.00$, synthesised at 950 °C is also close to 0.5. However, the degree of cation ordering for compositions $0.75 \leq x \leq 1.00$, synthesised at 1150 and 1350 °C, that exhibit the pyrochlore structure, show significant deviations from the expected values, indicative of significant anti-site cation disorder, especially for the $x = 0.75$ composition.

Table 3.14 Degree of cation ordering in the $(Yb_{1-x}Nd_x)_2Zr_2O_7$ system derived from Rietveld analysis.

Composition	Annealing Temperature (°C)	*Ln* occupancy, σ	Ø (%)
$x = 0.00$	1150	0.539(4)	7.78
$x = 0.25$	1150	0.509(5)	1.84
$x = 0.50$	1150	0.520(1)	3.94
$x = 0.75$	1350	0.903(5)	80.62
	1150	0.790(5)	58.08
	950	0.515(9)	3.08
$x = 0.80$	1150	0.779(10)	55.76
$x = 0.85$	1150	0.795(10)	58.94
$x = 0.90$	1150	0.841(9)	68.20
$x = 0.95$	1150	0.864(8)	72.88
$x = 1.00$	1350	0.934(7)	86.84
	1150	0.909(3)	81.82
	950	0.500(-)	0.00

3.3.3 Local structure

G(*r*) profiles for samples calcined at 1150°C are shown in **Fig. 3.29**. A gradual evolution of the pattern is seen as the structure changes from fluorite to pyrochlore.

(a)

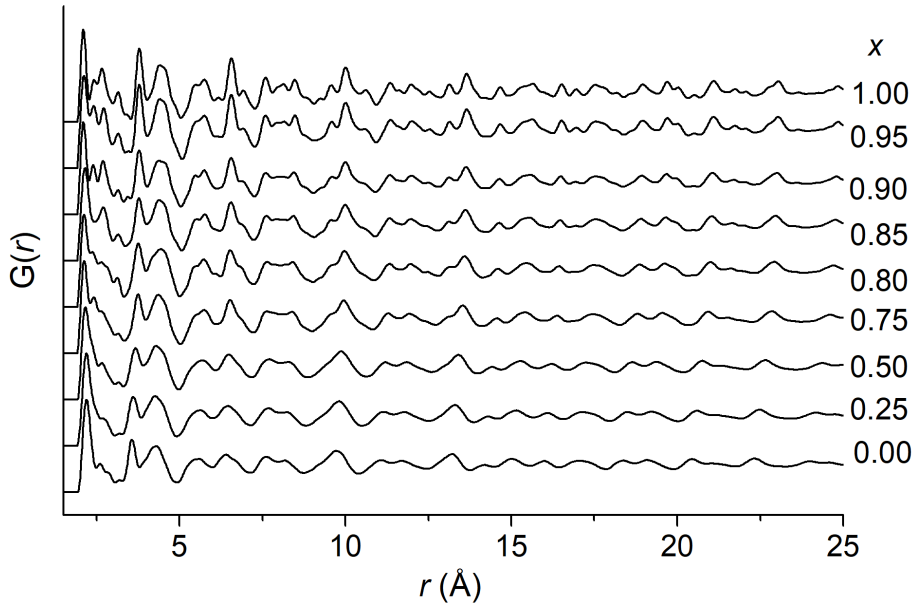

(b)

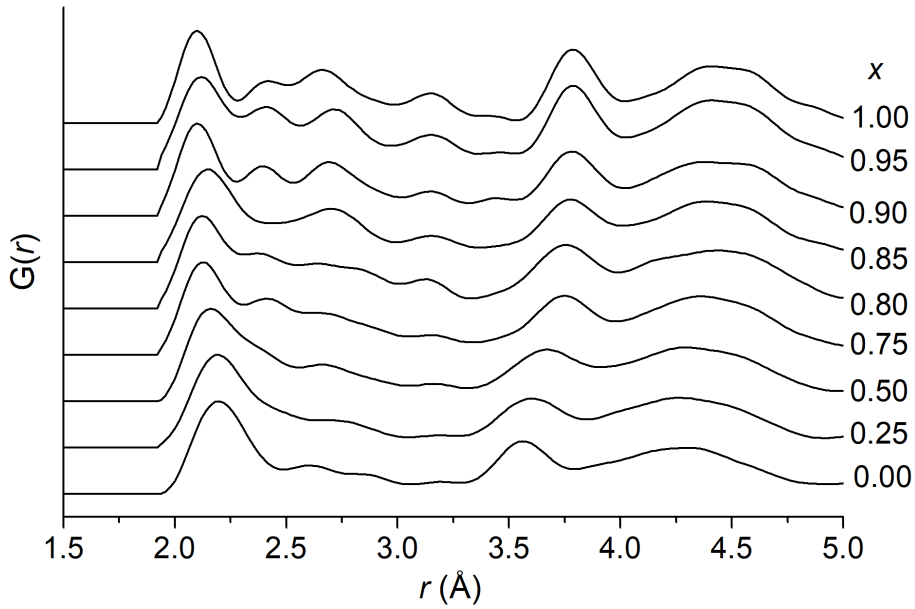

Fig. 3.29. G(*r*) profiles for samples of $(Yb_{1-x}Nd_x)_2Zr_2O_7$ calcined at 1150 °C, showing (a) full profile and (b) short range correlations.

Detail of the G(r) profiles for the x = 0.00 and x = 1.00 samples calcined at 1150 °C are shown in **Fig. 3.30**, as representative examples of fluorite and pyrochlore patterns, respectively. Individual types of pair correlations are indicated on the plots. The main difference between the pyrochlore and the fluorite patterns is the separation of the Zr-O and Ln-O correlations into distinguishable separate peaks, as local cation ordering occurs.

(a)

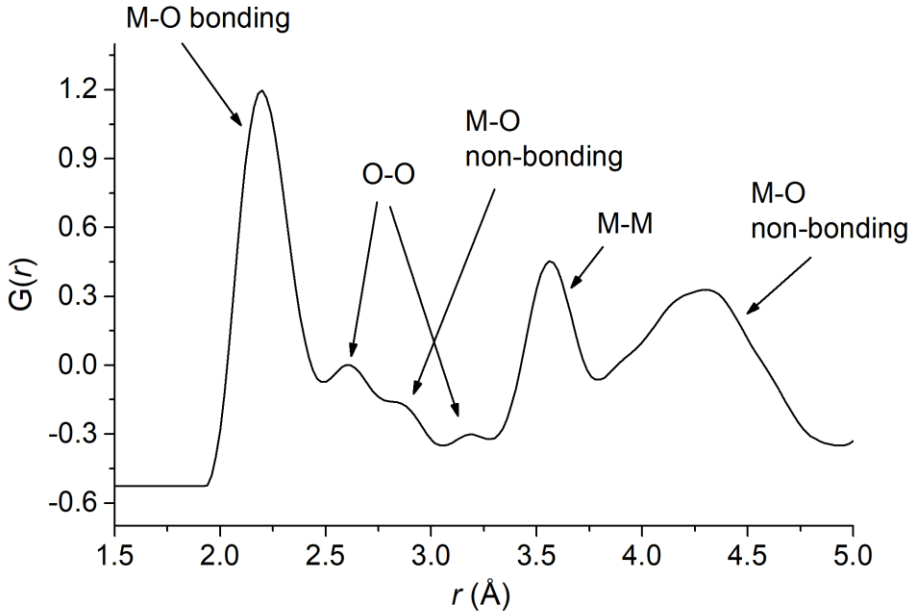

(b)

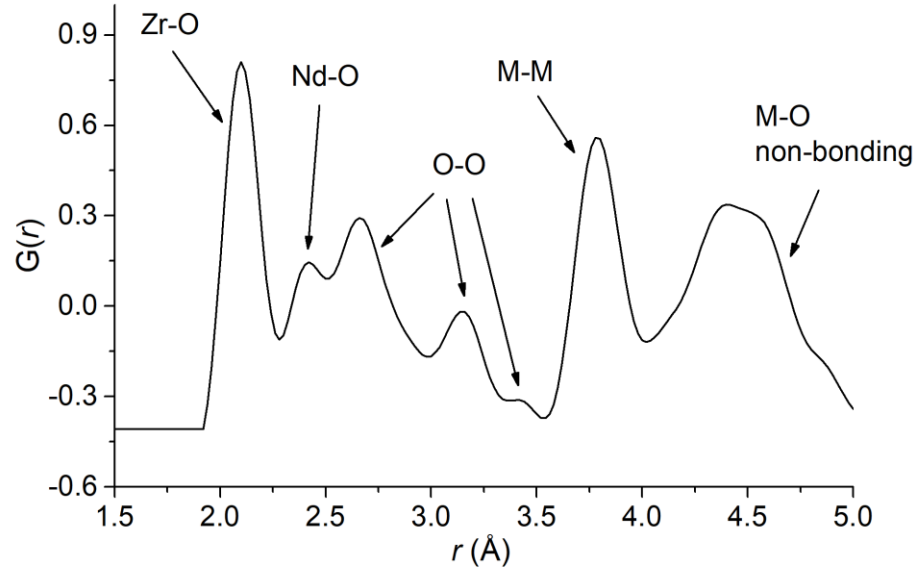

Fig. 3.30. Detail of G(r) profiles for $(Yb_{1-x}Nd_x)_2Zr_2O_7$ samples calcined at 1150 °C, showing (a) x = 0.00 (fluorite) and (b) x = 1.00 (pyrochlore) patterns, with individual types of pair correlation indicated.

A similar evolution of the total pair correlation function is seen when comparing the profiles for the x = 0.75 and 1.00 compositions, calcined at different temperatures (**Fig. 3.31**). For the samples calcined at 950 °C, the profiles are fluoritic, reflecting the absence of long-range order shown in the Bragg data, with pyrochlore features evident at 1150 °C and 1350 °C. It is interesting to note the difference in the sharpness of the features at 1150 and 1350 °C between the x = 0.75 and 1.00 compositions, with the former showing much broader correlations, reflecting the extent of disorder seen in the Rietveld analysis.

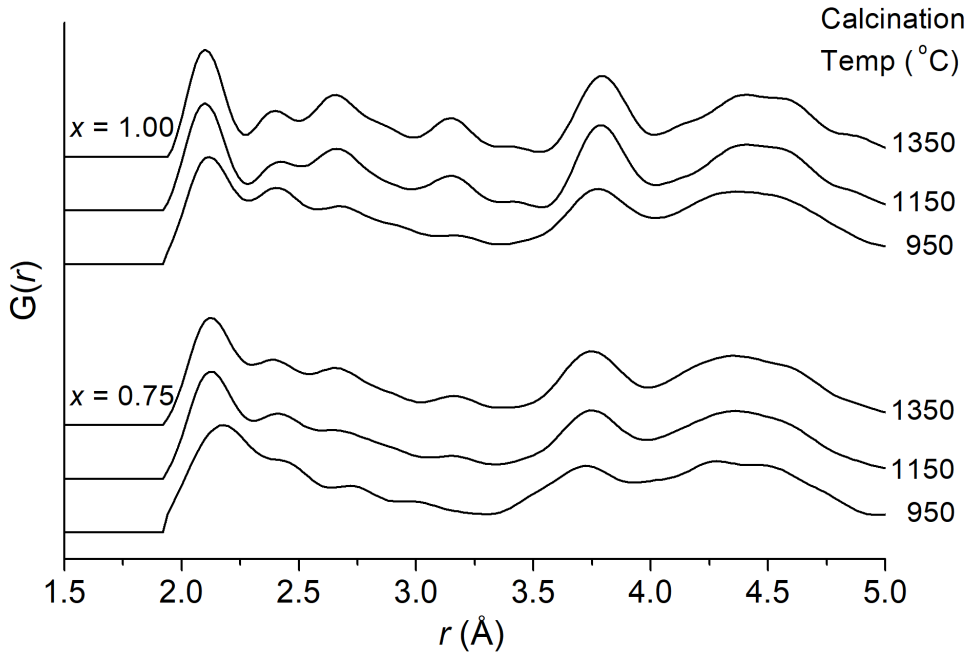

Fig. 3.31. Detail of G(r) profiles for $(Yb_{1-x}Nd_x)_2Zr_2O_7$ (x = 0.75 and 1.00) samples calcined at different temperatures.

Representative fits to the $S_{box}(Q)$ and G(r) data for a fluorite and a pyrochlore structured sample, derived from RMC analyses are shown in **Fig. 3.32** and **Fig. 3.33**, respectively. Fits to the data from all other samples are given in Appendix C. The quality of the fits is high and the BVS values are all reasonably close to the expected values (**Table 3.15**).

(a)

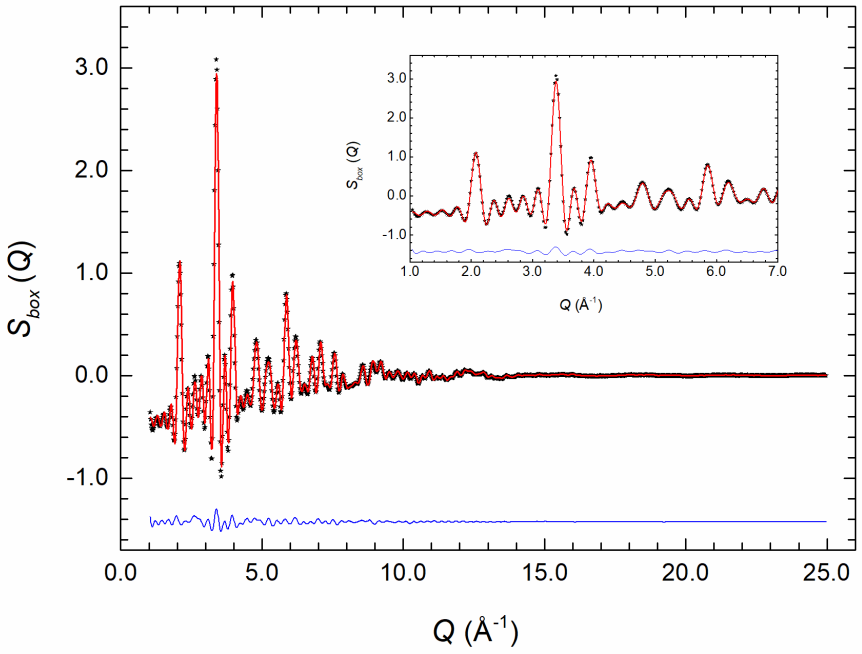

(b)

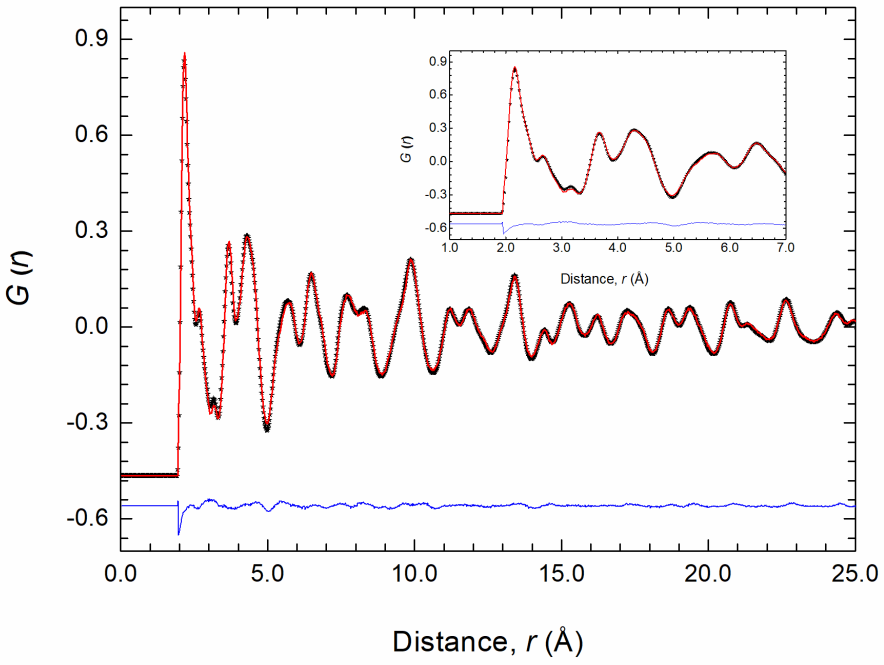

Fig. 3.32. Representative fits to (a) S(*Q*) and (b) G(*r*) profiles obtained by RMC modelling of neutron data from the $(Yb_{1-x}Nd_x)_2Zr_2O_7$ (x = 0.50), fluorite structured sample calcined at 1150 °C. The black dots show the experimental data, the solid red line shows the calculated profile, and the difference profile is shown by the solid blue line.

(a)

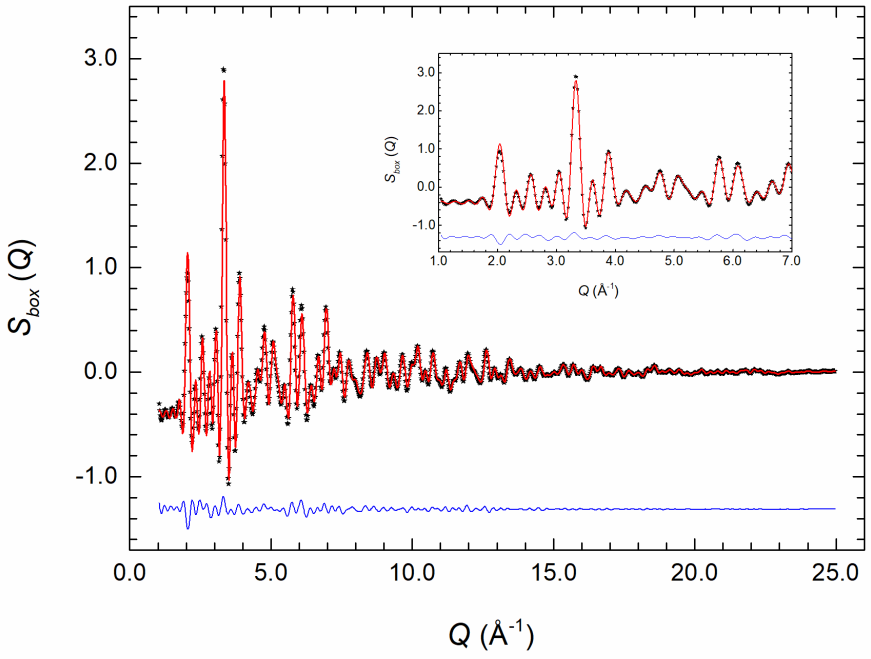

(b)

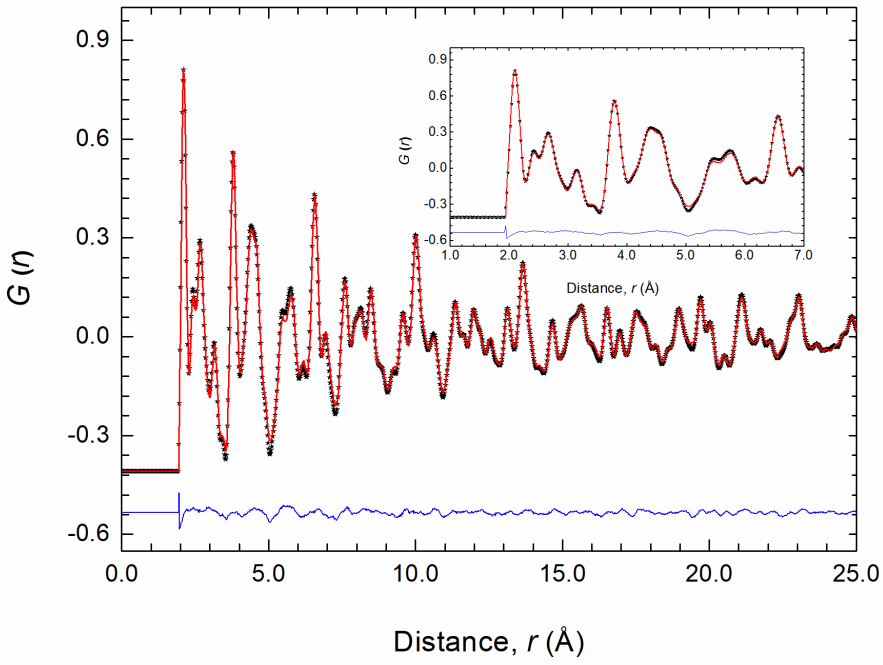

Fig. 3.33. Representative fits of (a) S(*Q*) and (b) G(*r*) profiles, obtained by RMC modelling of neutron data from the $(Yb_{1-x}Nd_x)_2Zr_2O_7$ (x = 1.00), pyrochlore structured sample calcined at 1150 °C. The black dots show the experimental data, the solid red line shows the calculated profile, and the difference profile is shown by the solid blue line.

Table 3.15 Bond valence sums (BVS) from RMC analyses

Composition	Calcination temp. (°C)	Nd^{3+}	Yb^{3+}	Zr^{4+}	O^{2-}
x = 0.00	1150	n/a	2.940(8)	3.831(5)	1.935(1)
x = 0.25	1150	3.041(9)	2.972(8)	3.833(5)	1.949(1)
x = 0.50	1150	3.023(7)	2.941(9)	3.828(5)	1.946(2)
x = 0.75	1350	2.982(3)	2.837(6)	3.822(9)	1.934(3)
	1150	3.016(3)	2.907(6)	3.828(9)	1.948(3)
	950	3.015(5)	2.929(9)	3.833(4)	1.950(1)
x = 1.00	1350	2.960(4)	n/a	3.877(2)	1.953(1)
	1150	2.995(3)	n/a	3.904(1)	1.971(1)
	950	2.995(3)	n/a	3.807(5)	1.943(1)

3.3.3.1 Bond lengths and coordination numbers

M-O and O-O pair correlation functions, $g_{ij}(r)$ for samples calcined at 1150 °C, derived from RMC analyses, are shown in **Figs. 3.34-3.36**. For the x = 0.00 composition, three peaks attributable to Zr-O, Yb-O and O-O are distinguished at around 2.0, 2.2 and 2.6 Å, respectively. The introduction of Nd into the system is characterised by an Nd-O correlation at around 2.4 Å, which overlaps considerably with the first O-O peak. At x = 1.00, the Nd-O correlation is broad, ranging from around 2.1 to 3.0 Å, with three maxima evident at 2.21, 2.41 and 2.55 Å, suggesting a range of Nd-O bonds. The shortest of these might arise through a degree of cation anti-site disorder, but in the absence of evidence of such disorder in the Rietveld analysis may simply be an artefact from the data. **Fig. 3.37** shows a comparison between the calculated $g_{OO}(r)$ profiles for the x = 0.75 and 1.00 compositions, calcined at 1150 °C. In the x = 0.75 composition, the first O-O peak is broad, indicative of significant positional disorder in the system, and the second maximum at around 3.15 Å is poorly developed, thus indicating that the composition x = 0.75 has an oxide ion sub-lattice that is more fluorite-like. At x = 1.00, the $g_{OO}(r)$ profile has developed into two sharp maxima at around 2.69 and 3.15 Å, corresponding to the first and second nearest O neighbours in the ordered pyrochlore structure. There is little evidence for an O-O correlation at around 2.25 Å, which would correspond to the O(1)-O(3) distance and is consistent with minimal occupation of the O(3) site at x = 1.00, as observed in the Rietveld analysis.

(a)

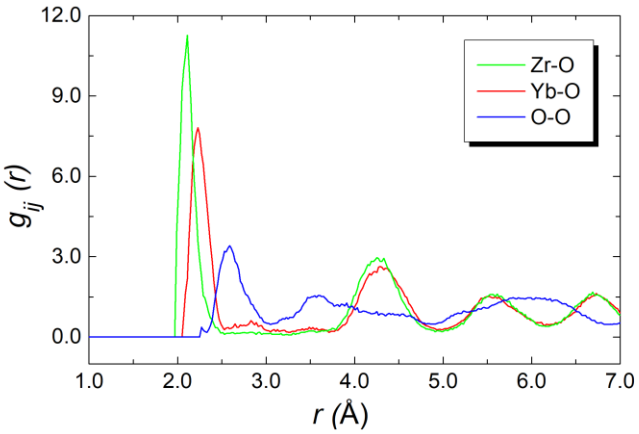

(b)

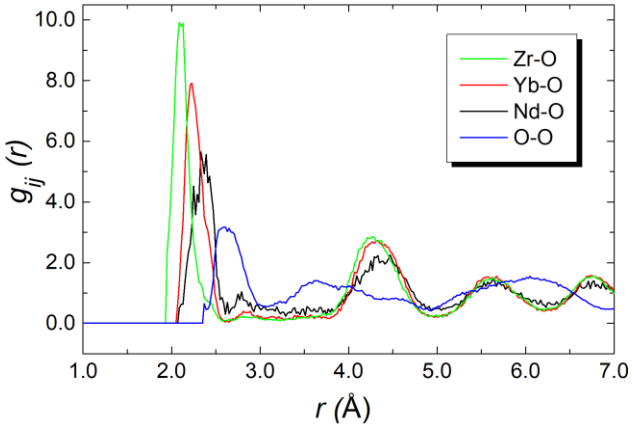

(c)

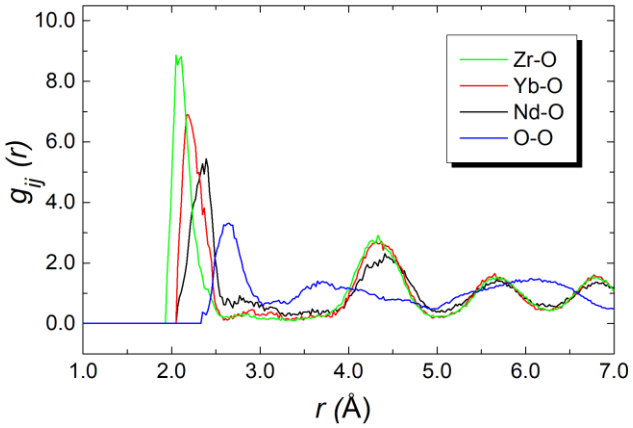

Fig. 3.34. Partial radial distribution functions, $g_{MO}(r)$ and $g_{OO}(r)$, determined from RMC modelling, in the system $(Yb_{1-x}Nd_x)_2Zr_2O_7$, calcined at 1150 °C; (a) x = 0.00, (b) x = 0.25, and (c) x = 0.50

(a)

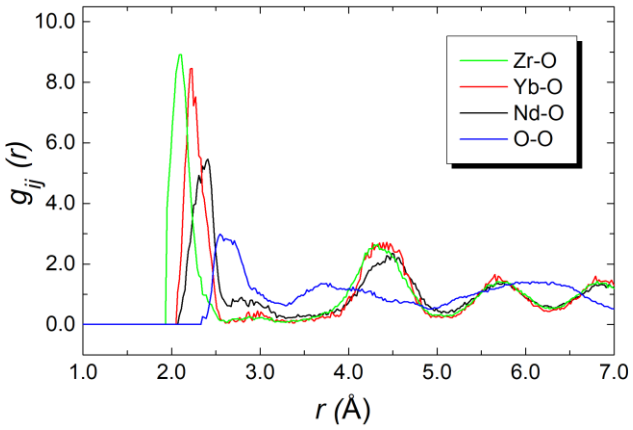

(b)

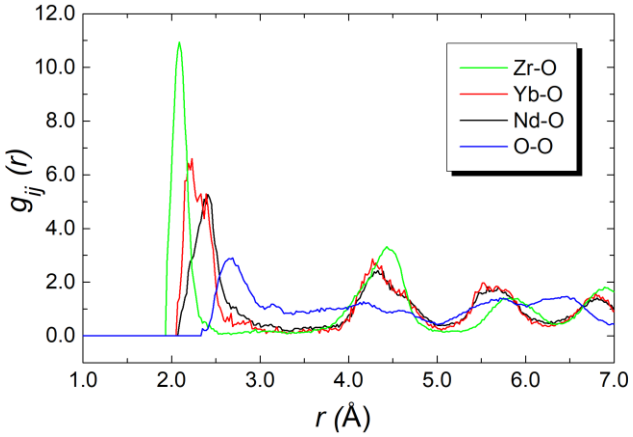

(c)

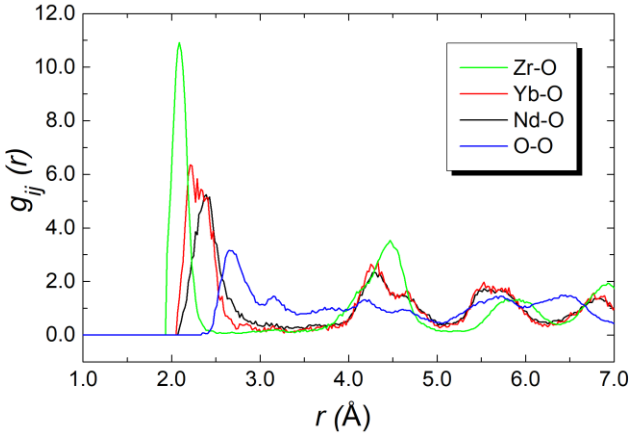

Fig. 3.35. Partial radial distribution functions, $g_{MO}(r)$ and $g_{OO}(r)$, determined from RMC modelling, in the system $(Yb_{1-x}Nd_x)_2Zr_2O_7$, x = 0.75; calcined at (a) 950 °C, (b) 1150 °C, and (c) 1350 °C.

(a)

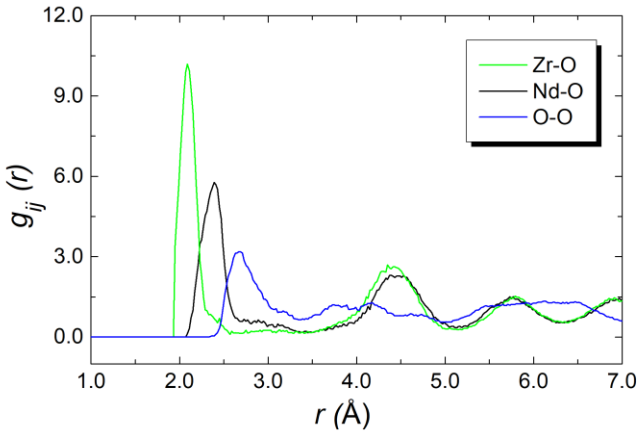

(b)

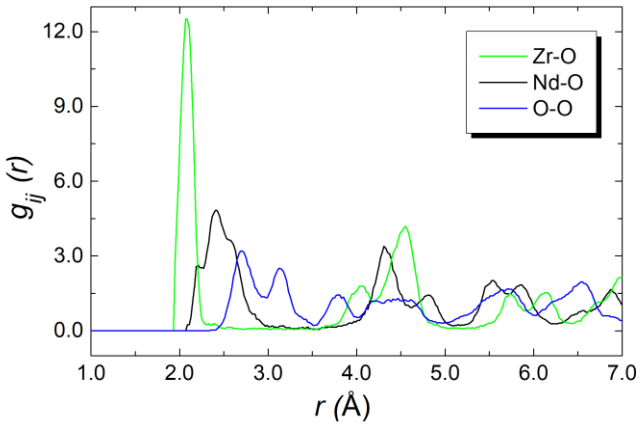

(c)

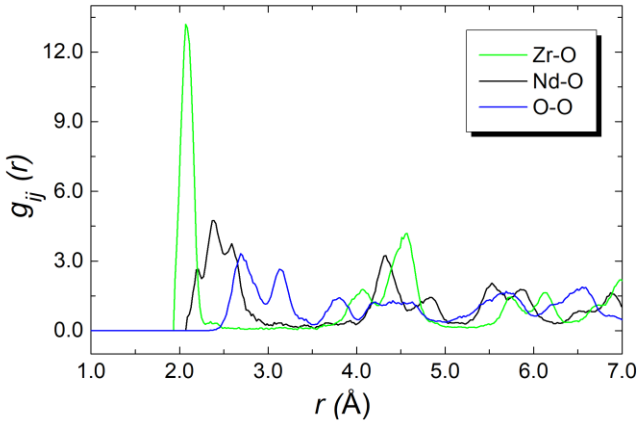

Fig. 3.36. Partial radial distribution functions, $g_{MO}(r)$ and $g_{OO}(r)$, determined from RMC modelling, in the system $(Yb_{1-x}Nd_x)_2Zr_2O_7$, x = 1.00; calcined at (a) 950 °C, (b) 1150 °C, and (c) 1350 °C.

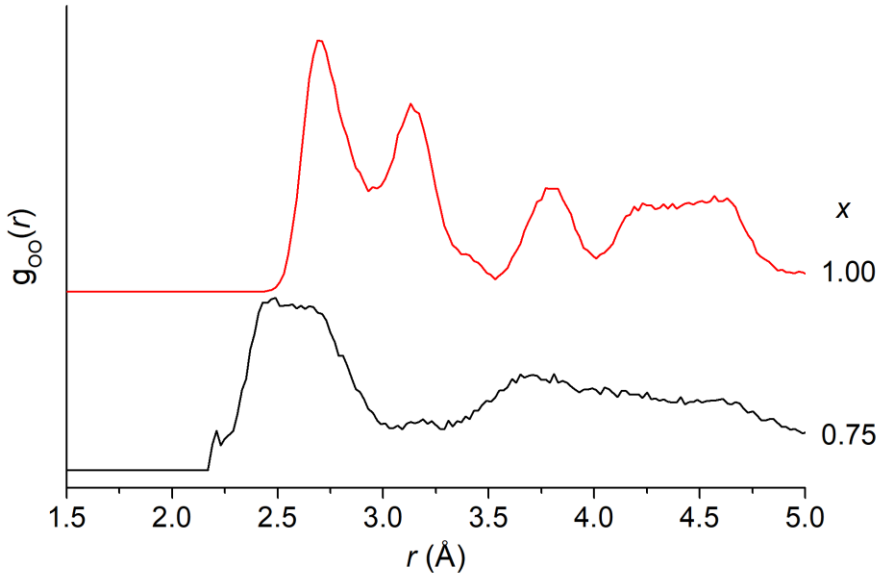

Fig. 3.37. Detail of calculated partial radial distribution functions, $g_{OO}(r)$ for $(Yb_{1-x}Nd_x)_2Zr_2O_7$ (x = 0.75 and 1.00), samples calcined at 1150 °C.

The M-O coordination numbers are given in **Table 3.16**. Two types of coordination number can be defined, depending on the type of interactions being considered. The site coordination number is based on integration of the $g_{MO}(r)$ curve up to 3.50 Å, corresponding approximately to the point at which the curve flattens out, and takes into account all M-O contacts, including bonding and non-bonding interactions. A local coordination number may also be calculated, through integration up to the first minimum in the $g_{MO}(r)$ plots (**Figs. 3.34-3.36** above), and gives a good approximation to the number of oxide ions in the immediate coordination sphere of the cations. The compositional variation of the local MO coordination numbers is illustrated graphically in **Fig. 3.38**. The coordination numbers of neodymium and ytterbium increase upon the fluorite to pyrochlore transition (at x = 0.75), whereas the coordination number of zirconium decreases with the fluorite to pyrochlore transition. The coordination numbers of Zr and Nd are close to those expected for six and eight coordinations, respectively. That for Yb is rather lower than expected. In the case of Yb, the site coordination numbers appear to give a more accurate picture of the true coordination number. Similar conclusions can be made when comparing the x = 0.75 and x = 1.00 compositions calcined at different temperatures (**Fig. 3.39**).

Table 3.16 M-O coordination numbers (CN) from RMC analysis. Estimated standard deviations are given in parentheses.

		Site CN			Local CN		
Comp.	Calcination temp. (°C)	Nd-O	Yb-O	Zr-O	Nd-O	Yb-O	Zr-O
x = 0.00	1150	n/a	7.46(8)	7.17(8)	n/a	6.16(6)	6.56(7)
x = 0.25	1150	7.48(20)	7.30(10)	7.16(8)	7.48(20)	6.39(6)	6.49(6)
x = 0.50	1150	7.55(14)	7.28(15)	7.13(9)	7.55(14)	6.28(11)	6.42(5)
x = 0.75	1350	7.69(2)	7.83(3)	6.61(2)	7.69(2)	6.77(7)	6.03(2)
	1150	7.62(2)	7.79(3)	6.71(2)	7.62(2)	6.68(7)	6.08(3)
	950	7.46(9)	7.21(22)	7.04(8)	7.46(9)	6.37(17)	6.37(5)
x = 1.00	1350	7.82(1)	n/a	6.37(1)	7.82(1)	n/a	5.97(1)
	1150	7.85(1)	n/a	6.29(1)	7.85(1)	n/a	5.98(1)
	950	7.36(1)	n/a	7.00(2)	7.36(1)	n/a	6.19(1)

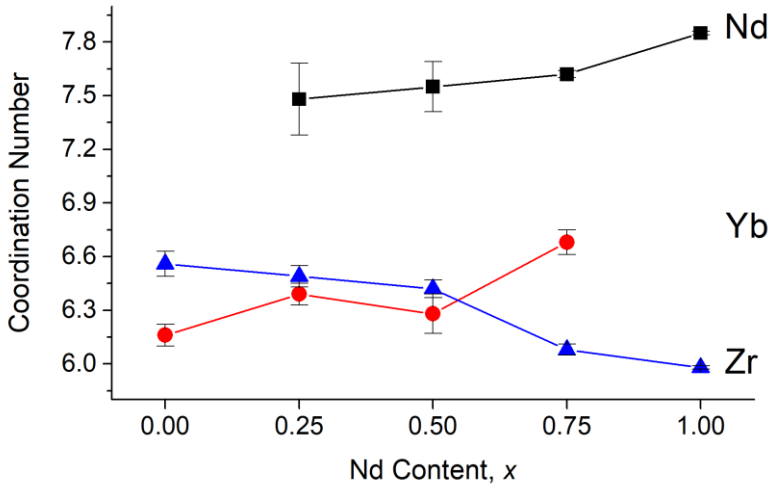

Fig. 3.38. Compositional variation of local coordination numbers in $(Yb_{1-x}Nd_x)_2Zr_2O_7$, samples calcined at 1150 °C, derived from RMC analyses. Error bars represent the standard deviation in the 10 parallel runs. The fluorite to pyrochlore transition occurs at x = 0.75.

(a)

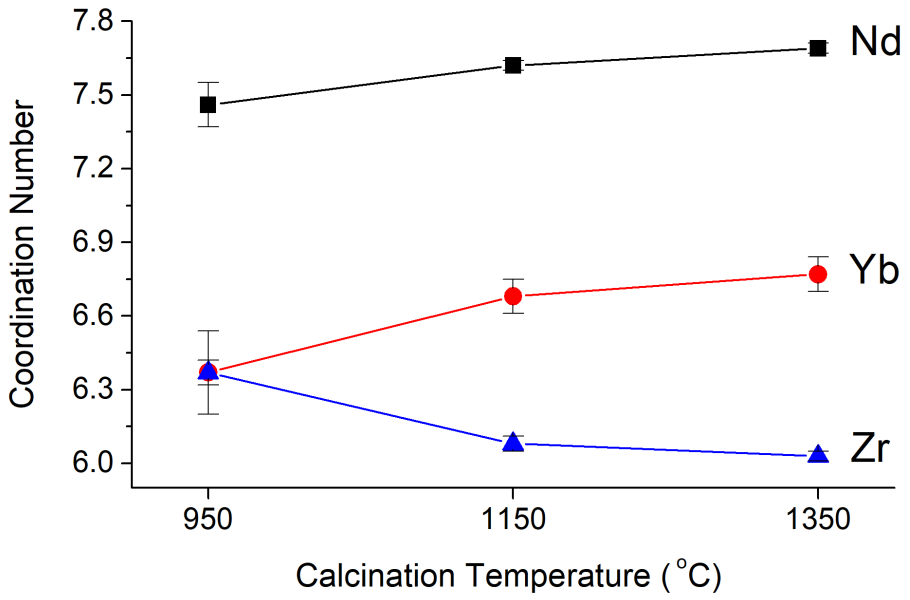

(b)

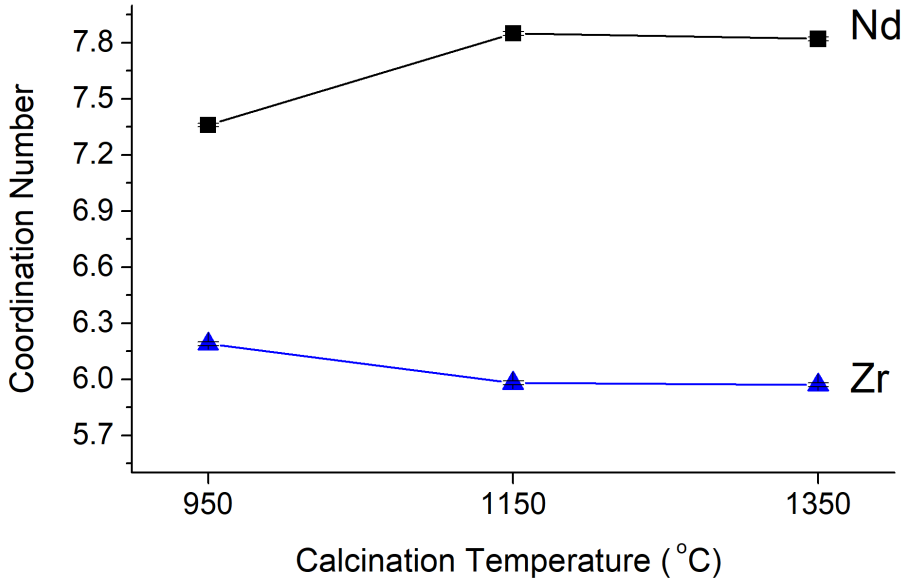

Fig. 3.39. Variation of local coordination numbers in $(Yb_{1-x}Nd_x)_2Zr_2O_7$ samples calcined at different temperatures, derived from RMC analyses: (a) x = 0.75 and (b) x = 1.00. The standard deviation in the 10 parallel runs are smaller than the symbols used.

The modal contact distances can be measured from the individual $g_{ij}(r)$ profiles, as the first peak maximum and are given in **Table 3.17a**. These show little variation, other than a slight lengthening of the Zr-O distance in the pyrochlore structured samples. In contrast, the weighted average M-O distance ($\overline{D_{\mathrm{MO}}}$) derived from these, equation 3.7, shows an increasing trend with increasing *x*-value, confirming that the change in lattice parameter seen in **Fig. 3.10** is predominantly due to the change in composition rather than significant changes in specific bond lengths associated with changes in coordination.

$$\overline{D_{\mathrm{MO}}} = \frac{CN_{\mathrm{NdO}} \times D_{\mathrm{NdO}} + CN_{\mathrm{YbO}} \times D_{\mathrm{YbO}} + CN_{\mathrm{ZrO}} \times D_{\mathrm{ZrO}}}{CN_{\mathrm{NdO}} + CN_{\mathrm{YbO}} + CN_{\mathrm{ZrO}}} \tag{3.7}$$

where CN_{MO} and D_{MO} represent the individual M-O coordination numbers and modal distances, respectively.

An alternative way to calculate the contact distances, is to take a mean value up to a certain cut off from the specific g*ij*(*r*) and these are shown in **Table 3.17b**. The values using this approach are directly comparable to those obtained from the Rietveld analysis given above in **Tables 3.6, 3.8, 3.10** and **3.13.** To examine the extent of cation ordering, it is helpful to look at the $g_{\mathrm{MM}}(r)$ correlations (**Figs. 3.40-3.42**). The most noticeable change in the $g_{\mathrm{MM}}(r)$ correlations is the absence of next-nearest neighbour correlations of the type Ln-Ln at around 5.3 Å in pyrochlore structured samples.

Table 3.17. M-O Contact distances (Å) derived from RMC analyses

(a) Modal contact distances

Composition	Calcination temp. (°C)	Nd-O	Yb-O	Zr-O	Av. M-O
$x = 0.00$	1150	n/a	2.238(4)	2.052(5)	2.142(1)
$x = 0.25$	1150	2.374(13)	2.230(4)	2.047(3)	2.225(6)
$x = 0.50$	1150	2.368(14)	2.227(8)	2.084(77)	2.234(26)
$x = 0.75$	1350	2.380(12)	2.224(9)	2.166(2)	2.266(5)
	1150	2.379(35)	2.200(10)	2.169(3)	2.258(11)
	950	2.381(6)	2.239(17)	2.089(53)	2.244(14)
$x = 1.00$	1350	2.362(28)	n/a	2.178(1)	2.282(16)
	1150	2.421(5)	n/a	2.172(1)	2.313(3)
	950	2.388(2)	n/a	2.163(1)	2.285(1)

(b) Mean contact distances

Composition	Calcination temp. (°C)	Nd-O	Yb-O	Zr-O	Av. M-O
$x = 0.00$	1150	n/a	2.271(3)	2.146(4)	2.206(1)
$x = 0.25$	1150	2.527(8)	2.281(3)	2.146(4)	2.327(4)
$x = 0.50$	1150	2.539(7)	2.278(6)	2.142(4)	2.332(4)
$x = 0.75$	1350	2.539(4)	2.325(3)	2.118(1)	2.344(2)
	1150	2.532(3)	2.312(3)	2.122(1)	2.337(1)
	950	2.527(5)	2.285(9)	2.140(4)	2.328(3)
$x = 1.00$	1350	2.540(2)	n/a	2.107(1)	2.352(1)
	1150	2.524(1)	n/a	2.105(1)	2.342(1)
	950	2.515(1)	n/a	2.133(1)	2.340(1)

(a)

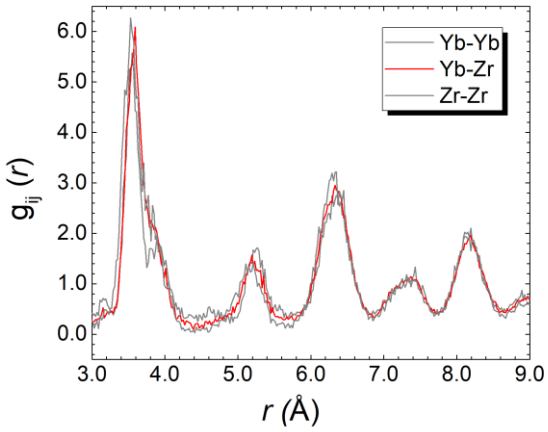

(b)

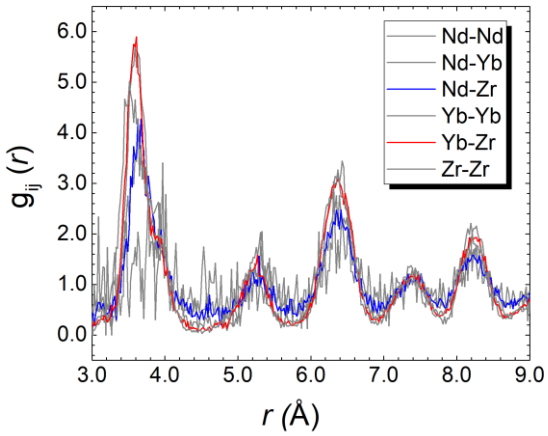

(c)

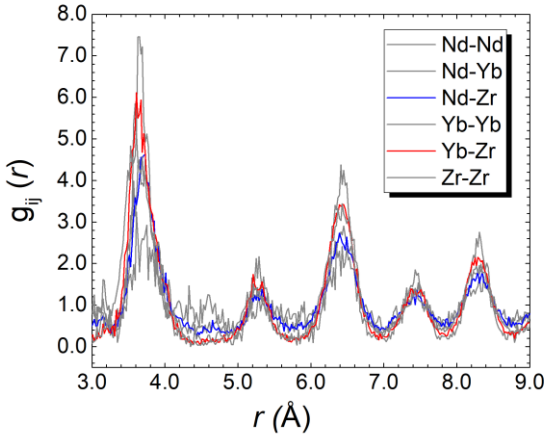

Fig. 3.40. Partial radial distribution functions, $g_{MM}(r)$, as determined from RMC modelling, in the system $(Yb_{1-x}Nd_x)_2Zr_2O_7$, calcined at 1150 °C; for (a) x = 0.00, (b) x = 0.25, and (c) x = 0.50. Nd-Zr (blue), Yb-Zr (red), all others (grey).

(a)

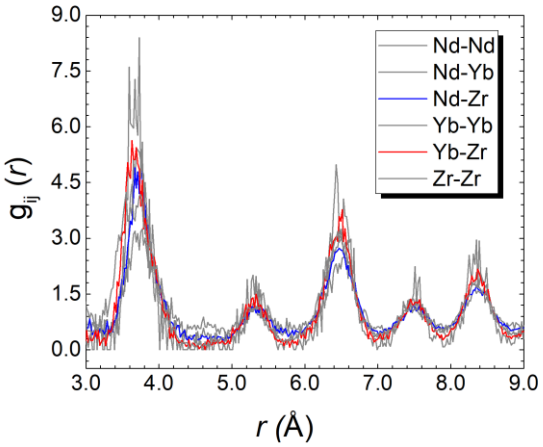

(b)

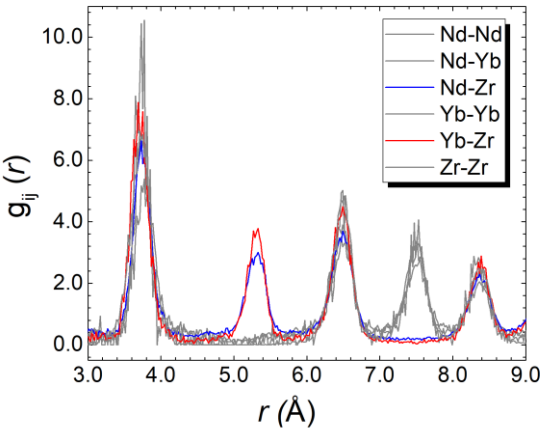

(c)

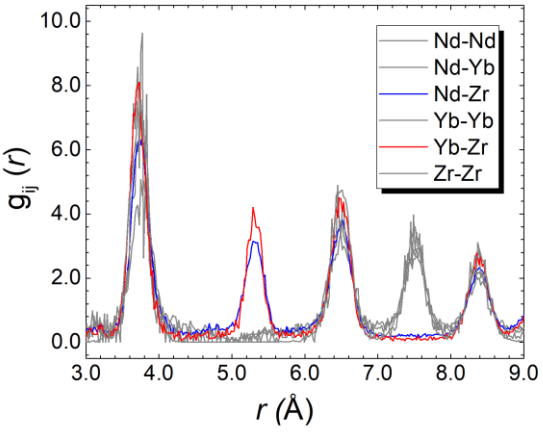

Fig. 3.41. Partial radial distribution functions, $g_{MM}(r)$, as determined from RMC modelling, in the system $(Yb_{1-x}Nd_x)_2Zr_2O_7$, x = 0.75; samples calcined at (a) 950 °C, (b) 1150 °C, and (c) 1350 °C. Nd-Zr (blue), Yb-Zr (red), all others (grey).

(a)

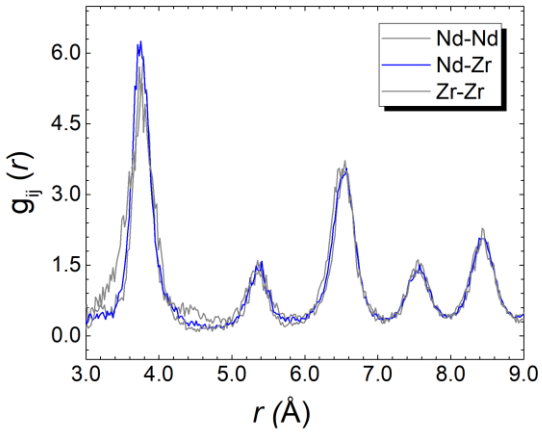

(b)

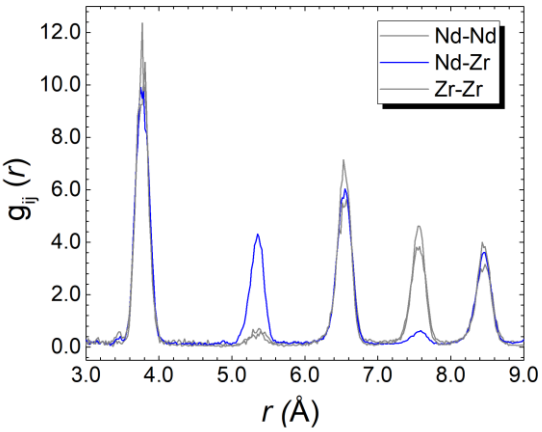

(c)

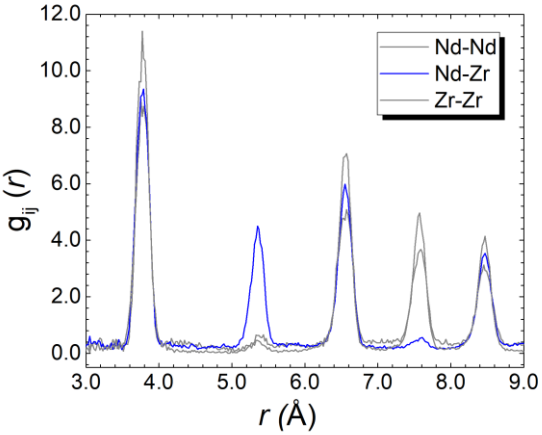

Fig. 3.42. Partial radial distribution functions, $g_{MM}(r)$, as determined from RMC modelling, in the system $(Yb_{1-x}Nd_x)_2Zr_2O_7$, x = 0.75; samples calcined at (a) 950 °C, (b) 1150 °C, and (c) 1350 °C. Nd-Zr (blue), Yb-Zr (red), all others (grey).

The final configuration from the RMC analysis is a box containing 11000 atoms. This model can be analysed in a number of ways, to reveal details of cation, anion and vacancy distributions. In the case of cation distributions, it is helpful to look at the cation-cation nearest neighbour (NN) and next-nearest neighbour (NNN) distances. For a completely random distribution of cations, as in the fully disordered fluorite phase, one would expect each cation to have a distribution of nearest neighbours and next-nearest neighbours reflecting the stoichiometry. For example, for the x = 0.50 composition, a purely random distribution should yield cation-cation nearest neighbour and next-nearest neighbour ratios of 1:1:2 for Yb:Nd:Zr. In contrast, for an ideal pyrochlore structure, the larger lanthanide cations and smaller zirconium cations are ordered. The nearest neighbours consist of six lanthanide and six zirconium cations and would thus be expected to show a nearest neighbour ratio reflecting stoichiometry. However, the next-nearest neighbours at about 5.2 Å are six cations of the other type, *i.e*. the lanthanide cations would have Zr^{4+} cations as exclusive next-nearest neighbours and *vice versa* (**Fig. 3.43**).

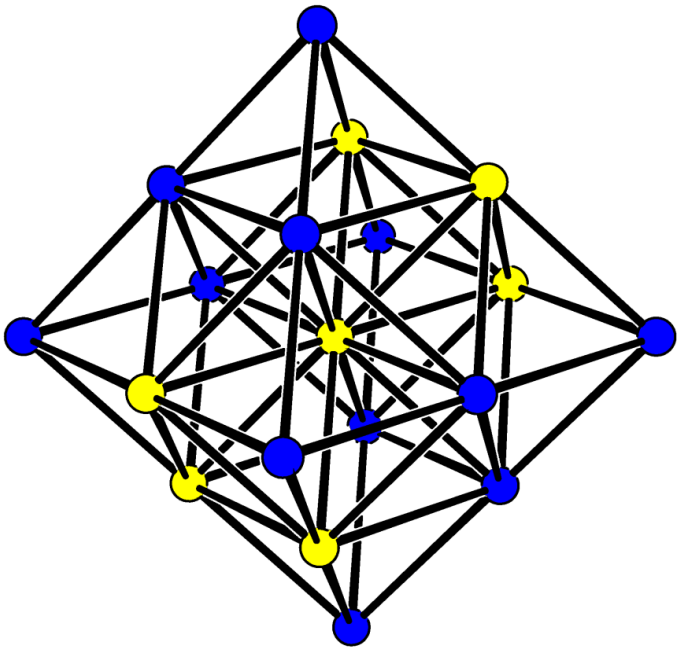

Fig. 3.43. Cation-cation nearest neighbour and next-nearest neighbour distributions in an ideal pyrochlore structure. Yellow and blue spheres represent 16*c* and 16*d* cation sites, respectively (or *vice versa*).

Table 3.18a summarises the NN and NNN distributions, around each cation type, in the studied compositions at the calcination temperatures studied. Theoretical NN and NNN distributions based on stoichiometry are shown for comparison in **Table 3.18b**. For the fluorite structured samples, the nearest neighbour distributions entirely reflect the stoichiometry of the compositions, confirming a random distribution of nearest neighbour cations. There is a small, but persistent, deviation from the random distribution values for next-nearest neighbour cations, with Nd^{3+}, Yb^{3+} and Zr^{4+} all slightly favouring Nd^{3+} as a next-nearest neighbour over Zr^{4+}. This may be associated with a minimization of long-range repulsion between the highly polarizing Zr^{4+} cations and the less polarizing Nd^{3+} cations, in a similar way to that described by Pauling's fourth rule of ionic crystal structures. However, this rule generally relates to nearest neighbour cations, and in the present case, the nearest neighbours also show a random distribution.

As for the fluorite structured samples, the pyrochlore structured samples show random nearest neighbour distributions of cations reflecting stoichiometry. However, the next-nearest neighbour cations show significant (~15%) deviations from the random distribution. As described above, in the absence of anti-site cation disorder, there should be negligible amounts of $A(NNN)_A$ and $B(NNN)_B$ contacts (where A is Nd or Yb and B is Zr). However, while in all cases the $A(NNN)_B$ and $B(NNN)_A$ contacts are predominant, there is evidence for some anti-site cation disorder with $Nd(NNN)_{Nd}$, $Nd(NNN)_{Yb}$, $Yb(NNN)_{Nd}$ $Yb(NNN)_{Yb}$ and $Zr(NNN)_{Zr}$ present. It is interesting that there are relatively few $Zr(NNN)_{Zr}$ contacts in the $x = 0.75$ pyrochlore structured samples, despite evidence from the other cation NNN distributions for anti-site cation disorder.

Table 3.18a. Percentage nearest neighbour (NN) and next-nearest neighbour (NNN) cation distributions in $(Yb_{1-x}Nd_x)_2Zr_2O_7$

Nd neighbours							
x	Annealing temperature (°C)	%Nd(NN)$_M$			%Nd(NNN)$_M$		
		Nd	Yb	Zr	Nd	Yb	Zr
0.00	1150	n/a	n/a	n/a	n/a	n/a	n/a
0.25	1150	11.8(7)	37.8(9)	50.4(6)	14.4(9)	37.8(6)	47.8(9)
0.50	1150	24.0(5)	25.2(5)	50.7(3)	27.8(9)	24.9(4)	47.2(6)
0.75	1350	36.1(2)	12.4(1)	51.4(2)	14.2(5)	3.5(2)	82.2(7)
	1150	36.0(3)	12.4(1)	51.5(2)	14.6(9)	3.5(2)	81.9(5)
	950	36.3(4)	12.7(2)	51.1(4)	40.4(4)	12.2(3)	47.4(5)
1.00	1350	49.1(2)	n/a	50.9(1)	20.4(5)	n/a	79.6(3)
	1150	49.6(3)	n/a	50.4(2)	18.5(7)	n/a	81.5(4)
	950	48.9(8)	n/a	51.1(7)	51.2(9)	n/a	48.8(9)

Yb neighbours							
x	Annealing temperature (°C)	%Yb(NN)$_M$			%Yb(NNN)$_M$		
		Nd	Yb	Zr	Nd	Yb	Zr
0.00	1150	n/a	49.7(3)	50.3(3)	n/a	52.8(5)	47.2(3)
0.25	1150	12.2(3)	37.6(5)	50.2(3)	14.9(2)	37.8(6)	47.2(5)
0.50	1150	24.3(5)	25.0(3)	50.6(3)	28.5(5)	24.6(6)	46.8(6)
0.75	1350	36.6(4)	12.5(3)	50.9(2)	11.1(7)	2.4(4)	86.5(9)
	1150	36.5(3)	12.6(4)	50.9(1)	11.1(5)	2.2(3)	86.7(6)
	950	36.8(5)	12.7(9)	50.5(9)	40.6(9)	11.9(2)	47.5(9)
1.00	1350	n/a	n/a	n/a	n/a	n/a	n/a
	1150	n/a	n/a	n/a	n/a	n/a	n/a
	950	n/a	n/a	n/a	n/a	n/a	n/a

Zr neighbours							
x	Annealing temperature (°C)	%Zr(NN)$_M$			%Zr(NNN)$_M$		
		Nd	Yb	Zr	Nd	Yb	Zr
0.00	1150	n/a	49.4(3)	50.6(2)	n/a	52.7(4)	47.3(5)
0.25	1150	12.1(1)	37.3(2)	50.6(3)	15.0(3)	37.4(4)	47.6(4)
0.50	1150	24.3(2)	25.1(2)	50.7(4)	28.2(4)	24.4(3)	47.4(4)
0.75	1350	37.2(2)	12.5(1)	50.3(1)	74.8(7)	24.9(2)	0.3(1)
	1150	37.3(1)	12.5(1)	50.2(1)	74.5(5)	24.7(2)	0.8(2)
	950	36.9(3)	12.6(2)	50.5(3)	40.3(4)	12.1(2)	47.6(5)
1.00	1350	49.7(1)	n/a	50.3(1)	89.6(3)	n/a	10.4(3)
	1150	49.9(2)	n/a	50.1(2)	86.4(4)	n/a	13.6(2)
	950	50.2(7)	n/a	49.8(8)	51.9(9)	n/a	48.1(9)

Table 3.18b. Theoretical nearest neighbour (NN) and next-nearest neighbour (NNN) cation distributions in $(Yb_{1-x}Nd_x)_2Zr_2O_7$

Nd neighbours							
x	Annealing temperature (°C)	%Nd(NN)$_M$			%Nd(NNN)$_M$		
		Nd	Yb	Zr	Nd	Yb	Zr
0.00	1150	n/a	n/a	n/a	n/a	n/a	n/a
0.25	1150	12.5	37.5	50.0	12.5	37.5	50.0
0.50	1150	25.0	25.0	50.0	25.0	25.0	50.0
0.75	1350	37.5	12.5	50.0	0.0	0.0	100.0
	1150	37.5	12.5	50.0	0.0	0.0	100.0
	950	37.5	12.5	50.0	37.5	12.5	50.0
1.00	1350	50.0	n/a	50.0	0.0	n/a	100.0
	1150	50.0	n/a	50.0	0.0	n/a	100.0
	950	50.0	n/a	50.0	50.0	n/a	50.0

Yb neighbours							
x	Annealing temperature (°C)	%Yb(NN)$_M$			%Yb(NNN)$_M$		
		Nd	Yb	Zr	Nd	Yb	Zr
0.00	1150	n/a	50.0	50.0	n/a	50.0	50.0
0.25	1150	12.5	37.5	50.0	12.5	37.5	50.0
0.50	1150	25.0	25.0	50.0	25.0	25.0	50.0
0.75	1350	37.5	12.5	50.0	0.0	0.0	100.0
	1150	37.5	12.5	50.0	0.0	0.0	100.0
	950	37.5	12.5	50.0	37.5	12.5	50.0
1.00	1350	n/a	n/a	n/a	n/a	n/a	n/a
	1150	n/a	n/a	n/a	n/a	n/a	n/a
	950	n/a	n/a	n/a	n/a	n/a	n/a

Zr neighbours							
x	Annealing temperature (°C)	%Zr(NN)$_M$			%Zr(NNN)$_M$		
		Nd	Yb	Zr	Nd	Yb	Zr
0.00	1150	n/a	50.0	50.0	n/a	50.0	50.0
0.25	1150	12.5	37.5	50.0	12.5	37.5	50.0
0.50	1150	25.0	25.0	50.0	25.0	25.0	50.0
0.75	1350	37.5	12.5	50.0	75.0	25.0	0.0
	1150	37.5	12.5	50.0	75.0	25.0	0.0
	950	37.5	12.5	50.0	37.5	12.5	50.0
1.00	1350	50.0	n/a	50.0	100.0	n/a	0.0
	1150	50.0	n/a	50.0	100.0	n/a	0.0
	950	50.0	n/a	50.0	50.0	n/a	50.0

3.3.3.2 Vacancy concentration and ordering

Three basic vacancy pair alignments can be defined with respect to the cubic coordination of the cation in the ideal fluorite structure, each characterized by a specific vacancy-vacancy distance and O-M-O angle (**Fig. 3.44**). Assuming a random distribution of vacancies, a ratio of 1:2:1.3 for <100>:<110>:<111> vacancy pairs is expected. The values given in **Table 3.19** show no significant departure from these ideal ratios in fluorite structured compositions. However, in pyrochlore structured compositions, ($0.75 \leq x \leq 1.00$ calcined at 1150-1350 °C) there is a clear and significant preference for <111> ordering, compared to the random situation. In the ideal pyrochlore structure, the vacancies show exclusive <111> ordering. The observed distributions are consistent with a high degree of pyrochlore-type ordering on the oxide sub-lattice, but with both <100> and <110> aligned vacancy pairs still present, reflecting the additional oxygen Frenkel defects seen in the Rietveld analysis.

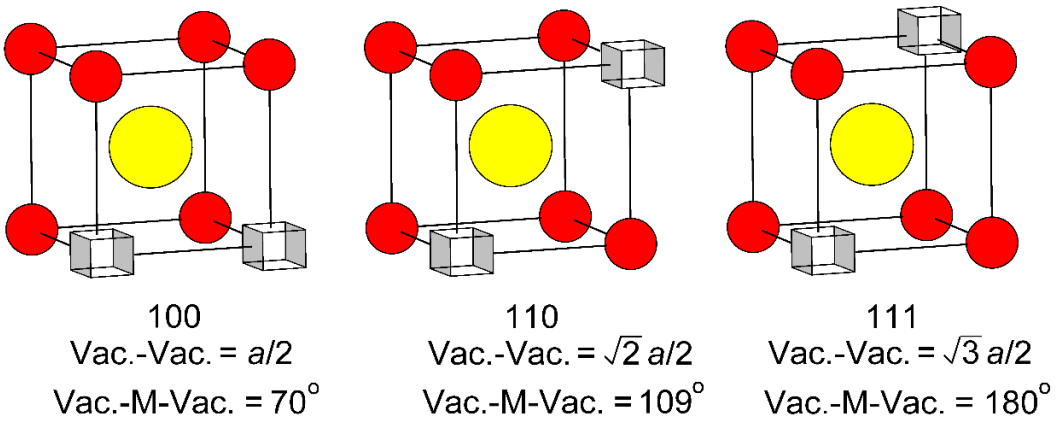

Fig. 3.44 Possible vacancy pair alignments around cations in the ideal fluorite structure, with characteristic vacancy-vacancy distances and vacancy-metal-vacancy angles shown.

It is possible to reveal details of the local environment around vacancies through careful examination of the RMC configurations. Using a similar approach to that discussed above, the vacancy "coordination" environment can be probed to reveal evidence of preferential distribution of vacancies between cations. The nearest neighbour

cation distributions around oxide ion vacancies are presented as percentages of the total number of nearest neighbour cations in **Table 3.19**. A random distribution of vacancies would be expected to yield percentage distributions reflecting the stoichiometry. However, the values in **Table 3.19** for the percentage of cation nearest neighbours around a vacancy, $\%vac(NN)_M$, show appreciable deviation from a purely random distribution.

The high percentage of Nd^{3+}/Yb^{3+} nearest neighbours in the fluorite type compositions, strongly suggests preferential association of vacancies with these cations. However, in the end member compositions with the fluorite type structure, this preference is less clear, with values close to those expected for a random vacancy distribution. For the x = 0.75 pyrochlore structured samples, vacancies appear to be preferentially associated with Yb^{3+}, while for the x = 1.00 pyrochlore structured samples, there is clear preferential association of vacancies with Zr^{4+}, consistent with previous work on similar systems.[242]

Table 3.19 Tetrahedral site oxygen vacancy concentrations per fluorite cell, oxide ion vacancy pair alignment ratios and vacancy nearest neighbours in $(Yb_{1-x}Nd_x)_2Zr_2O_7$

x	Calcination temp. (°C)	No. vac. per fluorite cell	Pair alignment ratio 100:110:111	$\%V(NN)_{Nd}$	$\%V(NN)_{Yb}$	$\%V(NN)_{Zr}$
0.00	1150	1.04(2)	1.00:2.13:1.38	n/a	51.3(3)	48.7(3)
0.25	1150	0.97(2)	1.00:2.09:1.38	24.6(7)	33.5(14)	41.9(14)
0.50	1150	0.97(1)	1.00:1.98:1.34	30.4(11)	27.5(14)	42.0(18)
0.75	1350	0.93(1)	1.00:6.35:15.01	30.6(2)	19.0(2)	50.5(3)
	1150	0.97(1)	1.00:4.88:7.47	31.4(2)	19.5(3)	49.1(3)
	950	0.99(1)	1.00:1.94:1.26	34.46(12)	22.7(10)	42.8(16)
1.00	1350	0.97(2)	1.00:4.68:48.47	36.4(4)	n/a	63.6(4)
	1150	0.96(1)	1.00:6.83:198.10	32.2(5)	n/a	67.8(5)
	950	0.96(1)	1.00:6.15:17.50	46.6(3)	n/a	53.4(3)

3.3.3.3 Cation coordination

The bond angles in the fluorite and pyrochlore structures provide a sensitive means of differentiating between the two structures. In the ideal pyrochlore structure, two values are expected at around 74° and two around 109° (determined by the 48*f* oxygen *x* fractional coordinate) for the O-Ln-O angles and two around 90° for the O–Zr–O angles (**Fig. 3.45**); whereas in the fluorite structure, the two O–Zr–O angles are expected at around 70 and 110°, corresponding to O atoms aligned on the <100> and <110> directions, in the cubic coordination environment around a cation, in the same way as seen for vacancy pairs in **Fig. 3.44** above.[234]

The O-M-O angular distribution functions $A_{OMO}(\Theta)$, derived from the RMC configurations are shown in **Figs. 3.46-3.48**. In compositions x = 0.00 to 0.50 calcined at 1150 °C and x = 0.75 and 1.00 calcined at 950 °C, the distribution of O–Zr–O angles is close to the expected values for the ideal fluorite structure. However, the O-Nd-O distribution is significantly different, particularly at lower angles, where the peak maximum is seen approximately 5° lower than seen for the other two distributions. This difference suggests a greater local distortion away from the fluorite structure around Nd^{3+} than around the other cations. In compositions x = 0.75 and 1.00 calcined at 1150 and 1350 °C, the O–Zr–O angles correspond very closely to those expected from the ideal pyrochlore structure, especially for x = 1.00.

(a)

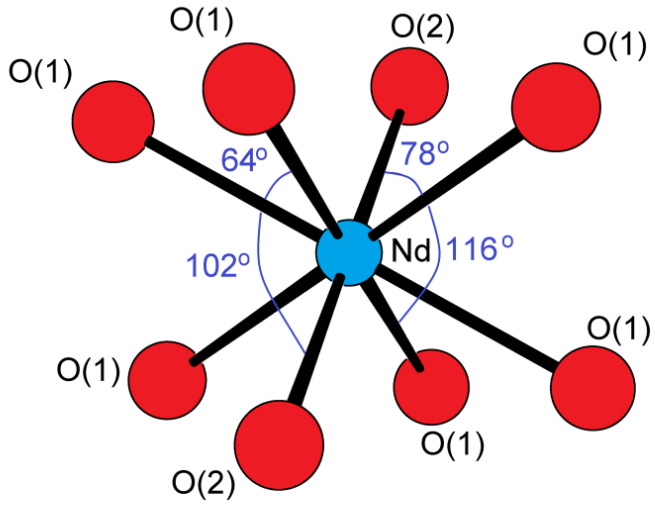

(b)

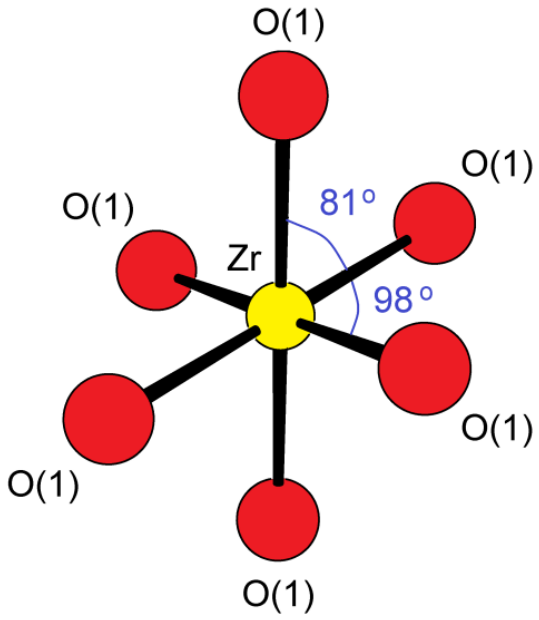

Fig. 3.45. O-M-O angles in $Nd_2Zr_2O_7$, calcined at 1350 °C.

(a)

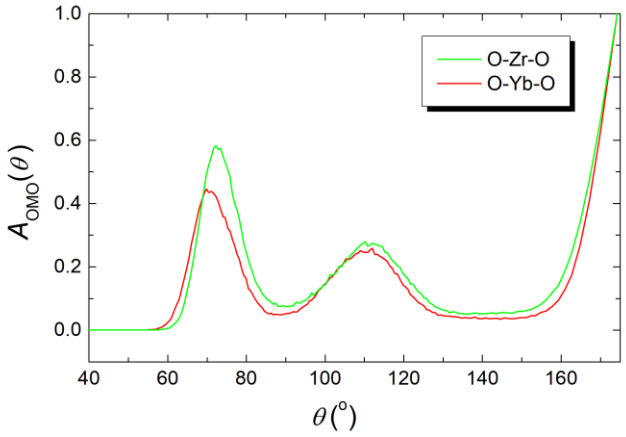

(b)

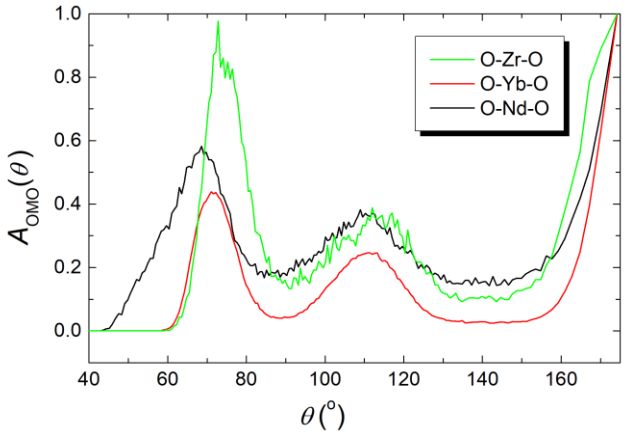

(c)

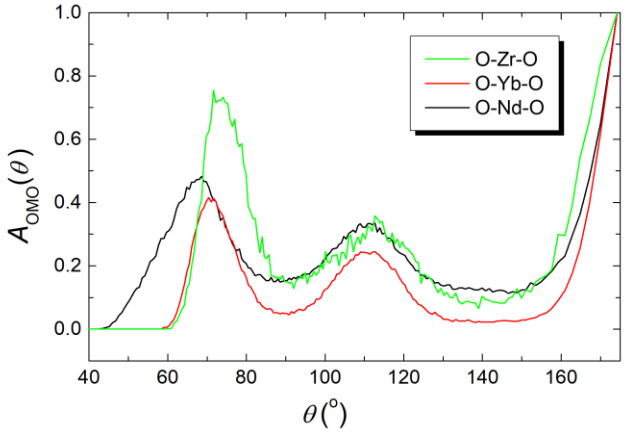

Fig. 3.46. O-M-O angular distribution functions as determined from RMC modelling, in the system $(Yb_{1-x}Nd_x)_2Zr_2O_7$, calcined at 1150 °C; for (a) x = 0.0, (b) x = 0.25, and (c) x = 0.50.

(a)

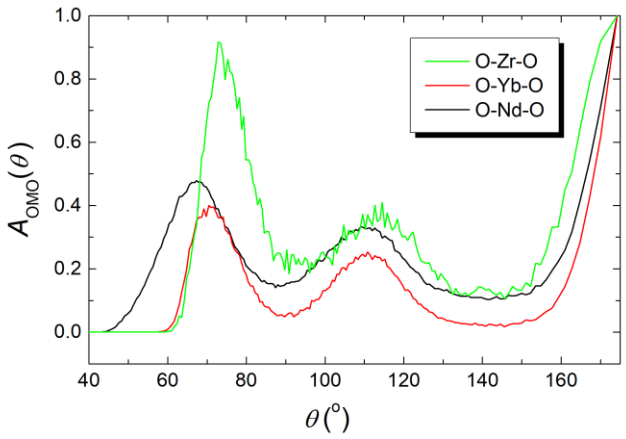

(b)

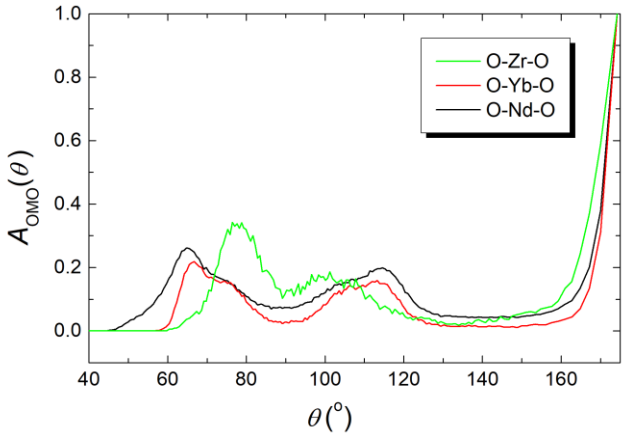

(c)

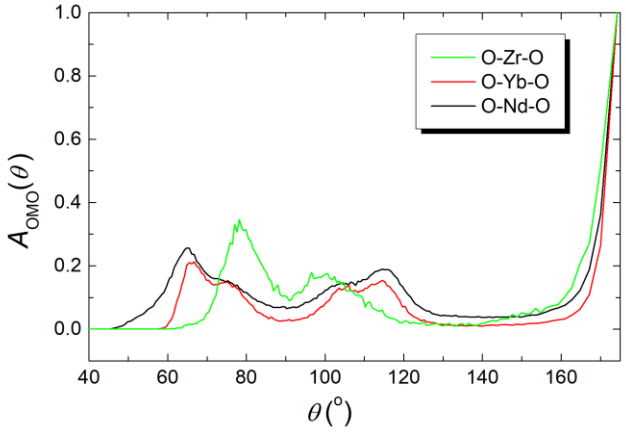

Fig. 3.47. O-M-O angular distribution functions as determined from RMC modelling, in the system $(Yb_{1-x}Nd_x)_2Zr_2O_7$, x = 0.75; calcined at (a) 950 °C, (b) 1150 °C, and (c) 1350 °C.

(a)

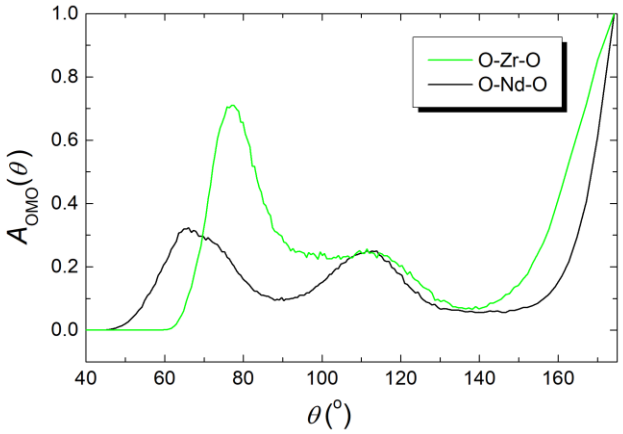

(b)

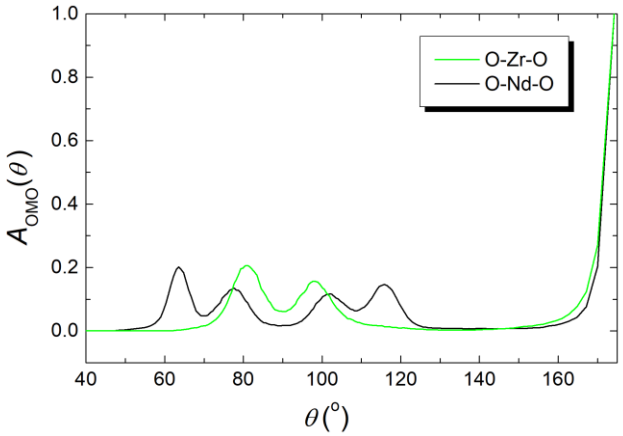

(c)

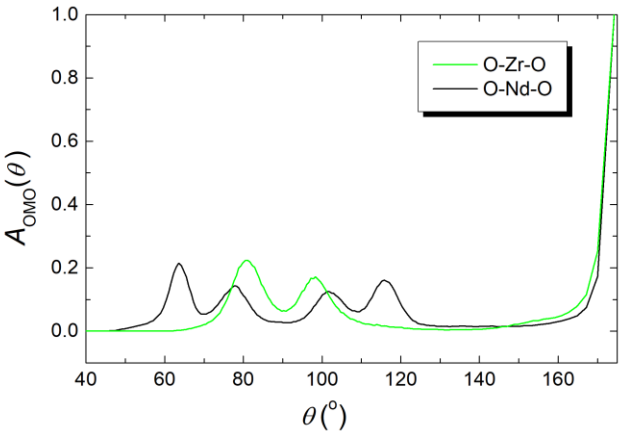

Fig. 3.48. O-M-O angular distribution functions as determined from RMC modelling, in the system $(Yb_{1-x}Nd_x)_2Zr_2O_7$, x = 1.00; calcined at (a) 950 °C, (b) 1150 °C, and (c) 1350 °C.

3.3.4 Electrical conductivity

To analyse the IS data, the following overall expanded equivalent circuit was assumed, **Fig. 3.49**, based on an equivalent circuit described for the oxygen ion conductor BIMEVOX.[243] The equivalent circuit was built of resistors, *R*, capacitors, *C*, and constant phase elements (cpe), *P*, whose complex capacitance was expressed as:

$$C^*(\omega) = A\left(\frac{j\omega}{Hz}\right)^{1-n} \tag{3.8}$$

Thus, the magnitude *A* of the cpe is expressed in farads. If $n = 0$ then this element behaves like a pure capacitor, when $n = 1$ it behaves as a pure resistor, and a cpe with exponent $n = 0.5$ can be denoted as a Warburg element, W.

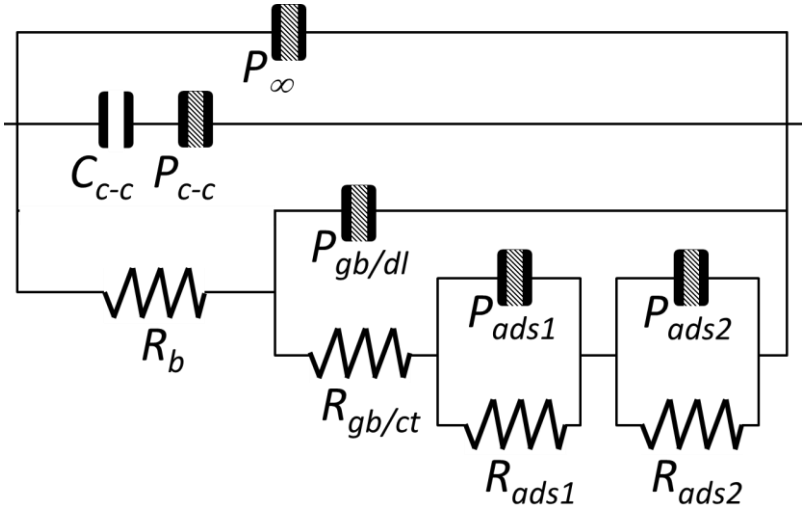

Fig. 3.49 Electrical equivalent circuit model used for IS data analysis.

The electrical properties of the sample-material itself are included mainly in the elements P_∞, R_g, P_{gb}, R_{gb}, $P_{C\text{-}C}$, and $R_{C\text{-}C}$. The cpe P_∞ models the complex capacitance of the sample at high frequencies and represents the high frequency permittivity. The DC conductivity of the grain interiors of a polycrystalline sample are represented by the resistor R_g. The frequency dependence of ionic conductivity and of the permittivity of the grains (dielectric relaxation process) is modelled by the capacitor $C_{C\text{-}C}$ and the cpe

element $P_{C\text{-}C}$ connected in series constitute the Cole–Cole complex dielectric function.[244] The contribution of grain boundaries to the impedance of the polycrystalline sample is represented by the resistance R_{gb} and the cpe element P_{gb}. The rest of the elements $P_{dl,}$ R_{ct}, P_{ads} and R_{ads} correspond to properties of the electrode-electrolyte interface, i.e. double layer capacitance, charge transfer resistance and adsorption of oxygen on the porous platinum electrode. At higher temperatures the elements P_{ads} and R_{ads} had to be doubled due to more complex electrochemical behaviour (however detailed and more systematic studies of the electrode-electrolyte processes were not a subject of this work).

It was not possible to fit all parameters of the equivalent circuit to impedance spectra over the whole temperature range, due to the shift of the frequency window; the applied frequency range only covers a limited range of values corresponding to relaxation times, $\tau = RC$, where frequency $f = 1/\tau$. Therefore at lower temperatures, impedance spectra reflected mainly the bulk properties of samples, while at higher temperatures features associated with the electrode-electrolyte interface were more evident. For example, in the case of the $Nd_{1.5}Yb_{0.5}Zr_2O_7$ composition, the following impedance spectra analysis was performed which was similar to the analysis of all other compositions included in this chapter as well as in chapter 4, **Fig. 3.50**. At lower temperatures, around 100 – 200 °C, one full semicircle dispersion was observed with a second one only partially visible. Therefore, the equivalent circuit had to be reduced to those elements sensitive to higher frequencies and elements which simulate smaller capacitances.

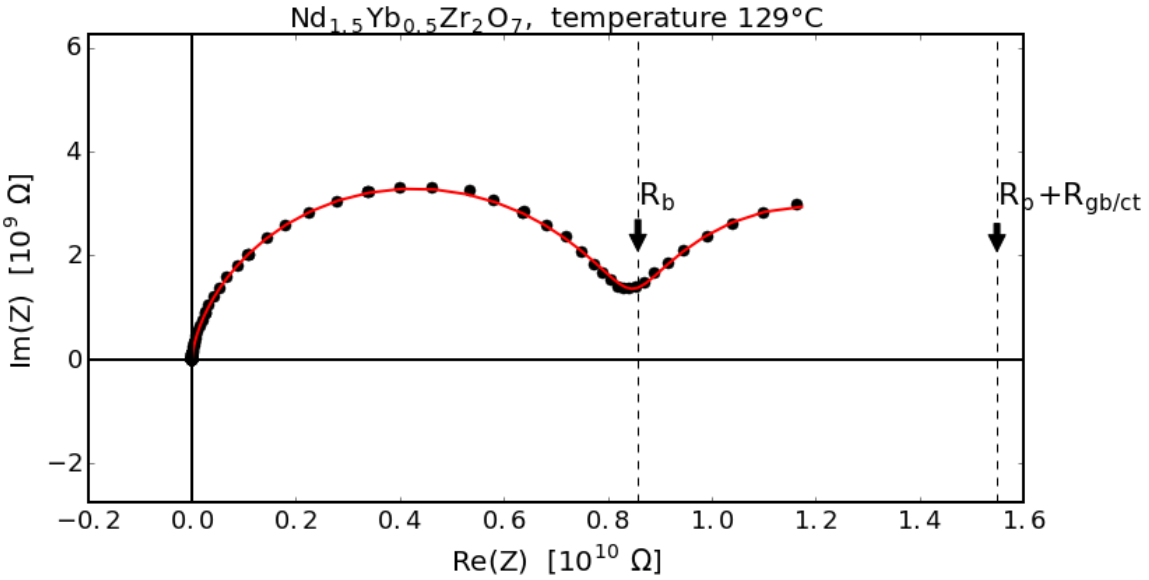

Circuit description code: (P(CP)(R(RP))); Temp. = 129.1 °C; Rms = 1.37;
Geometrical factor l/s = 0.407 cm^{-1}

Parameter	Estimated value	Confidence limit
$\mathbf{P}_{\infty}$	4.0700e-12 F	2.%
$\mathbf{n}_{\infty}$	0.000	0.1%
$\mathbf{P}_{c\text{-}c}$	1.9500e-11 F	10%
$\mathbf{n}_{c\text{-}c}$	0.462	4.%
$\mathbf{R}_{b}$	8.5770e+09 Ω	1.%
$\mathbf{R}_{gb}$	6.9060e+09 Ω	11%
$\mathbf{P}_{gb}$	1.7460e-09 F	13%
$\mathbf{n}_{gb}$	0.128	37%

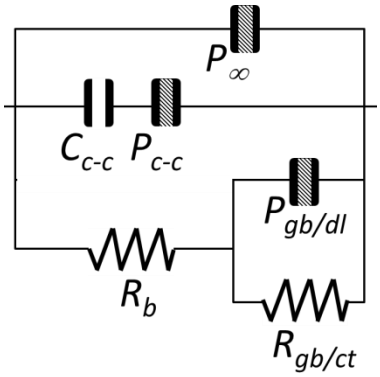

Fig. 3.50 Values of parameters of the equivalent circuit estimated for impedance spectra measured for a polycrystalline sample of $Nd_{1.5}Yb_{0.5}Zr_2O_7$ at 129 °C. Resistance R_b is indicated as the intercept of the semicircle dispersion with the Re(Z) axis.

The high frequency permittivity is represented by the constant phase element, P_∞, which proved to provide a better quality of fit than an ordinary capacitor. The fitted value of the exponent n_∞ is close to 0, which can be interpreted as a capacitance with nearly constant low loss. The elements $C_{c\text{-}c}$, $P_{c\text{-}c}$ are characteristic for the Cole-Cole relaxation function with an $n_{c\text{-}c}$ value close to 0.5. These parameters were able to be estimated only at lower temperatures when long range ionic movement (d.c. conductivity) is reduced. The second semicircle exhibits capacitance values (P_{gb}) in the order of 10^{-9} F (with n_{gb} close to 0), this may be associated with a grain boundary dispersion of a polycrystalline sample. The processes connected with the electrode-electrolyte interface dispersion were not observed at this temperature.

At higher temperatures, around 200 - 400 °C, the impedance spectra evolved and the lower frequency dispersion was more pronounced, **Fig. 3.51**, including the additional elements P_{ads} and R_{ads}, simulating adsorption or ionic diffusion in the non-blocking porous Pt electrode, with P_{ads} around 10^{-7} F and n_{ads} close to 0.5. P_{gb} values remain in the order of 10^{-9} F, previously indicated as the grain boundary capacitance. However the shape of the impedance spectra may suggest that this semicircle can be regarded as a double layer capacitance connected with charge transfer resistance at the electrode.

In the temperature range 400 - 800 °C the impedance spectra, **Fig. 3.52**, shifted to the impedance of an electrode-electrolyte interface and again additional elements P_{ads2} and R_{ads2} were added to the equivalent circuit model to satisfy the fitting procedure. At high frequencies the properties of the bulk material were hardly seen and some elements had to be deleted from the equivalent circuit model.

Based on visual inspection of the data, only one parameter could be estimated precisely over the whole temperature range, i.e. the resistance of the bulk sample, probably associated with grain interior resistance. Taking into account the dimensions of the sample, the conductivity values were calculated and analysed further as a function of temperature and material composition.

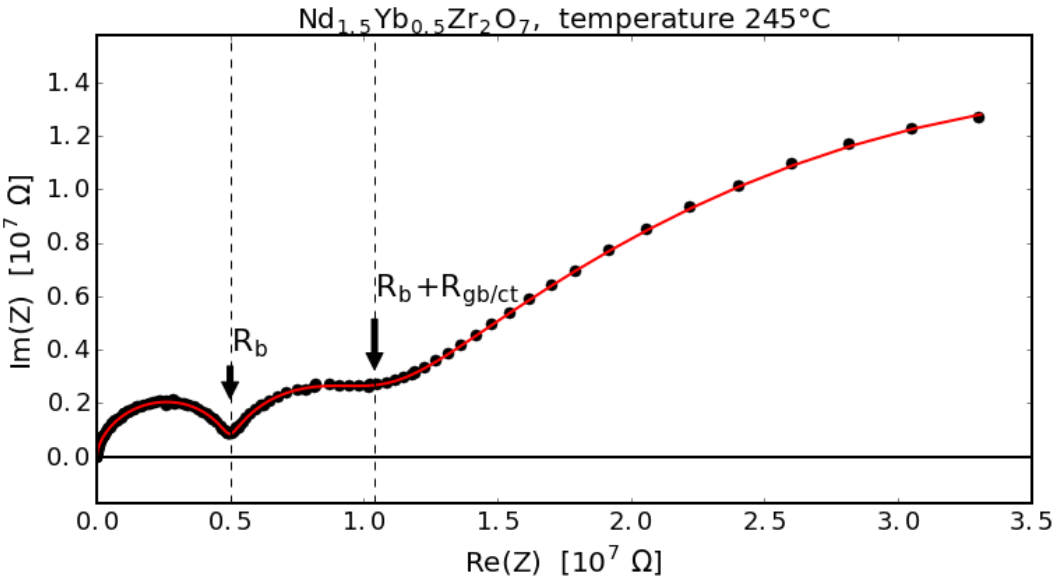

Circuit description code: (P(CP)(R(P(R(RP))))); Temp. = 245.4 °C; Rms = 0.606
Geometrical factor = 0.407cm^{-1}

Parameter	Estimated value	Confidence limit
$\mathbf{P}_{\infty}$	8.0700e-12 F	3.%
$\mathbf{n}_{\infty}$	0.032	6.%
$\mathbf{P}_{c\text{-}c}$	4.5280e-09 F	17%
$\mathbf{n}_{c\text{-}c}$	0.683	3.%
$\mathbf{R}_{b}$	4.9960e+0 Ω	.3%
$\mathbf{P}_{gb}$	3.8140e-09 F	4.%
$\mathbf{n}_{gb}$	0.140	6.%
$\mathbf{R}_{gb}$	5.4090e+0 Ω	2.%
$\mathbf{R}_{ads}$	6.1100e+0 Ω	3.%
$\mathbf{P}_{ads}$	1.0660e-07 F	.9%
$\mathbf{n}_{ads}$	0.476	1.%

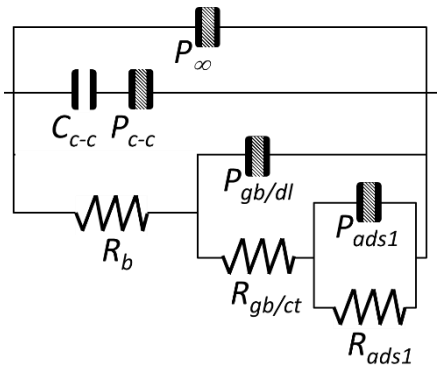

Fig. 3.51 Values of parameters of the equivalent circuit estimated for impedance spectra measured for the polycrystalline sample of $Nd_{1.5}Yb_{0.5}Zr_2O_7$ at 245 °C.

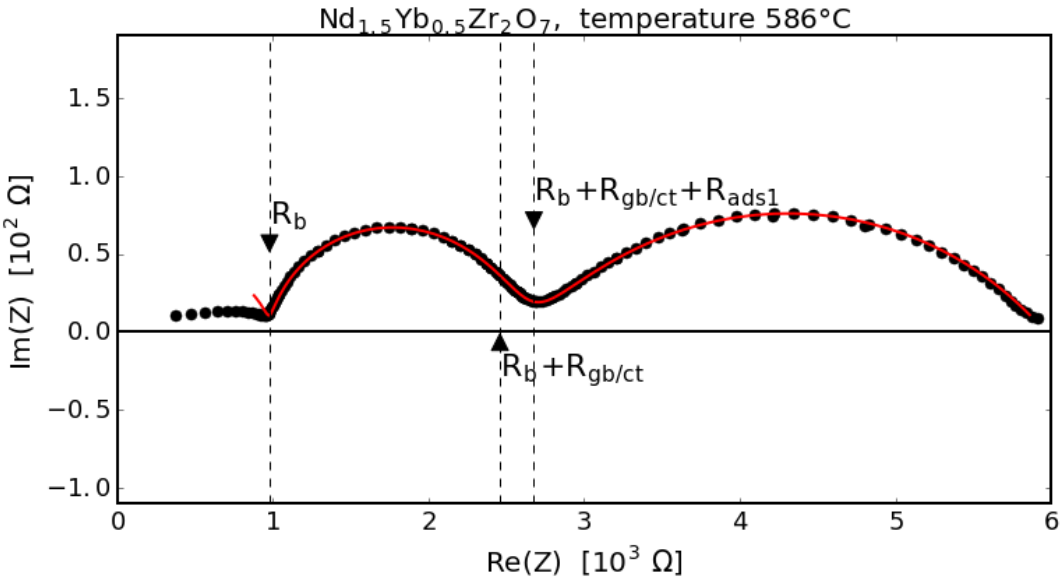

Circuit description code: (PR)(P(R(RP)(RP))); Temp. = 586.5 °C; Rms = 0.136
Geometrical factor = 0.407cm^{-1}

Parameter	Estimated value	Confidence limit
$\mathbf{P}_{\infty}$	3.3500e-11 F	25%
$\mathbf{n}_{\infty}$	0.113	16%
$\mathbf{R_b}$	9.7870e+02 Ω	.2%
$\mathbf{P_{gb}}$	7.8280e-09 F	5.%
$\mathbf{n_{gb}}$	0.093	4.%
$\mathbf{R_{gb}}$	1.4800e+03 Ω	2.%
$\mathbf{R_{ads1}}$	2.1840e+02 Ω	14%
$\mathbf{P_{ads1}}$	1.4420e-05 F	21%
$\mathbf{n_{ads1}}$	0.451	9.%
$\mathbf{R_{ads2}}$	3.2840e+03 Ω	.3%
$\mathbf{P_{ads2}}$	6.4660e-05 F	.4%
$\mathbf{n_{ads2}}$	0.451	.3%

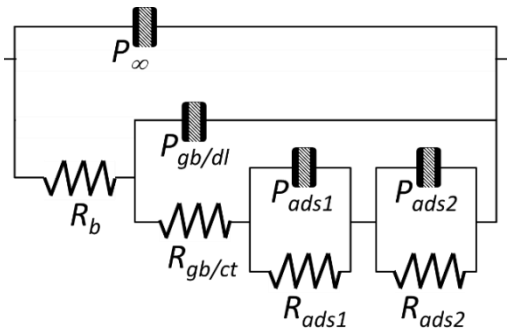

Fig. 3.52 Values of parameters of the equivalent circuit estimated for impedance spectra measured for a polycrystalline sample of $Nd_{1.5}Yb_{0.5}Zr_2O_7$ at 586 °C.

The Arrhenius plots for $(Yb_{1-x}Nd_x)_2Zr_2O_{7-\delta}$ ($0.00 \leq x \leq 1.00$) are shown in **Fig. 3.53**, with the compositional variation of activation energies and total conductivities shown in **Fig. 3.54**. For the fluorite structured compositions ($0.00 \leq x \leq 0.50$), the plots show near linear behaviour, with only the $x = 0.00$ composition showing some deviation at low temperatures. For the pyrochlore structured compositions ($x = 0.75$ and $x = 1.00$) there is deviation from linearity. For the $x = 0.75$ composition, three linear regions are observed. The low temperature region below *ca*. 350 °C and the high temperature region above ca. 430 °C have very similar activation energies and are linked by an intermediate temperature region with lower activation energy. For the $x = 1.00$ composition, a much lower conductivity is observed than at $x = 0.75$.

The activation energies decrease with increasing Nd content over the entire compositional range studied. Only in the case of the end members, do the activation energies in the high and low temperature regions differ appreciably. Attempts to measure transport numbers in this system have so far been unsuccessful. However, the values of activation energy in both high and low temperature regions of around 1 eV are typical of ionic conductors. Characteristic values of conductivity in the high and low temperature regions typified by the conductivities at 300 °C and 700 °C (σ_{300} and σ_{700}, respectively) show a maximum for the $x = 0.75$ composition with a value of 6.82×10^{-4} S cm^{-1} at 700 °C. This composition corresponds to the sample with the highest level of oxygen Frenkel defects, as found in the Rietveld analysis.

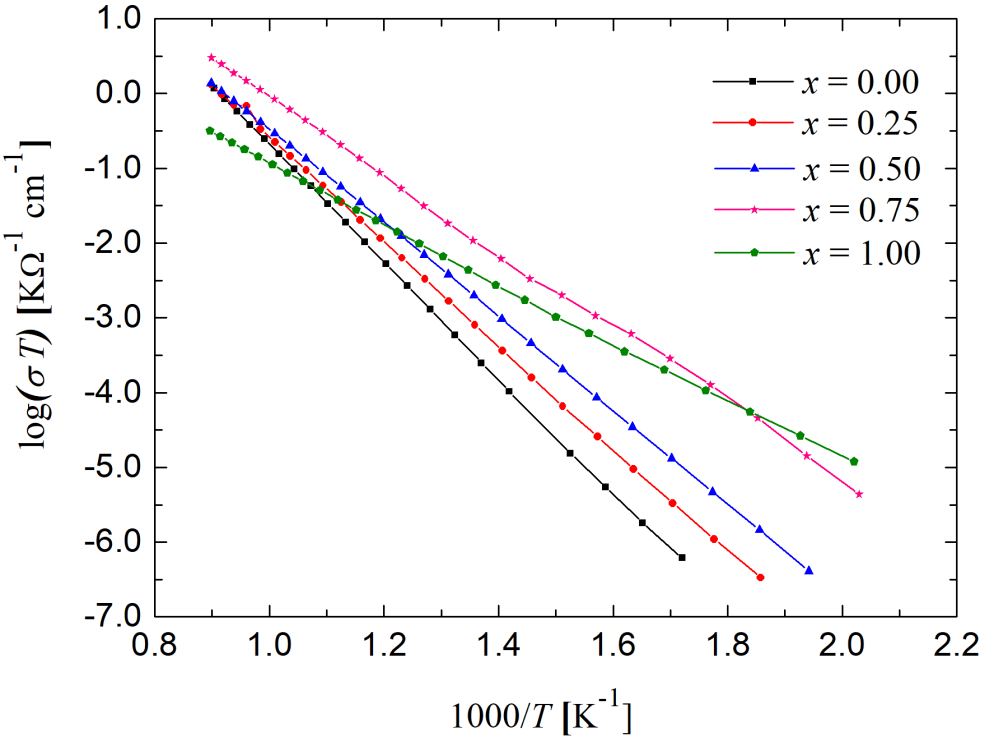

Fig. 3.53. Arrhenius plots of total conductivity for $(Yb_{1-x}Nd_x)_2Zr_2O_7$ compositions with x = 0.00, 0.25, 0.50, 0.75, and 1.00. Samples were synthesised at 1150 °C and sintered at 1600 °C.

(a)

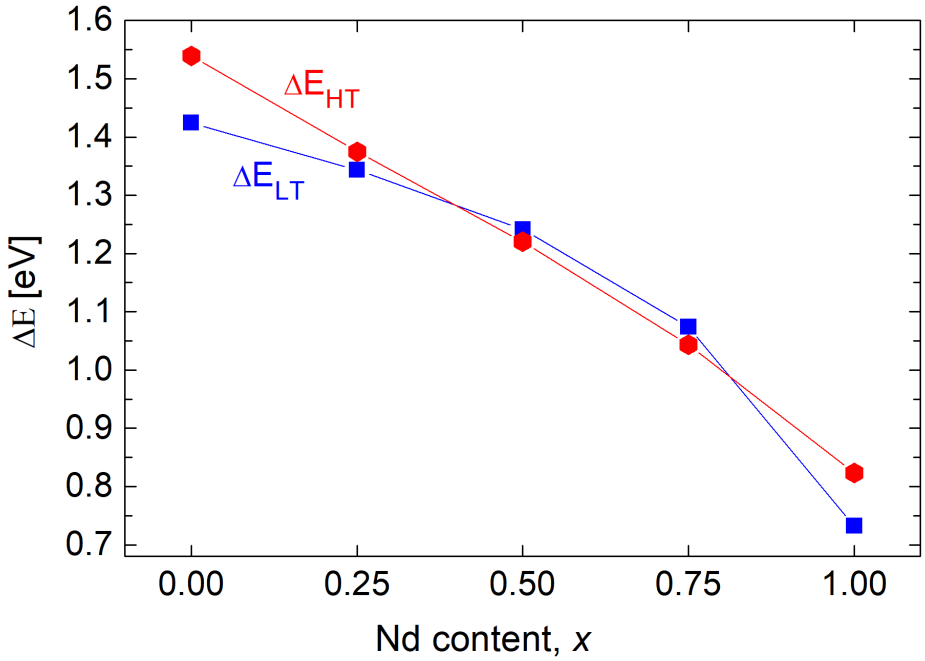

(b)

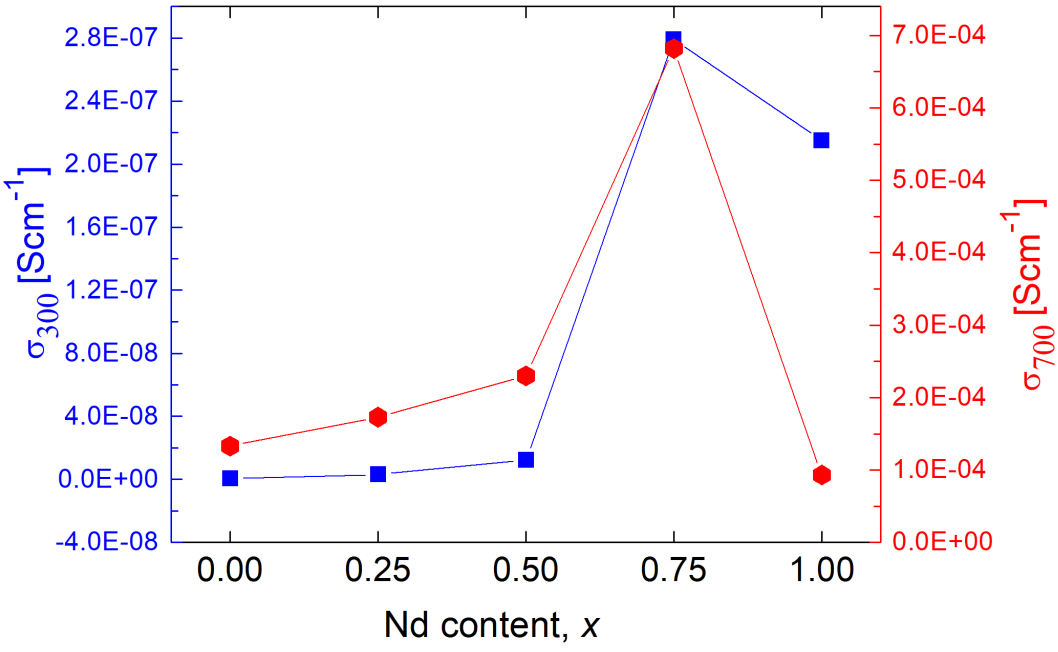

Fig. 3.54. Compositional variation of (a) high temperature ΔE_{HT} and low temperature ΔE_{LT} activation energies, and (b) total conductivity at 300 °C (σ_{300}) (blue) and 700 °C (σ_{700}) (red) in $(Yb_{1-x}Nd_x)_2Zr_2O_7$, with x = 0.00, 0.25, 0.50, 0.75, and 1.00, at 300 and 700 °C.

3.4 Conclusions

Samples of ytterbium neodymium zirconate $(Yb_{1-x}Nd_x)_2Zr_2O_7$ ($0.00 \leq x \leq 1.00$) were synthesised via a co-precipitation method. Powder X-ray and neutron diffraction results and structural analyses via the Rietveld refinement method, show that at low neodymium contents ($0.00 \leq x \leq 0.50$), these systems crystallize in the fluorite structure with space group $Fm\bar{3}m$, whereas at high neodymium content ($0.75 \leq x \leq 1.00$) a pyrochlore structure with space group $Fd\bar{3}m$ is observed. At 75% neodymium content, the material undergoes a fluorite/pyrochlore phase transition. For compositions with high neodymium content prepared at lower temperatures (950 °C), a fluorite structure is observed, which shows gradual evolution of pyrochlore ordering with increasing calcination temperature (1150-1350 °C). The transition from the fluorite to pyrochlore structures is believed to proceed via the intermediate emergence, and progressive growth, of pyrochlore-type microdomains in a fluorite matrix.

In compositions which retain the fluorite structure, considerable non-equivalence of the cation local environment was observed, with variation in composition. Coordination numbers, derived from total neutron scattering analyses, indicate the coordination number of Zr^{4+} to be close to 6 in the pyrochlore structure and close to 7 in the fluorite structure. The coordination numbers of Nd^{3+} and Yb^{3+} were close to 7 and showed little variation with the extent of disorder. Evidence for anti-site cation disorder is found in the pyrochlore structured samples.

For fluorite structured samples, total electrical conductivity generally shows classical Arrhenius behaviour up to around 800 °C. Activation energies decrease as the average size of the cation at the A-site decreases, with increasing Nd content. Total conductivity increases with increasing Nd content, up to a maximum at $x = 0.75$ and then decrease; this appears to be correlated with the concentration of oxygen Frenkel defects in the pyrochlore structure. The conductivity of these oxides is of the order of 10^{-4} S cm^{-1} at 700 °C.

Chapter 4 – Structure and Conductivity in Neodymium Calcium Zirconate

4.1 Introduction

Isovalent substitution has been found to increase the ionic conductivity of pyrochlore-type oxides by at least four orders of magnitude, which has been attributed to increased disorder in both the cation and anion sub-latices.[127] However, optimum conductivity is crucially dependent on dopant concentration, with maximum conductivity corresponding to a minimum in activation energy. Furthermore, activation energy has been shown to be hugely determined by structural disorder, often increasing with increased disorder,[110] due to the formation of oxygen-vacancy dopant association.[76]

Di-valent dopant cations have been incorporated substitutionally into the host lattice of pyrochlore oxides, wherein, structural effects of dopant concentration and the resulting ionic conductivities were investigated. When divalent ions are accommodated in a pyrochlore host lattice, they must be charge-compensated by a positively charged lattice defect.[245] The resultant defect cluster consists of a cation anti-site pair, adjacent to an oxygen Frenkel pair, described by Eq. (4.1) in Kröger–Vink notation as:

$$\mathrm{Nd}_{\mathrm{Nd}}^{X} + \mathrm{Ca}_{\mathrm{Ca}}^{X} + \mathrm{O}_{\mathrm{O}}^{X} \Rightarrow \mathrm{Nd}'_{\mathrm{Ca}} + \mathrm{Ca}_{\mathrm{Nd}}^{\bullet} + \mathrm{V}_{\mathrm{O}(48f)}^{\bullet\bullet} + \mathrm{O}''_{\mathrm{i}(8a)} \qquad (4.1)$$

Therefore, doping with lower valence cations causes a local charge imbalance and thus promotes the formation of charge-compensating oxygen vacancies,[137] with anion Frenkel being the most likely defect.[84] As compared to other divalent dopants, Ca^{2+} has been shown to be most effective in enhancing electrical conductivity in titanate pyrochlore oxides.[104] Kramer and Tuller have shown that the substitution of 10% Ca for Gd in $Gd_2Ti_2O_7$, results in ionic conductivities in the range of 10^{-2} S cm^{-1} at 1000 °C, which is substantially higher than in the un-doped compound.[127] Similar enhancements in conductivities were achieved via Ca doping at the A-site in $Y_2Ti_2O_7$, $Sm_2Ti_2O_7$, and $Gd_2Sn_2O_7$.[104,246]

More recently, Shlyakhtina *et al*. have shown that 10% Ca doped $Yb_2Ti_2O_7$ at the A-site resulted in exceptionally high electrical conductivities, *i.e*. $\approx 2 \times 10^{-2}$ S cm^{-1} 740 °C and $\approx$ 0.2 S cm^{-1} at 1000 °C.[247] Belov *et al*. found that the doping of intermediate lanthanide titanate oxides with divalent cations enhanced conductivity, with the optimum conductivity achieved at 10% substitution.[132] While the effect of divalent and trivalent dopants on oxide ion conductivity in pyrochlore titanium oxides has been studied extensively, few systematic studies have been performed on the effect of divalent dopants on oxide ion conductivity in pyrochlore zirconium oxides.

In this chapter, a variable-temperature neutron powder diffraction experiment was carried out on the $(Nd_{1-x}Ca_x)_2Zr_2O_{7-x}$ ($0.10 \leq x \leq 0.50$) system, in order to investigate the local structural evolution as a function of composition and temperature. Total scattering analysis has been used to examine the thermal variation of oxide ion and vacancy distribution in the system $(Nd_{1-x}Ca_x)_2Zr_2O_{7-x}$ ($x = 0.50$).

4.2 Experimental

4.2.1 Synthesis

Samples of $(Nd_{1-x}Ca_x)_2Zr_2O_{7-x}$ ($0.00 \leq x \leq 0.50$) were prepared via the co-precipitation method, in which stoichiometric amounts of neodymium oxide (Nd_2O_3, purity 99.9%, Sigma Aldrich) and calcium nitrate ($Ca(NO_3)_2$, purity 99.9%, Sigma Aldrich) were dissolved in nitric acid (2 M) and distilled water, respectively, **Table 4.1**. The solutions were then mixed together, along with the zirconyl chloride solution, and stirred for 60 min. The mixed solution was slowly added under stirring to excess dilute ammonia solution with a pH value of 13 to obtain a gel-like precipitate. The gel was filtered, washed with distilled water several times to a pH value of 7, and then washed twice with industrial methylated spirits (IMS). The washed precipitate was dried at 80 °C for 24 h. The dried mixture was ground uisng a mortar and pestle, placed in a Pt crucible and heated in an electric furnace to 1350 °C for 24 h in air. Full solubility of calcium was achieved over the entire composition range studied.

Table 4.1 Masses of reactants and volume of solvents used in the synthesis of the compositions of $(Nd_{1-x}Ca_x)_2Zr_2O_{7-x}$ $(0.00 \leq x \leq 0.50)$ studied in this chapter

Composition	$x = 0.10$	$x = 0.20$	$x = 0.30$	$x = 0.40$	$x = 0.50$
Nd_2O_3 Mass (g)	10.78	9.95	9.05	8.08	7.03
$Ca(NO_3)_2$ Mass (g)	1.17	2.43	3.78	5.26	6.85
2M nitric acid volume (ml)	150	150	150	150	150
$ZrOCl_2 \cdot 8H_2O$ Mass (g)	22.93	23.81	24.77	25.80	26.92
H_2O Volume (ml)	150	150	150	150	150
Ammonia Volume (ml)	300	300	300	300	300
Product Mass (g)	20	20	20	20	20

4.2.2 Diffraction

X-ray powder diffraction data were collected on an PANalytical X'Pert Pro diffractometer fitted with an X'Celerator detector, using Ni-filtered CuKα radiation (λ = 1.5418 Å). Data were collected in flat plate θ/θ geometry in steps of 0.033°, with an effective scan time of 250 s per step, over the range 5 to 120° 2θ. Calibration was carried out with an external LaB_6 standard. For variable temperature measurements, samples were mounted on a Pt strip in an Anton Paar HTK-16 high temperature camera. Data were collected at 25 °C and at 50 °C intervals from 100 °C to 800 °C in steps of 0.0167°, over the 2θ range 5 to 120°, with scan stimes of 200 s per step for the collections at 25 and 800 °C and 50 s per step for all other temperatures.

Variable-temperature neutron diffraction data were obtained at the ISIS facility, in the temperature range 20–800 °C, using the POLARIS diffractometer. Data were collected, on back-scattering (average angle 146.72°), 90° (average angle 92.5°), intermediate-angle (average angle 52.21°), low-angle (average angle 33.5°) and very low angle (average angle 24.75°) detectors, corresponding to the approximate *d*-spacing ranges 0.04-2.6 Å, 0.05-4.1 Å, 0.73-7.0 Å. 0.3-48 Å and 0.13-13.8 Å, respectively. The samples were placed in a sealed silica glass tube inside an 11 mm diameter V can. Data were collected, at room temperature and from 300 to 800 °C, ion steps of 50 °C, corresponding to total proton beam charge values of 30 μA h. For the x = 0.1 to 0.3 compositions, at 800 °C an extended data collection of 200 μA was carried out to afford

higher quality data, while for the x = 0.5 composition extended collections of *ca*. 1000 μA h were made at 500 and 800 °C. Unfortunately, due to time constraints on the instrument, the 800 °C data set for the x = 0.3 composition could only be collected for a proton beam charge equivalent of 30 μA h.

Total scattering measurements,[182] were carried out for the most heavily doped sample at 20, 500, and 800 °C, consisting of a minimum of 8-hour collection time. Each collection corresponded to a total proton beam charge ranging from 1000 μA h to 1200 μA h. Long-range structure was analysed by the Rietveld method using the General Structure Analysis System (GSAS) set of programs,[199] and the EXPGUI interface.[198] XRD and NPD data were used simultaneously. The background for each bank was modelled as a 24-term shifted Chebyshev polynomial, and the peak profiles were fited using the GSAS type 2 profile. A cubic subcell model in space group $Fd\bar{3}m$ was used for refinement; Nd and Ca were located on the 16*d* site 0.5, 0.5, 0.5, Zr was located on the 16*c* site 0,0,0, and oxide ions were distributed over three sites: 48*f* at *ca*. 0.375, 0.125, 0.125; 8*a* at 0.125, 0.125, 0.125, and 8*b* at 0.375, 0.375, 0.375.

Total neutron scattering, involving analysis of both Bragg and diffuse scattering, was used to shed light on vacancy ordering.[248,249] The program Gudrun,[178] was used to apply corrections for background scattering and beam attenuation and the resulting normalized total scattering structure factors, S(Q), were then used to obtain the corresponding total radial distribution function, G(r), via Fourier transformation. RMCProfile was used for reverse Monte Carlo (RMC) modelling of the pair distribution function (PDF) data.[189] A 5 × 5 × 5 pyrochlore super-cell, containing a total of about 10000 atoms, was used as the starting configuration for RMC modelling. Vacancies were distributed randomly in the starting configuration over the sites corresponding to O(1) and O(3) in the $Fd\bar{3}m$ pyrochlore subcell according to the Rietveld analysis results. BVS restraints were used, to favour configurations with chemically sensible geometries and to help guide the refinements in the initial stages.[209] A closest approach distance was used to avoid unrealistically short M-O and O-O contacts. An O-O interatomic potential with low relative weighting was used to ensure a relaistic O-O distribution. Fitting was carried out against S(Q), G(r), and the Bragg profile data, the latter to provide a constraint for the long-range crystallinity. S(Q) was broadened by convolution with a box function (chapter 2, equation 2.38), in order to reflect the finite size of the simulation box. A set of 10 parallel calculations was carried out to ensure satisfactory statistics.

4.2.3 Electrical measurements

For electrical measurements, the powders were finely ground in a mortar and pestle, pressed uniaxially into cylindrical pellets of approximate dimensions 11 mm diameter and 2 mm thick, by applying a pressure of 180 MPa and then sintered in air at 1600 °C for 12 h. Sintered pellets had densities of ~ 93 % of the theoretical value, **Table 4.2a**, as determined by the Archimedes method. The samples were prepared as rectangular blocks, **Table 4.2b**, cut from slowly cooled sintered pellets, using a diamond saw. Platinum electrodes were sputtered by cathodic discharge on the two smallest faces. Electrical measurements were carried out via a.c. impedance spectroscopy up to *ca*. 850 °C, using a fully automated Solartron 1255/1286 system, in the frequency range from 1 Hz to 5×10^5 Hz. Impedance spectra were acquired over two cycles of heating and cooling at stabilized temperatures. Impedance at each frequency was measured repeatedly until consistency (2% tolerance in drift) was achieved or a maximum number of 25 repeats had been reached.

Table 4.2a Measured pellet densities and theoretical densities for compositions in the $(Nd_{1-x}Ca_x)_2Zr_2O_{7-x}$ system

Composition	$x = 0.10$	$x = 0.20$	$x = 0.30$	$x = 0.40$	$x = 0.50$
Measured density (g cm^{-3})	5.712	5.324	5.150	5.041	5.019
Theoretical density (g cm^{-3})	6.067	5.720	5.521	5.407	5.401
Relative Density (%)	94.1	93.1	93.3	93.2	92.9

Table 4.2b Pellet dimensions for electrical measurements for compositions of $(Nd_{1-x}Ca_x)_2Zr_2O_{7-x}$

Composition	$x = 0.10$	$x = 0.20$	$x = 0.30$	$x = 0.40$	$x = 0.50$
Length (mm)	8.65	9.24	8.45	8.12	8.69
Height (mm)	5.61	6.19	5.34	5.71	4.95
Width (mm)	1.56	1.68	1.86	1.67	1.71
L/A (cm^{-1})[a]	9.87	8.74	8.51	8.52	10.27

[a]Where L/A = Length/(Height × Width)

4.3 Results and discussion

4.3.1 Average structure

Fig. 4.1 shows diffraction patterns of $(Nd_{1-x}Ca_x)_2Zr_2O_{7-x}$ ($0.00 \leq x \leq 0.50$) powders sintered in air at 1350 °C, for 12 h. All of the compositions studied exhibited a single phase with a pyrochlore-type structure. The adoption of a pyrochlore-type structure in these systems can be rationalised based on the fact that the average cation radius ratio of A and B cations, R_A/R_B, is greater than 1.36 (**Table 4.3**).[250,251] In both the X-ray and neutron data, the pyrochlore ordering peaks are seen to weaken, with increasing *x*-value, suggesting greater disorder with increasing calcium content. **Fig. 4.2** shows detail of the X-ray diffraction patterns in the 2θ range 56 to 61°. The $(311)_F/(622)_{Py}$ (where F represents fluorite and Py pyrochlore) peak gradually shifts towards higher 2θ with increasing calcium content, which is attributed to the change in the average ionic radius of the cations on the A site, *i.e.* (1-*x*) Nd^{3+} and *x* Ca^{2+} cations. The narrower peaks of the *x* = 0.0 composition reflect its higher crystallinity. The refined lattice parameters as a function of calcium content are depicted in **Fig. 4.3** and exhibit an approximately linear decrease with increasing calcium content from *x* = 0.00 to *x* = 0.50, which agrees well with Vegard's law [*a*(nm) = 0.5288 + 0.0146*x*]. This is attributed to the substitution of the larger Nd^{3+} cations [ionic radius (8-coordinate) = 1.11 Å] for the smaller Ca^{2+} cations [ionic radius (6-coordinate) = 1.00 Å].[25]

Table 4.3 A/B site average ionic radius ratios in $(Nd_{1-x}Ca_x)_2Zr_2O_{7-x}$ ($0.00 \leq x \leq 0.50$). Ionic radii used were: Nd^{3+} (8-coordinate), 1.11 Å; Ca^{2+} (6-coordinate), 1.00 Å and Zr^{4+} (6-coordinate), 0.72 Å.[25]

Composition	R_A/R_B
x = 0.10	1.526
x = 0.20	1.511
x = 0.30	1.496
x = 0.40	1.481
x = 0.50	1.465

(a)

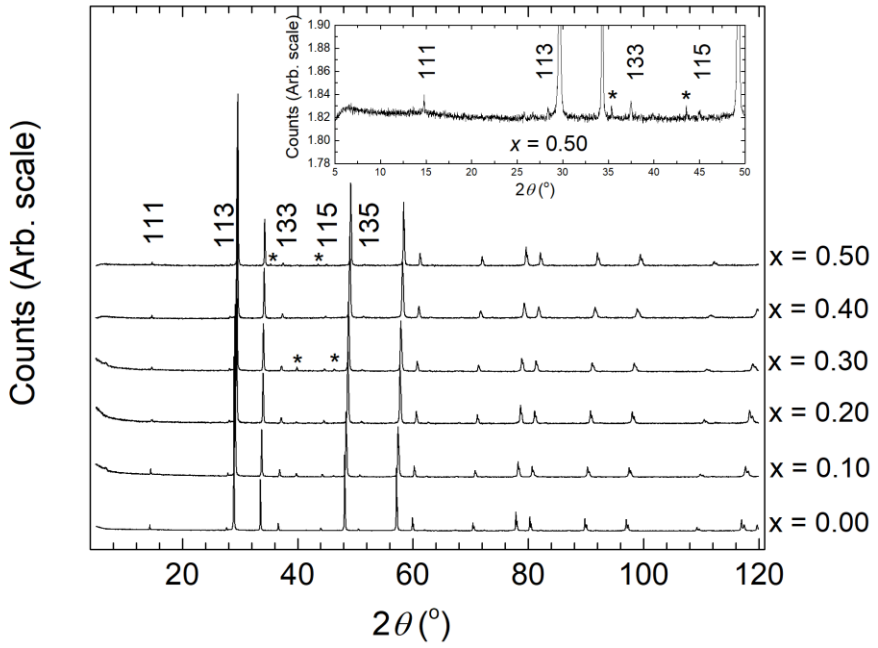

(b)

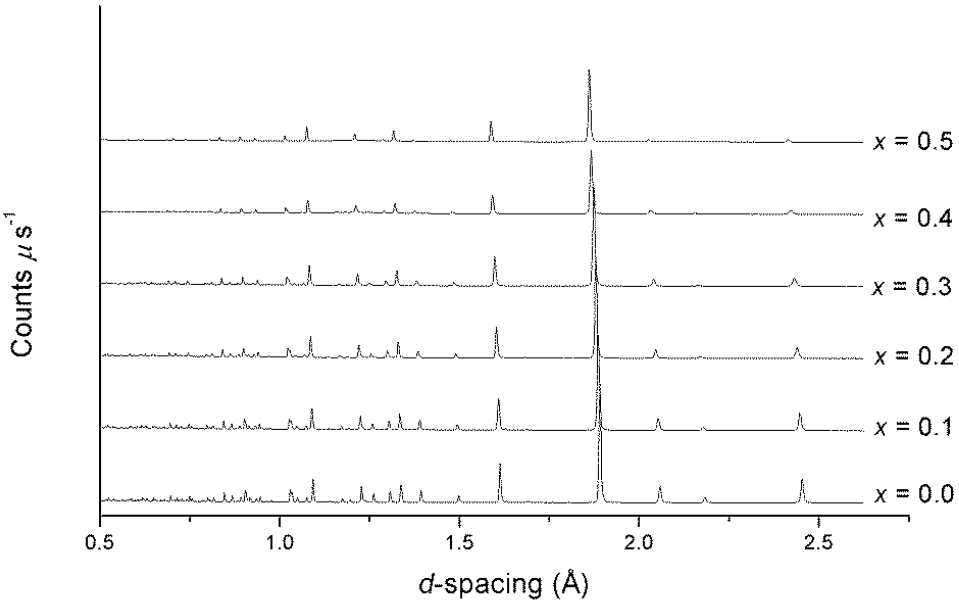

Fig. 4.1. Room temperature powder diffraction patterns for samples of general formula $(Nd_{1-x}Nd_x)_2Zr_2O_{7-x}$ ($0.00 \leq x \leq 0.50$) calcined at 1350 °C, (a) X-ray and (b) neutron back-scattering. Pt peaks from the sample holder are indicated by asterisks in the X-ray data, with indices of the pyrochlore ordering peaks shown in the inset.

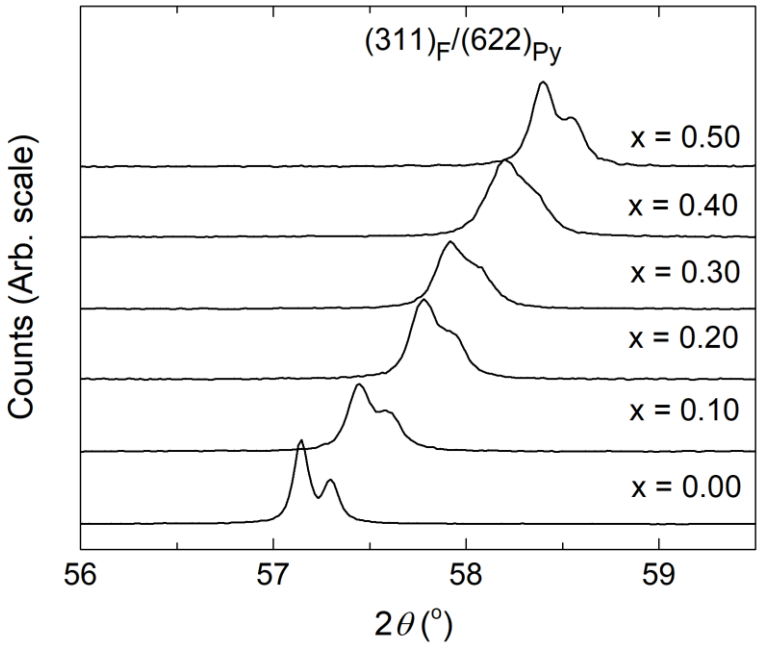

Fig. 4.2. Detail of the room temperature X-ray powder diffraction patterns for samples of general formula $(Nd_{1-x}Ca_x)_2Zr_2O_{7-x}$ ($0.00 \leq x \leq 0.50$), showing the $(311)_F/(622)_{Py}$ peak in the 2θ range of 56-61°.

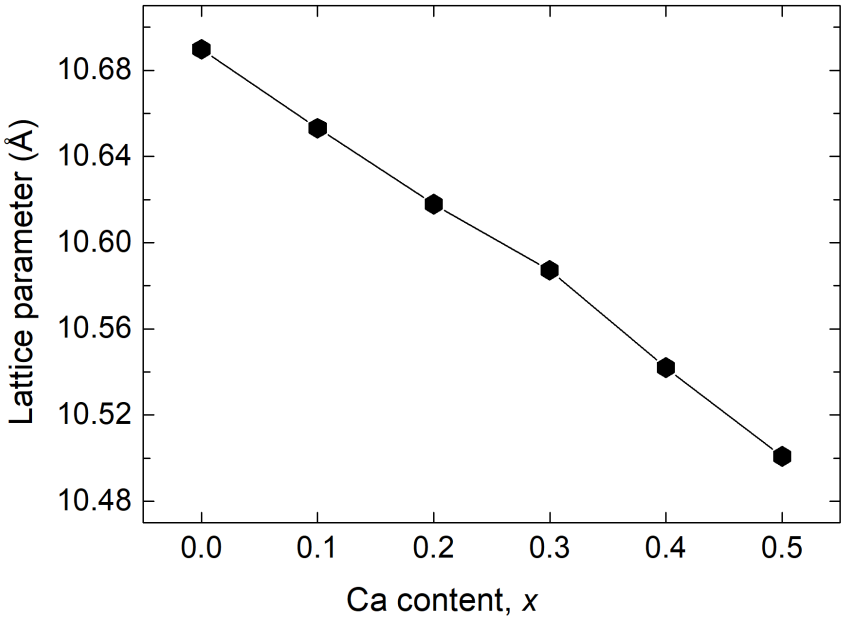

Fig. 4.3. Compositional variation of lattice parameter for co-precipitated samples of composition $(Nd_{1-x}Ca_x)_2Zr_2O_{7-x}$ ($0.00 \leq x \leq 0.50$). Error bars are smaller than the symbols used.

Average crystallite sizes were determined from the peak widths in the X-ray powder diffraction data of the studied compositions, using equation 3.3 (Chapter 3). As shown in **Table 4.4**, there appears to be no significant correlation between composition and the crystallite size and all samples showed good crystallinity.

Table 4.4 Average crystallite size as a function of composition and calcination temperature in $(Yb_{1-x}Nd_x)_2Zr_2O_{7-x}$

Composition	Annealing Temperature (°C)	Lx	Crystallite Size (Å)
$x = 0.00$	1350	4.7(1)	1692
$x = 0.10$	1350	6.3(1)	1258
$x = 0.20$	1350	7.3(2)	1082
$x = 0.30$	1350	6.1(2)	1307
$x = 0.40$	1350	6.3(1)	1268
$x = 0.50$	1350	5.5(2)	1434

The fitted diffraction profiles for a representative composition ($x = 0.5$) at room temperature are shown in **Fig. 4.4**, with those from other compositions given in Appendix B. Good fits to the data were obtained for all compositions. The crystal and refinement parameters for all compositions at room temperature are given in **Table 4.5**, with the refined structural parameters and significant contact distances in **Table 4.6**.

The diffraction data for the $(Nd_{1-x}Ca_x)_2Zr_2O_{7-x}$ ($0.10 \leq x \leq 0.50$) system can be fully indexed in the cubic $Fd\bar{3}m$ space group. Using origin setting 2 (with origin at 0, 0, 0), the Zr^{4+} cations are placed on the 16*c* (0, 0, 0) site, the Nd^{3+} and Ca^{2+} cations are distributed randomly on the 16*d* (1/2, 1/2, 1/2) site, with the oxide ions O(1), O(2), and O(3) distributed over three sites at 48*f* (*ca*. 0.375, 1/8, 1/8), 8*a* (1/8, 1/8, 1/8), and 8*b* (3/8, 3/8, 3/8) sites, respectively. Initial refinements of the oxygen site occupancies showed no appreciable departure away from unity for the O(2) site and subsequent refinements were carried with the O(2) site fully occupied and a total occupancy constraint beteen O(1) and

O(3). Isotropic displacement parameters were refined for all atoms. In all cases, when attempts were made to allow for cation disorder, negative occupancies for the anti-sites were obtained. The best fit was ultimately achieved for a unit cell with complete cation order, but for which the occupancy of the oxygen 8*b* was 1.0, and both the 8*a* and 48*f* oxygen sites are only partially occupied.

The refined structural parameters in **Table 4.6** show that the oxide ions are predominantly located in the 48*f* and 8*b* sites. However, there is also considerable occupation of the 8*a* site, which increases with increasing calcium content. This reflects progressive disorder, evident in the weakening of the pyrochlore ordering peaks with increasing Ca content seen in the diffraction patterns (**Fig. 4.1** above). This type of distribution is common in ordered pyrochlore structures.[252,253] Neodymium and calcium coordinate eight O^{2-} ions in scalenohedra (distorted cubes), with two short bonds to O(2) at approximately 2.29 Å and six longer bonds to O(1) at approximately 2.50 Å. There are also eight contacts to zirconium, in the structure with six bonds to O(1) at approximately 2.10 Å, forming trigonal antiprisms (distorted octahedra), and two longer contacts to O(3) at approximately 2.30 Å.

(a)

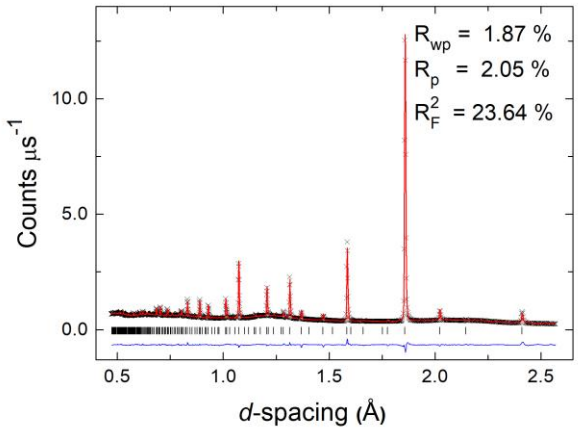

(b)

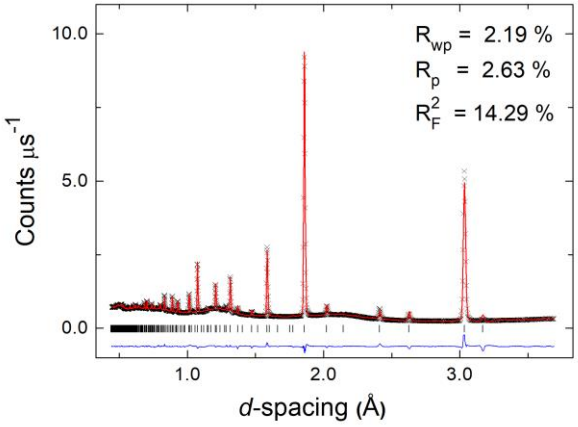

(c)

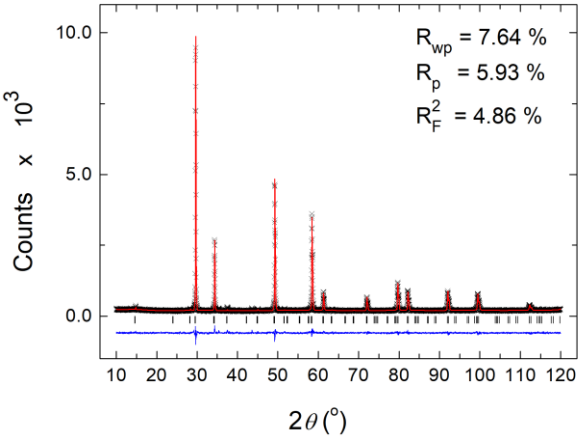

Fig. 4.4. Fitted diffraction profiles for $(Nd_{0.5}Ca_{0.5})_2Zr_2O_{6.5}$ (x = 0.50) at room temperature, showing fits to (a) neutron back-scattering, (b) neutron 90° and (c) X-ray data. Observed (crosses), calculated (solid line), and difference (lower) profiles are shown. Reflection positions are indicated by markers.

Table 4.5. Crystal and refinement parameters for pyrochlore structured compositions in the system $(Nd_{1-x}Ca_x)_2Zr_2O_{7-x}$ ($0.10 \leq x \leq 0.50$) at room temperature. Estimated standard deviations are given in parentheses.

Composition	$x = 0.10$	$x = 0.20$	$x = 0.30$
Calcination temp. (°C)	1350	1350	1350
Formula	$Nd_{1.8}Ca_{0.2}Zr_2O_{6.9}$	$Nd_{1.6}Ca_{0.4}Zr_2O_{6.8}$	$Nd_{1.4}Ca_{0.6}Zr_2O_{6.7}$
M_r (g mol^{-1})	560.49	538.06	515.63
Crystal system	Cubic	Cubic	Cubic
Space group	$Fd\bar{3}m$	$Fd\bar{3}m$	$Fd\bar{3}m$
Lattice parameter (Å)	10.6532(2)	10.6179(3)	10.5873(3)
Volume (Å^3)	1209.0(1)	1197.1(9)	1186.7(1)
Z	8	8	8
D_{calc} (g cm^{-3})	6.176	6.006	5.826
R-factors:			
Neutron back scattering	$R_{wp} = 0.0217$	$R_{wp} = 0.0278$	$R_{wp} = 0.0290$
	$R_p = 0.0250$	$R_p = 0.0347$	$R_p = 0.0346$
	$R_{ex} = 0.0055$	$R_{ex} = 0.0055$	$R_{ex} = 0.0057$
	$R_F2 = 0.0739$	$R_F2 = 0.1205$	$R_F2 = 0.1370$
Neutron 90°	$R_{wp} = 0.0220$	$R_{wp} = 0.0302$	$R_{wp} = 0.0326$
	$R_p = 0.0281$	$R_p = 0.0359$	$R_p = 0.0369$
	$R_{ex} = 0.0052$	$R_{ex} = 0.0053$	$R_{ex} = 0.0054$
	$R_F2 = 0.0558$	$R_F2 = 0.1003$	$R_F2 = 0.1085$
X-ray	$R_{wp} = 0.0769$	$R_{wp} = 0.0794$	$R_{wp} = 0.0809$
	$R_p = 0.0563$	$R_p = 0.0619$	$R_p = 0.0621$
	$R_{ex} = 0.0570$	$R_{ex} = 0.0614$	$R_{ex} = 0.0550$
	$R_F2 = 0.0712$	$R_F2 = 0.0757$	$R_F2 = 0.0759$
Totals	$R_{wp} = 0.0235$	$R_{wp} = 0.0303$	$R_{wp} = 0.0324$
	$R_p = 0.0560$	$R_p = 0.0616$	$R_p = 0.0619$
χ^2	7.59	12.19	13.37
Total no. of variables	115	115	115
No. of profile points:			
Neutron back scattering	1991	1991	1991
Neutron 90°	2116	2116	2116
X-ray	6581	6582	6582
Total	10688	10689	10689
No. of reflections:			
Neutron back scattering	781	779	771
Neutron 90°	406	403	397
X-ray	126	124	122

Table 4.5. Continued

Composition	$x = 0.40$	$x = 0.50$
Calcination temp. (°C)	1350	1350
Formula	$Nd_{1.2}Ca_{0.8}Zr_2O_{6.6}$	$NdCaZr_2O_{6.5}$
M_r (g mol^{-1})	493.19	470.76
Crystal system	Cubic	Cubic
Space group	$Fd\bar{3}m$	$Fd\bar{3}m$
Lattice parameter (Å)	10.5408(3)	10.5008(4)
Volume (Å^3)	1171.2(1)	1157.9(1)
Z	8	8
D_{calc} (g cm^{-3})	5.667	5.493
R-factors:		
Neutron back scattering	$R_{wp} = 0.0205$	$R_{wp} = 0.0187$
	$R_p = 0.0231$	$R_p = 0.0205$
	$R_{ex} = 0.0057$	$R_{ex} = 0.0026$
	$R_F2 = 0.2071$	$R_F2 = 0.2364$
Neutron 90°	$R_{wp} = 0.0224$	$R_{wp} = 0.0219$
	$R_p = 0.0263$	$R_p = 0.0263$
	$R_{ex} = 0.0054$	$R_{ex} = 0.0026$
	$R_F2 = 0.1193$	$R_F2 = 0.1429$
X-ray	$R_{wp} = 0.0741$	$R_{wp} = 0.0764$
	$R_p = 0.0582$	$R_p = 0.0593$
	$R_{ex} = 0.0590$	$R_{ex} = 0.0638$
	$R_F2 = 0.0617$	$R_F2 = 0.0486$
Totals	$R_{wp} = 0.0231$	$R_{wp} = 0.0208$
	$R_p = 0.0579$	$R_p = 0.0589$
χ^2	6.83	24.52
Total no. of variables	115	115
No. of profile points:		
Neutron back scattering	1991	1991
Neutron 90°	2116	2116
X-ray	6582	6581
Total	10689	10688
No. of reflections:		
Neutron back scattering	769	758
Neutron 90°	392	386
X-ray	122	122

Table 4.6. Refined atomic parameters and significant contact distances for compositions in the system $(Nd_{1-x}Ca_x)_2Zr_2O_{7-x}$ at room temperature. Estimated standard deviations are given in parentheses.

Composition	$x = 0.10$	$x = 0.20$	$x = 0.30$	$x = 0.40$	$x = 0.50$
Ca/Nd site	16*d*	16*d*	16*d*	16*d*	16*d*
Ca/Nd *x,y,z*	0.5	0.5	0.5	0.5	0.5
Ca/Nd Occ.	0.1/0.9	0.2/0.8	0.3/0.7	0.4/0.6	0.5/0.5
Zr site	16*c*	16*c*	16*c*	16*c*	16*c*
Zr *x,y,z*	0.0	0.0	0.0	0.0	0.0
Zr Occ.	1.0	1.0	1.0	1.0	1.0
Ca/Nd/Zr U_{iso} ($Å^2$)	0.00702(5)	0.00887(8)	0.01021	0.0118(1)	0.0131(1)
O(1) site	48*f*	48*f*	48*f*	48*f*	48*f*
O(1) *x*	0.33665(3)	0.33961(4)	0.34205(5)	0.34597(7)	0.35218(9)
O(1) y,z	0.125	0.125	0.125	0.125	0.125
O(1) Occ.	0.983(1)	0.960(1)	0.939(1)	0.915(1)	0.890(1)
O(1) U_{iso} ($Å^2$)	0.01239(7)	0.0177(1)	0.0219(2)	0.0289(3)	0.0384(3)
O(2) site	8*b*	8*b*	8*b*	8*b*	8*b*
O(2) *x,y,z*	0.375	0.375	0.375	0.375	0.375
O(2) Occ.	1.0	1.0	1.0	1.0	1.0
O(2) U_{iso} ($Å^2$)	0.0067(1)	0.0130(2)	0.0194(3)	0.0283(4)	0.0358(6)
O(3) site	8*a*	8*a*	8*a*	8*a*	8*a*
O(3) *x,y,z*	0.125	0.125	0.125	0.125	0.125
O(3) Occ.	0.099(3)	0.238(4)	0.364(5)	0.508(7)	0.658(9)
O(3) U_{iso} ($Å^{2)}$	0.0067(1)	0.0130(2)	0.0194(3)	0.0283(4)	0.0358(6)
Ca/Nd-O(1) (Å)	2.5641(2)	2.5344(3)	2.5098(4)	2.4715(5)	2.4197(6)
Ca/Nd-O(2) (Å)	2.30648(3)	2.29885(4)	2.29221(5)	2.28215(4)	2.27349(6)
Zr-O(1) (Å)	2.0973(1)	2.1044(2)	2.1101(3)	2.1202(4)	2.1441(5)
Zr-O(3) (Å)	2.30648(3)	2.29885(4)	2.29221(5)	2.28215(4)	2.27349(6)
Nd/Ca-O wt. av. (Å)	2.499(1)	2.474(1)	2.453(1)	2.421(1)	2.380(1)
Zr-O wt. av. (Å)	2.104(2)	2.119(2)	2.131(3)	2.145(3)	2.170(4)

Taking into account the partial occupancies of O(1) and O(3) sites, the average coordination numbers for Nd^{3+}/Ca^{2+} and Zr^{4+} can be calculated (**Table 4.7**). The average Nd^{3+}/Ca^{2+} coordination number decreases and that of Zr^{4+} increases with increasing calcium content. This reflects the increasing number of oxygen Frenkel defects, as oxide ions on the O(1) site are displaced onto the O(3) site.

From the values in **Table 4.7**, it is possible to speculate on the local coordination of Ca^{2+} and Nd^{3+}. If the system showed an ideal pyrochlore structure, where O(1) and O(2) were fully occupied and O(3) was vacant, there would be a 1:3:0.5 ratio of Nd/Ca:O(1):O(2) atoms in the cell, giving a coordination number of 8 for ions on the A site. As seen in **Table 4.7**, the observed A-site coordination number is lower than this figure. If it is assumed that all Nd^{3+} cations do indeed adopt eight-coordination, as is found to be close to the case in the unsubstituted system $Nd_2Zr_2O_7$ (x = 0.0, Chapter 3, Table 3.12), then it is possible to calculate the coordination number of calcium.

Taking the x = 0.1 composition as an example, there are 14.4 Nd^{3+}, 1.6 Ca^{2+} ions per cell, with 47.184 O^{2-} ions in the O(1) site and 8 in the O(2) site. To achieve eight-coordination for all the Nd^{3+} cations requires 43.2 oxide ions on the O(1) site (*i.e.* 14.4 × 3) and 7.2 on the O(2) site (*i.e.* 14.4 × 0.5). This leaves 3.984 O(1) and 0.8 O(2) oxide ions to coordinate to 1.6 Ca^{2+} ions per cell giving 2.49 O(1) and 0.5 O(2) oxide ions per Ca^{2+}. The observed ratio Ca:O(1):O(2) of 1:2.49:0.5 is approximately halfway between the ideal eight coordinate ratio 1:3:0.5 and that for six coordination of 1:2:0.5. Since each O(1) bonds to 2 Nd^{3+}/Ca^{2+} ions (and 2 Zr^{4+} ions) and O(2) bonds exclusively to 4 Nd^{3+}/Ca^{2+}, this gives a coordination number of 6.98 (*i.e.* 2 × 2.49 + 4 × 0.5) for Ca^{2+}. As seen in **Table 4.7**, calcium coordination number is seen to decrease somewhat with increasing x-value. The cation coordination environments are illustrated in **Fig. 4.5**.

Table 4.7. Average cation coordination numbers (CN) in the $(Nd_{1-x}Ca_x)_2Zr_2O_{7-x}$ system at room temperature. Those for Ca^{2+} are based on the assumption of eight-coordinate geometry for Nd^{3+}.

Cation	x = 0.10	x = 0.20	x = 0.30	x = 0.40	x = 0.50
Nd^{3+}/Ca^{2+} CN	7.90	7.76	7.63	7.49	7.34
Zr^{4+} CN	6.10	6.24	6.36	6.50	6.66
Nd^{3+} CN	8	8	8	8	8
Ca^{2+} CN	6.98	6.80	6.78	6.73	6.68

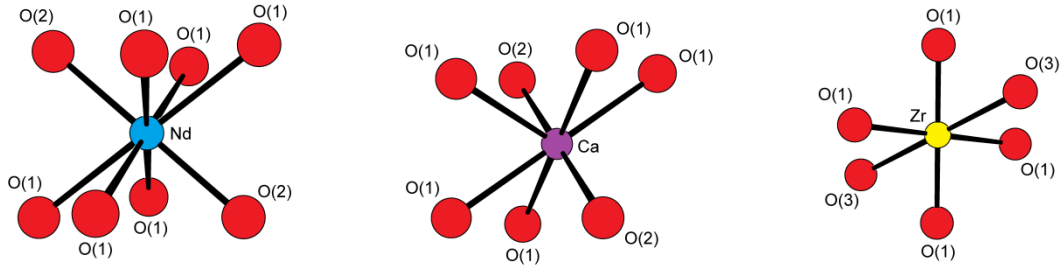

(a) **(b)** **(c)**

Fig. 4.5. Cation site coordination in $(Nd_{1-x}Ca_x)_2Zr_2O_{7-x}$; (a) Nd^{3+} (b) Zr^{4+} and (c) Ca^{2+}. Results for the x = 0.1 composition at room temperature were used to generate the images.

Fig. 4.6a shows the compositional variation of M-O distances as a function of composition. Nd/Ca-O(1) and M-O(2/3) decrease with increasing x-value. In the case of the M-O(2)/3 distance this reflects the decreasing unit cell volume. However, in the case of the M-O(1) distances, the unit cell contraction does not account fully for the observed decrease. As seen in Chapter 3, the distance between O(1) and the centre of the tetrahedral site at 0.375, 0.125, 0.125 (**Fig. 4.6b**) reveals the underlying trend of a curved decrease in this distance, indicating reduced cation site distortion, with increasing calcium content.

The thermal behaviour of this system was studied by variable-temperature XRD and neutron diffraction, from ambient temperature to 800 °C. **Fig. 4.7a** and **Fig. 4.8** show X-ray and neutron powder diffraction patterns for the x = 0.5 composition which are representative (the rest of the diffraction patterns are given in Appendix A). The patterns show that the pyrochlore structure is maintained throughout the temperature range studied, which was repeated across the compositional range explored. **Fig. 4.7b** shows detail of XRD patterns for the x = 0.50 at the studied temperatures in the 2θ range of 28° to 35°. It can be observed that as the temperature increases, the reflections progressively move towards lower angles as the crystal lattice expands.

(a)

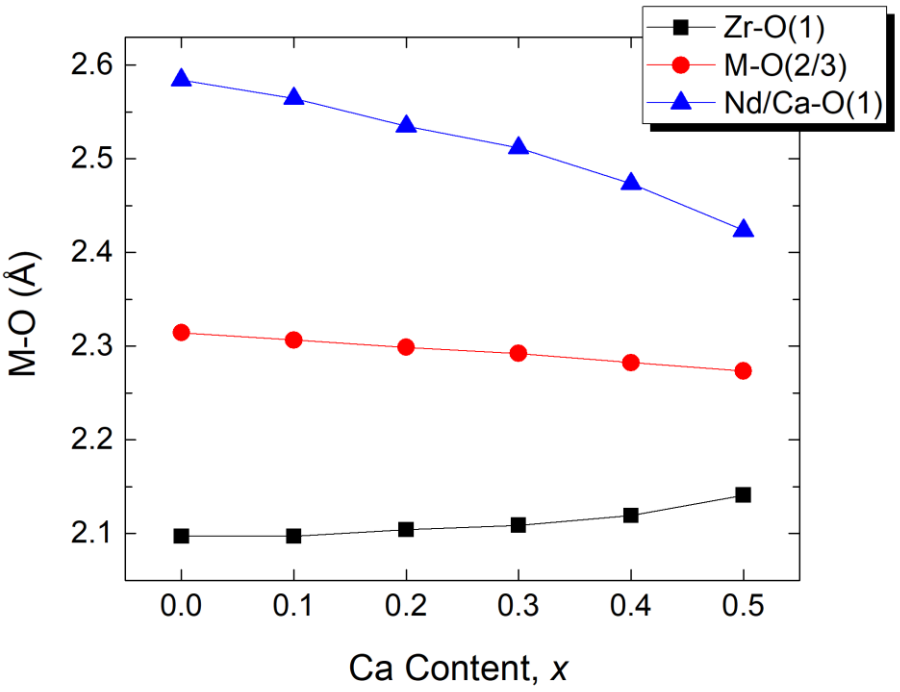

(b)

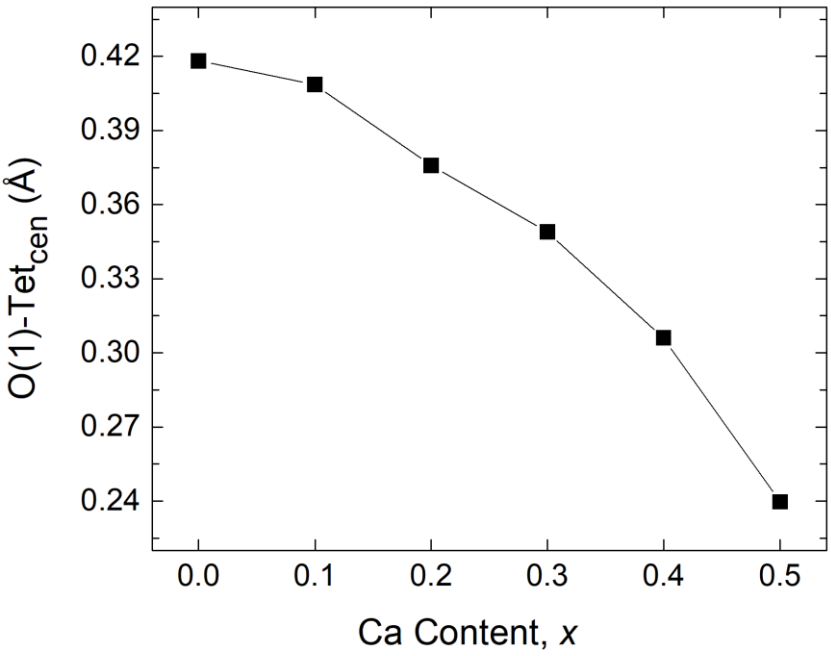

Fig. 4.6. Compositional variation of (a) M-O distances and (b) the displacement of the O(1) site from the ideal tetrahedral site centre in $(Nd_{1-x}Ca_x)_2Zr_2O_{7-x}$ ($0.00 \leq x \leq 0.50$). Error bars are smaller than the symbols used.

(a)

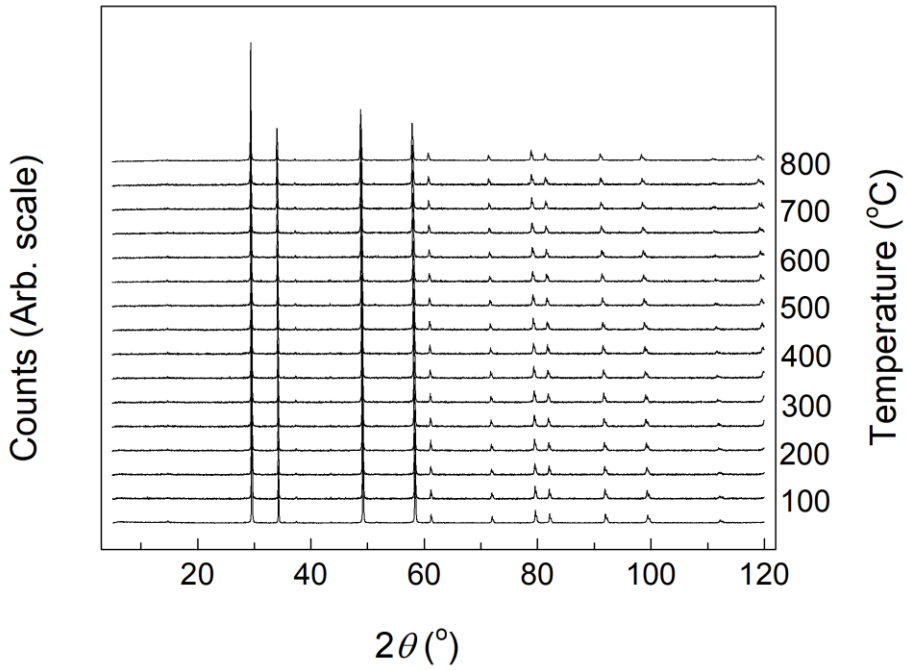

(b)

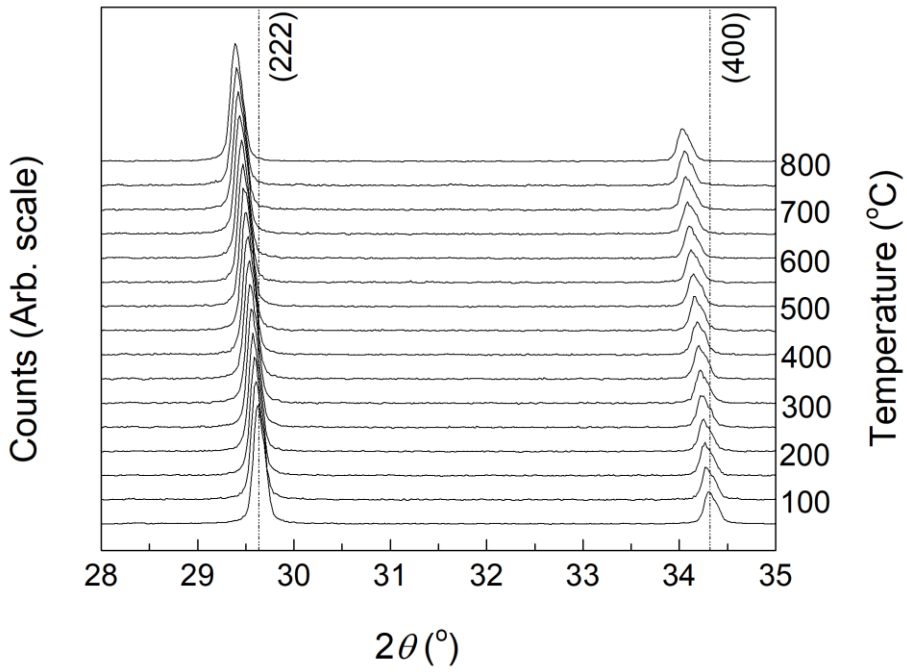

Fig. 4.7. Variable temperature X-ray powder diffraction data for $(Nd_{0.5}Ca_{0.5})_2Zr_2O_{6.5}$ (x = 0.50) from room temperature to 800 °C, showing (a) full patterns and (b) detail of the 222 and 400 Bragg peaks.

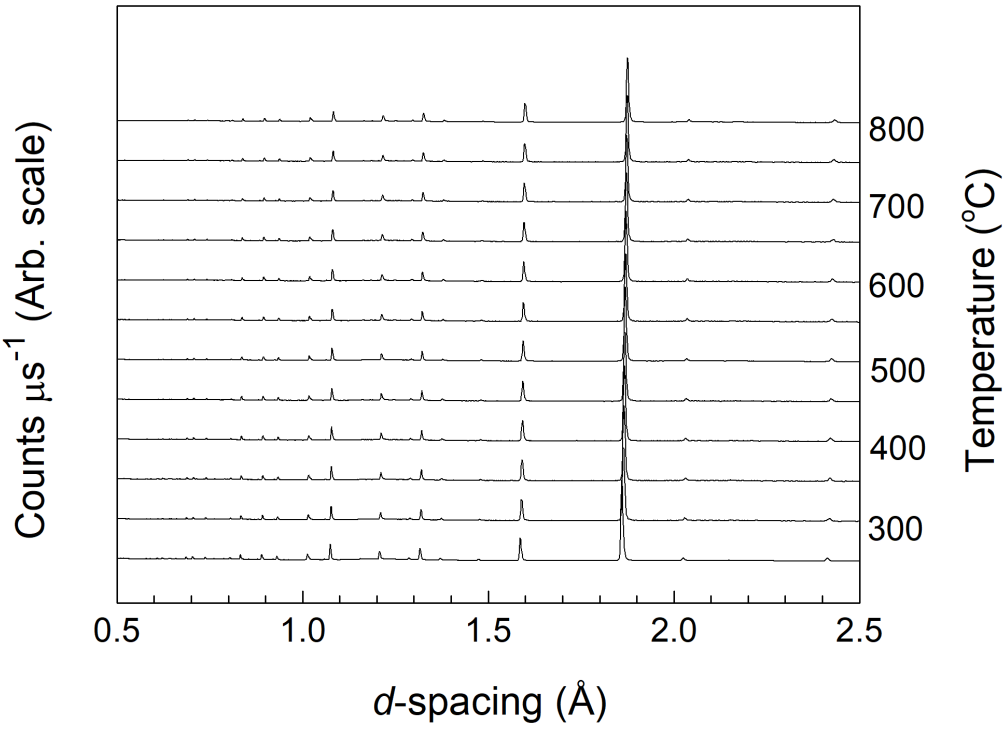

Fig. 4.8. Powder neutron diffraction data for $(Nd_{0.5}Ca_{0.5})_2Zr_2O_{6.5}$ (x = 0.5) at selected temperatures up to 800 °C.

The thermal variation of the cubic lattice parameter for the studied compositions is shown in **Fig. 4.9,** for both heating and cooling. The lattice parameter of each sample shows a linear increase with increasing temperature, as was indicated by the qualitative inspection of their XRD and neutron diffraction patterns in **Fig. 4.7** and **Fig. 4.8** above, with little difference between heating and cooling plots.

The diffraction patterns at 800 °C are plotted in **Fig. 4.10**. The plots show no apparent changes from the room temperature plots shown in **Fig. 4.1b** above, other than a thermal expansion. The fitted diffraction profiles for the x = 0.5 composition at 800 °C are shown in **Fig. 4.11**, with those for the other studied compositions given in Appendix B. The crystal and refinement parameters for all the studied compositions at 800 °C are given in **Table 4.8**, with the refined structural parameters and significant contact distances in **Table 4.9**.

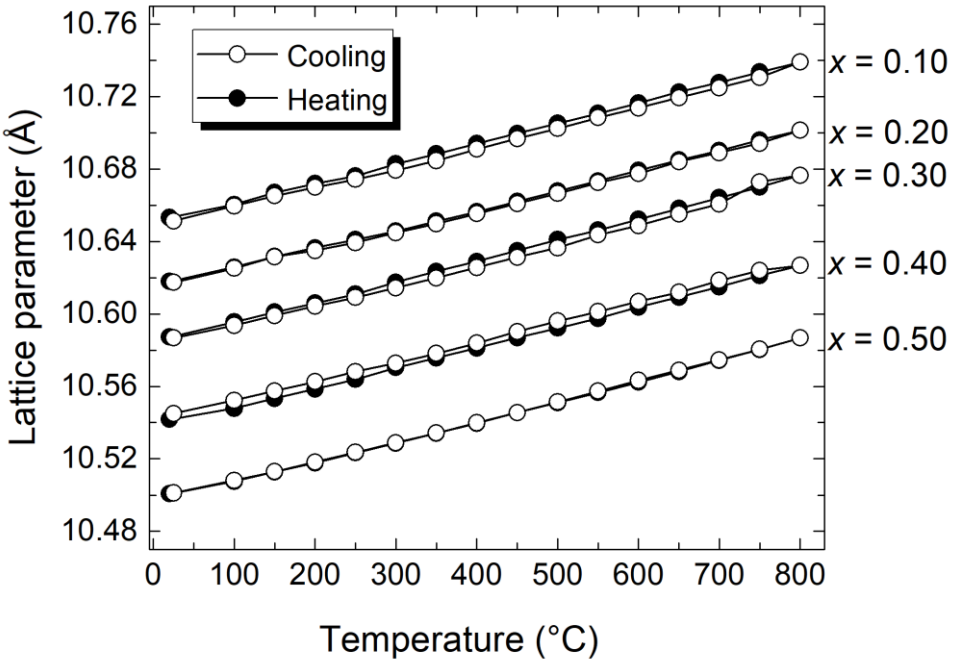

Fig. 4.9. Thermal variation of cubic lattice parameter for $(Nd_{1-x}Ca_x)_2Zr_2O_{7-x}$($0.10 \leq x \leq 0.50$)

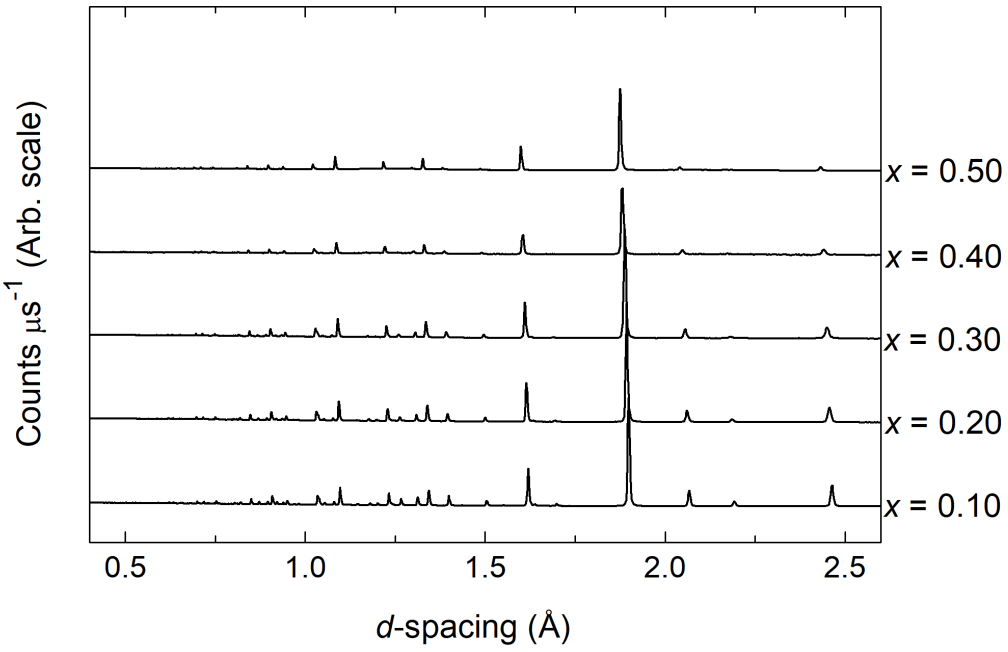

Fig. 4.10. Neutron diffraction patterns for $(Nd_{1-x}Ca_x)_2Zr_2O_{7-x}$ at 800 °C.

The diffraction data for the $(Nd_{1-x}Ca_x)_2Zr_2O_{7-x}$ ($0.10 \leq x \leq 0.50$) system at 800 °C can be fully indexed in the cubic $Fd\bar{3}m$ space group, as for the room temperature diffraction data above. In all cases, when attempts were made to allow for cation disorder, negative occupancies for the anti-sites were obtained. The best fit was ultimately achieved for a unit cell with complete cation order, but for which the occupancy of the oxygen 8*b* was 1.0, and both the 8*a* and 48*f* oxygen sites were only partially occupied.

The refined structural parameters are given in **Table 4.9** and show that the oxide ions are predominantly located in the 48*f* and 8*b* sites, as was seen in the room temperature data above. However, there is a slight increase in the occupancy of the 48*f* sites and a slight decrease in that of the 8*a* sites at 800 °C, compared to those of the same composition at room temperature, indicating a more ordered anion sub-lattice at 800 °C. Both the weighted average Nd/Ca-O and Zr-O distances increase in going from room temperature to 800 °C for the same composition.

(a)

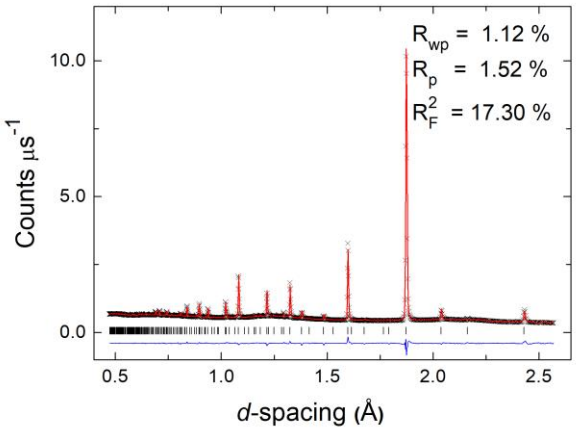

(b)

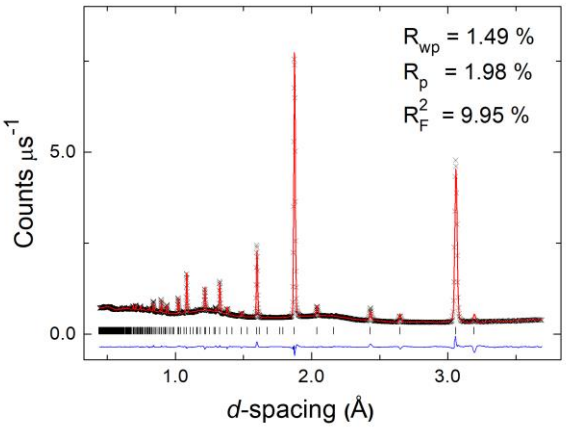

(c)

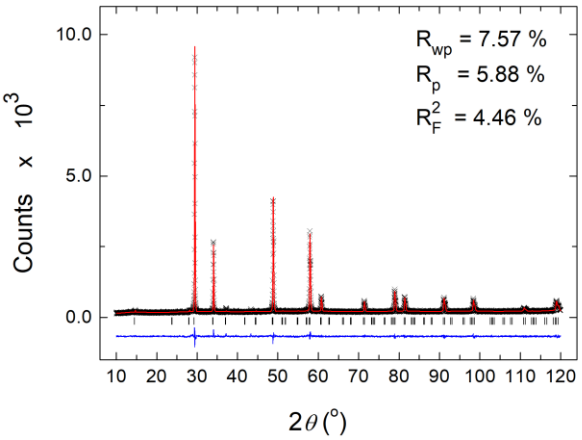

Fig. 4.11. Fitted diffraction profiles for $(Nd_{0.5}Ca_{0.5})_2Zr_2O_{6.5}$ (x = 0.50) at 800 °C, showing fits to (a) neutron back-scattering, (b) neutron 90° and (c) X-ray data. Observed (crosses), calculated (solid line), and difference (lower) profiles of are shown. Reflection positions are indicated by markers.

Table 4.8. Crystal and refinement parameters for pyrochlore structured compositions in the system $(Nd_{1-x}Ca_x)_2Zr_2O_{7-x}$ ($0.10 \leq x \leq 0.50$) at 800 °C. Estimated standard deviations are given in parentheses.

Composition	$x = 0.10$	$x = 0.20$	$x = 0.30$
Calcination temp. (°C)	1350	1350	1350
Formula	$Nd_{1.8}Ca_{0.2}Zr_2O_{6.9}$	$Nd_{1.6}Ca_{0.4}Zr_2O_{6.8}$	$Nd_{1.4}Ca_{0.6}Zr_2O_{6.7}$
M_r (g mol^{-1})	560.49	538.06	515.63
Crystal system	Cubic	Cubic	Cubic
Space group	$Fd\bar{3}m$	$Fd\bar{3}m$	$Fd\bar{3}m$
Lattice parameter (Å)	10.7390(2)	10.7012(2)	10.6745(3)
Volume (Å^3)	1238.5(1)	1225.5(1)	1216.3(1)
Z	8	8	8
D_{calc} (g cm^{-3})	6.029	5.867	5.684
R-factors:			
Neutron back scattering	$R_{wp} = 0.0168$	$R_{wp} = 0.0171$	$R_{wp} = 0.0174$
	$R_p = 0.0220$	$R_p = 0.0242$	$R_p = 0.0242$
	$R_{ex} = 0.0057$	$R_{ex} = 0.0055$	$R_{ex} = 0.0056$
	$R_F2 = 0.1014$	$R_F2 = 0.1189$	$R_F2 = 0.1577$
Neutron 90°	$R_{wp} = 0.0203$	$R_{wp} = 0.0218$	$R_{wp} = 0.0232$
	$R_p = 0.0247$	$R_p = 0.0289$	$R_p = 0.0308$
	$R_{ex} = 0.0054$	$R_{ex} = 0.0052$	$R_{ex} = 0.0053$
	$R_F2 = 0.0792$	$R_F2 = 0.1029$	$R_F2 = 0.1220$
X-ray	$R_{wp} = 0.0792$	$R_{wp} = 0.0820$	$R_{wp} = 0.0754$
	$R_p = 0.0583$	$R_p = 0.0648$	$R_p = 0.0592$
	$R_{ex} = 0.0584$	$R_{ex} = 0.0633$	$R_{ex} = 0.0566$
	$R_F2 = 0.0527$	$R_F2 = 0.0468$	$R_F2 = 0.0733$
Totals	$R_{wp} = 0.0209$	$R_{wp} = 0.0215$	$R_{wp} = 0.0225$
	$R_p = 0.0579$	$R_p = 0.0643$	$R_p = 0.0589$
χ^2	5.58	6.35	6.76
Total no. of variables	115	115	115
No. of profile points:			
Neutron back scattering	1991	1991	1991
Neutron 90°	2116	2116	2116
X-ray	6582	6582	6582
Total	10689	10689	10689
No. of reflections:			
Neutron back scattering	805	794	787
Neutron 90°	416	412	409
X-ray	128	126	126

Table 4.8. Continued

Composition	$x = 0.40$	$x = 0.50$
Calcination temp. (°C)	1350	1350
Formula	$Nd_{1.2}Ca_{0.8}Zr_2O_{6.6}$	$NdCaZr_2O_{6.5}$
M_r (g mol^{-1})	493.19	470.76
Crystal system	Cubic	Cubic
Space group	$Fd\bar{3}m$	$Fd\bar{3}m$
Lattice parameter (Å)	10.6256(1)	10.5867(3)
Volume (Å^3)	1199.7(1)	1186.5(1)
Z	8	8
D_{calc} (g cm^{-3})	5.532	5.360
R-factors:		
Neutron back scattering	$R_{wp} = 0.0172$	$R_{wp} = 0.0112$
	$R_p = 0.0270$	$R_p = 0.0152$
	$R_{ex} = 0.0152$	$R_{ex} = 0.0027$
	$R_F2 = 0.1934$	$R_F2 = 0.1730$
Neutron 90°	$R_{wp} = 0.0194$	$R_{wp} = 0.0149$
	$R_p = 0.0307$	$R_p = 0.0198$
	$R_{ex} = 0.0144$	$R_{ex} = 0.0027$
	$R_F2 = 0.1455$	$R_F2 = 0.0995$
X-ray	$R_{wp} = 0.0718$	$R_{wp} = 0.0757$
	$R_p = 0.0554$	$R_p = 0.0588$
	$R_{ex} = 0.0588$	$R_{ex} = 0.0637$
	$R_F2 = 0.0791$	$R_F2 = 0.0446$
Totals	$R_{wp} = 0.0280$	$R_{wp} = 0.0138$
	$R_p = 0.0551$	$R_p = 0.0583$
χ^2	1.54	10.35
Total no. of variables	115	115
No. of profile points:		
Neutron back scattering	1991	1991
Neutron 90°	2116	2116
X-ray	6582	6581
Total	10689	10688
No. of reflections:		
Neutron back scattering	781	777
Neutron 90°	404	403
X-ray	124	122

Table 4.9. Refined atomic parameters and significant contact distances for compositions in the system $(Nd_{1-x}Ca_x)_2Zr_2O_{7-x}$ at 800 °C. Estimated standard deviations are given in parentheses.

Composition	x = 0.10	x = 0.20	x = 0.30	x = 0.40	x = 0.50
Ca/Nd site	16*d*	16*d*	16*d*	16*d*	16*d*
Ca/Nd *x*,*y*,*z*	0.5	0.5	0.5	0.5	0.5
Ca/Nd Occ.	0.1/0.9	0.2/0.8	0.3/0.7	0.4/0.6	0.5/0.5
Zr site	16*c*	16*c*	16*c*	16*c*	16*c*
Zr *x*,*y*,*z*	0.0	0.0	0.0	0.0	0.0
Zr Occ.	1.0	1.0	1.0	1.0	1.0
Ca/Nd/Zr U_{iso} (Å^2)	0.0181(1)	0.0193(1)	0.0199(1)	0.0226(2)	0.0220(1)
O(1) site	48*f*	48*f*	48*f*	48*f*	48*f*
O(1) *x*	0.33510(5)	0.33851(5)	0.34124(6)	0.34535(15)	0.35175(9)
O(1) y,z	0.125	0.125	0.125	0.125	0.125
O(1) Occ.	0.988(1)	0.964(1)	0.945(1)	0.931(2)	0.902(1)
O(1) U_{iso} (Å^2)	0.0306(2)	0.0352(2)	0.0393(3)	0.0499(6)	0.0587(4)
O(2) site	8*b*	8*b*	8*b*	8*b*	8*b*
O(2) *x*,*y*,*z*	0.375	0.375	0.375	0.375	0.375
O(2) Occ.	1.0	1.0	1.0	1.0	1.0
O(2) U_{iso} (Å^2)	0.0164(2)	0.0239(3)	0.0302(4)	0.0389(9)	0.0432(6)
O(3) site	8*a*	8*a*	8*a*	8*a*	8*a*
O(3) *x*,*y*,*z*	0.125	0.125	0.125	0.125	0.125
O(3) Occ.	0.071(3)	0.215(4)	0.328(5)	0.414(9)	0.585(7)
O(3) U_{iso} (Å$^{2)}$	0.0164((2)	0.0239(3)	0.0302(4)	0.0389(9)	0.0432(6)
Ca/Nd-O(1) (Å)	2.59616(33)	2.5623(4)	2.5363(5)	2.4957(11)	2.4425(7)
Ca/Nd-O(2) (Å)	2.32506(3)	2.31688(4)	2.31109(5)	2.30051(2)	2.29208(5)
Zr-O(1) (Å)	2.10691(21)	2.11558(26)	2.12351(32)	2.1342(8)	2.1593(5)
Zr-O(3) (Å)	2.32506(3)	2.31688(4)	2.31109(5)	2.30051(2)	2.29208(5)
Nd/Ca-O wt. av. (Å)	2.528(4)	2.499(5)	2.478(6)	2.444(10)	2.402(8)
Zr-O wt. av. (Å)	2.112(4)	2.130(5)	2.143(6)	2.156(10)	2.183(8)

The cation coordination numbers at 800 °C derived from the Rietveld analysis are shown in **Table 4.10**. Those for Ca^{2+} are based on the assumption that Nd^{3+} adopts eight fold coordination. The average Nd^{3+}/Ca^{2+} coordination number decreases and that of Zr^{4+} increases with increasing calcium content, as was seen in the room temperature data. However, the Nd^{3+}/Ca^{2+} coordination numbers at 800 °C are consistently higher than those at room temperature, whereas the Zr^{4+} coordination numbers are consistently lower, indicating the cation sub-lattice to be more pyrochlore-like at 800 °C than at room temperature.

Table 4.10. Average cation coordination numbers (CN) in the $(Nd_{1-x}Ca_x)_2Zr_2O_{7-x}$ system at 800°C. Those for Ca^{2+} are based on the assumption of eight-coordinate geometry for Nd^{3+}.

Cation	$x = 0.10$	$x = 0.20$	$x = 0.30$	$x = 0.40$	$x = 0.50$
Nd^{3+}/Ca^{2+} CN	7.93	7.78	7.67	7.59	7.41
Zr^{4+} CN	6.07	6.21	6.33	6.41	6.58
Nd^{3+} CN	8	8	8	8	8
Ca^{2+} CN	7.28	6.92	6.90	6.87	6.82

A high quality neutron diffraction data set was collected on the $x = 0.5$ composition, at 500 °C for total scattering analysis. Prior to the RMC analysis, the data were modelled using conventional Rietveld analysis. The fitted diffraction profiles for this composition at 500 °C are shown in **Fig. 4.12**, with the crystal and refinement parameters given in **Table 4.11** and the refined structural parameters in **Table 4.12**. The occupancy of the 48*f* sites at 500 °C is higher than the corresponding values at room temperature, but lower than those at 800 °C. The occupancy of the 8*a* sites at 500 °C is lower than the corresponding values at room temperature, but higher than those at 800 °C. This reflects an anion sub-lattice that is intermediate between room temperature and 800 °C, as would be expected. The weighted average Nd/Ca-O and Zr-O bond distances at 500 °C are also intermediate to those at room temperature and those at 800 °C.

(a)

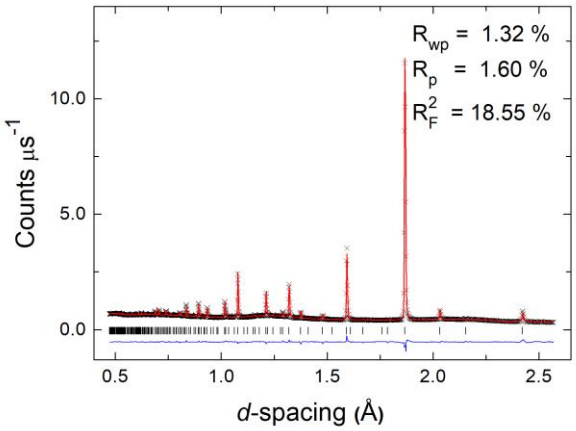

(b)

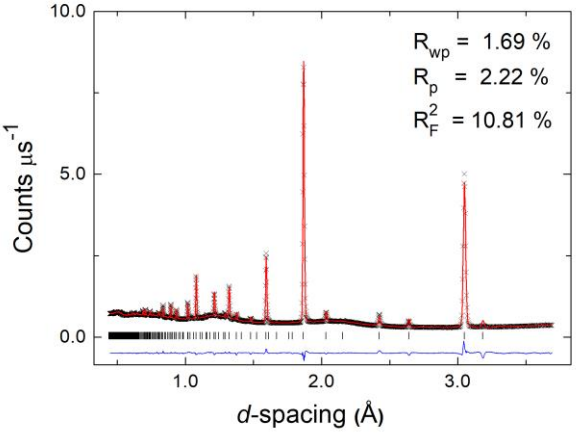

(c)

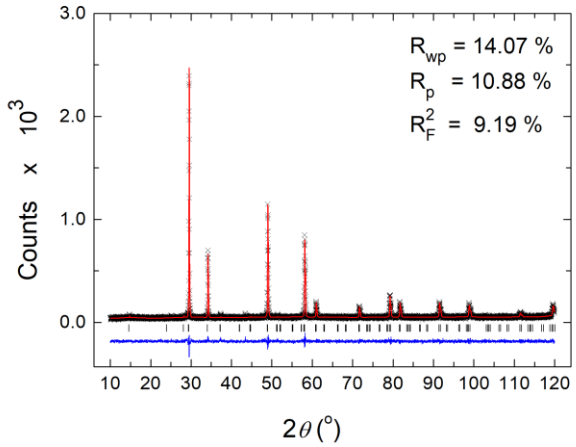

Fig. 4.12. Fitted diffraction profiles for $(Nd_{0.5}Ca_{0.5})_2Zr_2O_{6.5}$ (x = 0.50) at 500 °C, showing fits to (a) neutron back-scattering, (b) neutron 90° and (c) X-ray data. Observed (crosses), calculated (solid line), and difference (lower) profiles of are shown. Reflection positions are indicated by markers.

Table 4.11. Crystal and refinement parameters for $(Nd_{0.5}Ca_{0.5})_2Zr_2O_{6.5}$ at 500 °C. Estimated standard deviations are given in parentheses.

Composition	$x = 0.50$
Calcination temp. (°C)	1350
Formula	$NdCaZr_2O_{6.5}$
M_r (g mol^{-1})	470.76
Crystal system	Cubic
Space group	$Fd\bar{3}m$
Lattice parameter (Å)	10.5511(6)
Volume (Å^3)	1174.6(2)
Z	8
D_{calc} (g cm^{-3})	5.415
R-factors:	
Neutron back scattering	$R_{wp} = 0.0132$ $R_p = 0.0160$ $R_{ex} = 0.0027$ $R_F2 = 0.1855$
Neutron 90°	$R_{wp} = 0.0169$ $R_p = 0.0222$ $R_{ex} = 0.0027$ $R_F2 = 0.1081$
X-ray	$R_{wp} = 0.1407$ $R_p = 0.1088$ $R_{ex} = 0.1272$ $R_F2 = 0.0919$
Totals	$R_{wp} = 0.0157$ $R_p = 0.1048$ $\chi^{2\,=}13.31$
Total no. of variables	115
No. of profile points:	
	Neutron back scattering 1991 Neutron 90° 2116 X-ray 6581 Total 10688
No. of reflections:	Neutron back scattering 769 Neutron 90° 397 X-ray 122

Table 4.12. Refined atomic parameters and significant contact distances for compositions in the system $(Nd_{1-x}Ca_x)_2Zr_2O_{7-x}$ at 500 °C. Estimated standard deviations are given in parentheses.

Composition	$x = 0.50$	O(2) site	8*b*
Ca/Nd site	16*d*	O(2) *x,y,z*	0.375
Ca/Nd *x,y,z*	0.5	O(2) Occ.	1.0
Ca/Nd Occ.	0.5/0.5	O(2) U_{iso} (Å^2)	0.0402(5)
Zr site	16*c*	O(3) site	8*a*
Zr *x,y,z*	0.0	O(3) *x,y,z*	0.125
Zr Occ.	1.0	O(3) Occ.	0.617(8)
Ca/Nd/Zr U_{iso} (Å^2)	0.0182(1)	O(3) U_{iso} (Å$^{2)}$	0.0402(5)
O(1) site	48*f*		
O(1) *x*	0.35187(9)		
O(1) y,z	0.125		
O(1) Occ.	0.897(1)		
O(1) U_{iso} (Å^2)	0.0500(4)		
Ca/Nd-O(1) (Å)	2.4334(6)	Zr-O(1) (Å)	2.1527(5)
Ca/Nd-O(2) (Å)	2.28438(10)	Zr-O(3) (Å)	2.28438(10)
Nd/Ca-O wt. av. (Å)	2.400(1)	Zr-O wt. av. (Å)	2.177(8)

4.3.2 Local structure

G(r) profiles for $(Nd_{0.5}Ca_{0.5})_2Zr_2O_{6.5}$ (x = 0.50), at 20, 500, and 800 °C are shown in **Fig. 4.13**. A gradual evolution of the pattern is seen, as the temperature increases, reflecting the structural evolution with temperature.

(a)

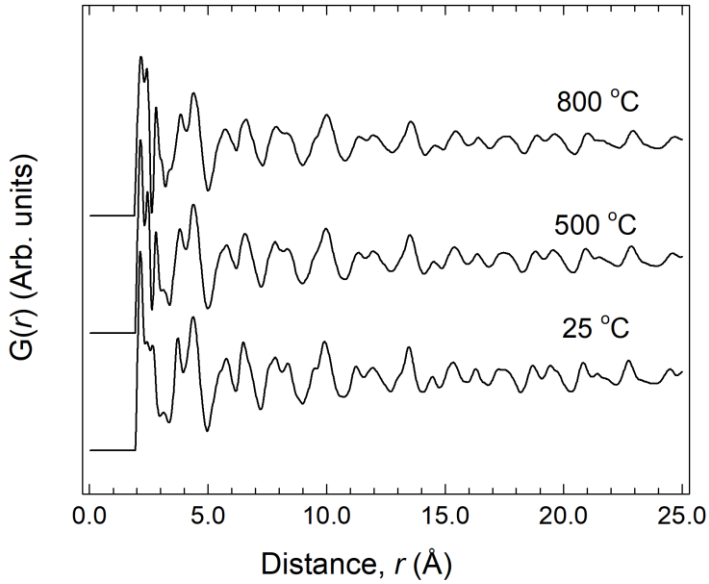

(b)

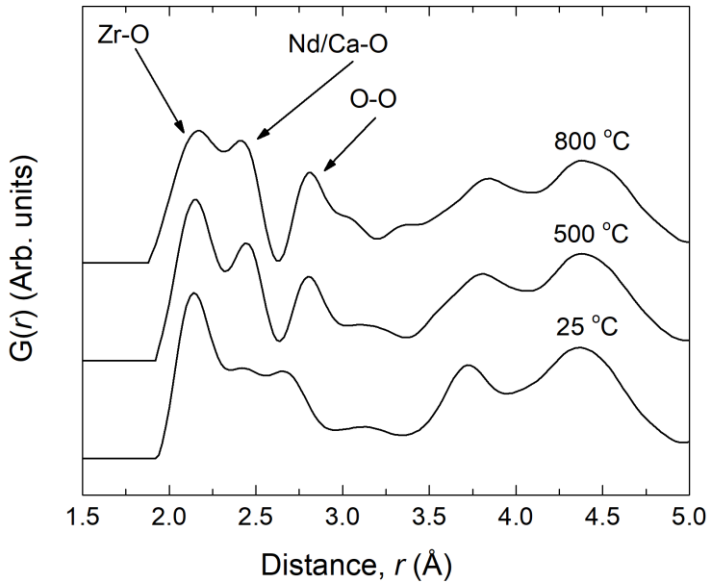

Fig. 4.13. G(r) profiles for samples of $(Nd_{0.5}Ca_{0.5})_2Zr_2O_{6.5}$, showing (a) full profile and (b) short range correlations.

The Nd/Ca-O correlation is seen to sharpen with increasing temperature, as the first O-O correlation shifts to longer distances. This can be explained by considering the Rietveld analysis results. **Table 4.13** shows the O-O distances for $(Nd_{0.5}Ca_{0.5})_2Zr_2O_{6.5}$ at 20, 500 and 800 °C. While there is some thermal expansion in these distances, alone this does not explain the observed changes in the G(*r*) profiles. However, taking into account the changes in oxide ion distribution at the three studied temperatures it is clear that the first O-O correlation at around 2.4 Å, associated with O(1)-O(3) in the average structure analysis, is expected to diminish in intensity with increasing temperature, while those for O(1)-O(1) (*ca*. 2.7 Å) and O(1)-O(2) (*ca*. 2.9 Å) are expected to increase in intensity, as is observed.

Table 4.13. Predicted O-O pair correlations and relative intensities derived from Rietveld analysis of $(Nd_{0.5}Ca_{0.5})_2Zr_2O_{6.5}$

Temp °C	O(1)-O(3)	O(1)-O(1)	O(1)-O(2)	%O(1)-O(3)	%O(1)-O(1)	%O(1)-O(2)
20	2.386	2.647	2.865	76.3	14.3	9.4
500	2.394	2.66	2.882	76.9	14.3	8.8
800	2.401	2.669	2.893	78.2	14.5	7.3
Mult	O1-O3 × 1 O3-O1 × 6	O1-O1 ×4	O1-O2 × 1 O2-O1 × 6			

Reverse Monte Carlo (RMC) analysis was used to model the G(*r*) and S(*Q*) profiles for $(Nd_{0.5}Ca_{0.5})_2Zr_2O_{6.5}$, generated from data collected at 20, 500, and 800 °C. The fit to the room temperature profiles are shown in **Fig. 4.14** as a representative example, with the fits to the other temperatures given in Appendix C.

(a)

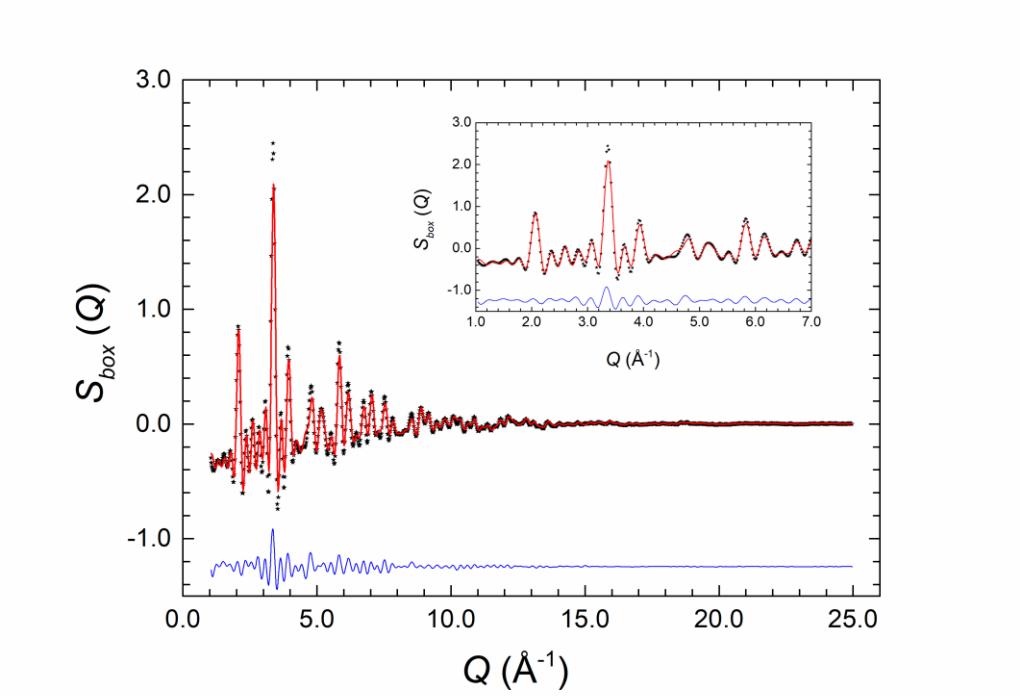

(b)

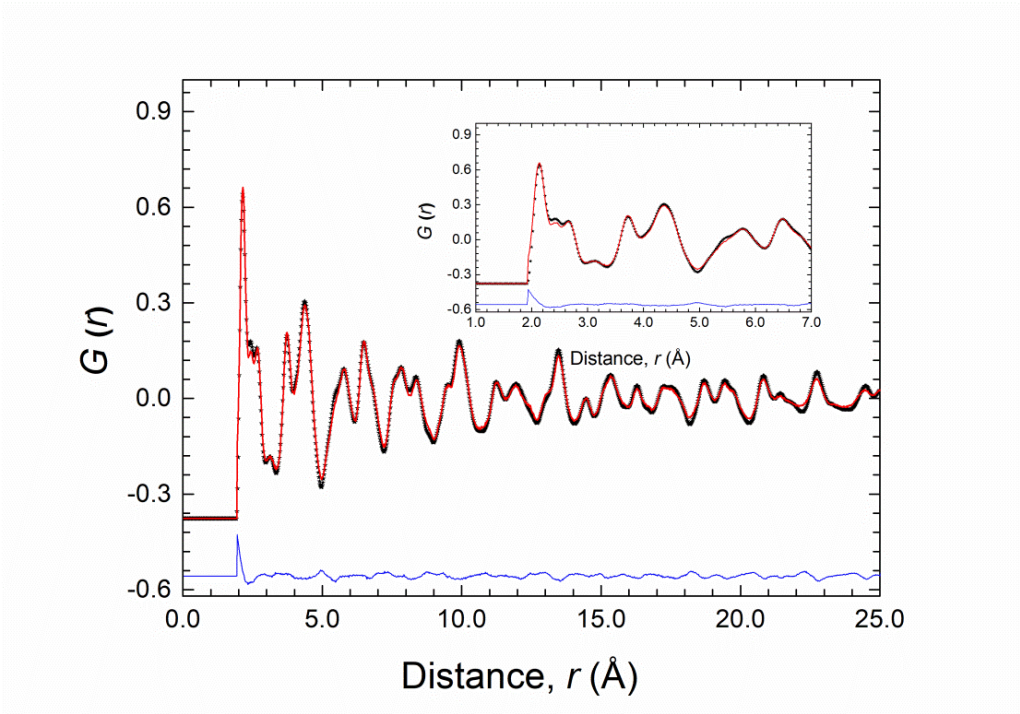

Fig. 4.14. Fitted (a) S(*Q*) and (b) G(*r*) profiles obtained by the RMC modelling of neutron scattering data from $(Nd_{0.5}Ca_{0.5})_2Zr_2O_{6.5}$, at room temperature. The black dots show the experimental data, the solid red line shows the calculated profile, and the difference profile is shown by the solid blue line.

The partial radial distribution functions, $g_{Nd\text{-}O}(r)$, $g_{Ca\text{-}O}(r)$, $g_{Zr\text{-}O}(r)$, and $g_{O\text{-}O}(r)$ extracted from the RMC configurations are shown in **Fig. 4.15**. The first peak in the $g_{Nd\text{-}O}(r)$, and $g_{Ca\text{-}O}(r)$ correlations narrows and appears to increase in intensity with increasing temperature, relative to the first $g_{Zr–O}(r)$ correlation. Another striking difference between the plots, is that the $g_{O\text{-}O}(r)$ peak splits into two peaks in going from room temperature to elevated temperatures, with the O-O correlation distinctly broader at room temperature than at elevated temperatures.

The final bond valence sums (BVS) along with M-O coordination numbers and modal and mean contact distances are given in **Table 4.14**. The BVS values are all very close to those expected. There is little variation in distances and coordination numbers between temperatures from the RMC analyses. Two types of coordination number can be defined, depending on the type of interaction being considered. Calculation of the site coordination number involved integration of the $g_{M\text{-}O}(r)$ curve up to the point at which it flattens out (taken as 3.35 Å), and includes all M-O interactions, as introduced in Chapter 3. As shown in **Table 4.14**, the site coordination numbers of Zr are significantly lower than the coordination numbers of Nd and Ca, as would be expected from the pyrochlore structure. The local coordination number, on the other hand, may be calculated by integration of the $g_{MO}(r)$ curve up to the first minimum, which gives a reasonable approximation to the number of anions in the immediate coordination sphere of the cations.

The results in **Table 4.14** show site and local coordination numbers agree very well for Nd^{3+} and Ca^{2+}, but differ considerably for Zr^{4+}, suggesting that the site coordination numbers reflect better the true coordination number for Zr^{4+}. Interestingly, there is little difference found between the Nd^{3+} and Ca^{2+} coordination numbers with both cations having values around 7.2, and Zr^{4+} significantly lower at around 6.2. These are slightly lower than those from the Rietveld analysis. To allow direct comparison with the crystallographic study, both mean and modal contact distances are shown in **Table 4.14**. The modal contact distances are all appreciably lower than the mean values. This is because the mean values include both the shorter bonding interactions, as well as the longer, weaker, interactions. In all cases, the mean values are close to the sum of the ionic radii (2.51 Å, 2.40 Å, and 2.12 Å, for Nd-O, Ca-O, and Zr-O respectively, based on an 8-fold coordination for Nd and a 6-fold coordination for Ca and for Zr).[25]

(a)

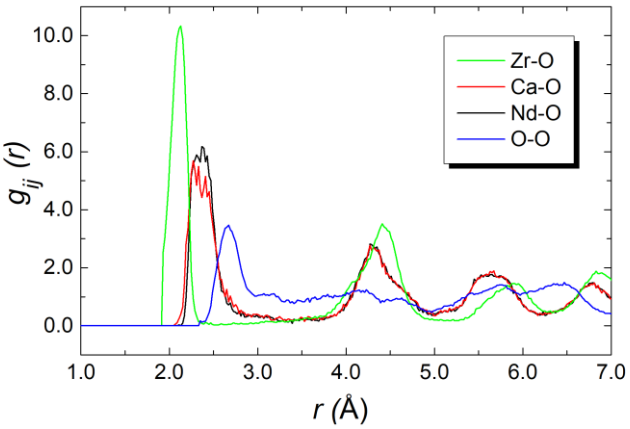

(b)

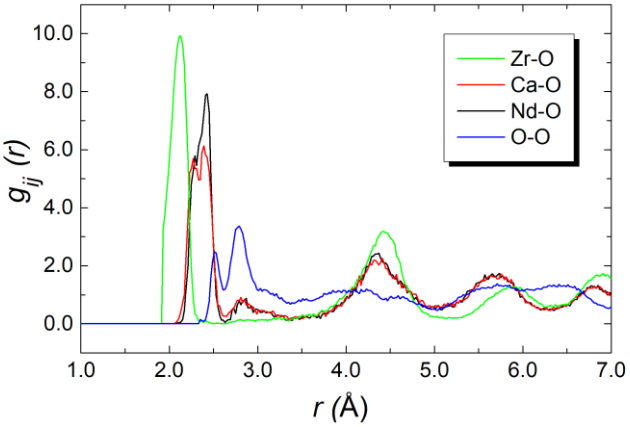

(c)

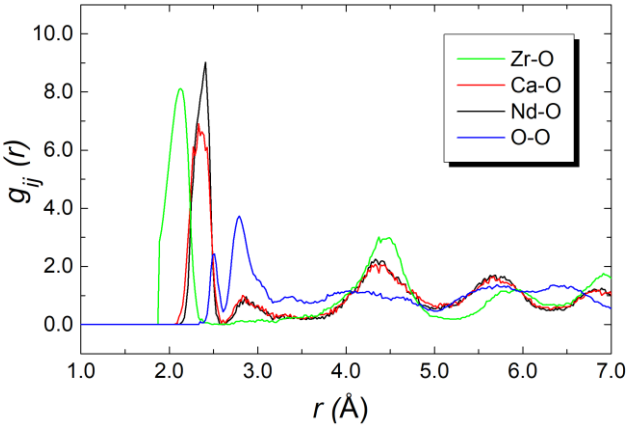

Fig. 4.15 Partial radial distribution functions, g_{ij}M-O(r) and g_{ij}O-O(r), as determined from RMC modelling, for $(Nd_{0.5}Ca_{0.5})_2Zr_2O_{6.5}$ at (a) 20 °C, (b) 500 °C, and (c) 800 °C

Table 4.14 Bond valence sums (BVS), M-O coordination numbers (CN) and modal and mean M-O contact distances (Å) from RMC analysis of $(Nd_{0.5}Ca_{0.5})_2Zr_2O_{6.5}$ at 20, 500 and 800 °C. Values are averages of 10 parallel calculations and standard deviations are given in parentheses. Site coordination numbers were derived by integration of $g_{M\text{-}O}(r)$ to a maximum of 3.35 Å.

		20 °C	500 °C	800 °C
BVS	Nd^{3+}	3.033(6)	3.023(3)	3.006(3)
	Ca^{2+}	2.039(4)	2.018(3)	1.998(3)
	Zr^{4+}	3.704(3)	3.678(7)	3.716(4)
	O^{2-}	1.919(2)	1.907(2)	1.913(1)
Site CN	Nd-O	7.20(2)	7.25(2)	7.27(3)
	Ca-O	7.18(3)	7.19(3)	7.19(2)
	Zr-O	6.28(1)	6.22(2)	6.20(2)
Local CN	Nd-O	7.20(2)	7.25(2)	7.27(3)
	Ca-O	7.18(3)	7.19(3)	7.19(2)
	Zr-O	5.91(1)	5.77(2)	5.70(2)
Distances	Nd-O Mode	2.36(1)	2.26(1)	2.42(1)
	Nd-O Mean	2.481(2)	2.495(2)	2.500(2)
	Ca-O Mode	2.32(1)	2.35(3)	2.37(1)
	Ca-O Mean	2.485(2)	2.501(3)	2.509(2)
	Zr-O Mode	2.07(1)	2.06(1)	2.11(1)
	Zr-O Mean	2.116(1)	2.110(1)	2.106(1)
	Nd/Ca Mean wt. av.	2.483(3)	2.498(5)	2.505(12)

The thermal variation of the site MO coordination numbers is illustrated graphically in **Fig. 4.16**. There is a slight increase in the coordination numbers of neodymium and calcium with increasing temperature, whereas the coordination number of zirconium decreases, indicating the structure to be more pyrochlore-like at elevated temperatures.

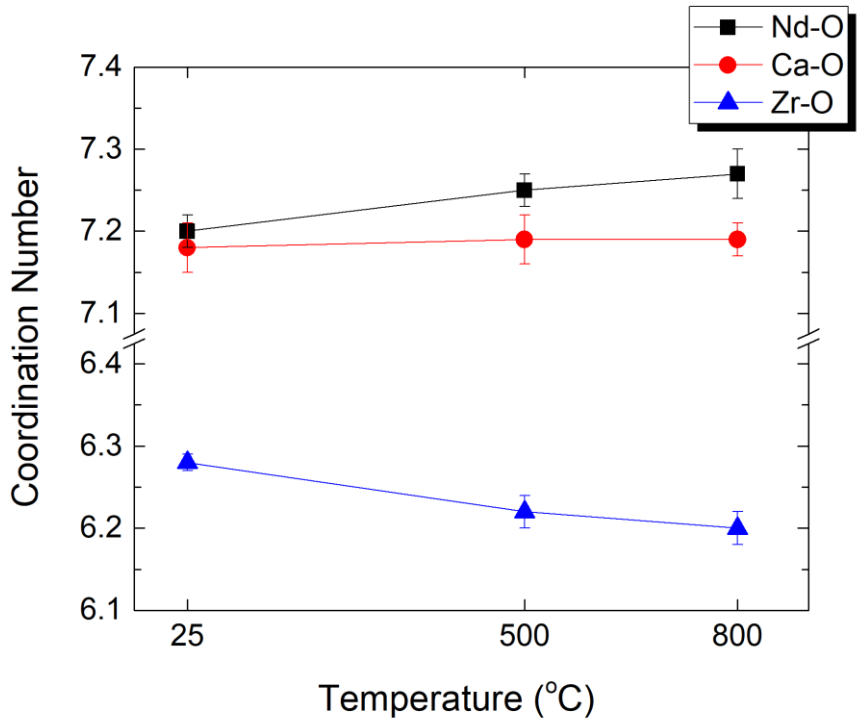

Fig. 4.16. Thermal variation of site coordination numbers in $(Nd_{0.5}Ca_{0.5})_2Zr_2O_{6.5}$ derived from RMC analyses.

The O-M-O angular distribution functions, $A_{OMO}(\Theta)$, derived from the RMC configurations at the three studied temperatures are shown in **Fig. 4.17**. The O-Nd-O and O-Ca-O distributions are similar to each other and show distributions around *ca*. 70°, 109° and 180°, corresponding to the angles between <100>, <110> and <111> aligned oxide ions, respectively, in the MO_8 distorted cubic coordination environments of the pyrochlore structure. There is little difference between the O-Nd-O and O-Ca-O distributions, underlining the difficulty in distinguishing between these atoms in the present system. In contrast, the O-Zr-O distribution shows maxima at around 80°, 100° and 180°, consistent with a trigonal anti-prismatic (distorted octahedral) geometry as evident in the Rietveld analysis.

(a)

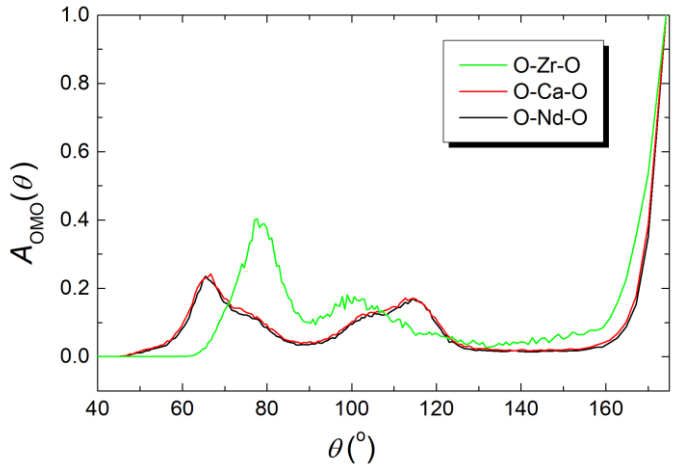

(b)

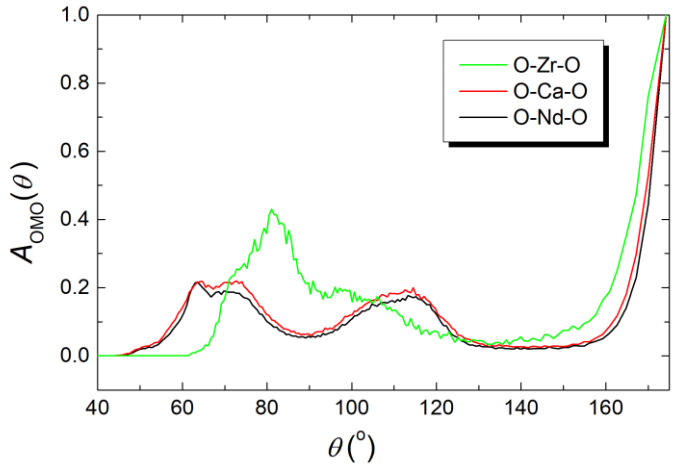

(c)

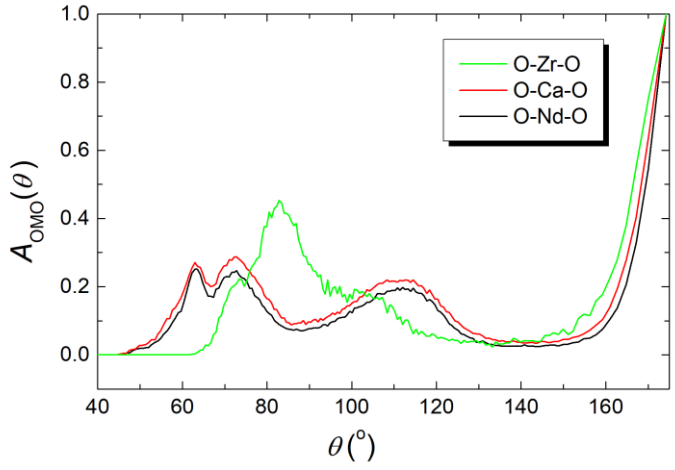

Fig. 4.17 O-M-O angular distribution functions for $(Nd_{0.5}Ca_{0.5})_2Zr_2O_{6.5}$ at (a) 20 °C, (b) 500 °C, and (c) 800 °C.

The final RMC configurations may be examined for vacancy concentration and vacancy ordering or clustering, as demonstrated in chapter 3. The defect distribution parameters obtained from the RMC calculations are summarized in **Table 4.15**. At each temperature, the tetrahedral vacancy concentration is seen to remain almost constant with increasing temperature, at around 1 per formula unit, which is lower than the calculated value of 1.5.

Three basic vacancy pair alignments can be defined with respect to the cubic coordination of the cation in the ideal fluorite structure, each characterized by a specific vacancy-vacancy distance, as demonstrated in chapter 3. Assuming a random distribution of vacancies, a ratio of 1:2:1.3 for <100>:<110>:<111> vacancy pairs is expected. As vacancies are introduced into the structure, any non-random distribution results in a change in this ratio. For an ideal pyrochlore, the expected ratio is 0:0:1 *i.e*. all vacancy pairs show <111> alignment. The values given in **Table 4.15** show a clear departure from these ideal ratios. Whilst there is a preference for <111> ordering compared to the random situation, there are still appreciable numbers of <100> and <110> aligned vacancy pairs. As the temperature increases the ratio begins to approach that of a random distribution.

Using a similar approach to that discussed above, the vacancy "coordination" environment can be probed to reveal evidence of preferential distribution of vacancies between the cations. The nearest neighbour cation distributions around oxide ion vacancies are presented as percentages of the total number of nearest neighbour cations in **Table 4.15**. A random distribution of vacancies would be expected to yield percentage distributions reflecting the stoichiometry, i.e. 25% Nd^{3+}, 25% Ca^{2+}, and 50% Zr^{4+}. The values given in **Table 4.15** for %vac(NN)M show no significant deviation from a purely random distribution, suggesting no preferential association of vacancies with any of the cations.

Table 4.15 Defect concentration and nearest neighbour distribution parameters derived from RMC analyses of $(Nd_{0.5}Ca_{0.5})_2Zr_2O_{6.5}$ at 20, 500 and 800 °C. Values are averages of 10 parallel calculations and standard deviations are given in parentheses.

	20 °C	500 °C	800 °C	Theoretical
No. tet. vacancies formula unit.	1.05(1)	0.98(1)	0.93(1)	1.5
100:110:111	1.00:2.14:2.50	1.00:2.15:2.15	1.00:1.96:1.83	Rand. 1.0:2.0:1.3 Pyr. 0:0:1
%vac(NN)Nd	25.6(2)	25.3(1)	25.0(3)	25
%vac(NN)Ca	26.2(3)	25.6(2)	25.7(2)	25
%vac(NN)Zr	48.3(3)	49.2(2)	49.4(3)	50
%Nd(NN)Nd	24.6(1)	24.7(1)	24.9(2)	25
%Nd(NN)Ca	24.4(2)	24.5(1)	24.4(2)	25
%Nd(NN)Zr	51.0(2)	50.8(1)	50.7(2)	50
%Ca(NN)Nd	24.5(2)	24.6(1)	24.5(2)	25
%Ca(NN)Ca	24.5(3)	24.7(1)	24.7(2)	25
%Ca(NN)Zr	51.0(2)	50.8(1)	50.7(1)	50
%Zr(NN)Nd	25.3(1)	25.2(1)	25.2(1)	25
%Zr(NN)Ca	25.2(1)	25.1(1)	25.1(1)	25
%Zr(NN)Zr	49.5(1)	49.7(1)	49.7(1)	50

The RMC configurations also allow for the examination of the specific local environment of the different types of cations, which is particularly relevant in the case of systems where different types of cation share the same crystallographic site and are hence effectively indistinguishable in the average structure analysis. **Fig. 4.18** shows the cation partial pair correlations. It is very evident that there is no significant change in the cation distributions in going from room temperature to 500 and 800 °C. The cation pair correlations of $g_{Nd\text{-}Zr}(r)$ and $g_{Ca\text{-}Zr}(r)$ show similar distributions to each other, however their distributions are significantly different to the $g_{Ca\text{-}Nd}(r)$, $g_{Nd\text{-}Nd}(r)$, $g_{Ca\text{-}Ca}(r)$ and $g_{Zr\text{-}Zr}(r)$ cation pair correlations. The percentage of each type of cation-cation nearest neighbours, $\%M(NN)_M$, **Table 4.15** above, at each of the studied temperatures, shows no significant deviation away from a random distribution. As explained in Chapter 3, for an ideal pyrochlore with no anti-site cation disorder, the nearest neighbours should reflect the stoichiometry. However, the next-nearest neighbours for cations are never on the same type of site (A or B). Thus $g_{A\text{-}A}(r)$ and $g_{B\text{-}B}(r)$ type correlations should show no peak at around 5.3 Å. Indeed, **Table 4.16** confirms this, with very low levels of anti-site cation disorder.

Table 4.16 Next-nearest neighbour distribution parameters derived from RMC analyses of $(Nd_{0.5}Ca_{0.5})_2Zr_2O_{6.5}$ at 20, 500 and 800 °C. Values are averages of 10 parallel calculations and standard deviations are given in parentheses.

	20 °C	500 °C	800 °C	Theoretical
%Nd(NNN)Nd	5.0(7)	4.5(3)	3.8(5)	0
%Nd(NNN)Ca	5.6(4)	5.1(2)	4.9(4)	0
%Nd(NNN)Zr	89.5(3)	90.4(2)	91.3(4)	100
%Ca(NNN)Nd	5.5(4)	5.1(2)	4.8(4)	0
%Ca(NNN)Ca	6.0(9)	5.4(6)	5.4(3)	0
%Ca(NNN)Zr	88.5(4)	89.6(2)	89.8(3)	100
%Zr(NNN)Nd	47.8(2)	48.7(1)	48.7(2)	50
%Zr(NNN)Ca	47.9(2)	48.7(1)	48.8(1)	50
%Zr(NNN)Zr	4.3(3)	2.6(4)	2.5(5)	0

(a)

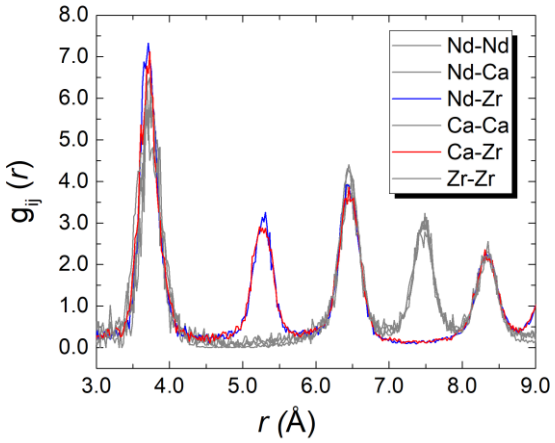

(b)

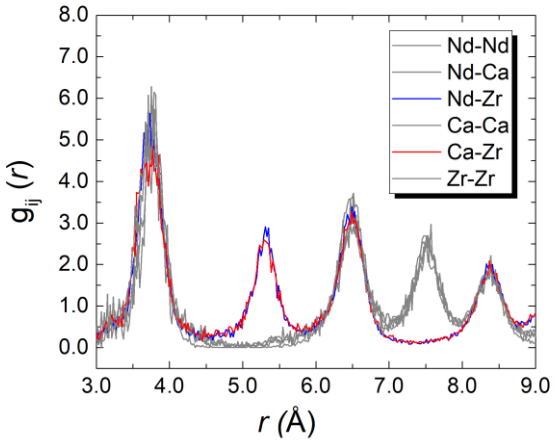

(c)

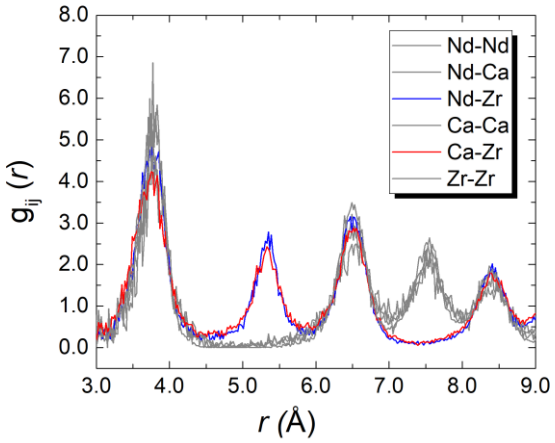

Fig. 4.18 Cation-cation partial radial distribution functions, $g_{M\text{-}M}(r)$, as determined from RMC modelling, for $(Nd_{0.5}Ca_{0.5})_2Zr_2O_{6.5}$ at (a) 20 °C, (b) 500 °C, and (c) 800 °C.

4.3.3 Electrical conductivity

The Arrhenius plots of total conductivity for $(Nd_{1-x}Ca_x)_2Zr_2O_{7-x}$ ($0.00 \leq x \leq 0.50$) are shown in **Fig. 4.19**. Each plot shows two linear regions with a transition at around 400 °C, similar to what was observed in the Yb doped system (Chapter 3). In all the Ca substituted compositions, the higher temperature region has a lower activation energy than the low temperature region. For the $x = 0.0$ composition, the Arrhenius plot is almost linear, with the activation energy of the high temperature region slightly higher than that of the low temperature region. This change in activation energy is likely to be associated with the change in oxide ion distribution seen in the Rietveld analysis (**Table 4.6** above) and the vacancy distribution (**Table 4.15** above).

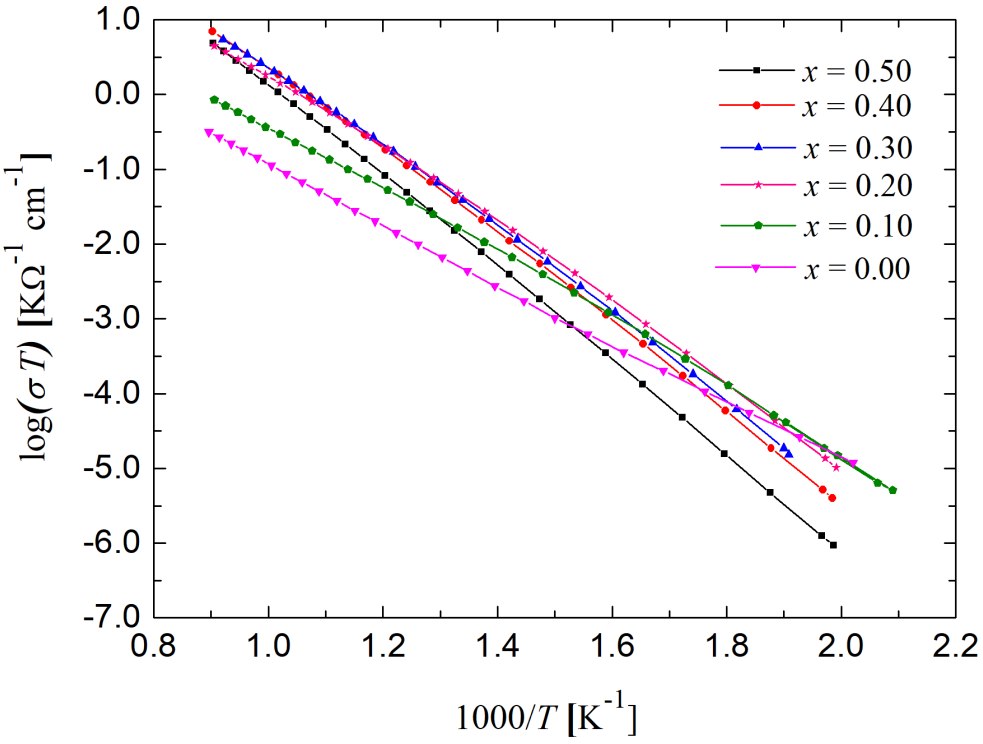

Fig. 4.19 Arrhenius plots of total conductivity for $(Nd_{1-x}Ca_x)_2Zr_2O_{7-x}$ ($0.00 \leq x \leq 0.50$).

The compositional variation of total conductivity is shown in **Fig. 4.20a**. The Ca substituted compositions all show higher conductivity than the un-substituted composition, particularly at higher temperatures. The low temperature conductivity, characterised by the conductivity at 300 °C (σ_{300}), has values in the order of 10^{-7} S cm^{-1} and exhibits a maximum at the x = 0.2 composition. For the high temperature region, the conductivity at 700 °C (σ_{700}) has values in the order of 10^{-3} S cm^{-1}, with a maximum at x = 0.3. Activation energies are in the range 0.80–1.30 eV (**Fig. 4.20b**). Both the low temperature activation energy, ΔE_{LT}, and that at high temperature, ΔE_{HT}, increase with increasing calcium content.

The increase in conductivity with calcium content is due to the higher concentration of charge carriers caused by Ca-substitution in $Nd_2Zr_2O_7$. Partial replacement of Nd^{3+} by Ca^{2+} cations cause a reduction in the positive charge, which is compensated by the formation of oxygen vacancies, which leads to an increase in ionic conductivity. However, above an optimum substitution level, vacancy-vacancy interactions become significant, thus reducing ion mobility.[254] The conductivity is much higher at 700 °C than at 300 °C for each composition, confirming that the oxide ion diffusion process is thermally activated. Optimum conductivity is obtained at compositions, x = 0.20-0.30, both in low and high temperature regions.

(a)

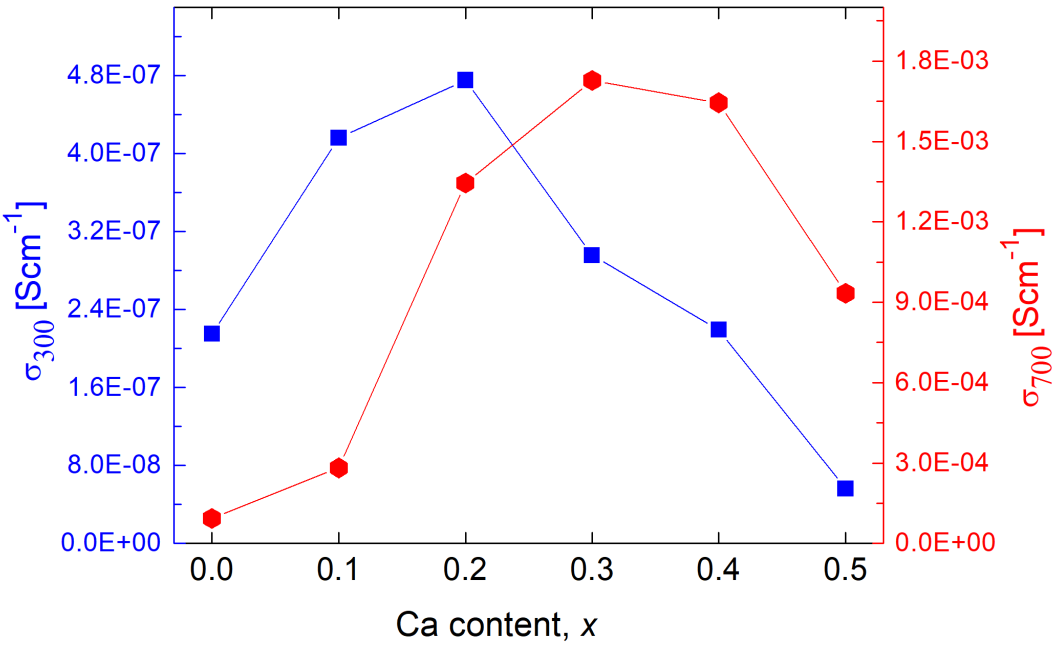

(b)

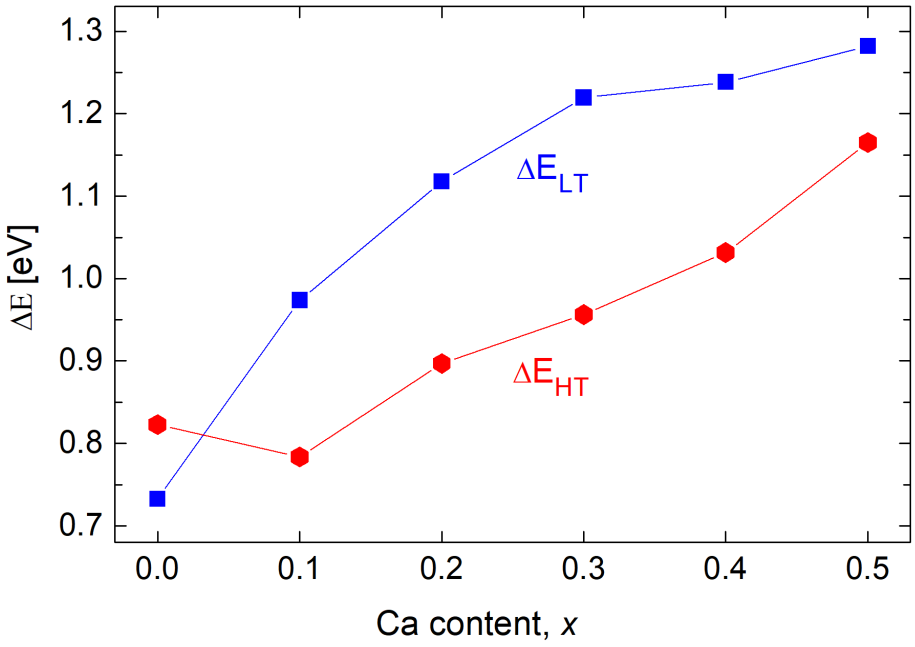

Fig. 4.20. Compositional variation of (a) total conductivity at 300 °C (σ_{300}) (blue) & 700 °C (σ_{700}) (red) and (b) high temperature ΔE_{HT} & low temperature ΔE_{LT} activation energies in $(Nd_{1-x}Ca_x)_2Zr_2O_{7-x}$, with x = 0.00, 0.10, 0.20, 0.30, 0.40 and 0.50, at 300 and 700 °C.

4.4 Conclusions

Phase pure compounds of $(Nd_{1-x}Ca_x)_2Zr_2O_{7-x}$ ($0.00 \leq x \leq 0.50$) were synthesised via a co-precipitation method. These compounds exhibit a defect pyrochlore structure, with no evidence of significant anti-site cation disorder, but increasing concentrations of oxygen Frenkel defects with increasing calcium content. The pyrochlore structure is maintained at temperatures up to 800 °C.

Coordination numbers around 7 for Ca^{2+}, 8 for Nd^{3+} and 6 for Zr^{4+} are indicated by Rietveld analysis. RMC modelling confirmed the coordination number for Zr^{4+}, however it yielded coordination numbers of around 7.2 for both Ca^{2+} and Nd^{3+} cations. A distorted cubic type coordination is observed for Nd^{3+} and Ca^{2+}, with Zr^{4+} in a trigonal anti-prismatic (distorted octahedral) coordination. A non-random vacancy distribution is observed with a clear preference for <111> ordering, consistent with a preferred pyrochlore-like distribution of vacancies. However, increasing temperature causes a more random distribution of vacancies and a partial redistribution of oxide ions, which appears to correlate with a change in activation energy at around 400 °C, seen in Arrhenius plots of conductivity.

Substitution by Ca^{2+} causes an increase in vacancy concentration, thus increasing electrical conductivity. However, the activation energy for conductivity also increases with calcium content, and optimum conductivity (10^{-3} S cm^{-1} at 700 °C) was achieved for composition $x = 0.3$.

Chapter 5 – Structural Behaviour of Cerium Zirconate

5.1 Introduction

Ceria-based materials possess a high oxygen storage capacity (OSC), accompanied with high oxygen uptake/release rates. These materials are therefore widely used as oxygen storage materials in automotive exhausts.[255] Of particular interest is the CeO_2-ZrO_2 solid solution, which has a much higher OSC than pure CeO_2. These properties are primarily the result of Ce cations undergoing fast oxidation/reduction reactions ($Ce^{3+} \leftrightarrow Ce^{4+}$), with varying temperatures and atmospheres.[256] Furthermore, the properties of these materials are strongly dependent on crystal structure, due to the various phases possessing different concentrations of Ce^{3+} cations. For example, the OSC of κ-$CeZrO_4$, in which the cerium and zirconium ions are ordered, was shown to be about twice as large as that of the fluorite-$CeZrO_4$.[257] The local structure, oxygen stoichiometry, and oxygen vacancies, are also pivotal to oxygen storage in these materials and their release capabilities.[258,259]

Cerium zirconate materials with the pyrochlore structure have previously been prepared via the intercalation of oxygen, as was first demonstrated by Thomson *et al.* in the synthesis of $Ce_2Zr_2O_7$.[260] Intercalation is defined as the insertion of a guest atom or molecule into a host solid structure, or the removal of such species from the solid structure, without inducing a major alteration of the host structure.[261] Through intercalation, new meta-stable structures with interesting properties may be produced, such as the fluorite-structured compound, $Ce_2Zr_2O_{7.97}$, which retains the cation ordering of the pyrochlore structure.[262] The process of intercalation was pivotal to the development of rechargeable lithium ion batteries,[263] and it is no less promising for the further advancement of SOFC electrode/electrolyte materials.[32]

While CeO_2 forms the cubic fluorite structure only, ZrO_2 can form three structural polymorphs, i.e. monoclinic, tetragonal, and cubic. As the content of CeO_2 in the CeO_2–ZrO_2 solid solution is increased from 20 to 80 mol%, tetragonal and cubic phases are formed.[264] Several studies have previously been performed on the CeO_2-ZrO_2 system under reducing and oxidising conditions, where pyrochlore-like phases have been seen in reducing conditions.[265,266,267]

The xCeO$_2$-(1-x)ZrO$_2$ system forms the cubic fluorite structure at high temperatures, over the entire compositional range, **Fig. 5.1**. However, for compositions with $x \leq 0.65$, a phase transition occurs upon cooling, forming the tetragonal t-(Ce$_x$Zr$_{1-x}$)O$_2$ phase, which is distinguished from the cubic fluorite phase by the splitting of the (400) Bragg peak.[268,269,270] Furthermore, the tetragonal phase exists in three forms, denoted t, t' and t'', all with space group $P4_2/nmc$.[269,270] In the compositional range $0.44 \leq x \leq 0.57$, the t-(Ce$_x$Zr$_{1-x}$)O$_2$ phase can be reduced at high temperatures, forming the pyrochlore phase, where both Ce and Zr cations are ordered in the <110> direction.[271]

Under controlled re-oxidation, the pyrochlore phase transforms to one of the two metastable cubic phases: β-Ce$_2$Zr$_2$O$_{7.5}$,[272] or κ-CeZrO$_4$ [273]. The β-Ce$_2$Zr$_2$O$_{7.5}$ phase is an oxygen-rich pyrochlore phase, where approximately half of the oxygen vacancy sites are occupied. The κ-CeZrO$_4$ phase is a fully oxidised fluorite phase, where the cation ordering of the pyrochlore structure is retained. As would be expected, the local structure symmetry of the κ-phase is significantly lower than that of the pyrochlore phase.

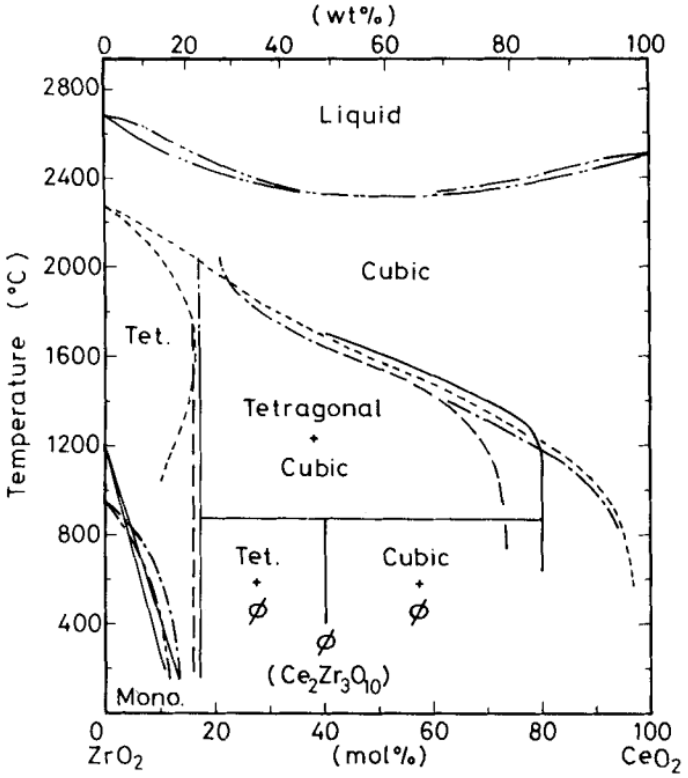

Fig. 5.1. Phase relations in the system ZrO$_2$-CeO$_2$.[274] ϕ is Ce$_2$Zr$_2$O$_{10}$

Using neutron diffraction, Achary *et al*. determined the crystal structures of $Ce_2Zr_2O_7$, β-$Ce_2Zr_2O_{7.5}$, and κ-$CeZrO_4$, **Fig. 5.2**.[275] The cubic lattice was maintained throughout the compositional range, but with a systematic decrease in lattice parameter with increasing oxygen content. Pyrochlore-type cation ordering was also maintained with increasing oxygen content, however, there was a systematic lowering of symmetry from space group $Fd\bar{3}m$, to $F\bar{4}3m$, to $P2_13$, and ultimately to $Fm\bar{3}m$. Sasaki *et al.* also assigned the $F\bar{4}3m$ space group to the intermediate phase, β-$Ce_2Zr_2O_{7.5}$,[266] and the primitive cubic $P2_13$ space group to the fully oxidised κ-$CeZrO_4$ phase.[276] However, space group $R\bar{3}m$ is the only maximal non-isomorphic subgroup of $Fd\bar{3}m$ that retains cation ordering. As such, Thomson *et al*. found the $R\bar{3}m$ space group to be most appropriate for describing the oxygen distribution in the nearly fully oxidised $Ce_2Zr_2O_{7.97}$ phase.[262]

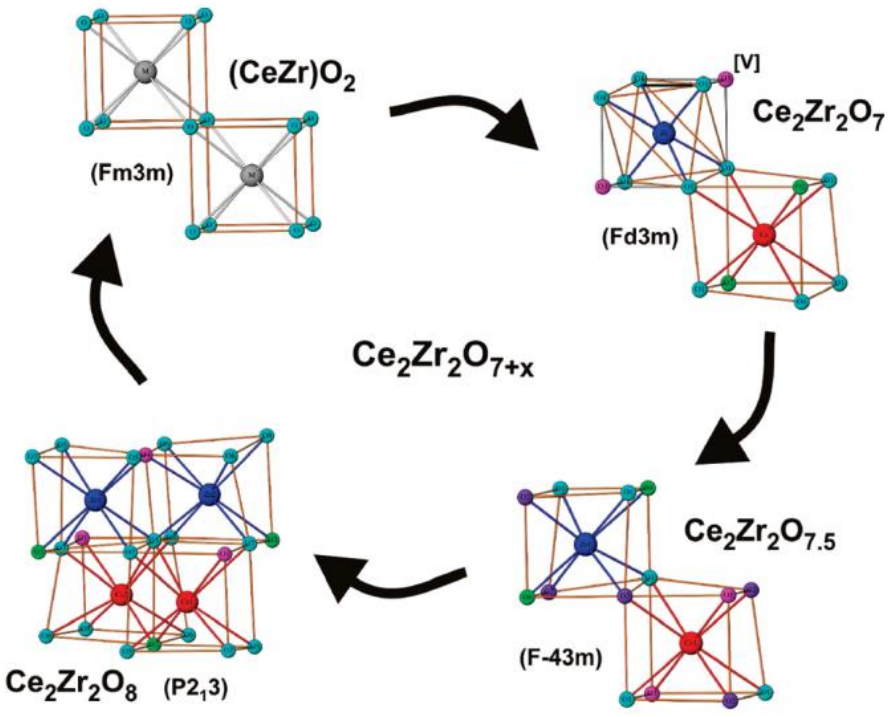

Fig. 5.2. Structural transformations in $Ce_2Zr_2O_7$, $Ce_2Zr_2O_{7.5}$, and $Ce_2Zr_2O_8$. [V] denotes an oxygen vacancy.[275]

In this chapter, structural details of the $Ce_2Zr_2O_{7-\delta}$ system have been characterised *in situ*, during chemical intercalation of oxygen at variable temperature. In particular, the work set out to identify an intermediate phase occurring at low temperatures under an atmosphere of O_2. Neutron diffraction was used to investigate the structural changes with the reaction, especially to elucidate the extent to which oxygen intercalation had taken place, and to establish the positions occupied by the interstitial oxide ions. A mechanistic correlation has been built between the lattice of the stoichiometric pyrochlore and its oxygen-rich counterpart. The compositional dependence of oxygen displacement has been investigated.

5.2 Experimental

The initial syntheses and data collection were carried out in 2012 by a team led by Dr S. Hull at the ISIS Facility, Rutherford Appleton Laboratory. Synthesis was carried out using the procedure of Burbano *et al.*[254]

Powder neutron diffraction data were collected on the Polaris diffractometer at the ISIS Facility, Rutherford Appleton Laboratory, UK. Pellets of κ-$CeZrO_4$ (nominal composition) were placed in a 12 mm diameter open quartz tube inside a vertical furnace with vanadium windows. Gas flow in and out of the tube was controlled using mass flow controllers, with a flow rate of *ca*. 10 sscm. To ensure reduction of the sample, it was first heated in situ to 600 °C in flowing CO, where a data set of 38 μA h was collected. After cooling, the sample was heated in flowing O_2, from 110 °C to 750 °C in steps of 10 °C and data collections of 20 μA h made at each step. At 750 °C an extended data collection of 373 μA h was carried out. After cooling to 100 °C, the atmosphere was changed to CO and the sample heated to 550 °C in steps of 10 °C. A data collection of 40 μA h was collected at each step. For total scattering analysis, data collections of 1455, 914 and 1163 μA h were carried out on samples of a fully disordered fluorite of the pyrochlore composition $Ce_2Zr_2O_7$, a sample of the same composition showing weak pyrochlore ordering and a sample of κ-$CeZrO_4$-δ, respectively in thin walled vanadium cans of 11 mm diameter at room temperature. Data on an empty vanadium can and the empty instrument were collected for data correction purposes.

For average structure analysis, data collected on the back-scattering (average angle 146.72°) detector bank was used in refinements using the Rietveld method with the GSAS set of programs,[199] and the EXPGUI interface,[198]. The starting models were based on the structures reported by Raison *et al.*[277] for the $Fd\bar{3}m$ pyrochlore structure; Sasaki *et al.*[272] for the β-phase structure in space group $F\bar{4}3m$, Kishimoto *et al.*[276] for the κ-phase in space group $P2_13$ and Kol'ko *et al.*[278] for the fluorite structure in space group $Fm\bar{3}m$. For neutron total scattering analysis, the background scattering and beam attenuation were corrected for using the program Gudrun,[178] and the resulting normalised total scattering structure factors, S(*Q*), were then used to obtain the corresponding total radial distribution function, G(*r*), via a Fourier transform, as described in Chapter 2. A *Q* maximum of 25 $Å^{-1}$ was used in calculations.

Analysis of the total neutron scattering data (Bragg peaks plus diffuse scattering components) was carried on the κ-$CeZrO_{4-\delta}$ structure.[232] RMC simulations used configuration boxes of 5 × 5 × 5 unit cells, with approximate dimensions of 50 Å × 50 Å × 50 Å, containing approximately 11000 atoms. Initial configurations were generated from supercells of the refined crystal structure, with atoms randomly distributed over sites in the supercell corresponding to those in the $P2_13$ crystallographic cell. Fitting was carried out against the reciprocal space data, S(*Q*), the real space data, G(*r*), and the Bragg profile data to provide a constraint for the long-range crystallinity. S(*Q*) was broadened by convolution with a box function (Chapter 2, equation 2.38), in order to reflect the finite size of the simulation box. Calculations were performed using bond valence summation (BVS) constraints.[209] M-O and O-O closest approach constraints ($g_{M\text{-}O}(r)$ and $g_{O\text{-}O}(r)$) were used, to avoid unrealistically short M-O and O-O contact distances. A loose inter-atomic potential was used to model the O-O bond distribution. A set of ten parallel runs were used to produce average $g_{ij}(r)$ plots and to calculate standard deviations on derived parameters.

5.3 Results and discussion

5.3.1 Heating under O_2

A sample of the κ-phase with nominal composition $CeZrO_4$ was first heated at 600 °C in flowing CO, to ensure complete reduction of cerium. **Fig. 5.3** shows the fitted diffraction profile for the data collected at 600 °C. The data were successfully modelled in space group $Fd\bar{3}m$. The crystal and refinement parameters are summarised in **Table 5.1** with refined structural parameters and significant contact distances in **Table 5.2**. The fit shows the sample to be phase pure (within the limits of the technique). Attempts to refine the oxygen stoichiometry and occupancy of the 8*a* site always resulted in the ordered pyrochlore model (*i.e.* the occupancy of 8*a* refined to a small negative value and that of the 8*b* and 48*f* sites around 1.0 or greater). Similarly, no cation anti-site disorder could be refined, confirming the sample to be a fully ordered pyrochlore, *i.e.* $Ce_2Zr_2O_7$.

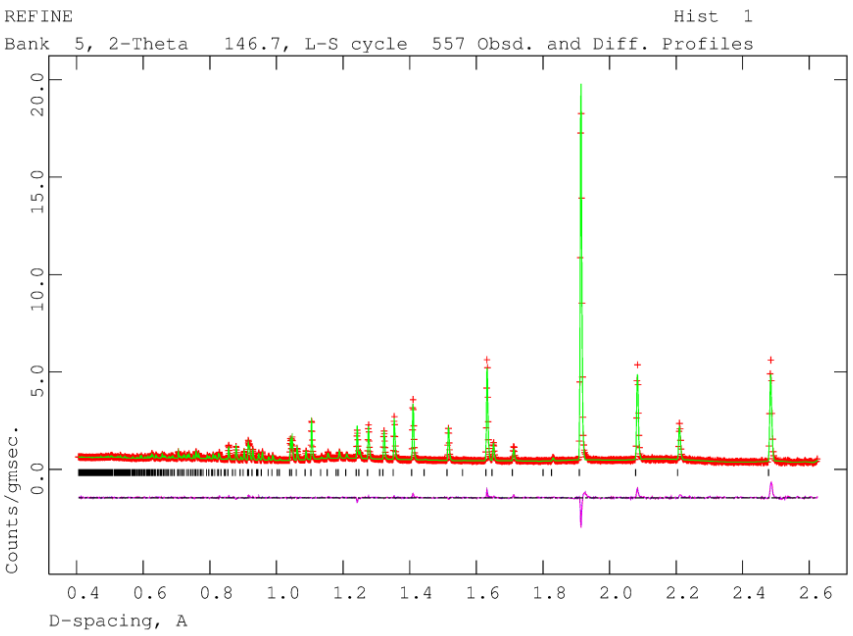

Fig. 5.3. Fitted neutron diffraction profile for $Ce_2Zr_2O_7$ at 600 °C, prepared by reducing ordered $Ce_2Zr_2O_8$ *in situ* in flowing CO. Observed (red + symbols), calculated (green line) and difference (violet line) profiles are shown. Reflection positions are indicated by markers.

Table 5.1 Crystal and refinement parameters for $Ce_2Zr_2O_7$ at 600 °C in flowing CO. Estimated standard deviations are given in parentheses.

Formula	$Ce_2Zr_2O_7$
M_r (g mol^{-1})	574.68
Crystal system	Cubic
Space group	$Fd\bar{3}m$
Lattice parameter (Å)	10.8225(2)
Volume (Å^3)	1267.60(6)
Z	8
D_{calc} (g cm^{-3})	6.023
Temperature (°C)	600
Atmosphere	Flowing CO
R-factors:	
Neutron back scattering data	R_{wp} = 0.0263
	R_p = 0.0404
	R_{ex} = 0.0175
	R_F2 = 0.1160
χ^2	2.309
Total no. of variables	44
No. of profile points	2668
No. of reflections	541

Table 5.2. Refined structural parameters and significant contact distances for $Ce_2Zr_2O_7$ at 600 °C in flowing CO. Estimated standard deviations are given in parentheses.

Atom	Site	*x*	*y*	*z*	Occ.	U_{iso} (Å^2)
Ce	16*d*	0.5	0.5	0.5	1.0	0.0139(2)
Zr	16*c*	0.0	0.0	0.0	1.0	0.0139(2)
O(1)	48*f*	0.33209(8)	0.125	0.125	1.0	0.0201(3)
O(2)	8*b*	0.375	0.375	0.375	1.0	0.0201(3)

Ce-O(1) (Å)	2.6387(6)	× 6
Ce-O(2) (Å)	2.34314(3)	× 2
Zr-O(1) (Å)	2.1094(4)	× 6

Following cooling in flowing CO, the atmosphere was switched to flowing O_2 and the sample heated. **Fig. 5.4a** shows the neutron diffraction patterns of $Ce_2Zr_2O_7$ on heating in flowing O_2, with detail shown in **Fig. 5.4b**. Three distinct regions can be identified with transitions at *ca*. 140 °C and 410 °C.

(a)

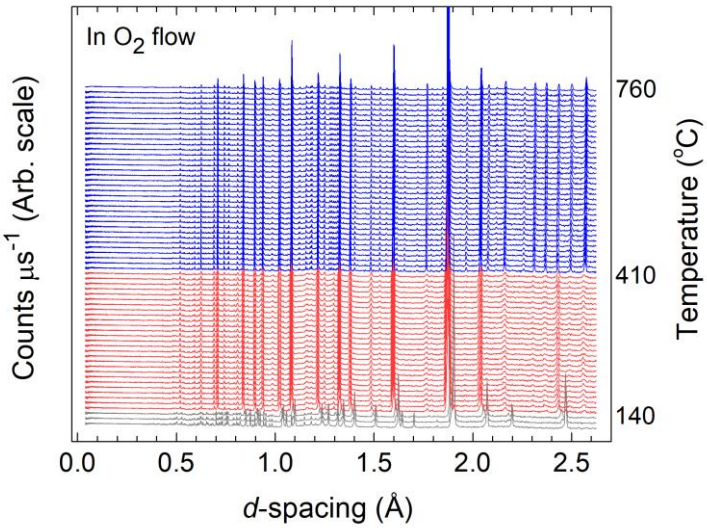

(b)

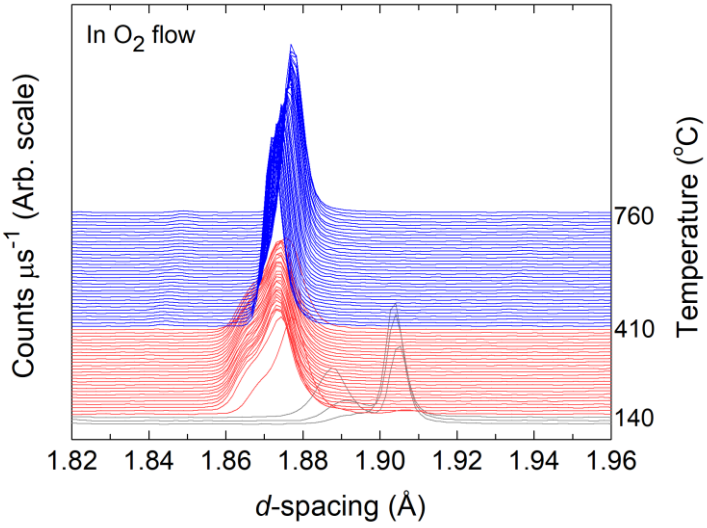

Fig. 5.4. Neutron diffraction patterns for $Ce_2Zr_2O_7$ on heating in flowing O_2, showing (a) full backscattering data and (b) detail of the patterns in the region of the pyrochlore (440) peak. Low temperature (110 to 130 °C), intermediate temperature (140 to 400 °C) and high temperature (410 to 500 °C) regions are indicated by grey, red and blue colours, respectively.

In the low temperature region from 110 to 130 °C, the diffraction patterns are dominated by a pyrochlore type phase, which was modelled satisfactorily using the standard pyrochlore model in space group $Fd\bar{3}m$, with a nominal composition of $Ce_2Zr_2O_7$ as previously identified.[275] However, weak features on the lower *d*-spacing side of the main peaks indicated a minor secondary phase which becomes more prominent with increasing temperature. This secondary phase is attributed to β-$Ce_2Zr_2O_{7.5}$ and was refined in space group $F\bar{4}3m$ using the model of Sasaki *et al*.[272]

The fit to the backscattering data at 130 °C using the two-phase model is shown as a representative example in **Fig. 5.5**, with the corresponding crystal and refinement parameters in **Table 5.3** and refined structural parameters and significant contact distances in **Table 5.4**.

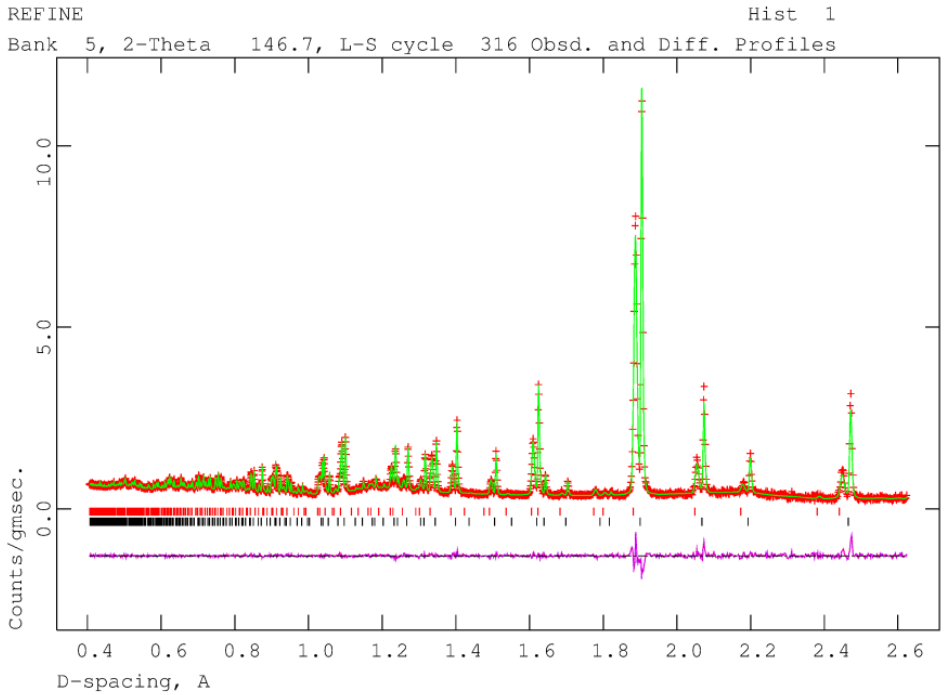

Fig. 5.5. Fitted neutron diffraction profile for a sample of composition $Ce_2Zr_2O_{7+\delta}$ at 130 °C, in flowing O_2. Observed (red + symbols), calculated (green line) and difference (violet line) profiles are shown. Reflection positions are indicated by markers: lower = $Ce_2Zr_2O_7$ ($Fd\bar{3}m$) and upper = β-$Ce_2Zr_2O_{7+\delta}$ ($F\bar{4}3m$).

Table 5.3. Crystal and refinement parameters for a sample of composition $Ce_2Zr_2O_{7+\delta}$ at 130 °C in flowing O_2. Estimated standard deviations are given in parentheses.

Phase	Phase 1	Phase 2
Formula	$Ce_2Zr_2O_7$	$Ce_2Zr_2O_{7.33(3)}$
M_r (g mol^{-1})	574.68	580.0
Crystal system	Cubic	Cubic
Space group	$Fd\bar{3}m$	$F\bar{4}3m$
Lattice parameter (Å)	10.7682(2)	10.6671(2)
Volume (Å^3)	1248.60(6)	1213.78(7)
Z	8	8
D_{calc} (g cm^{-3})	6.114	6.348
Weight fraction	0.535(5)	0.465(5)
Temperature (°C)	130	
Atmosphere	Flowing O_2	
R-factors:		
Neutron back scattering data	R_{wp} = 0.0261	
	R_p = 0.0469	
	R_{ex} = 0.0240	
	R_F2 = 0.0783	
χ^2	1.204	
Total no. of variables	54	
No. of profile points	2668	
No. of reflections	1120	

Table 5.4. Refined structural parameters and significant contact distances for $Ce_2Zr_2O_{7+\delta}$ at 130 °C in flowing O_2. Estimated standard deviations are given in parentheses.

(a) Phase 1 $Ce_2Zr_2O_7$						
Atom	Site	*x*	*y*	*z*	Occ.	U_{iso} (Å^2)
Ce	16*d*	0.5	0.5	0.5	1.0	0.0088(2)
Zr	16*c*	0.0	0.0	0.0	1.0	0.0060(2)
O(1)	48*f*	0.33218(9)	0.125	0.125	1.0	0.0100(2)
O(2)	8*b*	0.375	0.375	0.375	1.0	0.0081(2)

Ce-O(1) (Å)	2.6247(7)	× 6
Ce-O(2) (Å)	2.33137(3)	× 2
Zr-O(1) (Å)	2.0992(4)	× 6

(b) Phase 2 $Ce_2Zr_2O_{7.33(3)}$						
Atom	Site	*x*	*y*	*z*	Occ.	U_{iso} (Å^2)
Ce	16*e*	0.1242(4)	0.1242(4)	0.1242(4)	1.0	0.0090(3)
Zr	16*e*	0.6217(2)	0.6217(2)	0.6217(2)	1.0	0.0090(3)
O(1)	24*f*	0.2698(3)	0.0	0.0	1.0	0.0125(4)
O(2)	24*g*	0.5422(3)	0.25	0.25	1.0	0.0125(4)
O(3)	4*a*	0.0	0.0	0.0	1.0	0.0125(4)
O(4)	4*b*	0.5	0.5	0.5	0.667(34)	0.0125(4)
O(5)	4*c*	0.25	0.25	0.25	1.0	0.0125(4)
O(6)	4*d*	0.75	0.75	0.75	1.0	0.0125(4)

Ce-O(1) (Å)	2.434(3)	× 3
Ce-O(2) (Å)	2.598(3)	× 3
Ce-O(3) (Å)	2.295(7)	× 1
Ce-O(5) (Å)	2.324(7)	× 1

Zr-O(1) (Å)	2.170(2)	× 3
Zr-O(2) (Å)	2.114(3)	× 3
Zr-O(4) (Å)	2.248(4)	× 1
Zr-O(6) (Å)	2.371(4)	× 1

Unsurprisingly, the lattice parameter and M-O distances in phase 1 are smaller than the corresponding values for the same phase at 600 °C seen in **Table 5.2** above. In phase 2, Ce is in a distorted cubic coordination with O, with three bonds to O(1), three to O(2) and one each to O(3) and O(5) and an average Ce-O distance of 2.464(3) Å (**Fig. 5.6a**). Zr also sits in a distorted cubic site (**Fig. 5.6b**), however, the partial occupancy of O(4) lowers the average coordination number to 7.667, with a weighted average bond distance of 2.181(2) Å. These average distances compare with average values in the pyrochlore phase of 2.5514(5) Å and 2.0992(4) Å for Ce-O and Zr-O, respectively, showing that while the average Zr-O distance lengthens in the β-phase, the average Ce-O distance shortens.

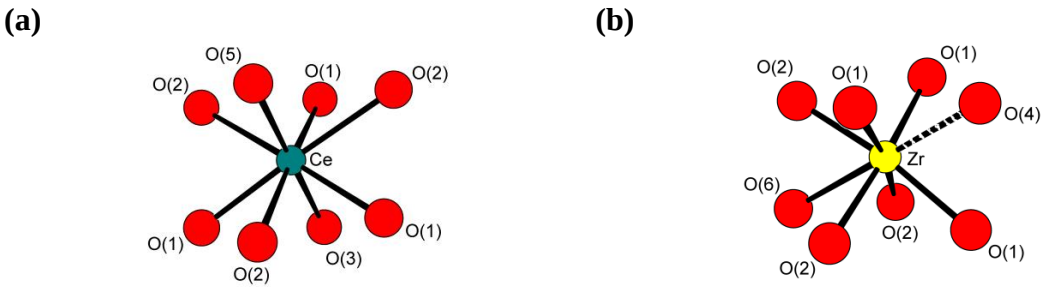

Fig. 5.6. Cation coordination in β-$Ce_2Zr_2O_{7.3335}$ (a) Ce coordination, (b) Zr coordination.

The variation in refined weight fraction for the two phases derived from the Rietveld analysis is shown in **Fig. 5.7**. The $Fd\bar{3}m$ phase remains the predominant phase throughout this temperature range. However, the non-stoichiometric $F\bar{4}3m$ phase fraction reaches as high as 46 wt% at 130 °C. Interestingly, the refined oxygen content of the secondary $F\bar{4}3m$ phase increases significantly with increasing temperature and taking this into account as well as the weight fractions (converted to mole fractions), allows for the average oxygen content (x) per $Ce_2Zr_2O_x$ formula unit in the sample to be calculated. This shows a significant increase from 7.03 to 7.15 per formula unit, between 110 and 130 °C (**Fig. 5.8**).

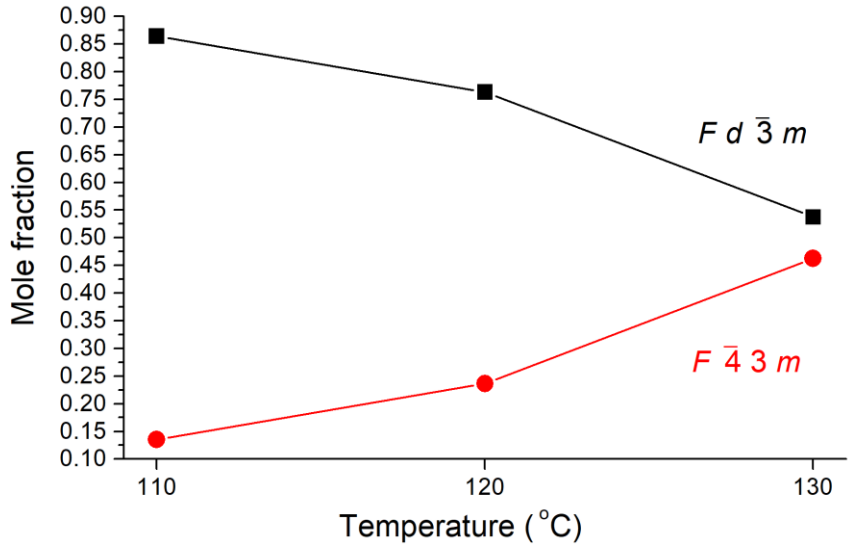

Fig. 5.7. Refined weight fractions for $Fd\bar{3}m$ and $F\bar{4}3m$ phases of $Ce_2Zr_2O_{7+\delta}$ on heating in O_2, over the temperature range 110 to 130 °C. Error bars are smaller than the symbols used.

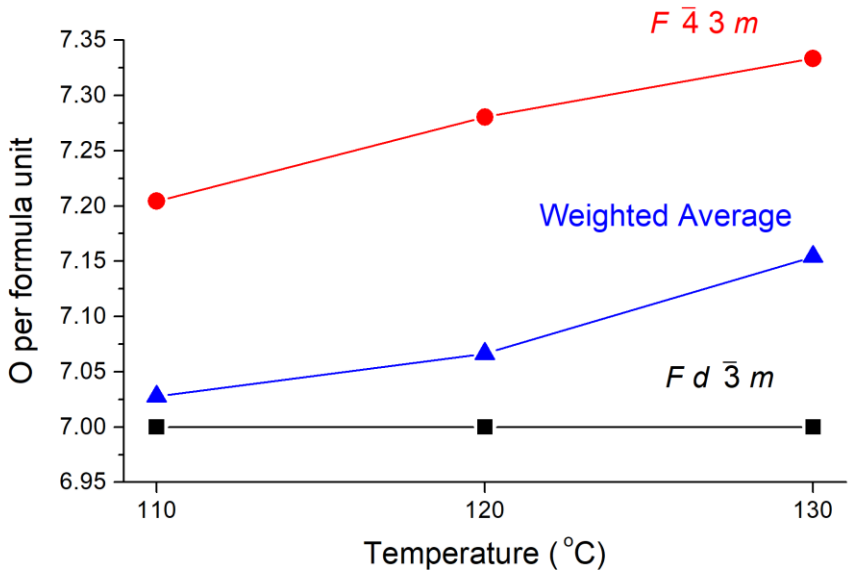

Fig. 5.8. Oxygen content per $Ce_2Zr_2O_x$ formula unit in $Fd\bar{3}m$ and $F\bar{4}3m$ phases and weighted average over the sample on heating in O_2, over the temperature range 110 to 130 °C. Error bars are smaller than the symbols used.

At around 140 °C, the $F\bar{4}3m$ phase disappears and a previously unidentified phase appears alongside a small amount of the $Fd\bar{3}m$ phase. This new phase is phase pure by 150 °C. Additional reflections in the diffraction pattern suggested a lowering of symmetry to the cubic κ-phase (in space group $P2_13$). However, the fit to the data (**Fig. 5.9a**) showed significant differences especially around 1.87 Å, where the cubic (440) peak was clearly split (**Fig. 5.9b**). A number of models were tried to fit these data, including LeBail fits in rhombohedral ($R\bar{3}m$), tetragonal ($I4/mmm$ and $P4/mmm$), orthorhombic ($P2_12_12_1$ and $Pmmm$) and monoclinic distortions ($C2/m$, $P2/m$ and $P2_1$) of the cubic $P2_13$ phase. None of these models could satisfactorily fit the observed peak splitting of the cubic (440) peak. The only model that satisfactorily fitted the profile was a triclinic model, the details of which are presented below.

The fitted diffraction profile using the triclinic model for the data at 150 °C is shown in **Fig. 5.10** as a representative example, with the crystal and refinement parameters summarised in **Table 5.5**, refined structural parameters in **Table 5.6** and significant contact distances in **Table 5.7**.

(a)

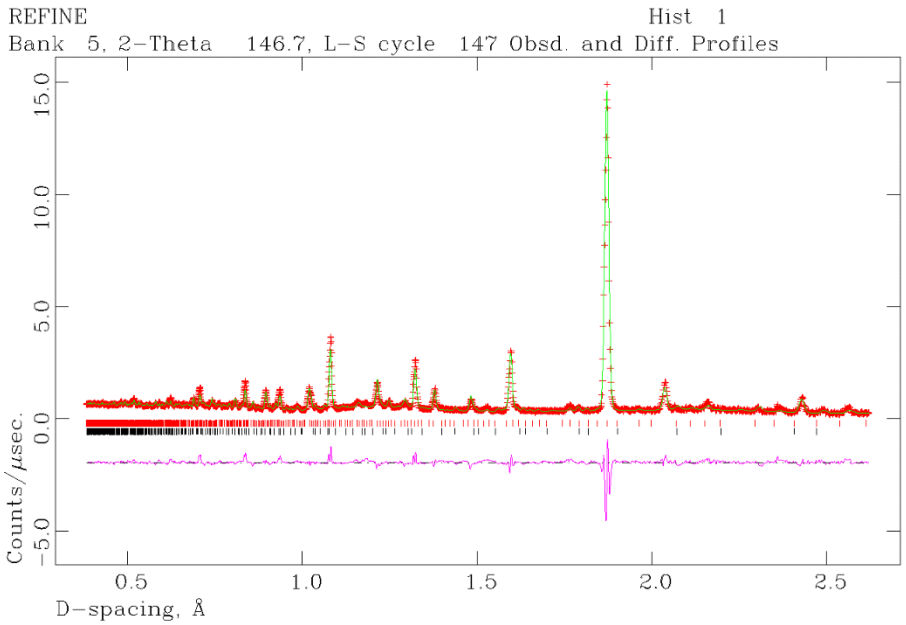

(b)

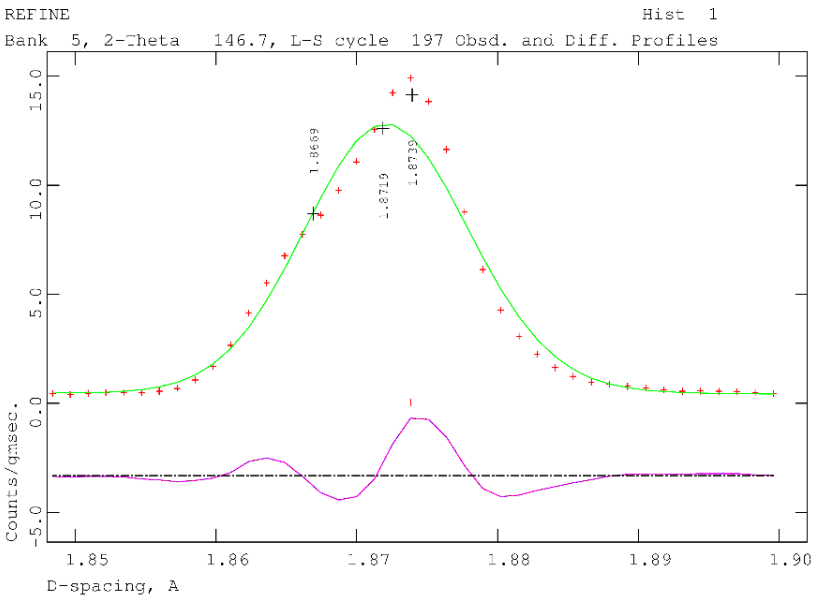

Fig. 5.9. (a) Fitted neutron diffraction profile for $Ce_2Zr_2O_{7+\delta}$ at 150 °C in flowing O_2. Fit performed using a cubic model in space group $P2_13$ with a = 10.5811(5) Å and (b) detail of the fit showing splitting of the cubic 440 peak. Observed (red + symbols), calculated (green line) and difference (violet line) profiles are shown. Reflection positions are indicated by markers.

(a)

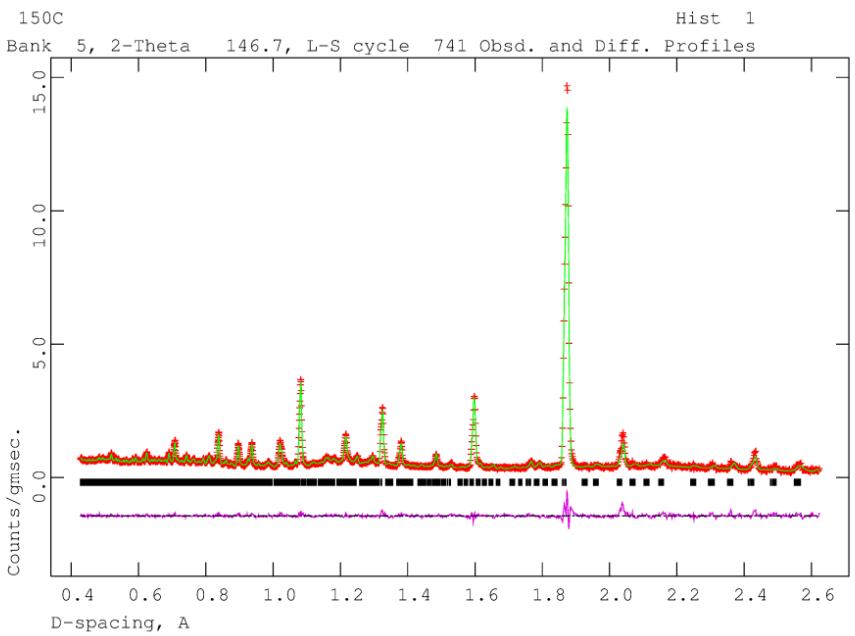

(b)

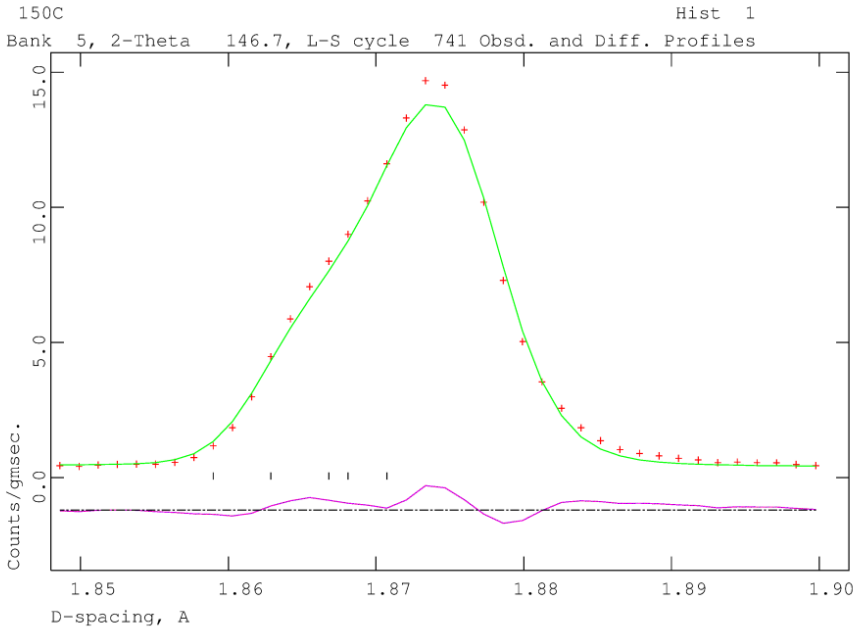

Fig. 5.10. (a) Fitted neutron diffraction profile for $Ce_2Zr_2O_{7+\delta}$ at 150 °C in flowing O_2 using a triclinic model and (b) detail of the fit showing fit to split cubic 440 peak. Observed (red + symbols), calculated (green line) and difference (violet line) profiles are shown. Reflection positions are indicated by markers.

Table 5.5. Crystal and refinement parameters for $Ce_2Zr_2O_{7+\delta}$ at 150 °C in flowing O_2. Estimated standard deviations are given in parentheses.

Formula	$Ce_2Zr_2O_{7.44(2)}$
M_r (g mol^{-1})	574.68
Crystal system	Triclinic
Space group	*P*-1
Lattice parameters:	*a* = 10.6004(10) Å, *b* = 10.5520(8) Å, *c* = 10.5911(13) Å α = 90.346(7)°, β = 89.878(10)°, γ = 89.859(8)°
Volume (Å^3)	1184.6(2)
Z	8
D_{calc} (g cm^{-3})	6.523
Temperature (°C)	150
Atmosphere	Flowing O_2
R-factors:	
Neutron back scattering data	R_{wp} = 0.0375
	R_p = 0.0571
	R_{ex} = 0.0240
	R_F2 = 0.0731
χ^2	2.632
Total no. of variables	187
No. of profile points	2592
No. of reflections	33252

Table 5.6. Refined structural parameters for $Ce_2Zr_2O_{7+\delta}$ at 150 °C in flowing O_2. Estimated standard deviations are given in parentheses.

Atom	Site	*x*	*y*	*z*	Occ.	U_{iso} (Å^2)
Ce(1)	1*a*	0.0	0.0	0.0	1.0	0.0062(13)
Ce(2)	2*i*	0.504(7)	0.253(8)	0.749(9)	1.0	0.0062(13)
Ce(3)	2*i*	0.752(8)	0.500(8)	0.251(8)	1.0	0.0062(13)
Ce(4)	2*i*	0.245(9)	0.749(9)	0.503(10)	1.0	0.0062(13)
Ce(5)	2*i*	-0.004(11)	0.246(8)	0.257(8)	1.0	0.0062(13)
Ce(6)	2*i*	0.254(8)	-0.001(9)	0.249(7)	1.0	0.0062(13)
Ce(7)	2*i*	0.246(8)	0.252(7)	0.005(8)	1.0	0.0062(13)
Ce(8)	1*f*	0.5	0.0	0.5	1.0	0.0062(13)
Ce(9)	1*e*	0.5	0.5	0.0	1.0	0.0062(13)
Ce(10)	1*g*	0.0	0.5	0.5	1.0	0.0062(13)
Zr(1)	1*h*	0.5	0.5	0.5	1.0	0.0064(9)
Zr(2)	2*i*	-0.008(5)	0.758(5)	0.258(5)	1.0	0.0064(9)
Zr(3)	2*i*	0.261(6)	-0.005(6)	0.759(4)	1.0	0.0064(9)
Zr(4)	2*i*	0.762(5)	0.260(5)	-0.008(5)	1.0	0.0064(9)
Zr(5)	2*i*	0.504(7)	0.750(6)	0.753(6)	1.0	0.0064(9)
Zr(6)	2*i*	0.746(5)	0.506(6)	0.744(5)	1.0	0.0064(9)
Zr(7)	2*i*	0.756(5)	0.756(6)	0.492(5)	1.0	0.0064(9)

Table 5.6 Continued

Zr(8)	1*c*	0.0	0.5	0.0	1.0	0.0064(9)
Zr(9)	1*b*	0.0	0.0	0.5	1.0	0.0064(9)
Zr(10)	1*d*	0.5	0.0	0.0	1.0	0.0064(9)
O(1)	2*i*	0.377(7)	0.878(5)	0.377(6)	1.0	0.0061(6)
O(2)	2*i*	0.386(5)	0.386(5)	0.866(5)	1.0	0.0061(6)
O(3)	2*i*	0.123(8)	0.617(6)	0.616(6)	1.0	0.0061(6)
O(4)	2*i*	0.122(7)	0.125(6)	0.122(6)	1.0	0.0061(6)
O(5)	2*i*	0.396(10)	0.868(10)	0.869(10)	0.52(23)	0.0061(6)
O(6)	2*i*	0.385(9)	0.377(10)	0.368(9)	0.74(23)	0.0061(6)
O(7)	2*i*	0.097(18)	0.677(22)	0.174(23)	0.20(12)	0.0061(6)
O(8)	2*i*	0.106(8)	0.122(10)	0.628(10)	0.54(24)	0.0061(6)
O(9)	2*i*	0.134(7)	0.877(6)	0.617(5)	1.0	0.0061(6)
O(10)	2*i*	0.131(6)	0.130(4)	0.832(5)	1.0	0.0061(6)
O(11)	2*i*	0.123(7)	0.634(6)	0.360(5)	1.0	0.0061(6)
O(12)	2*i*	0.127(8)	0.861(6)	0.131(6)	1.0	0.0061(6)
O(13)	2*i*	0.357(5)	0.121(6)	0.628(6)	1.0	0.0061(6)
O(14)	2*i*	0.370(8)	0.623(8)	0.633(9)	0.80(23)	0.0061(6)
O(15)	2*i*	0.133(5)	0.438(4)	0.133(4)	1.0	0.0061(6)
O(16)	2*i*	0.133(6)	0.122(6)	0.420(5)	1.0	0.0061(6)
O(17)	2*i*	0.128(5)	0.639(5)	0.935(4)	1.0	0.0061(6)
O(18)	2*i*	0.126(7)	0.357(6)	0.624(6)	1.0	0.0061(6)
O(19)	2*i*	0.347(6)	0.629(6)	0.134(6)	1.0	0.0061(6)
O(20)	2*i*	0.371(7)	0.124(6)	0.138(6)	0.96(23)	0.0061(6)
O(21)	2*i*	0.129(7)	0.877(5)	0.361(5)	1.0	0.0061(6)
O(22)	2*i*	0.166(5)	0.872(6)	0.867(6)	1.0	0.0061(6)
O(23)	2*i*	0.373(8)	0.616(6)	0.378(6)	1.0	0.0061(6)
O(24)	2*i*	0.367(7)	0.378(5)	0.580(5)	1.0	0.0061(6)
O(25)	2*i*	0.373(8)	0.872(6)	0.648(6)	1.0	0.0061(6)
O(26)	2*i*	0.363(7)	0.114(6)	0.879(6)	1.0	0.0061(6)
O(27)	2*i*	0.100(4)	0.382(5)	0.856(5)	1.0	0.0061(6)
O(28)	2*i*	0.147(7)	0.381(7)	0.372(6)	1.0	0.0061(6)
O(29)	2*i*	0.367(7)	0.882(6)	0.107(5)	1.0	0.0061(6)
O(30)	2*i*	0.371(7)	0.149(5)	0.371(6)	1.0	0.0061(6)
O(31)	2*i*	0.376(7)	0.637(6)	0.869(7)	1.0	0.0061(6)
O(32)	2*i*	0.374(8)	0.368(7)	0.138(6)	1.0	0.0061(6)

Table 5.7. Significant contact distances in $Ce_2Zr_2O_{7+\delta}$ at 150 °C in flowing O_2. Estimated standard deviations are given in parentheses.

Contact	Distance (Å)	Contact	Distance (Å)
Ce(1)-O(4)	2.25(7)	Zr(1)-O(6)	2.26(10)
Ce(1)-O(4)	2.25(7)	Zr(1)-O(6)	2.26(10)
Ce(1)-O(10)	2.65(5)	Zr(1)-O(14)	2.35(8)
Ce(1)-O(10)	2.65(5)	Zr(1)-O(14)	2.35(8)
Ce(1)-O(12)	2.43(7)	Zr(1)-O(23)	2.23(8)
Ce(1)-O(12)	2.43(7)	Zr(1)-O(23)	2.23(8)
Ce(1)-O(22)	2.61(6)	Zr(1)-O(24)	2.09(7)
Ce(1)-O(22)	2.61(6)	Zr(1)-O(24)	2.09(7)
Ce(2)-O(1)	2.29(9)	Zr(2)-O(7)	1.66(18)
Ce(2)-O(2)	2.25(9)	Zr(2)-O(8)	2.03(9)
Ce(2)-O(13)	2.45(9)	Zr(2)-O(10)	2.00(8)
Ce(2)-O(19)	2.36(10)	Zr(2)-O(11)	2.20(9)
Ce(2)-O(23)	2.34(12)	Zr(2)-O(12)	2.25(9)
Ce(2)-O(24)	2.67(11)	Zr(2)-O(18)	2.15(9)
Ce(2)-O(26)	2.51(11)	Zr(2)-O(21)	2.21(7)
Ce(2)-O(29)	2.49(10)	Zr(2)-O(27)	2.14(7)
Ce(3)-O(2)	2.27(11)	Zr(3)-O(5)	2.29(13)
Ce(3)-O(3)	2.29(11)	Zr(3)-O(8)	2.53(11)
Ce(3)-O(14)	2.21(12)	Zr(3)-O(9)	2.38(8)
Ce(3)-O(17)	2.75(10)	Zr(3)-O(10)	2.11(7)
Ce(3)-O(18)	2.39(11)	Zr(3)-O(13)	2.18(9)
Ce(3)-O(24)	2.54(10)	Zr(3)-O(22)	2.01(8)
Ce(3)-O(27)	2.30(10)	Zr(3)-O(25)	2.11(9)
Ce(3)-O(31)	2.36(12)	Zr(3)-O(26)	2.09(8)
Ce(4)-O(1)	2.37(10)	Zr(4)-O(5)	2.61(12)
Ce(4)-O(3)	2.25(12)	Zr(4)-O(7)	2.41(23)
Ce(4)-O(9)	2.15(11)	Zr(4)-O(12)	2.17(8)
Ce(4)-O(11)	2.33(12)	Zr(4)-O(17)	1.76(7)
Ce(4)-O(14)	2.33(16)	Zr(4)-O(19)	2.13(8)
Ce(4)-O(21)	2.37(13)	Zr(4)-O(22)	2.19(8)
Ce(4)-O(23)	2.36(11)	Zr(4)-O(29)	2.29(9)
Ce(4)-O(25)	2.42(13)	Zr(4)-O(31)	2.33(7)
Ce(5)-O(3)	2.34(9)	Zr(5)-O(5)	2.08(12)
Ce(5)-O(4)	2.33(11)	Zr(5)-O(6)	2.19(11)
Ce(5)-O(9)	2.32(12)	Zr(5)-O(14)	2.33(12)
Ce(5)-O(15)	2.82(11)	Zr(5)-O(20)	2.20(11)
Ce(5)-O(16)	2.62(10)	Zr(5)-O(25)	2.19(11)
Ce(5)-O(17)	2.71(9)	Zr(5)-O(30)	2.15(9)
Ce(5)-O(22)	2.50(13)	Zr(5)-O(31)	2.19(10)
Ce(5)-O(28)	2.46(15)	Zr(5)-O(32)	2.14(10)
Ce(6)-O(1)	2.28(11)	Zr(6)-O(6)	2.21(12)
Ce(6)-O(4)	2.36(10)	Zr(6)-O(7)	2.69(26)

Table 5.7. Continued

Ce(6)-O(12)	2.35(11)	Zr(6)-O(11)	2.30(8)
Ce(6)-O(16)	2.55(9)	Zr(6)-O(15)	1.92(8)
Ce(6)-O(20)	2.16(12)	Zr(6)-O(19)	2.17(9)
Ce(6)-O(21)	2.20(11)	Zr(6)-O(23)	2.22(9)
Ce(6)-O(29)	2.28(10)	Zr(6)-O(28)	2.05(8)
Ce(6)-O(30)	2.39(11)	Zr(6)-O(32)	2.22(9)
Ce(7)-O(2)	2.53(10)	Zr(7)-O(6)	2.53(11)
Ce(7)-O(4)	2.26(11)	Zr(7)-O(8)	2.33(12)
Ce(7)-O(10)	2.54(10)	Zr(7)-O(13)	2.18(9)
Ce(7)-O(15)	2.66(9)	Zr(7)-O(16)	1.98(9)
Ce(7)-O(20)	2.37(12)	Zr(7)-O(18)	2.12(8)
Ce(7)-O(26)	2.32(9)	Zr(7)-O(24)	2.08(8)
Ce(7)-O(27)	2.60(9)	Zr(7)-O(28)	2.29(9)
Ce(7)-O(32)	2.31(12)	Zr(7)-O(30)	2.22(9)
Ce(8)-O(1)	2.24(6)	Zr(8)-O(7)	2.81(20)
Ce(8)-O(1)	2.24(6)	Zr(8)-O(7)	2.81(20)
Ce(8)-O(13)	2.40(5)	Zr(8)-O(15)	2.10(6)
Ce(8)-O(13)	2.40(5)	Zr(8)-O(15)	2.10(6)
Ce(8)-O(25)	2.47(8)	Zr(8)-O(17)	2.11(6)
Ce(8)-O(25)	2.47(8)	Zr(8)-O(17)	2.11(6)
Ce(8)-O(30)	2.49(6)	Zr(8)-O(27)	2.22(5)
Ce(8)-O(30)	2.49(6)	Zr(8)-O(27)	2.22(5)
Ce(9)-O(2)	2.22(6)	Zr(9)-O(8)	2.18(11)
Ce(9)-O(2)	2.22(6)	Zr(9)-O(8)	2.18(11)
Ce(9)-O(19)	2.54(6)	Zr(9)-O(9)	2.29(7)
Ce(9)-O(19)	2.54(6)	Zr(9)-O(9)	2.29(7)
Ce(9)-O(31)	2.40(7)	Zr(9)-O(16)	2.09(7)
Ce(9)-O(31)	2.40(7)	Zr(9)-O(16)	2.09(7)
Ce(9)-O(32)	2.43(9)	Zr(9)-O(21)	2.38(6)
Ce(9)-O(32)	2.43(9)	Zr(9)-O(21)	2.38(6)
Ce(10)-O(3)	2.18(7)	Zr(10)-O(5)	2.25(12)
Ce(10)-O(3)	2.18(7)	Zr(10)-O(5)	2.25(12)
Ce(10)-O(11)	2.44(7)	Zr(10)-O(20)	2.38(6)
Ce(10)-O(11)	2.44(7)	Zr(10)-O(20)	2.38(6)
Ce(10)-O(18)	2.41(8)	Zr(10)-O(26)	2.28(6)
Ce(10)-O(18)	2.41(8)	Zr(10)-O(26)	2.28(6)
Ce(10)-O(28)	2.41(7)	Zr(10)-O(29)	2.20(7)
Ce(10)-O(28)	2.41(7)	Zr(10)-O(29)	2.20(7)

The structure contains 10 Ce and 10 Zr crystallographically unique atoms each within a distorted cubic site. The Ce-O contact distances range from 2.15 to 2.82 Å, with a weighted average of 2.41(10) Å, while Zr-O contacts range from 1.66 to 2.81 Å, with a

weighted average of 2.19(12) Å. Each of the Ce and Zr coordination environments are illustrated in **Fig. 5.11** and **Fig. 5.12**, respectively.

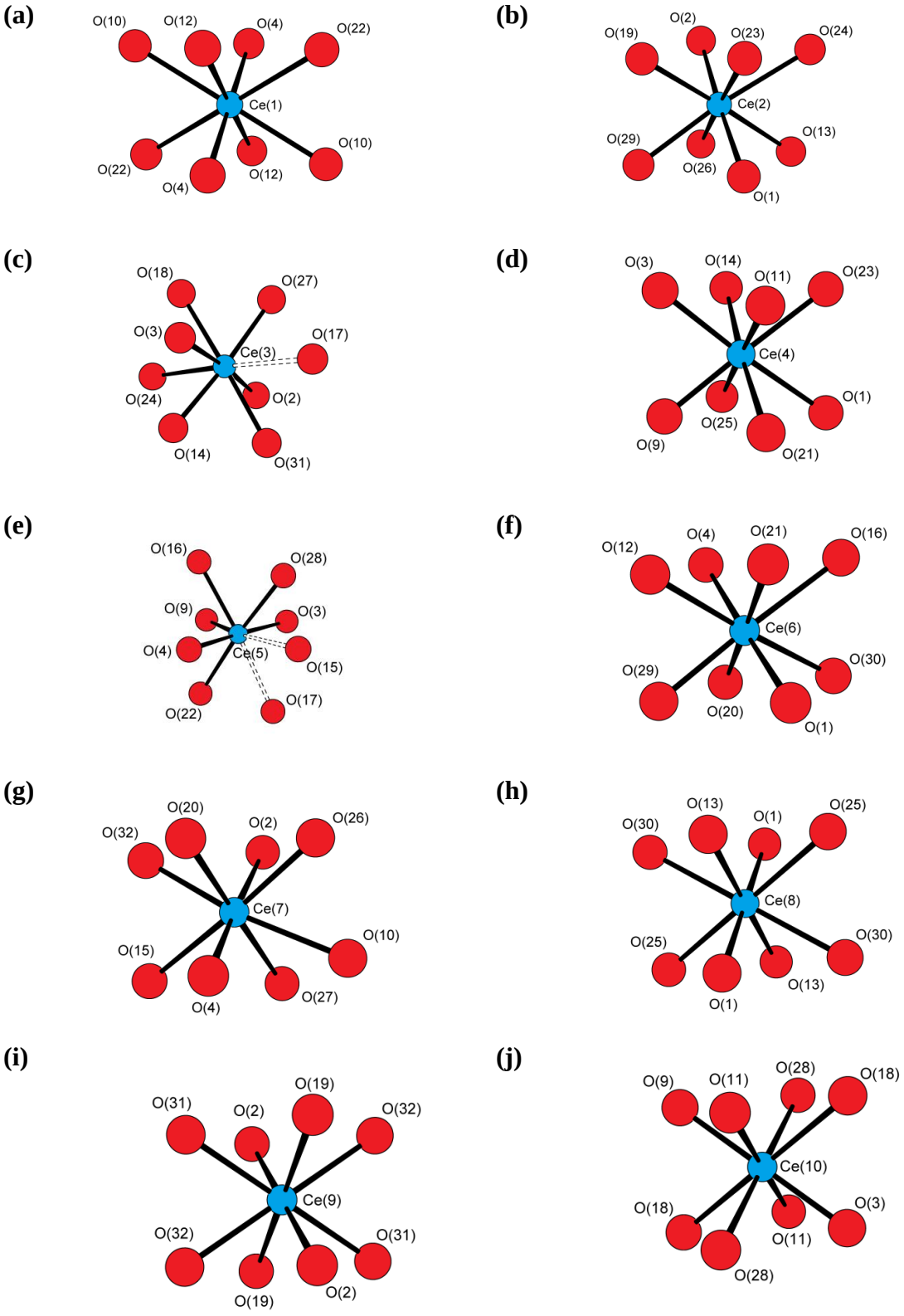

Fig. 5.11. Cerium coordination geometries in $Ce_2Zr_2O_{7+\delta}$ at 150 °C in flowing O_2.

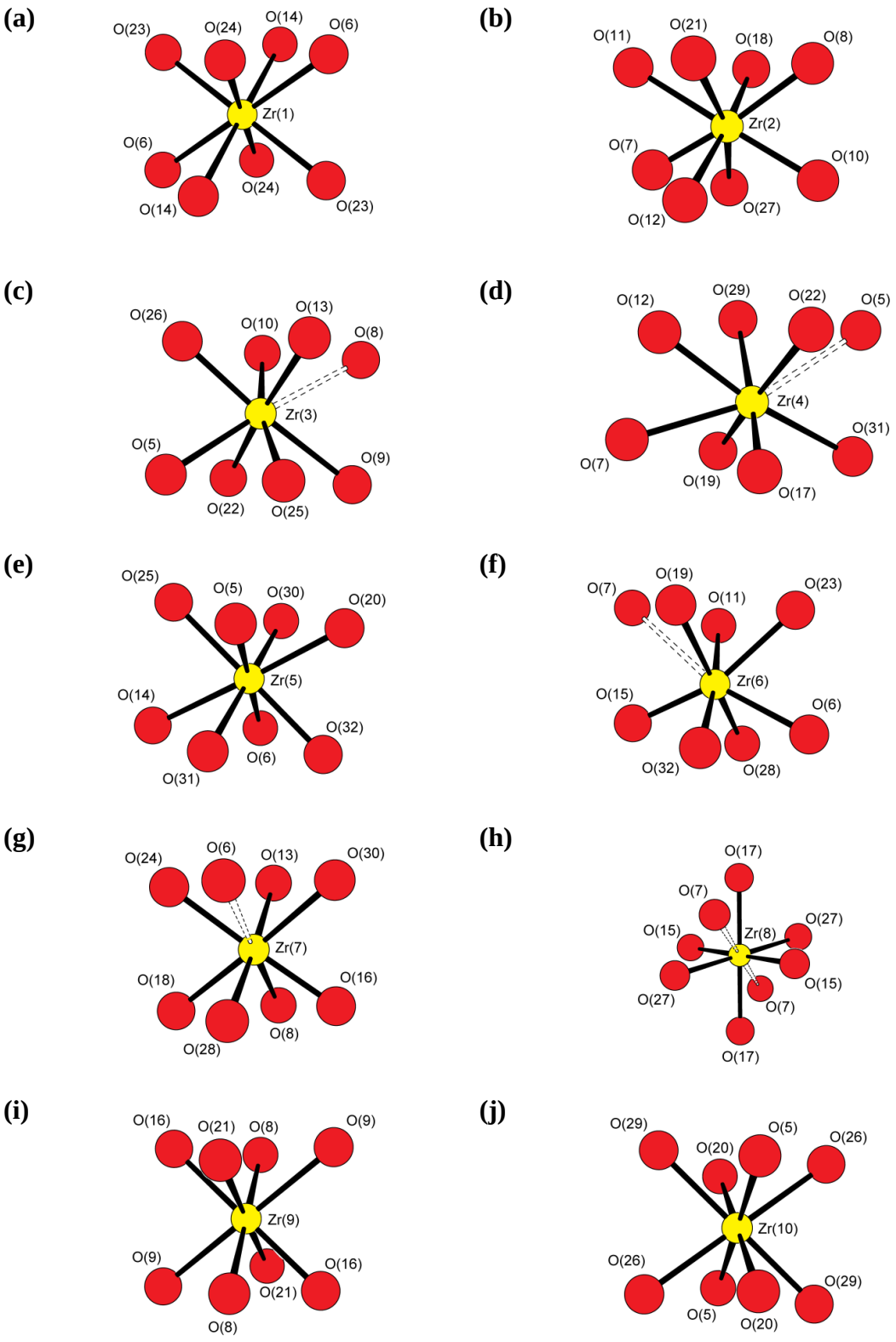

Fig. 5.12. Zirconium coordination geometries in $Ce_2Zr_2O_{7+\delta}$ at 150 °C in flowing O_2.

It is observed that Ce(3), Zr(3), Zr(4), Zr(6) and Zr(7) adopt seven-coordinate geometries with oxygen atoms, with the eighth contact essentially a non-bonding interaction. In the cases of Ce(5) and Zr(8), six-coordinate geometries are observed, giving trigonal prismatic and distorted octahedral geometries, respectively. Additionally, the partial occupancies of O(5), O(6), O(7), O(8), O(14) and O(20) lower coordination numbers even further (**Table 5.8**).

Table 5.8. Cation coordination numbers in $Ce_2Zr_2O_{7+\delta}$ at 150 °C in flowing O_2.

Atom	CN	Atom	CN	Atom	CN	Atom	CN	Atom	CN
Ce(1)	8.00	Ce(2)	8.00	Ce(3)	6.80	Ce(4)	7.80	Ce(5)	6.00
Ce(6)	7.96	Ce(7)	7.96	Ce(8)	8.00	Ce(9)	8.00	Ce(10)	8.00
Zr(1)	7.08	Zr(2)	7.20	Zr(3)	7.00	Zr(4)	6.20	Zr(5)	7.02
Zr(6)	6.74	Zr(7)	6.54	Zr(8)	6.00	Zr(9)	6.08	Zr(10)	6.96

The values in **Table 5.8** give average coordination numbers of 7.7(7) and 6.7(4) for Ce and Zr, respectively. Due to the relatively short data collection time of the runs in this study, the values of the site occupancies and hence the derived coordination numbers, must be treated cautiously. Nevertheless, the numbers appear to be consistent with those expected for a partially stuffed pyrochlore, where additional oxygen is present in the interstitial site (corresponding to the 8*b* site in the cubic $Fd\bar{3}m$ structure).

On further heating the sample above 410 °C, a transition occurs from the triclinic phase to a cubic phase, corresponding to the κ-phase (space group $P2_13$). The data at 750 °C were collected for 373 μA h and represent a high quality data set. The fitted neutron diffraction profile of the sample at 750 °C is shown in **Fig. 5.13**, with the corresponding crystal and refinement parameters in **Table 5.9** and the refined structural parameters and significant contact distances in **Table 5.10**.

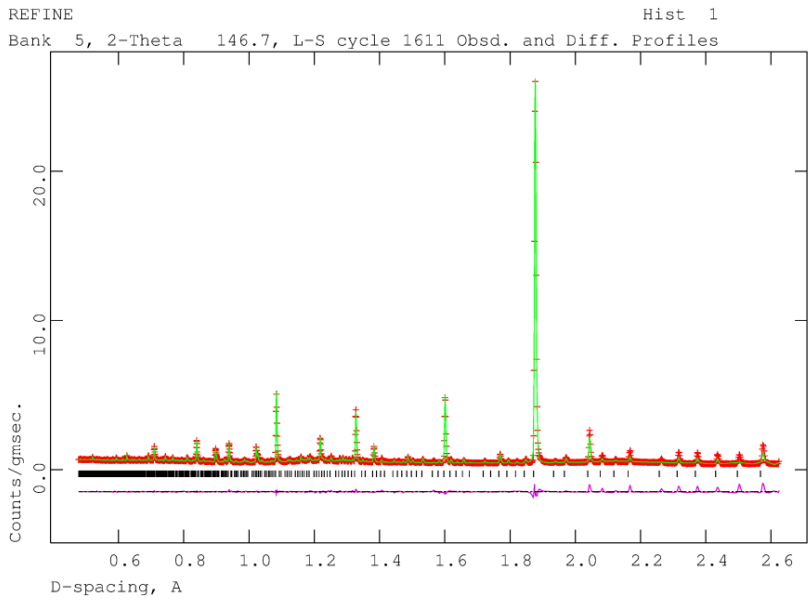

Fig. 5.13. Fitted neutron diffraction profile for κ-$CeZrO_{4-\delta}$ at 750 °C in flowing O_2. Observed (red + symbols), calculated (green line) and difference (violet line) profiles are shown. Reflection positions are indicated by markers.

Table 5.9. Crystal and refinement parameters for κ-$Ce_2Zr_2O_{7+\delta}$ at 750 °C in flowing O_2. Estimated standard deviations are given in parentheses.

Formula	$Ce_2Zr_2O_{7.41(3)}$
M_r (g mol^{-1})	581.24
Crystal system	Cubic
Space group	$P2_13$
Lattice parameter (Å)	a = 10.6127(2)
Volume (Å^3)	1195.29(5)
Z	8
D_{calc} (g cm^{-3})	6.457
Temperature (°C)	750
Atmosphere	Flowing O_2
R-factors:	
Neutron back scattering data	R_{wp} = 0.0260
	R_p = 0.0449
	R_{ex} = 0.0058
	R_F2 = 0.0679
χ^2	20.73
Total no. of variables	71
No. of profile points	2433
No. of reflections	2209

Table 5.10. (a) Refined structural parameters and (b) significant contact distances for κ-$Ce_2Zr_2O_{7+\delta}$ at 750 °C in flowing O_2. Estimated standard deviations are given in parentheses.

(a)

Atom	Site	*x*	*y*	*z*	Occ.	U_{iso} (Å^2)
Ce(1)	4*a*	0.1317(10)	0.1317(10)	0.1317(10)	1.0	0.0148(8)
Ce(2)	12*b*	0.1274(9)	0.3750(11)	0.3750(9)	1.0	0.0148(8)
Zr(1)	4*a*	0.6168(7)	0.6168(7)	0.6168(7)	1.0	0.0149(5)
Zr(2)	12*b*	0.6164(6)	0.8807(8)	0.8795(6)	1.0	0.0149(6)
O(1)	4*a*	0.0064(10)	0.0064(10)	0.0064(10)	1.0	0.0155(4)
O(2)	4*a*	0.2476(9)	0.2476(9)	0.2476(9)	0.84(3)	0.0155(4)
O(3)	4*a*	0.4899(7)	0.4899(7)	0.4899(7)	1.0	0.0155(4)
O(4)	4*a*	0.7701(14)	0.7701(14)	0.7701(14)	0.43(3)	0.0155(4)
O(5)	12*b*	0.2551(7)	0.2631(6)	-0.0519(4)	1.0	0.0155(4)
O(6)	12*b*	0.2471(8)	0.2448(9)	0.5095(5)	0.85(2)	0.0155(4)
O(7)	12*b*	0.0159(11)	0.0003(7)	0.2620(6)	1.0	0.0155(4)
O(8)	12*b*	0.0015(9)	0.0014(7)	0.7526(5)	1.0	0.0155(4)

(b)

Contact	Distance (Å)	Contact	Distance (Å)
Ce(1)-O(1)	2.303(26)	Zr1-O(3)	2.333(20)
Ce(1)-O(2)	2.130(25)	Zr1-O(4)	2.819(27)
Ce(1)-O(5)	2.731(6) × 3	Zr1-O(5)	2.176(10)
Ce(1)-O(7)	2.401(12) × 3	Zr1-O(7)	2.166(10)
Ce(2)-O(1)	2.355(9)	Zr2-O(3)	2.130(6)
Ce(2)-O(2)	2.298(9)	Zr2-O(4)	2.320(6)
Ce(2)-O(5)	2.579(12)	Zr2-O(5)	2.018(10)
Ce(2)-O(6)	2.358(13)	Zr2-O(6)	2.241(13)
Ce(2)-O(6)′	2.331(17)	Zr2-O(6)′	2.359(11)
Ce(2)-O(7)	2.440(13)	Zr2-O(7)	2.172(12)
Ce(2)-O(8)	2.268(12)	Zr2-O(8)	2.326(10)
Ce(2)-O(8)′	2.297(14)	Zr2-O(8)′	2.254(12)

The cation coordination environments for this composition at 750°C are shown in **Fig. 5.14**.

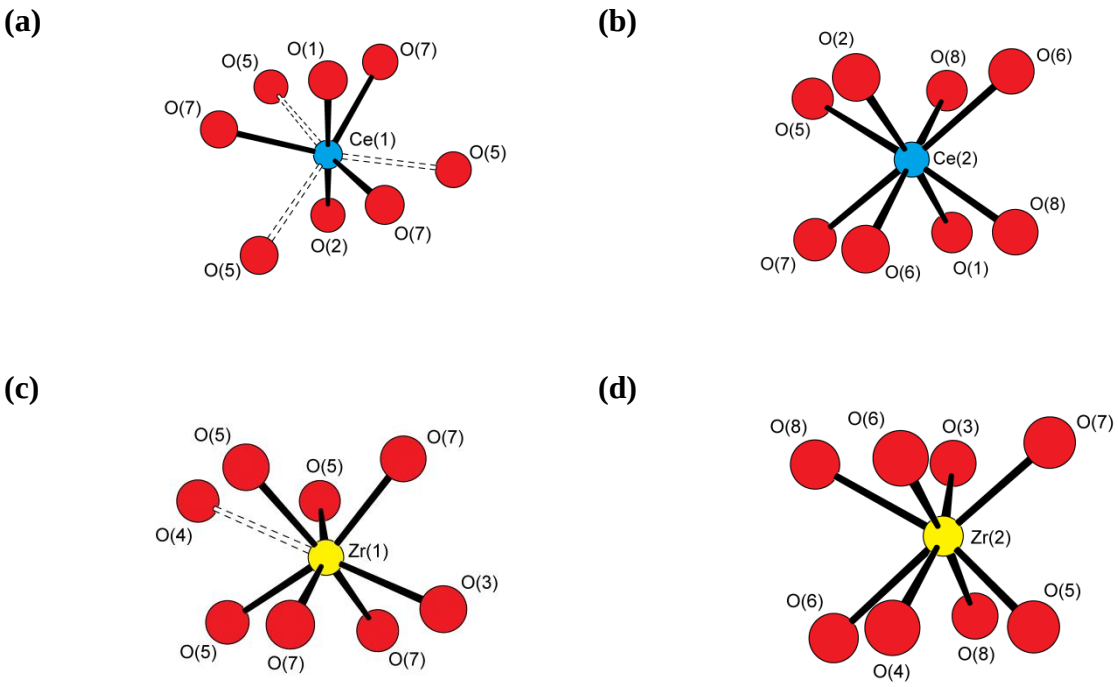

Fig. 5.14. Cation coordination environments in κ-$Ce_2Zr_2O_{7+\delta}$ at 750 °C in flowing O_2.

While all cations sit in cubic sites, it can be seen that Ce(1) and Zr(1), coordinate only 5 and 7 of the oxygen atoms, respectively. Taking into account the partial occupancy of O(2), O(4) and O(6), the cations Ce(1), Ce(2), Zr(1) and Zr(2) have a coordination numbers of 4.84, 7.54, 7.00 and 7.13, respectively. This gives average coordination numbers of 6.87 and 7.10 for Ce and Zr, respectively.

The variation of cubic unit cell parameter on heating in flowing O_2 is shown in **Fig. 5.15**. The lattice parameter is seen to drop sharply on the transition from the cubic phase to the triclinic phase at around 140 °C. There is a second significant drop, although not as great, on the transition from the triclinic phase to the cubic κ-phase.

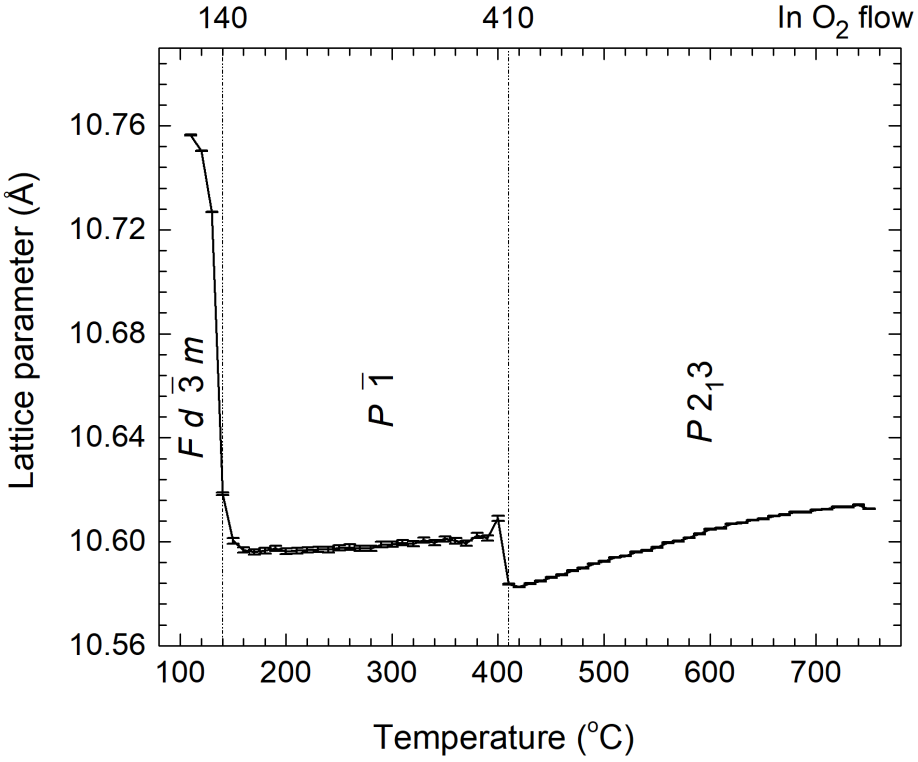

Fig. 5.15. Variation of cubic lattice parameter on heating $Ce_2Zr_2O_7$ from 100 °C to 750 °C in flowing O_2.

The variation in O content, *x*, per $Ce_2Zr_2O_x$ formula unit is shown in **Fig. 5.16**. There is a significant increase in oxygen content on the transition from the pyrochlore phase to the triclinic phase. This occurs at a point where there is a significant decrease in lattice parameter and hence volume, which is associated with the oxidation of Ce^{3+} to the smaller Ce^{4+}, with respective ionic radii of 1.143 and 0.97 Å, for the ions in eight coordinate geometry.[25] There is little significant change in oxygen content on the transition from the triclinic phase to the cubic κ-phase. This suggests that the change in lattice parameter seen in **Fig. 5.15** above is due to ordering processes, with the more disordered phase (triclinic) showing a larger volume than the more ordered cubic phase.

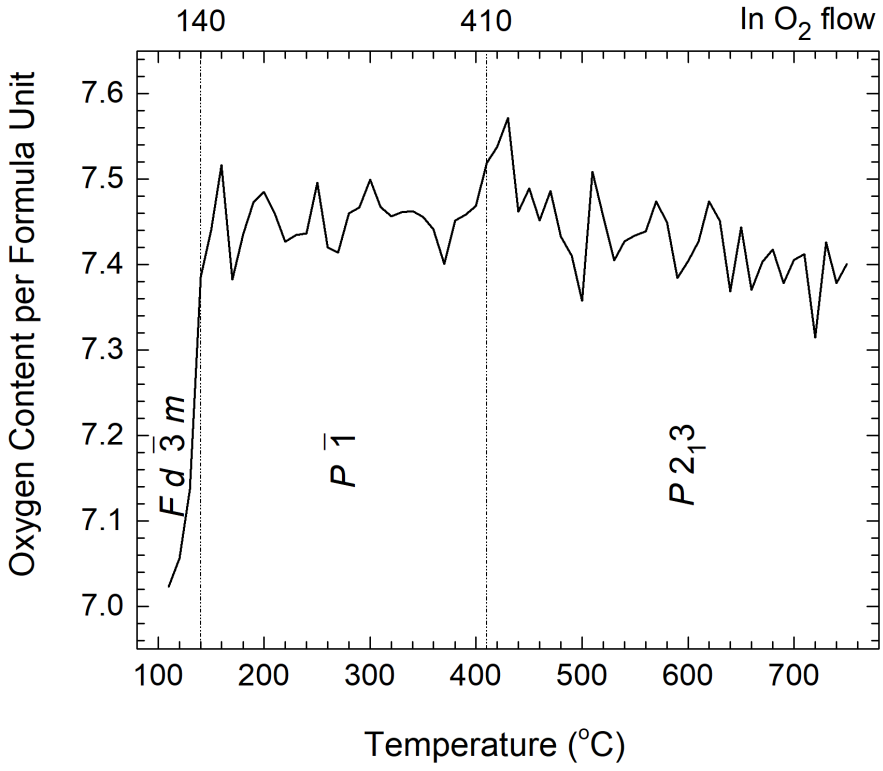

Fig. 5.16. Oxygen content per $Ce_2Zr_2O_x$ formula unit on heating in O_2, over the temperature range 110 to 750 °C.

5.3.2 Heating under CO

After cooling to 100 °C, the atmosphere was switched to flowing CO and the sample reheated in 10 °C steps up to 550 °C. **Fig. 5.17a** shows the neutron diffraction profiles over this temperature range, with detail shown in **Fig. 5.17b**. The κ-$CeZrO_{4-\delta}$ phase seen at 750 °C in flowing O_2, persists at 100 °C in flowing CO up to around 190 °C, where a second phase appears. This is evident in **Fig. 5.17b**, with a peak appearing at *ca*. 1.87 Å. This second phase was modelled on the β-$Ce_2Zr_2O_{7.5-\delta}$ phase in space group $F\bar{4}3m$, as seen on heating in flowing O_2. At around 260 °C, a third phase is evident with a peak at around 1.91 Å in **Fig. 5.17b**. The third phase corresponds to a pyrochlore phase in space group $Fd\bar{3}m$. At 290 °C the κ-phase has completely disappeared and at 310 °C the pyrochlore phase is pure (within the limits of the technique).

Fig. 5.18 shows the fitted diffraction profile for the sample at 550 °C in flowing CO, with the corresponding crystal and refinement parameters in **Table 5.11** and refined structural parameters and significant contact distances in **Table 5.12**. No attempt was made to model any cation disorder using these data. The refined oxygen content showed some deficiency on the 48*f* site suggesting some possible additional oxygen on the 8*a* site (0.125 0.125 0.125) is required to achieve electroneutrality, although this was not refined in the model.

(a)

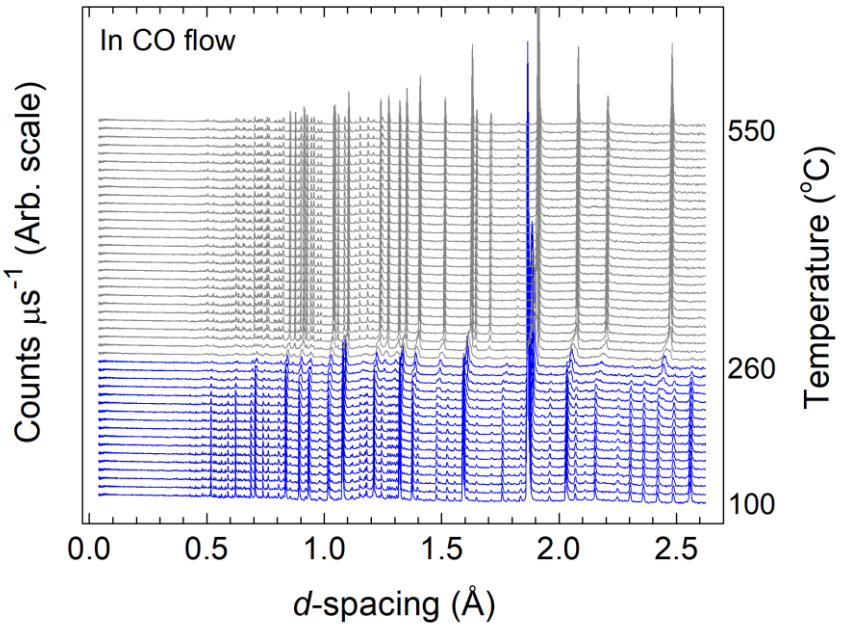

(b)

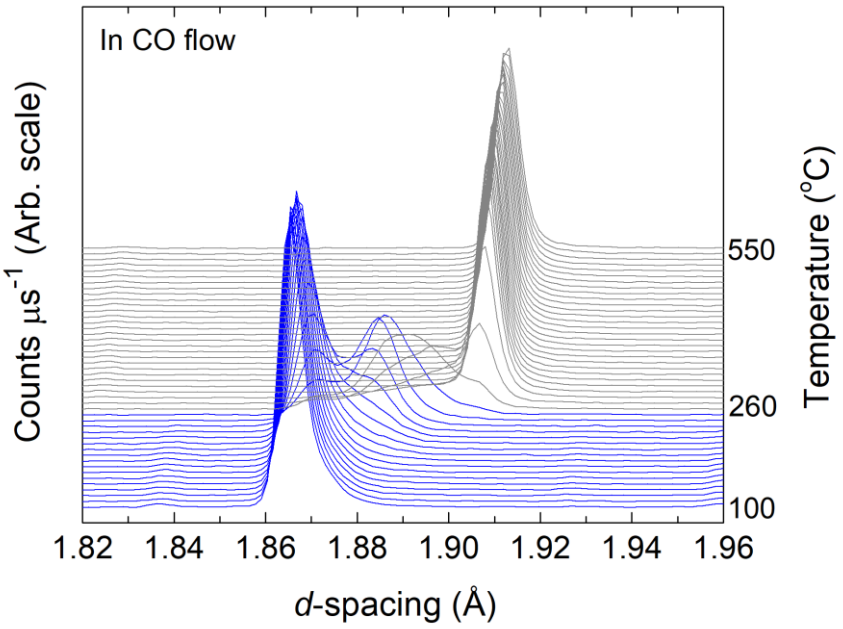

Fig. 5.17. Neutron diffraction patterns for κ-$CeZrO_{4-\delta}$ on heating in flowing CO showing (a) full backscattering data and (b) detail of the patterns in the region of the pyrochlore (440) peak. Low temperature (100 to 260 °C) and high temperature (270 to 550 °C) regions are indicated by blue and grey colours, respectively.

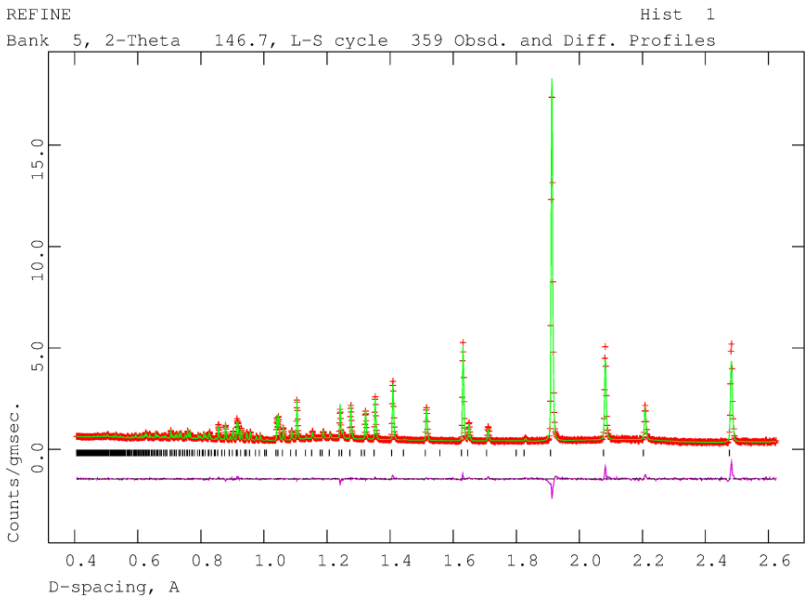

Fig. 5.18. Fitted neutron diffraction profile for $Ce_2Zr_2O_{7-\delta}$ at 550 °C in flowing CO. Observed (red + symbols), calculated (green line) and difference (violet line) profiles are shown. Reflection positions are indicated by markers.

Table 5.11. Crystal and refinement parameters for $Ce_2Zr_2O_{7-\delta}$ at 550 °C in flowing CO. Estimated standard deviations are given in parentheses.

Formula	$Ce_2Zr_2O_{6.77(2)}$
M_r (g mol^{-1})	571.03
Crystal system	Cubic
Space group	$Fd\bar{3}m$
Lattice parameter (Å)	a = 10.8137(2)
Volume (Å^3)	1264.53(6)
Z	8
D_{calc} (g cm^{-3})	5.999
Temperature (°C)	550
Atmosphere	Flowing CO
R-factors:	
Neutron back scattering data	R_{wp} = 0.0257
	R_p = 0.0400
	R_{ex} = 0.0173
	R_F2 = 0.1025
χ^2	2.42
Total no. of variables	45
No. of profile points	2668
No. of reflections	541

Table 5.12. Refined structural parameters and significant contact distances (Å) for $Ce_2Zr_2O_{7-\delta}$ at 550 °C in flowing CO. Estimated standard deviations are given in parentheses.

Atom	Site	*x*	*y*	*z*	Occ.	U_{iso} (Å^2)
Ce	16*d*	0.5	0.5	0.5	1.0	0.0130(2)
Zr	16*c*	0.0	0.0	0.0	1.0	0.0130(2)
O(1)	48*f*	0.33193(8)	0.125	0.125	0.962(5)	0.0173(3)
O(2)	8*b*	0.375	0.375	0.375	1.0	0.0173(3)

Ce-O(1)	2.6377(6)	× 6
Ce-O(2)	2.34125(3)	× 2
Zr-O(1)	2.1069(4)	× 6

The lattice parameter evolution on heating in CO is seen in **Fig. 5.19**. There is a simple thermal expansion of the cubic lattice from 100 °C to around 240 °C, where the lattice parameter sharply rises, until around 290 °C, corresponding to the appearance of the pyrochlore phase. Variation of the refined oxygen content *x* in the $Ce_2Zr_2O_x$ formula unit, during heating in flowing CO is shown in **Fig. 5.20**. The oxygen content is seen to drop dramatically at around 240 °C, corresponding to the point where the reduced $Fd\bar{3}m$ phase is formed.

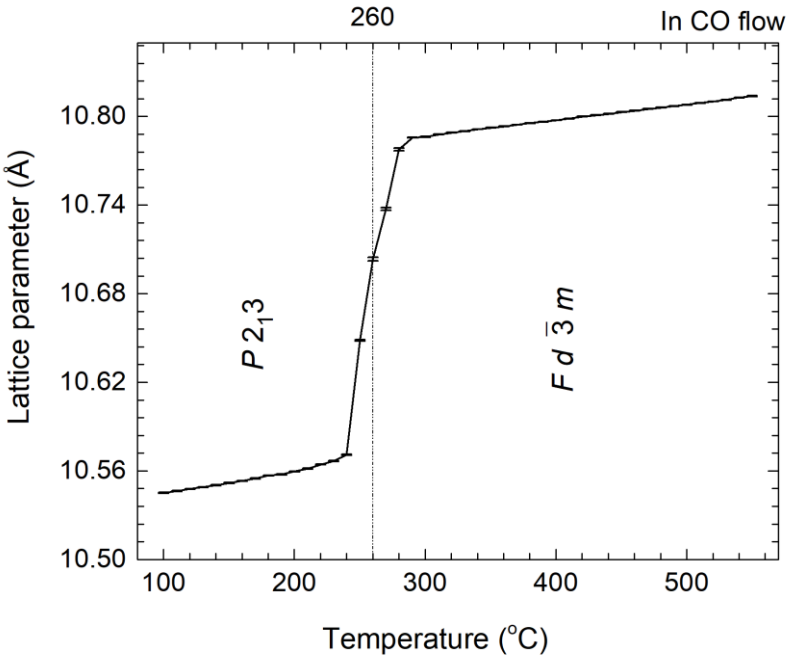

Fig. 5.19. Variation of cubic lattice parameter on heating κ-$CeZrO_{4-\delta}$ from 100 °C to 550 °C in flowing CO.

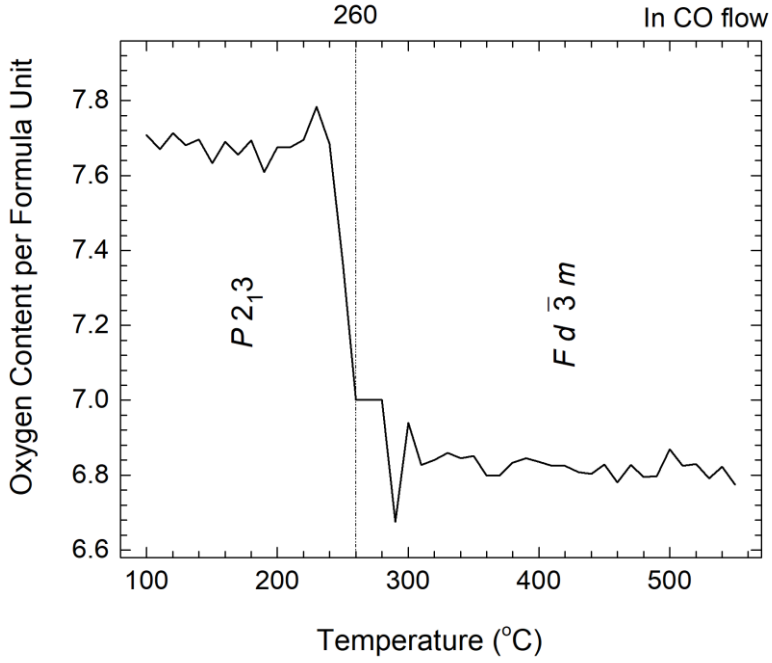

Fig. 5.20. Oxygen content per $Ce_2Zr_2O_x$ formula unit on heating in CO, over the temperature range 100 to 150 °C.

5.3.3 Room Temperature Structures

Long data collections were performed at room temperature on samples of fluorite-$Ce_2Zr_2O_7$, a sample of $Ce_2Zr_2O_7$ with partial pyrochlore ordering and κ-$CeZrO_{4-\delta}$ in order to obtain high quality data suitable for total scattering analysis. Prior to the total scattering analysis, the long range structures were characterised by Rietveld analysis using these data. The fitted diffraction profiles from the Rietveld analysis for each of the three samples are shown in **Fig. 5.21**, with the crystal and refinement parameters given in **Table 5.13**. The refined structural parameters and significant contact distances are given in **Tables 5.14, 5.15 and 5.16** for the fluorite- $Ce_2Zr_2O_7$, pyrochlore-$Ce_2Zr_2O_7$ and κ-$CeZrO_{4-\delta}$ structures, respectively.

(a)

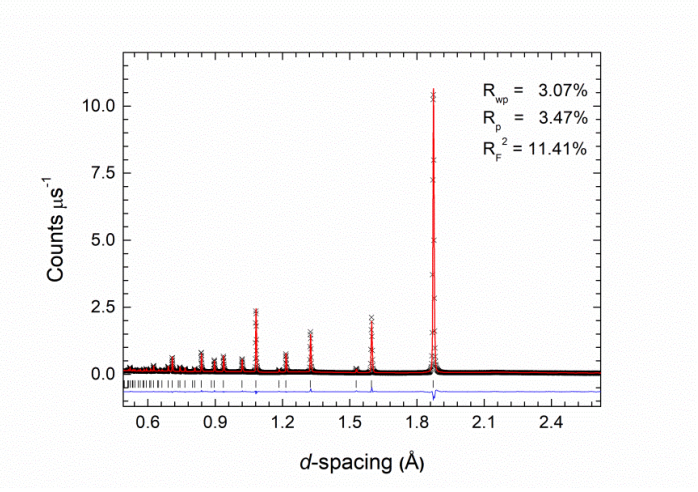

(b)

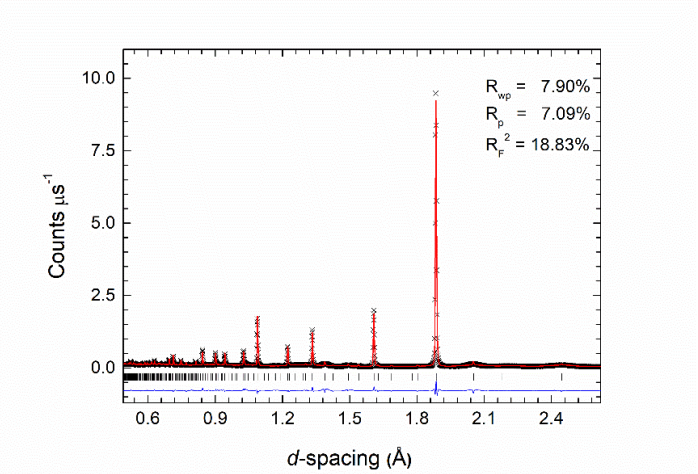

(c)

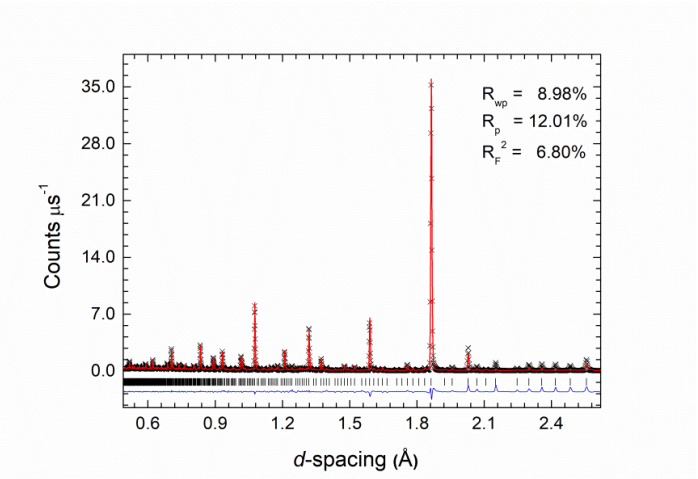

Fig. 5.21. Fitted back scattering neutron diffraction profiles for cerium zirconate samples at room temperature, (a) fluorite- $Ce_2Zr_2O_7$ ($Fm\bar{3}m$), (b) pyrochlore-$Ce_2Zr_2O_7$ ($Fd\bar{3}m$) and (c) κ-$CeZrO_{4-\delta}$ ($P2_13$). Observed (crosses), calculated (solid line), and difference (lower) profiles are shown. Reflection positions are indicated by markers.

Table 5.13. Crystal and refinement parameters for cerium zirconate samples (fluorite-$Ce_2Zr_2O_7$, pyrochlore-$Ce_2Zr_2O_7$ and κ-$CeZrO_{4-\delta}$) at room temperature. Estimated standard deviations are given in parentheses.

Chemical formula	$Ce_2Zr_2O_7$	$Ce_2Zr_2O_7$	$Ce_2Zr_2O_{7.48(5)}$
Phase	Fluorite	Pyrochlore	κ
M_r (g mol^{-1})	574.68	574.68	582.44
Crystal System	Cubic	Cubic	Cubic
Space group	$Fm\bar{3}m$	$Fd\bar{3}m$	$P2_13$
Lattice parameter (Å)	5.29408(5)	10.6512(8)	10.5338(2)
Volume (Å^3)	148.379(4)	1208.3(1)	1168.83(8)
Z	1	8	8
D_{calc} (g cm^{-3})	6.431	6.098	6.619
Temperature (°C)	20	20	20
Atmosphere	Vacuum	Vacuum	Vacuum
R-factors:			
Neutron backscattering	R_{wp} = 0.0305 R_p = 0.0349 R_{ex} = 0.0063 R_F^2 = 0.1150	R_{wp} = 0.0762 R_p = 0.0728 R_{ex} = 0.0081 R_F^2 = 0.1842	R_{wp} = 0.0898 R_p = 0.1201 R_{ex}= 0.0045 R_F^2 = 0.0680
χ^2	24.02	90.02	419.0
No. of variables	45	51	71
No. of profile points used	2760	2668	2433
No. of reflections	105	519	2165

Table 5.14. Refined atomic parameters and significant contact distances for fluorite-$Ce_2Zr_2O_7$ in space group $Fm\bar{3}m$. Estimated standard deviations are given in parentheses.

Atom	Site	*x*	*y*	*z*	Occ.	U_{iso} (Å^2)
Ce	4*a*	0.5	0.5	0.5	0.5	0.0089(1)
Zr	4*a*	0.0	0.0	0.0	0.5	0.0089(1)
O(1)	32*f*	0.2612(7)	0.2612(7)	0.2612(7)	0.21875	0.0189(6)

Ce-O(1)	2.260(2)
Ce-O(1)′	2.395(7)

Table 5.15. Refined atomic parameters and significant contact distances for pyrochlore-$Ce_2Zr_2O_7$ in space group $Fd\bar{3}m$ at room temperature. Estimated standard deviations are given in parentheses.

Atom	Site	*x*	*y*	*z*	Occ.	U_{iso} (Å^2)
Ce(1)	16*d*	0.5	0.5	0.5	0.62(3)	0.0083(3)
Ce(2)	16*c*	0.0	0.0	0.0	0.38(3)	0.0083(3)
Zr(1)	16*d*	0.5	0.5	0.5	0.38(3)	0.0083(3)
Zr(2)	16*c*	0.0	0.0	0.0	0.62(3)	0.0083(3)
O(1)	48*f*	0.3605(4)	0.125	0.125	0.70(2)	0.0252(9)
O(2)	8*b*	0.375	0.375	0.375	0.86(4)	0.0252(9)
O(3)	8*a*	0.125	0.125	0.125	0.69(3)	0.0252(9)

Ce/Zr(1)-O(1)	2.398(2)	× 6
Ce/Zr(1)-O(2)	2.30605(3)	× 2
Ce/Zr(2)-O(1)	2.221(2)	× 6
Ce/Zr(2)-O(3)	2.30605(3)	× 2

Table 5.16. (a) refined structural parameters and (b) significant contact distances for κ-$CeZrO_{4-\delta}$ in space group $P2_13$ at room temperature. Estimated standard deviations are given in parentheses.

(a)

Atom	Site	*x*	*y*	*z*	Occ.	U_{iso} (Å^2)
Ce(1)	4*a*	0.1328(9)	0.1328(9)	0.1328(9)	1.0	0.0037(7)
Ce(2)	12*b*	0.1284(8)	0.3755(10)	0.3730(7)	1.0	0.0037(7)
Zr(1)	4*a*	0.6166(6)	0.6166(6)	0.6166(6)	1.0	0.0054(5)
Zr(2)	12*b*	0.6165(6)	0.8801(7)	0.8811(5)	1.0	0.0054(5)
O(1)	4*a*	0.0029(8)	0.0029(8)	0.0029(8)	1.0	0.0051(3)
O(2)	4*a*	0.2430(5)	0.2430(5)	0.2430(5)	1.0	0.0051(3)
O(3)	4*a*	0.4838(8)	0.4838(8)	0.4838(8)	1.0	0.0051(3)
O(4)	4*a*	0.7685(7)	0.7685(7)	0.7685(7)	0.72(3)	0.0051(3)
O(5)	12*b*	0.2550(7)	0.2595(7)	-0.0504(5)	0.87(2)	0.0051(3)
O(6)	12*b*	0.2463(7)	0.2459(9)	0.5110(6)	0.88(2)	0.0051(3)
O(7)	12*b*	-0.0016(8)	-0.0032(7)	0.2624(5)	1.0	0.0051(3)
O(8)	12*b*	0.0005(8)	0.0026(4)	0.7532(5)	1.0	0.0051(3)

Table 5.16. Continued

(b)

Contact	Distance (Å)	Contact	Distance (Å)
Ce(1)-O(1)	2.369(22)	Zr1-O(3)	2.241(17)
Ce(1)-O(2)	2.012(19)	Zr(1)-O(4)	2.772(15)
Ce(1)-O(5)	2.677(6) × 3	Zr(1)-O(5) × 3	2.140(10) × 3
Ce(1)-O(7)	2.433(9) × 3	Zr(1)-O(7) × 3	2.145(8) × 3
Ce(2)-O(1)	2.329(7)	Zr(2)-O(3)	2.125(6)
Ce(2)-O(2)	2.298(6)	Zr(2)-O(4)	2.314(5)
Ce(2)-O(5)	2.567(10)	Zr(2)-O(5)	2.038(10)
Ce(2)-O(6)	2.349(11)	Zr(2)-O(6)	2.230(11)
Ce(2)-O(6)′	2.313(14)	Zr(2)-O(6)′	2.319(10)
Ce(2)-O(7)	2.335(13)	Zr(2)-O(7)	2.170(10)
Ce(2)-O(8)	2.237(9)	Zr(2)-O(8)	2.306(7)
Ce(2)-O(8)′	2.311(12)	Zr(2)-O(8)′	2.228(9)

The diffraction pattern of the fluorite structured composition (**Fig. 5.21a**) shows no evidence of pyrochlore ordering. As seen in the $Yb_{1-x}Nd_xZr_2O_7$ system (Chapter 3) the fluorite structure shows oxide ions located on the 32*f* site within the tetrahedral cavity of the ccp lattice. The displacement of the 32*f* site from the tetrahedral site centre at 0.25, 0.25, 0.25 is around 0.10 Å, which is smaller than seen in the fluorite structured compositions in the $Yb_{1-x}Nd_xZr_2O_7$ system and indicates less cation site distortion than in the system with three different cations occupying the 4*a* site. When refined freely, the oxygen site occupancy gave a value close to the calculated value and in the final refinements was fixed at the stoichiometric value.

Comparison of the diffraction patterns in **Fig. 5.21a** and **Fig. 5.21b** reveals that although very similar, the pyrochlore structured sample shows weak pyrochlore ordering peaks that are broadened in comparison to the fluorite sub-lattice peaks. This is indicative of partial ordering. Indeed, the results in **Table 5.15** reveal both anti-site cation disorder and oxygen Frenkel defects present, with around 38% anti-site cation disorder and 28% Frenkel defects. Oxygen Frenkel interstitials are located on the 8*a* site and vacancies on both the 8*b* and 48*f* sites. The extent of disorder in the compound is reflected in the weakness of the pyrochlore ordering peaks and can be compared with those in **Fig. 5.3** for a fully ordered pyrochlore.

The additional peaks of the κ-phase are clearly evident in **Fig. 5.21c**. The refined oxygen stoichiometry of 7.485 is significantly lower than that in a fully oxidised sample and corresponds to an average oxidation state for Ce of 3.485, indicating roughly equal amounts of Ce^{3+} and Ce^{4+}. The extent of oxidation is slightly higher than seen in the sample in flowing O_2 at 750 °C (**Table 5.10**) and in the room temperature case it is O(4), O(5), and O(6) rather than O(2), O(4) and O(6) that are partially occupied. The cation coordination geometries are very similar to those seen at 750 °C.

The main difference in the coordination geometries between those at room temperature and at 750 °C lies in the Ce(1) coordination. Whereas the Ce(1)-O(5) interactions were clearly non-bonding at 750 °C (at 2.73 Å) at room temperature they are shorter at 2.567 Å. However, this is still outside the sum of the ionic radii (2.523 Å), assuming all the Ce was in the 3+ oxidation state. This value lowers to 2.44 Å if half the Ce is in the +4 state as observed (values based on ionic radii of cations in eight coordinate geometry).[25] As for the structure at 750 °C, by taking into account the partial occupancies and the non-bonding interactions, the individual cation coordination numbers can be calculated as 5, 7.63, 6.61 and 7.35 for Ce(1), Ce(2), Zr(1) and Zr(2), respectively, giving overall weighted averages of 7.0 and 7.2 for Ce and Zr, respectively

5.3.3 Local structure

Reverse Monte Carlo (RMC) analysis was used to model the G(r) and S(Q) profiles for κ-$CeZrO_{4-\delta}$ generated from data collected at room temperature. The fits to the profiles are shown in **Fig. 5.22**.

(a)

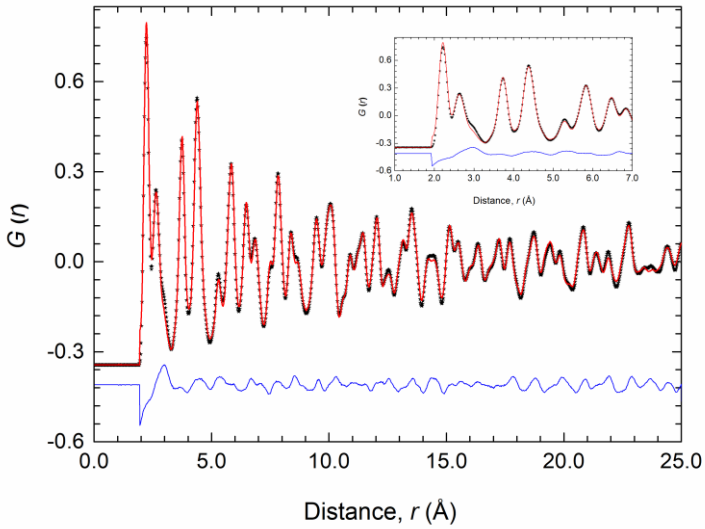

(b)

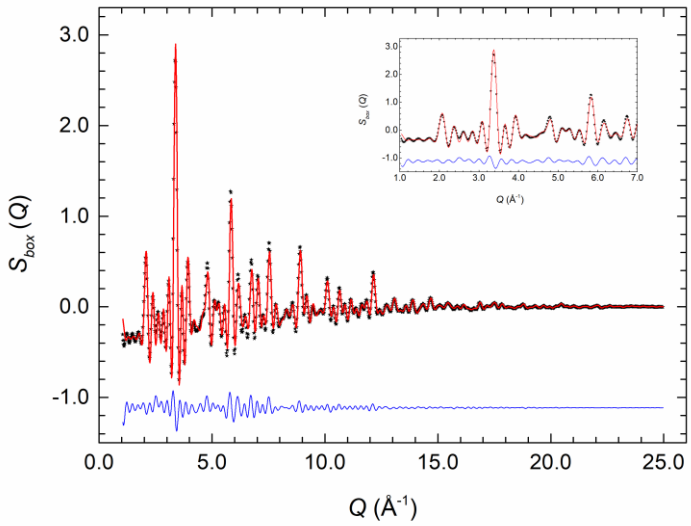

Fig. 5.22 The (a) $G(r)$ and (b) $S_{box}(Q)$ fits obtained by the RMC modelling of neutron data from κ-$CeZrO_{4-\delta}$ at room temperature, refined using average starting models in space groups $P2_13$.

The partial radial distribution functions, $g_{Ce\text{-}O}(r)$, $g_{Zr\text{-}O}(r)$, and $g_{O\text{-}O}(r)$ extracted from the RMC configurations are shown in **Fig. 5.23**. The first peak in the $g_{Ce\text{-}O}(r)$ plot is narrower and has a higher intensity relative to the first $g_{Zr–O}(r)$ correlation. The O-O correlation is a broad single peak, resembling those seen in the fluorite structured compounds in chapter 3.

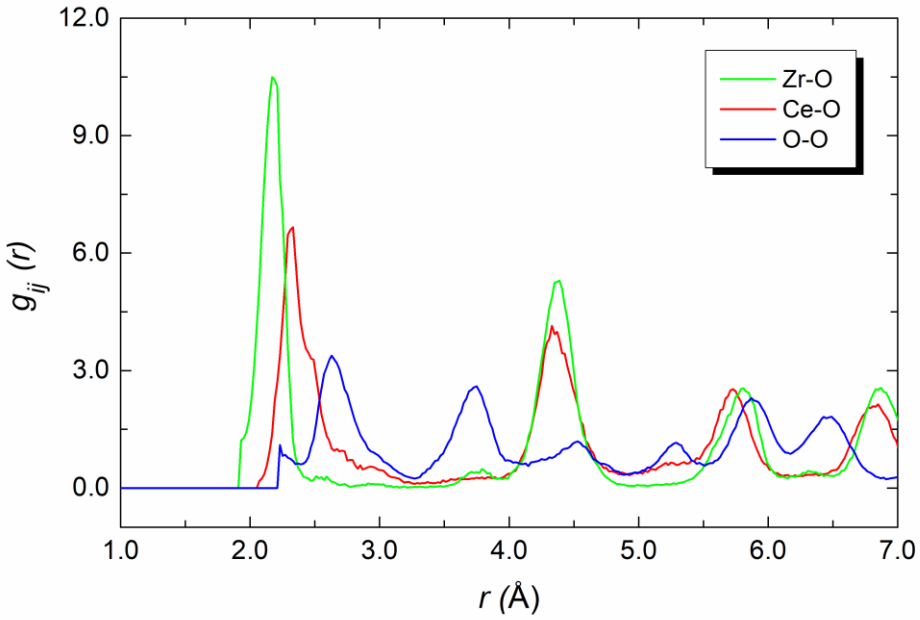

Fig. 5.23. Partial radial distribution functions, $g_{M\text{-}O}(r)$ and $g_{O\text{-}O}(r)$, as determined from RMC modelling of data from κ-$CeZrO_{4-\delta}$ collected at room temperature.

The final bond valence sums (BVS) along with M-O coordination numbers and modal and mean contact distances are given in **Table 5.17**. The BVS values for Zr^{4+} and O^{2-} ions are all very close to those expected. A BVS value of 3.7 for Ce^{3+} reflects the fact that the system is not fully oxidised, as seen in the Rietveld analysis where an average oxidation state of *ca*. 3.5 was found (**Table 5.16**). As described in Chapter 3, two types of coordination number can be defined, *i.e.* the site and local coordination numbers. As shown in **Table 5.17**, the site coordination number for Zr is significantly lower than that for Ce, but the local coordination numbers for these cations are both fairly close to 7, as seen in the average weighted values from the Rietveld analysis.

The mean contact distance for Ce-O is larger than the modal Ce-O distance, while the reverse is true for Zr-O. These compare with average values from the Rietveld analysis of 2.40 and 2.22 Å for Ce-O and Zr-O. The mean values from both the Rietveld and RMC analyses are close to the sum of the ionic radii, taking into account the average oxidation state of cerium derived from the Rietveld analysis, with Ce-O and Zr-O values of 2.44 Å and 2.10 Å, respectively, based on an 8-fold coordination for Ce, a 6-fold coordination for Zr and a 4-fold coordination for oxygen).[25]

Table 5.17. Bond valence sums (BVS), M-O coordination numbers (CN) and modal and mean M-O contact distances (Å) from RMC analysis of κ-$CeZrO_{4-\delta}$ collected at room temperature. Values are averages of 10 parallel calculations and standard deviations are given in parentheses. Site coordination numbers were derived by integration of $g_{MO}(r)$ to a maximum of 3.47 Å.

BVS	Ce^{3+}	3.722(13)
	Zr^{4+}	3.830(28)
	O^{2-}	2.019(27)
Site CN	Ce-O	8.13(2)
	Zr-O	7.43(1)
Local CN	Ce-O	7.13(8)
	Zr-O	7.03(4)
Distances	Ce-O Mode	2.31(1)
	Ce-O Mean	2.42(1)
	Zr-O Mode	2.22(1)
	Zr-O Mean	2.17(0)
	Av. M-O Mode	2.27(1)
	Av. M-O Mean	2.30(0)

The O-M-O angular distribution functions, $A_{OMO}(\Theta)$, derived from the RMC configurations at the three studied temperatures are shown in **Fig. 5.24**. The O-Ce-O distribution is centred around *ca*. 70°, 109° and 180°, corresponding to the angles between <100>, <110> and <111> aligned oxide ions, respectively, in the MO_8 distorted cubic coordination environments. However, the O-Ce-O distribution is significantly different to that of O-Zr-O, particularly at lower angles, where the peak maximum for <100> aligned oxygen is seen approximately 5° lower than seen for the O-Zr-O distribution. This difference suggests a greater local distortion around the cerium cations compared to zirconium. Both distributions are closer to that of pyrochlore than of fluorite.

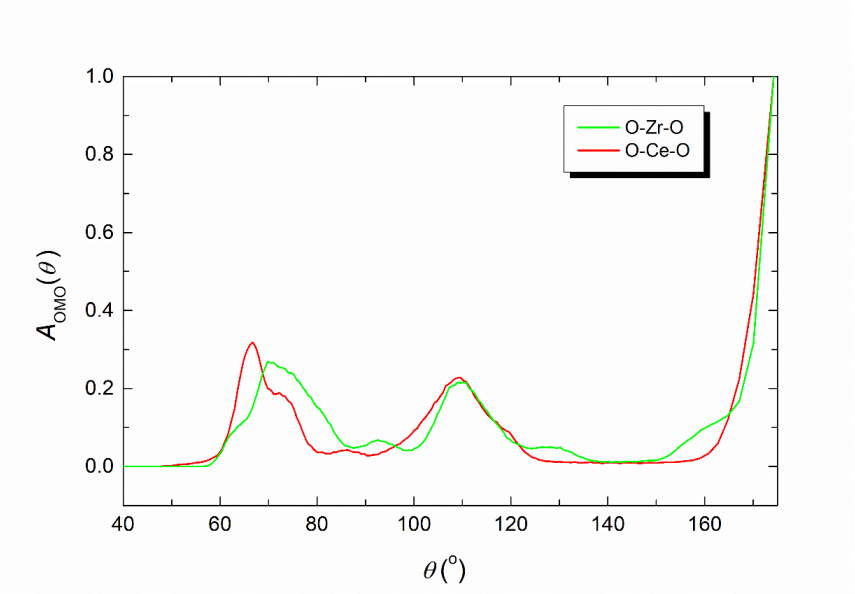

Fig. 5.24. O-M-O angular distribution functions as determined from RMC modelling of data from κ-$CeZrO_{4-\delta}$ collected at room temperature

As was shown in Chapters 3 and 4, three basic vacancy pair alignments can be defined with respect to the cubic coordination of the cation, each characterized by a specific vacancy-vacancy distance. Assuming a random distribution of vacancies, a ratio of 1:2:1.3 for <100>:<110>:<111> vacancy pairs is expected. The values given in **Table 5.18** show considerable departure from a random distribution, with a clear and significant preference for <111> ordering, compared to the random situation, confirming a more pyrochlore like vacancy ordering.

It is possible to reveal details of the local environment around vacancies through careful examination of the RMC configurations. Using a similar approach to that discussed in chapters 3 and 4, the vacancy "coordination" environment can be probed to reveal evidence of preferential distribution of vacancies between cations. The nearest neighbour cation distributions around oxide ion vacancies are presented as percentages of the total number of nearest neighbour cations in **Table 5.18**. A random distribution of cations would be expected to yield percentage distributions reflecting the stoichiometry. However, the values in **Table 5.18** for the percentage of cation nearest neighbours around a vacancy, %vac(NN)M, show significant deviation from a purely random distribution. The high percentage of Zr^{4+} nearest neighbours strongly suggests preferential association of vacancies with these cations.

Table 5.18 Defect concentration and distribution parameters derived from RMC analysis of data collected for κ-$CeZrO_{4-\delta}$ at room temperature. Values are averages of 10 parallel calculations and standard deviations are given in parentheses.

		Theoretical
No. tet. vacancies per $Ce_2Zr_2O_x$ formula unit	0.88(4)	1.5
100:110:111	1.00:1.62:1.55	Rand. 1.0:2.0:1.3 Pyr. 0:0:1
$\%vac(NN)_{Ce}$	44.4(13)	50
$\%vac(NN)_{Zr}$	55.6(13)	50
$\%Ce(NN)_{Ce}$	49.0(2)	50
$\%Ce(NN)_{Zr}$	51.0(4)	50
$\%Zr(NN)_{Ce}$	49.8(3)	50
$\%Zr(NN)_{Zr}$	50.2(1)	50
$\%Ce(NNN)_{Ce}$	15.0(5)	0
$\%Ce(NNN)_{Zr}$	85.0(9)	100
$\%Zr(NNN)_{Ce}$	99.9(9)	100
$\%Zr(NNN)_{Zr}$	0.1(1)	0

The extent of cation ordering, can be examined through the $g_{MM}(r)$ correlations (**Fig. 5.25**). The most noticeable change is the absence of next-nearest neighbour correlations of the type Ln-Ln at around 5.3 Å, indicating an ordered cation sublattice, as found in the pyrochlore structure.

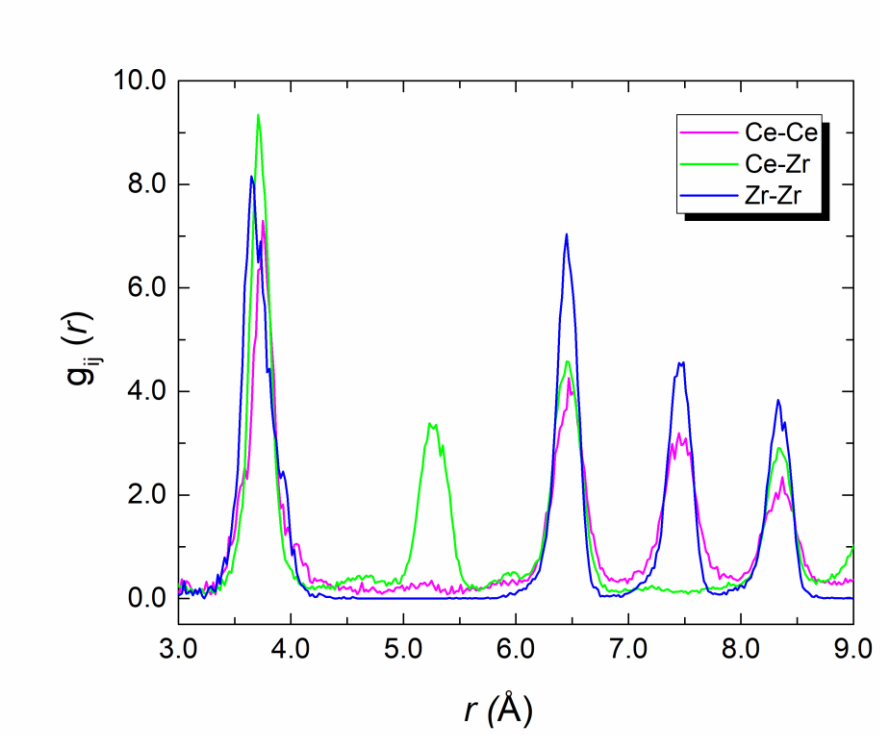

Fig. 5.25. Cation-cation partial radial distribution functions, $g_{M\text{-}M}(r)$, as determined from RMC modelling of data from κ-$CeZrO_{4-\delta}$ collected at room temperature.

Table 5.18 also summarises the NN and NNN distributions around each cation type. The NN distributions around both cations show no significant deviation away from a random situation. There is some deviation away from the expected values in the next-nearest neighbour distributions, for example the value for $Ce(NNN)_{Ce}$ is higher than should be expected. While this may indicate some degree of anti-site cation disorder, this was not evident in the Rietveld analysis and examination of Fig 5.25 suggests that this may be due to noise in the $g_{CeCe}(r)$ distribution.

5.4 Conclusions

Reduction of the κ-phase, in flowing CO at 600 °C, produced the fully ordered pyrochlore phase, *i.e*. $Ce_2Zr_2O_7$. Upon heating the pyrochlore phase in flowing O_2, three distinct phases were observed, with transitions at *ca*. 140 °C and 410 °C. In the low temperature region, the neutron diffraction patterns were dominated by the pyrochlore type phase. However, a minor secondary phase was also present which became more prominent with increasing temperature, reaching a weight fraction as high as 46 wt% at 130 °C. The secondary phase was attributed to β-$Ce_2Zr_2O_{7.5}$ and was refined in space group $F\bar{4}3m$. The β-phase was found to consist of longer Zr-O, but shorter Ce-O distances, as compared to the pyrochlore phase.

At around 140 °C, the β-phase disappeared and a previously un-identified phase appeared alongside a small amount of the pyrochlore phase. This new phase was phase pure by 150 °C. A number of models were tried to fit the neutron diffraction data of the new phase, including, rhombohedral, tetragonal, orthorhombic and monoclinic distortions of the cubic $P2_13$ phase. The only model that satisfactorily fitted the profile was a triclinic model, which contained 10 Ce and 10 Zr sites, each with a distorted cubic coordination. There was a significant increase in oxygen content on the transition from the cubic phase to the triclinic phase. This occurred at a point where there was a significant decrease in lattice parameter and hence volume, which was associated with the oxidation of Ce^{3+} to the smaller Ce^{4+}.

On further heating the sample above 410 °C, a transition occurred, from the triclinic phase to a cubic phase, corresponding to the κ-phase (space group $P2_13$), but with little significant change in oxygen content at this transition. RMC modelling of the local structure of the κ-phase, revealed an ordered, pyrochlore-like, cation sub-lattice, with a disordered anion sub-lattice. On re-heating the κ-phase in flowing CO, a second phase appeared at around 190 °C, which was modelled on the β-$Ce_2Zr_2O_{7.5-\delta}$ phase in space group $F\bar{4}3m$, as seen on heating in flowing O_2. At around 260 °C, the pyrochlore phase re-appeared alongside the κ- and the β-phases. At 290 °C, the pyrochlore phase was phase pure. The oxygen content dropped dramatically upon the formation of the pyrochlore phase.

Chapter 6 – Overall Conclusions

The work described in this thesis has focused on achieving a greater fundamental understanding of the structural, defect and mechanistic features of lanthanide zirconate materials as potential electrolytes for intermediate temperature sold oxide fuel cells (IT-SOFCs). Multiple strategies were employed to optimise these materials, including chemical substitution, thermal treatments, and different synthetic routes. This was necessary for these materials, since they show order-disorder phase transitions, which are accompanied by significant changes in electrical conducting properties. Of the many material types studied previously for such purposes, fluorite/pyrochlore related compounds were chosen in this study, for their wide range of potential properties. In order to achieve high oxide ion conductivities in these materials, attempts were made to create high concentrations of mobile vacancies, with low activation energies for ion migration. In particular, vacancy concentration was promoted via the formation of Frenkel defects, through increased disorder in both the cation and anion sub-lattices.

The use of the co-precipitation method for the synthesis of the materials studied in this thesis, allowed for lower calcination temperatures, as compared to the conventional solid-state reaction method. The combined use of X-ray and neutron diffraction allowed for the precise determination of the anion sub-lattice and its defects, which would have not been possible otherwise. The use of total scattering through PDF analysis, as opposed to Bragg scattering alone, allowed for the determination of the local structure that relied on experimental data. Furthermore, modelling of the PDF data via the RMC method allowed for much more structural information to be revealed, than straight model independent analysis. In this way, the distribution of atoms on an absolute scale was possible (from the Bragg scattering), as well as the arrangement of atoms relative to each other (from the diffuse scattering), both of which were essential for the purposes of the study. Finally, the use of impedance spectroscopy (IS) allowed for the electrical properties to be determined, the results of which, were interpreted in light of the data from the structural analyses.

The local structure evolution as a function of composition and temperature, and the resulting electrical conductivities were studied in samples with general composition $(Yb_{1-x}Nd_x)_2Zr_2O_7$. Variable-temperature neutron powder diffraction experiments were carried out on the $(Nd_{1-x}Ca_x)_2Zr_2O_{7-x}$ ($0.10 \leq x \leq 0.50$) system, in order to investigate the local structural evolution as a function of composition and temperature. Structural evolution in oxidising and reducing atmospheres was investigated in cerium zirconate, $Ce_2Zr_2O_{7+\delta}$.

Fluorite/pyrochlore phase transformations were observed in the $(Yb_{1-x}Nd_x)_2Zr_2O_7$ system, that depended on the composition and on the calcination temperature of the material. At relatively low calcination temperatures (800 °C), all of the samples showed broad peaks in X-ray and neutron diffraction patterns, characteristic of the fluorite structure. With increased calcination temperature (1150 and 1350 °C), ytterbium rich compositions retained the fluorite structure, whereas neodymium rich compositions exhibited fluorite to pyrochlore phase transformations. The fluorite to pyrochlore transformation occurs in a gradual manner, with pyrochlore structured micro-domains spread in the fluorite matrix. The best example of this was seen in the $x = 0.75$ composition calcined at 1150 °C, where fits to the Bragg data were significantly improved by the use of a two-phase pyrochlore plus defect fluorite model. The pyrochlore micro-domains grow with increasing neodymium content and/or increasing calcination temperature, eventually becoming the dominant phase. There was a significant increase in the coordination numbers of neodymium and ytterbium upon the fluorite to pyrochlore transition, whereas the coordination number of zirconium decreased on this transition. Anti-site cation disorder was evident across the compositional range, but decreased with increasing Nd content. At $x = 0.75$, the system contains around 20% anti-site cation disorder, decreasing to less than 10% at $x = 1.00$.

All of the compositions in the $(Nd_{1-x}Ca_x)_2Zr_2O_{7-x}$ ($0.10 \leq x \leq 0.50$) system exhibit a single phase with a pyrochlore-type structure. In contrast to the Nd/Yb system, no fluorite to pyrochlore phase transformations were observed. However, in both the X-ray and neutron data in the Nd/Ca system, the pyrochlore ordering peaks were seen to weaken with increasing x-value, suggesting greater disorder with increasing calcium content. The best fit to the Bragg data was ultimately achieved for a unit cell with complete cation order, again in contrast to the Nd/Yb system, where significant amounts of cation anti-site disorder were found to exist in the pyrochlore structured sompositions.

The average Nd^{3+}/Ca^{2+} coordination number decreased and that of Zr^{4+} increased with increasing calcium content. This reflects the increasing number of oxygen Frenkel defects as oxide ions on the O(1) site are displaced onto the O(3) site. The variable-temperature study showed that the pyrochlore structure in the Nd/Ca system is maintained throughout the temperature range studied. The diffraction patterns at 800 °C showed no significant changes from the room temperature plots, other than a thermal expansion. In samples of $x = 0.75$ and $x = 1.00$ compositions calcined at 1350 °C, there was a reduction of cation anti-site disorder and the concentration of oxide ion Frenkel defects, compared to when the samples were calcined at 1150 °C.

G(r) profiles for both the Nd/Yb and Nd/Ca systems showed a gradual evolution of the pattern with calcination temperature in the case of the former and sample temperature in the case of the latter, reflecting structural change. The M-O correlations were seen to sharpen with increasing temperature, as the first O-O correlation shifted to longer distances. There were slight increases in the coordination numbers of neodymium, ytterbium and calcium with increasing temperature, whereas the coordination number of zirconium decreased, indicating the structure to be more pyrochlore-like at elevated temperatures. There was no significant change in the cation-cation pair distributions in the Nd/Ca system, in heating from room temperature to 500 and 800 °C. The high percentage of Nd^{3+}/Yb^{3+} nearest neighbours around a vacancy in the fluorite type compositions, strongly suggests preferential association of vacancies with these cations. Whilst there was a clear preference for <111> vacancy ordering in the Nd/Ca system compared to the random situation, there were still appreciable numbers of <100> and <110> aligned vacancy pairs. In pyrochlore structured compositions ($0.75 \leq x \leq 1.00$ calcined at 1150-1350 °C) of the Nd/Yb system, there was also a clear and significant preference for <111> ordering, compared to the random situation. However, both <100> and <110> aligned vacancy pairs were still present, which reflected the additional oxygen Frenkel defects seen in the Rietveld analyses.

Structural analyses of cerium zirconate, revealed a number of phase transformations, depending on the atmosphere (O_2/CO) and temperature. Reduction of the κ-phase, in flowing CO at 600 °C, produced the fully ordered pyrochlore phase, *i.e.* $Ce_2Zr_2O_7$. Upon heating the pyrochlore phase in flowing O_2, three distinct phases were observed, with transitions at *ca*. 140 °C and 410 °C. In the low temperature region, the neutron diffraction patterns were dominated by the pyrochlore type phase ($Ce_2Zr_2O_7$) and the β-phase ($Ce_2Zr_2O_{7.5}$).

At around 140 °C, the β-phase was transformed to a previously un-identified phase. The only model that satisfactorily fitted the profile of the new phase was a triclinic model, which contained 10 Ce and 10 Zr sites, each with a distorted cubic coordination. There was a significant increase in oxygen content on the transition from the cubic phase to the triclinic phase. On further heating the sample above 410 °C, a transition occurred, from the triclinic phase to a cubic phase, corresponding to the κ-phase (space group $P2_13$). RMC modelling of the local structure of the κ-phase revealed an ordered, pyrochlore-like cation sub-lattice, with a disordered anion sub-lattice. On re-heating the κ-phase in flowing CO, the β-phase appeared as a second phase at around 190 °C. At around 260 °C, the pyrochlore phase re-appeared alongside the κ- and the β-phases. At 290 °C, the pyrochlore phase was phase pure.

The Arrhenius plots for $(Yb_{1-x}Nd_x)_2Zr_2O_{7-\delta}$ ($0.00 \leq x \leq 0.50$) compositions show near linear behaviour, with only the $x = 0.00$ composition showing some deviation at low temperatures. For the pyrochlore structured compositions ($x = 0.75$ and $x = 1.00$) there is deviation from linearity. For the $x = 0.75$ composition, three linear regions were observed. Characteristic values of conductivity in the high and low temperature regions, typified by the conductivities at 300 °C and 700 °C (σ_{300} and σ_{700}, respectively), show a maximum for the $x = 0.75$ composition, with a value of 6.82×10^{-4} S cm^{-1} at 700 °C. This composition corresponds to the sample with the highest level of oxygen Frenkel defects, as found in the Rietveld analysis.

The Arrhenius plots of total conductivity for $(Nd_{1-x}Ca_x)_2Zr_2O_{7-x}$ ($0.00 \leq x \leq 0.50$) show two linear regions with a transition at around 400 °C, similar to what was observed for pyrochlore structured compositions in the Yb-doped system. In all the Ca substituted compositions, the high-temperature region has a lower activation energy than the low-temperature region. Like the Nd/Yb system, the Ca substituted compositions show higher conductivity than the un-substituted composition, particularly at higher temperatures. For the high-temperature region, the conductivity at 700 °C (σ_{700}) has values in the order of 10^{-3} S cm^{-1}, with a maximum at $x = 0.3$. Both the low-temperature activation energy, ΔE_{LT}, and that at high-temperature, ΔE_{HT}, increase with increasing calcium content. The increase in conductivity with calcium content is due to the higher concentration of charge carriers caused by Ca-doped $Nd_2Zr_2O_7$. However, above an optimum substitution level, vacancy-vacancy interactions become significant, thus reducing ion mobility.

6.1 Wider Implications

The work carried out in this thesis has shown how the local structural disorder can prevail in materials that contain long-range order. Furthermore, RMC modelling of total scattering data has been shown to be a powerful technique of studying materials that exhibit subtle phase transformations. RMC modelling allowed for both the cation and anion coordination environments to be probed, thus revealing the nature and extent of oxygen vacancies present. Reasonable levels of oxide ion conductivity were obtained, particularly in the $(Nd_{1-x}Ca_x)_2Zr_2O_{7-x}$ system. However, it is clear that higher conductivity is associated with greater disorder. The work has shown that optimising the level of disorder through modification of both synthesis conditions and composition is key to achieving high conductivity.

6.2 Future Work

Time did not permit the inclusion of a total scattering study in the cerium zirconate system of a fully disordered fluorite and a partially ordered pyrochlore, both with the composition $Ce_2Zr_2O_7$. This will make an interesting comparison with the Yb/Nd system, where both these structural types were seen. Further work on the triclinic phase in the cerium zirconate system is needed. In particular, a higher quality data set would be useful in allowing for better determination of the individual cation environments. In the Nd/Ca system, the limit of the solid solution requires investigation as does the effect of higher sintering temperatures. For example, would higher sintering temperatures for the $x = 0.5$ composition afford greater order?

It is evident from the study of the Yb/Nd system that the concentration of Frenkel defects has a significant influence on conductivity. Variation of the defect concentration through modifying composition and calcination/annealing temperature has been shown to enhance conductivity. However, further optimization and investigation of related systems is required, in order to reach the values of conductivity necessary for use in IT-SOFCs. In addition, measurements of transference numbers are needed to confirm that conductivity is predominantly ionic.

Appendices

Appendix A – VT diffraction patterns

(a)

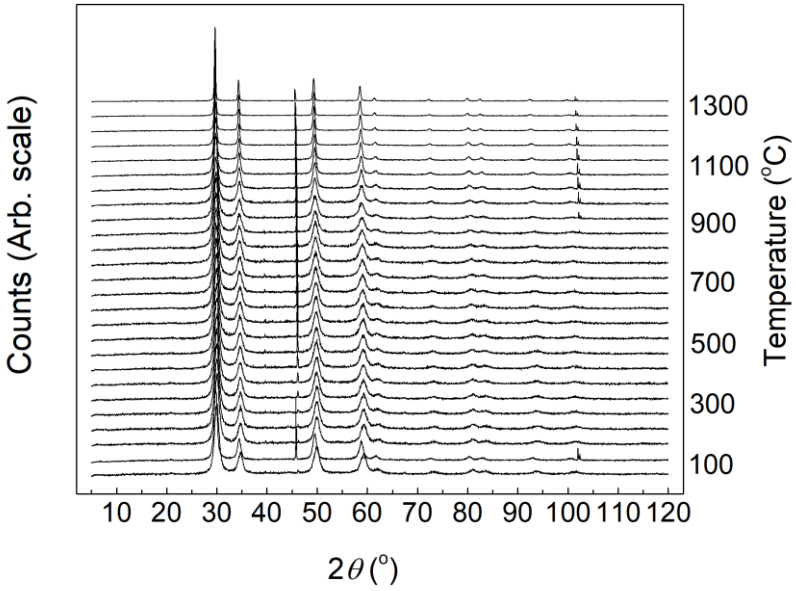

(b)

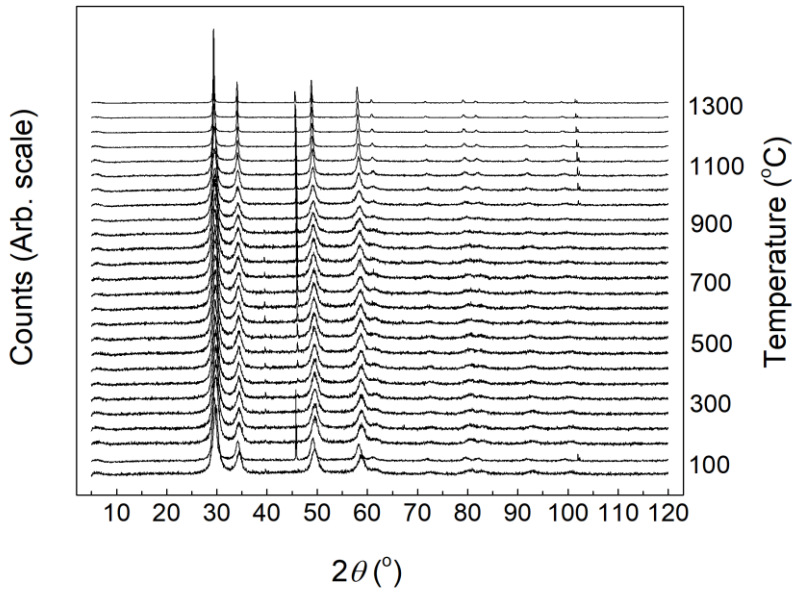

Fig. 7.1. Variable temperature X-ray diffraction data for $(Yb_{1-x}Nd_x)_2Zr_2O_7$; (a) x = 0.00, and (b) x = 0.25.

(a)

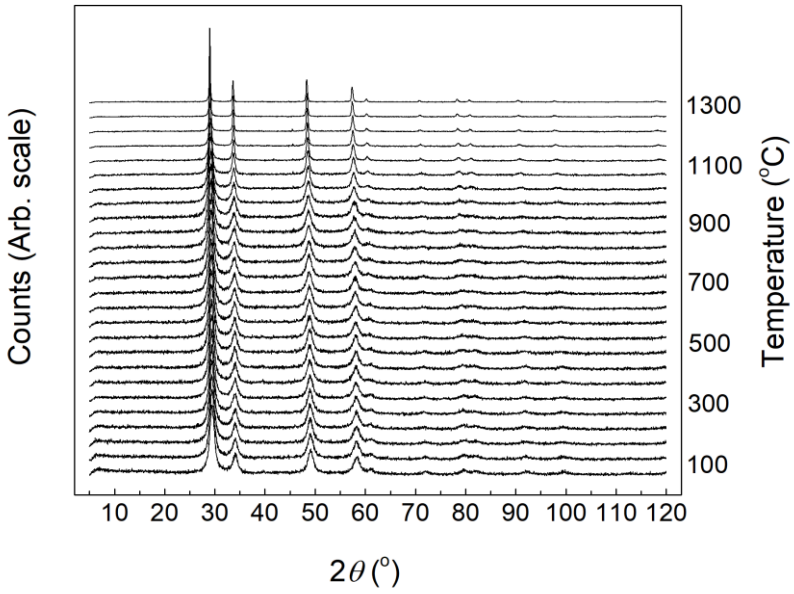

(b)

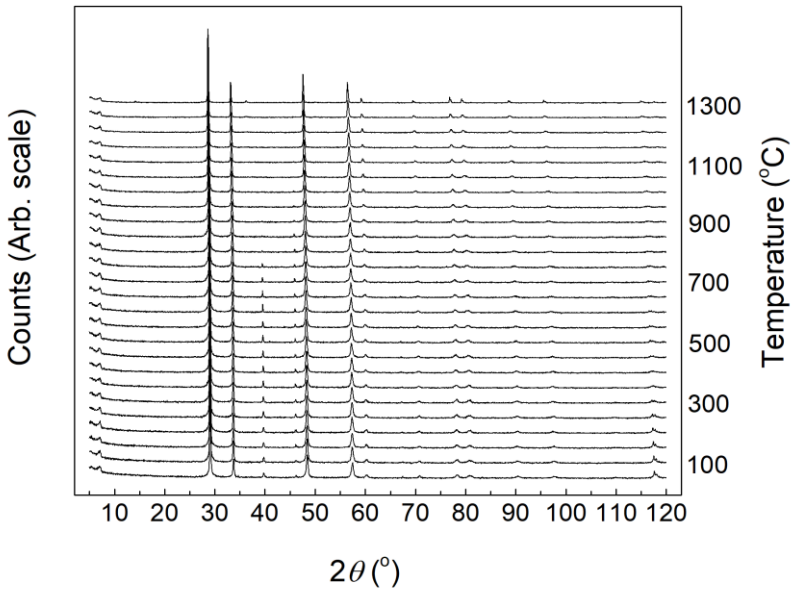

Fig. 7.2. Variable temperature X-ray diffraction data for $(Yb_{1-x}Nd_x)_2Zr_2O_7$; (a) x = 0.50, and (b) x = 1.00.

(a)

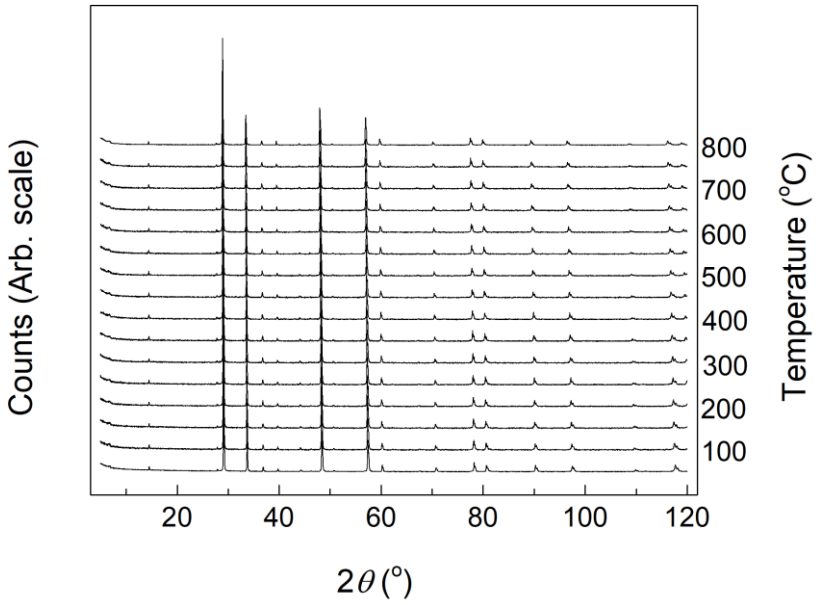

(b)

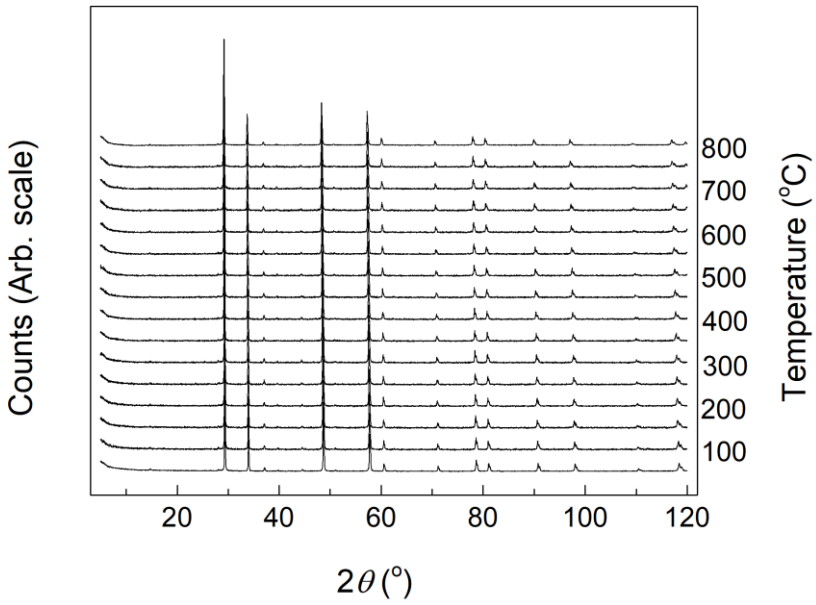

Fig. 7.3. Variable temperature X-ray diffraction data for $(Nd_{1-x}Ca_x)_2Zr_2O_{7-x}$; (a) x = 0.10, and (b) x = 0.20.

(a)

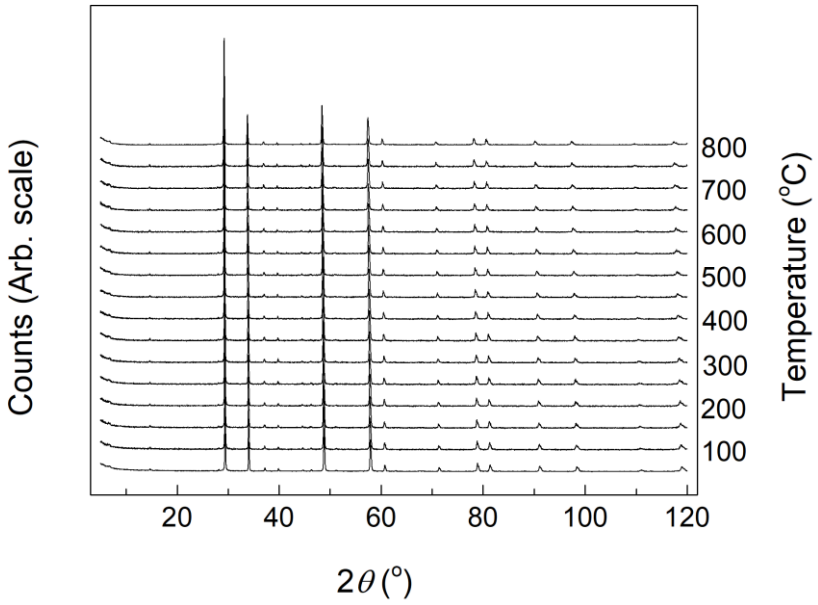

(b)

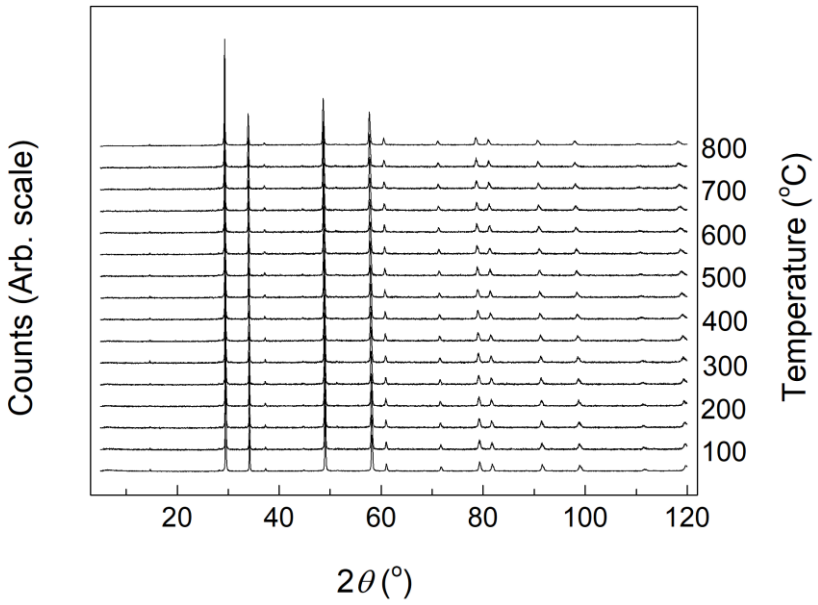

Fig. 7.4. Variable temperature X-ray diffraction data for $(Nd_{1-x}Ca_x)_2Zr_2O_{7-x}$; (a) x = 0.30, and (b) x = 0.40.

(a)

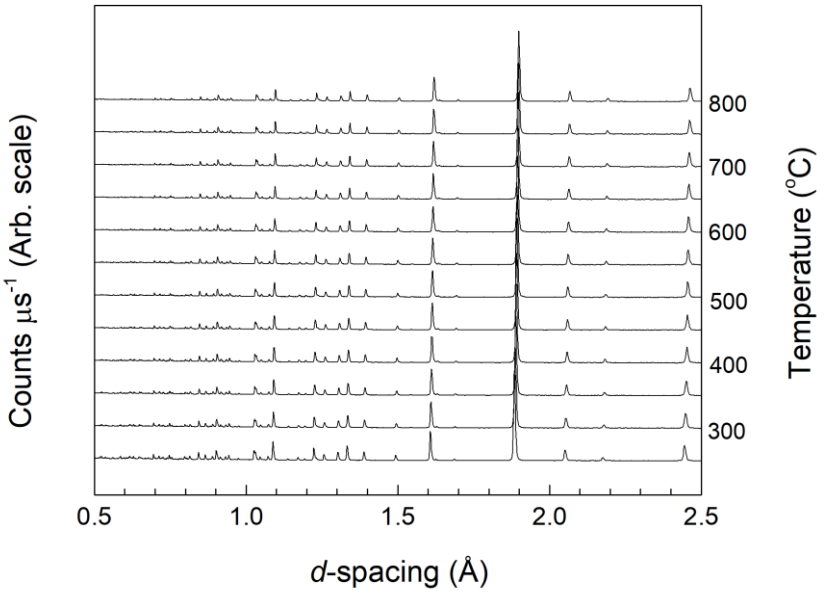

(b)

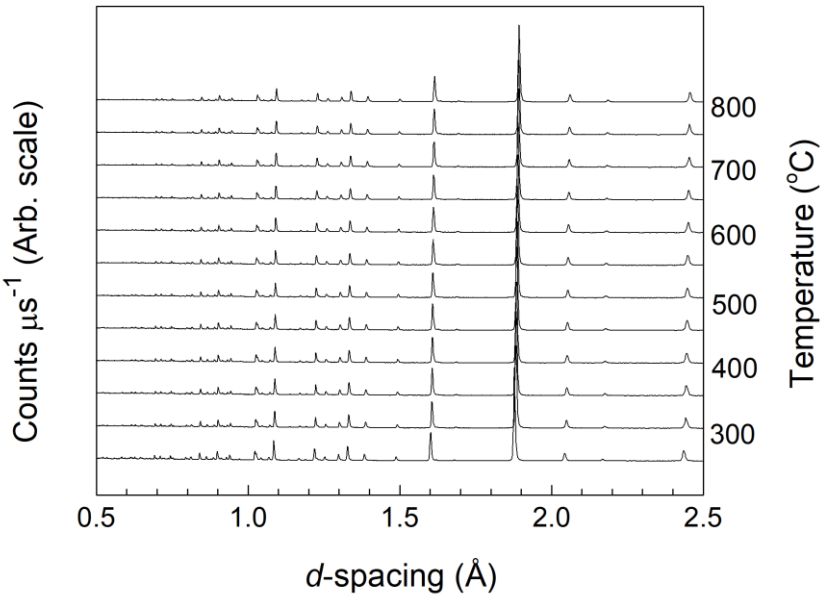

Fig. 7.5. Variable temperature neutron diffraction data for $(Nd_{1-x}Ca_x)_2Zr_2O_{7-x}$; (a) x = 0.10, and (b) x = 0.20.

(a)

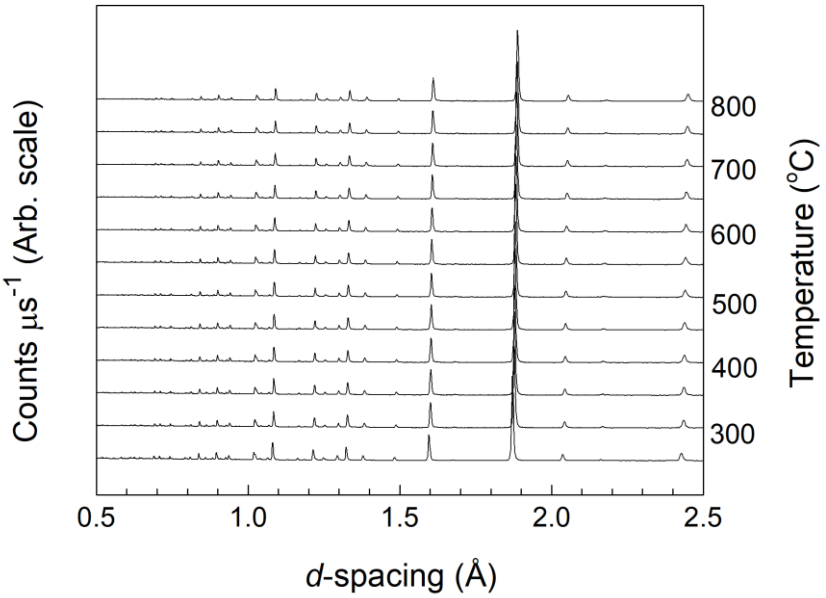

(b)

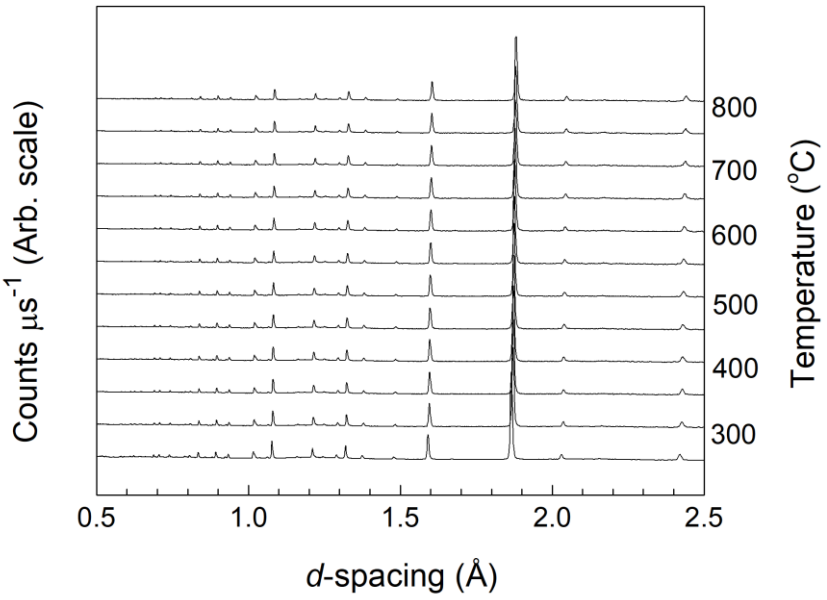

Fig. 7.6. Variable temperature neutron diffraction data for $(Nd_{1-x}Ca_x)_2Zr_2O_{7-x}$; (a) x = 0.30, and (b) x = 0.40.

Appendix B – GSAS Fits

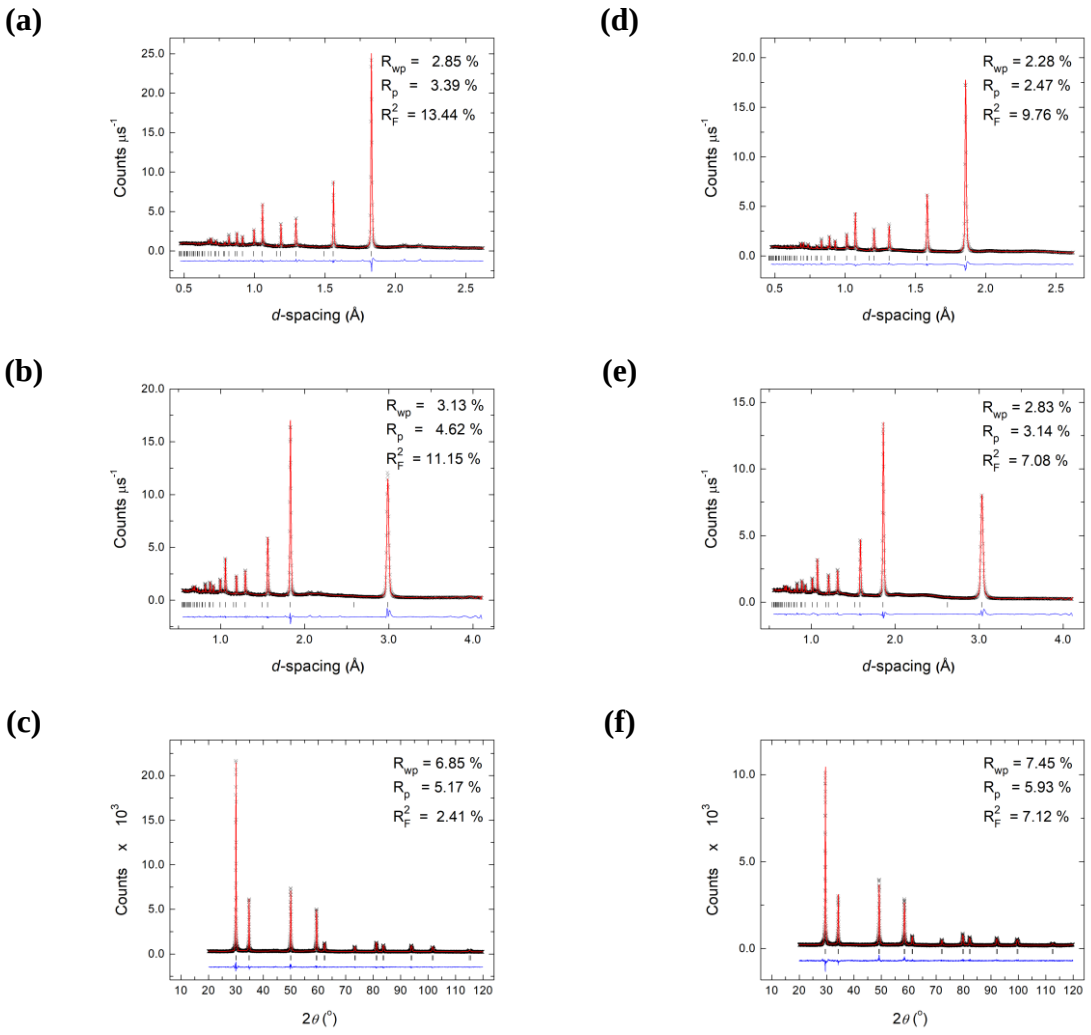

Fig. 7.7. Fitted diffraction profiles for fluorite structured samples in the system $(Yb_{1-x}Nd_x)_2Zr_2O_7$ for (a) to (c) $x = 0.00$ and (d) to (f) $x = 0.50$ compositions. Fits to (a) and (d) neutron back scattering, (b) and (e) neutron 90° and (c) and (f) X-ray data are shown. Observed (crosses), calculated (solid line), and difference (lower) profiles of are shown. Reflection positions are indicated by markers.

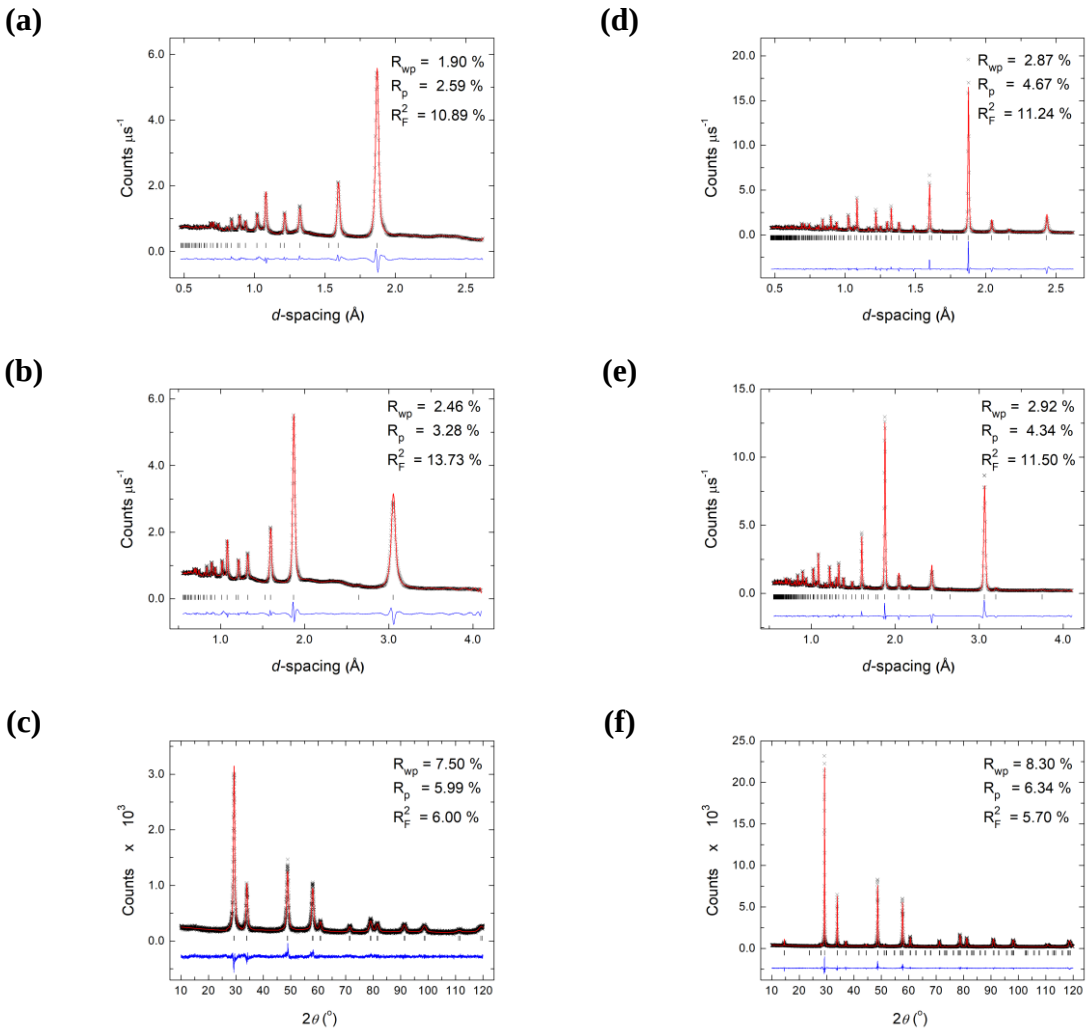

Fig. 7.8. Fitted diffraction profiles for fluorite/pyrochlore samples in the system $(Yb_{1-x}Nd_x)_2Zr_2O_7$, x = 0.75; for (a) to (c) calcined at 950 °C and (d) to (f) calcined at 1350 °C. Fits to (a) and (d) neutron back scattering, (b) and (e) neutron 90° and (c) and (f) X-ray data are shown. Observed (crosses), calculated (solid line), and difference (lower) profiles of are shown. Reflection positions are indicated by markers.

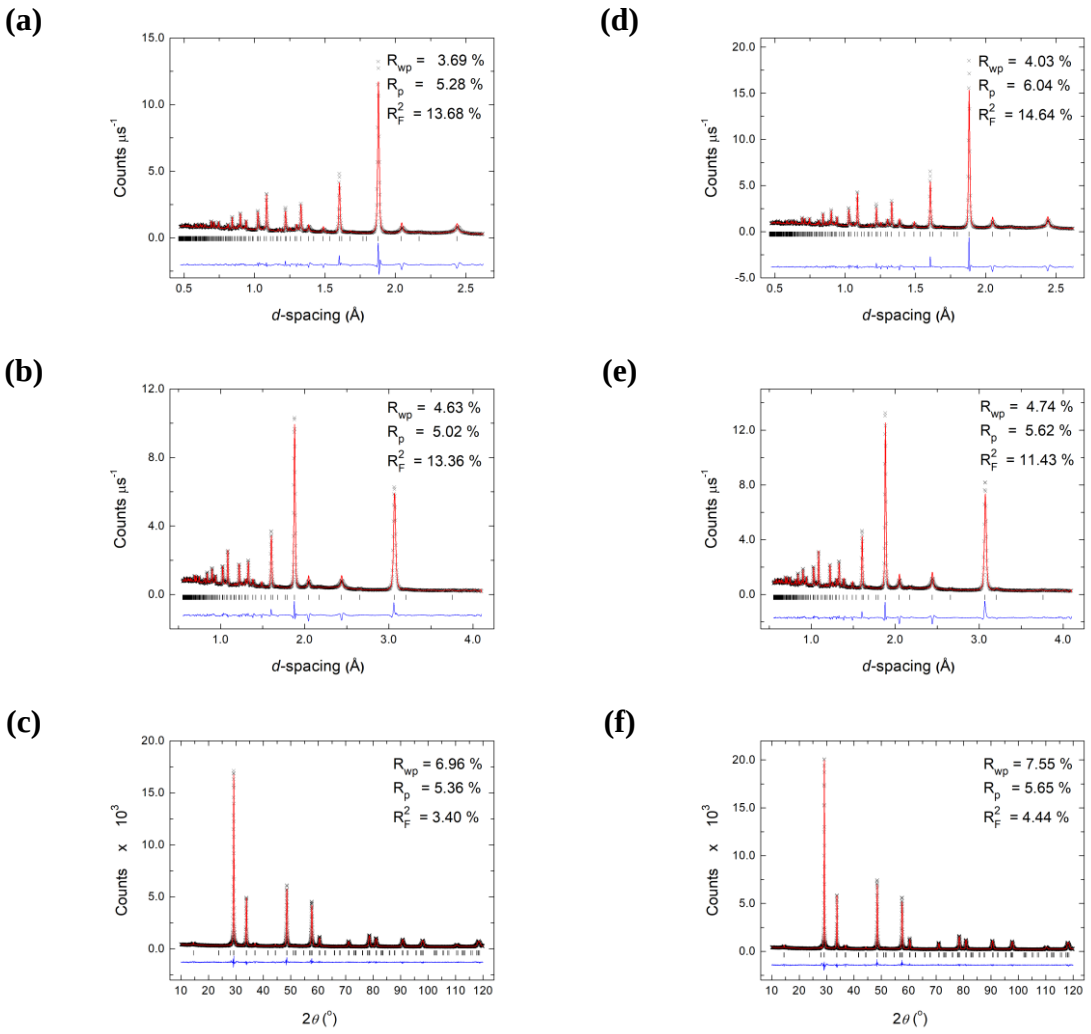

Fig. 7.9. Fitted diffraction profiles for pyrochlore structured samples in the system $(Yb_{1-x}Nd_x)_2Zr_2O_7$ for (a) to (c) $x = 0.80$ and (d) to (f) $x = 0.85$ compositions. Fits to (a) and (d) neutron back scattering, (b) and (e) neutron 90° and (c) and (f) X-ray data are shown. Observed (crosses), calculated (solid line), and difference (lower) profiles of are shown. Reflection positions are indicated by markers.

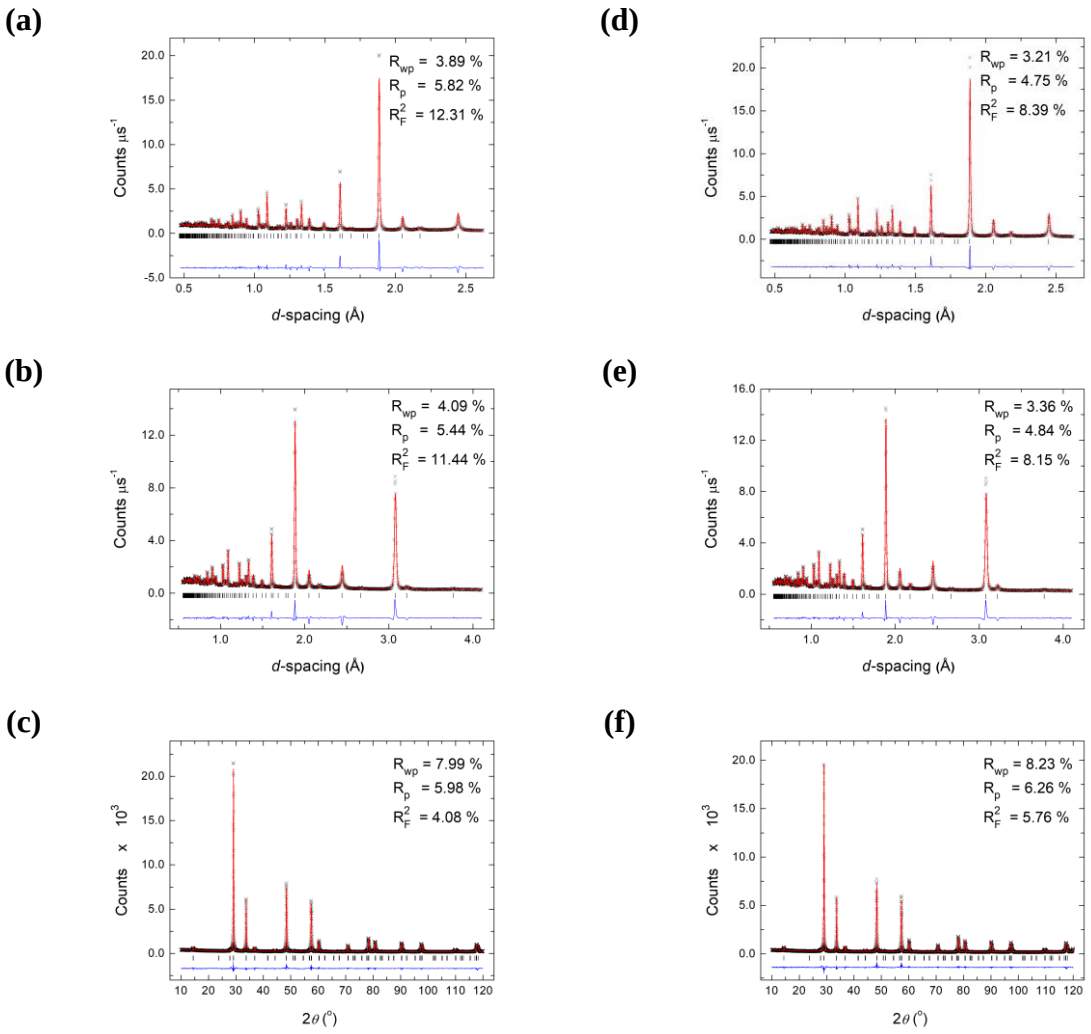

Fig. 7.10. Fitted diffraction profiles for pyrochlore structured samples in the system $(Yb_{1-x}Nd_x)_2Zr_2O_7$ for (a) to (c) $x = 0.90$ and (d) to (f) $x = 0.95$ compositions. Fits to (a) and (d) neutron back scattering, (b) and (e) neutron 90° and (c) and (f) X-ray data are shown. Observed (crosses), calculated (solid line), and difference (lower) profiles of are shown. Reflection positions are indicated by markers.

(a)

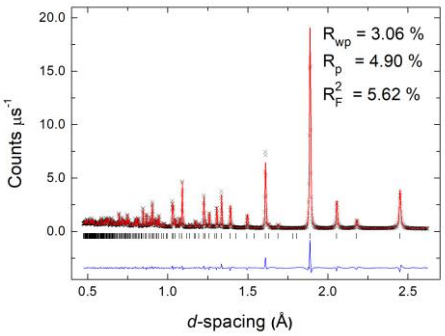

(b)

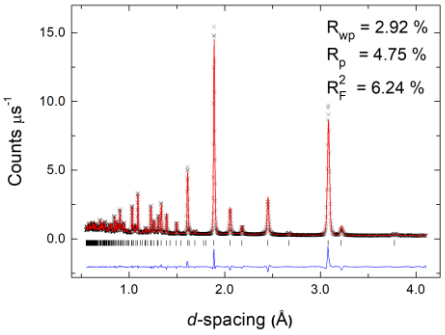

(c)

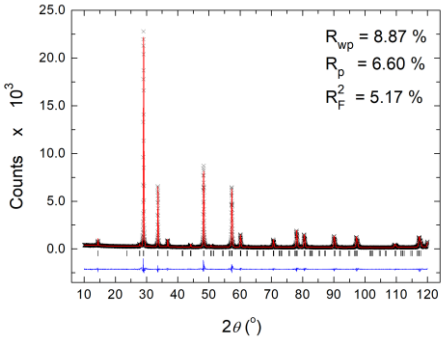

Fig. 7.11. Fitted diffraction profiles for pyrochlore samples in the system $(Yb_{1-x}Nd_x)_2Zr_2O_7$, x = 1.00; calcined at 1150 °C. Fits to (a) neutron back scattering, (b) neutron 90° and (c) X-ray data are shown. Observed (crosses), calculated (solid line), and difference (lower) profiles of are shown. Reflection positions are indicated by markers.

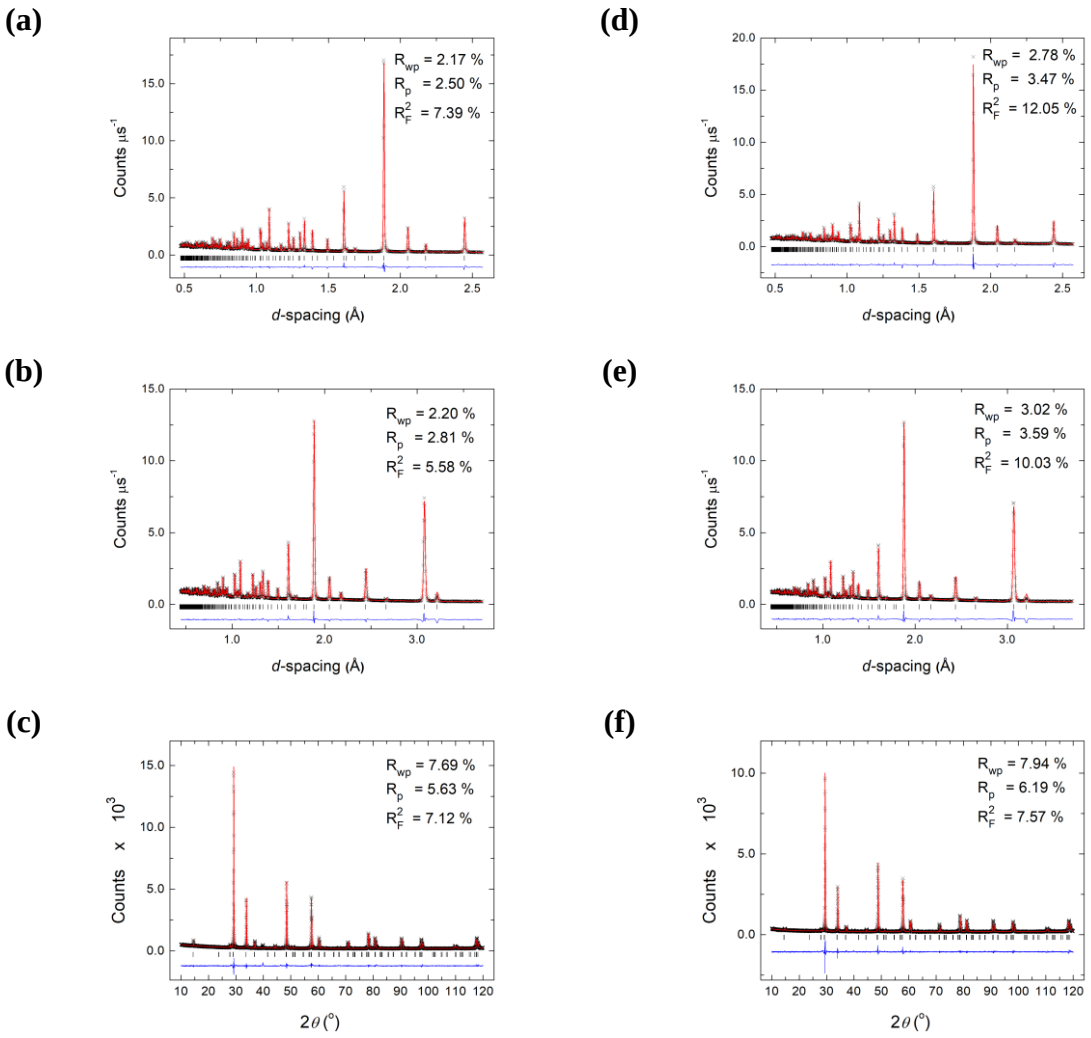

Fig. 7.12. Fitted diffraction profiles for samples in the system $(Nd_{1-x}Ca_x)_2Zr_2O_{7-x}$ for (a) to (c) x = 0.10 and (d) to (f) x = 0.20 compositions. Fits to (a) and (d) neutron back scattering, (b) and (e) neutron 90° and (c) and (f) X-ray data are shown. Observed (crosses), calculated (solid line), and difference (lower) profiles of are shown. Reflection positions are indicated by markers.

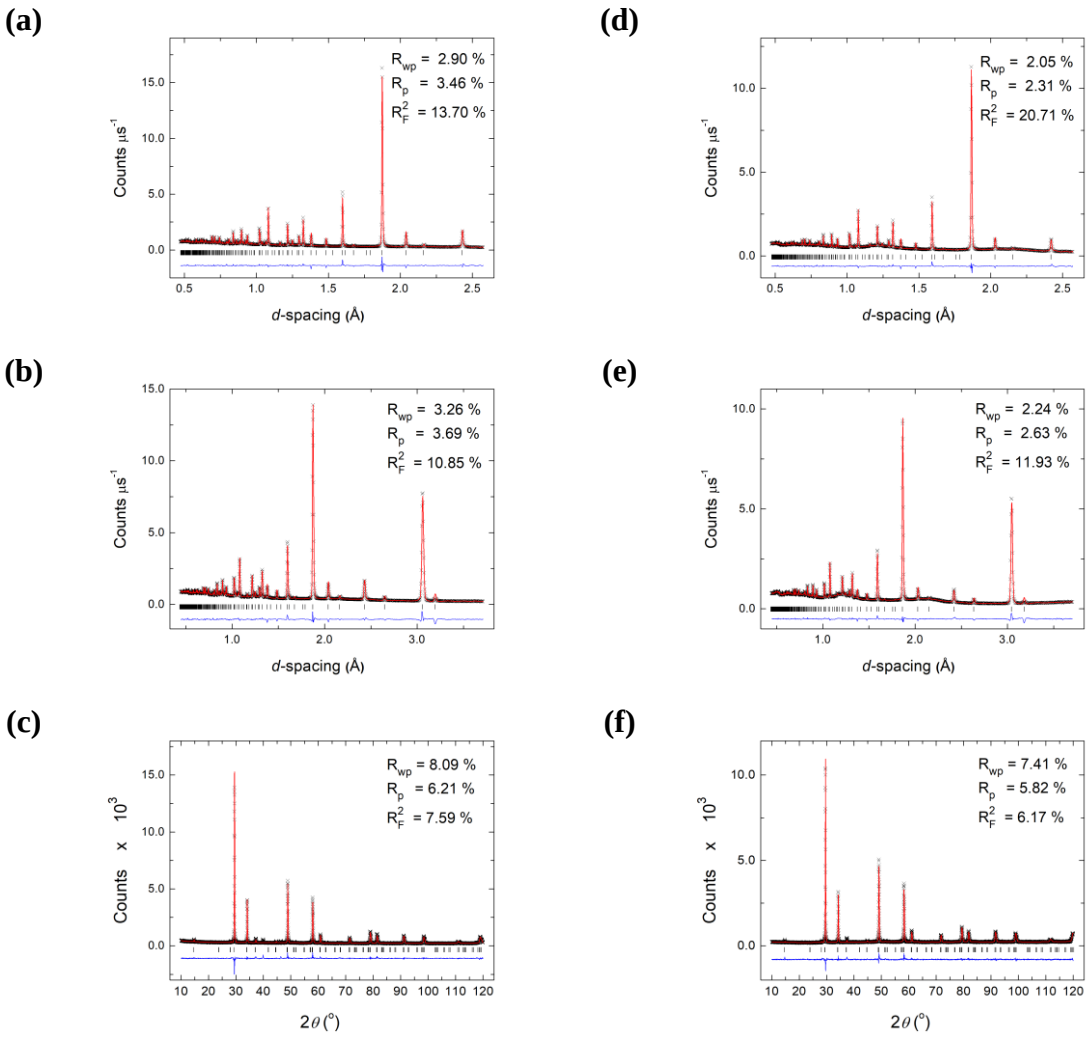

Fig. 7.13. Fitted diffraction profiles for samples in the system $(Nd_{1-x}Ca_x)_2Zr_2O_{7-x}$ for (a) to (c) x = 0.30 and (d) to (f) x = 0.40 compositions. Fits to (a) and (d) neutron back scattering, (b) and (e) neutron 90° and (c) and (f) X-ray data are shown. Observed (crosses), calculated (solid line), and difference (lower) profiles of are shown. Reflection positions are indicated by markers.

Appendix C – S(*Q*) and G(*r*) Fits

(a)

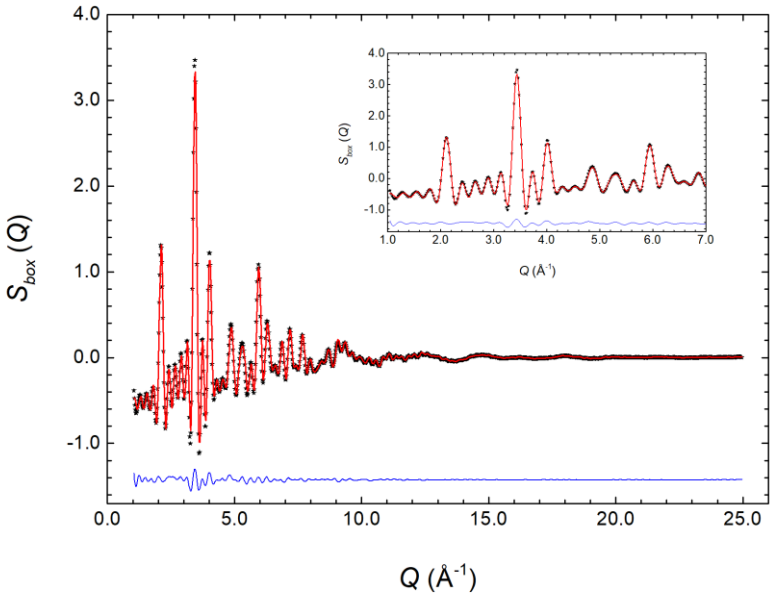

(b)

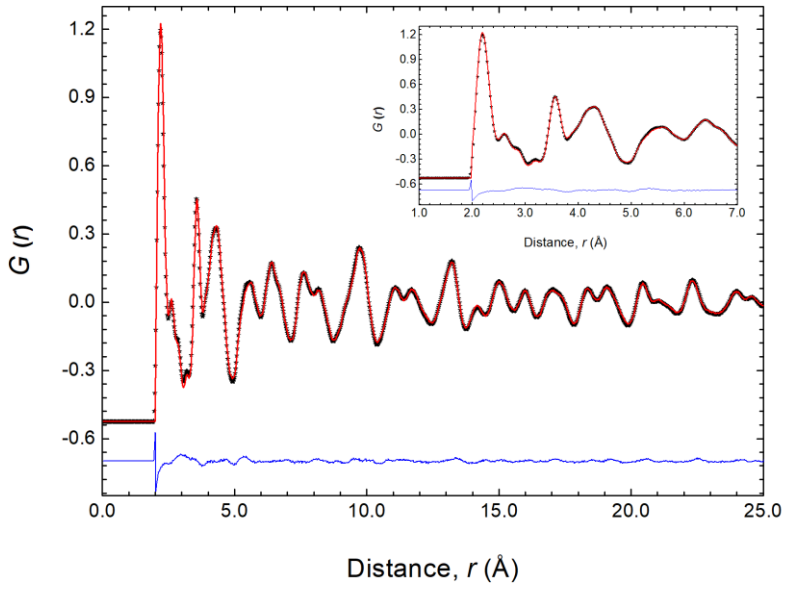

Fig. 7.14. Fits to (a) S(*Q*) and (b) G(*r*) profiles obtained by the RMC modelling of neutron data from the $(Yb_{1-x}Nd_x)_2Zr_2O_7$, x = 0.00. The black dots show the experimental data, the solid red line shows the calculated profile, and the difference profile is shown by the solid blue line.

(a)

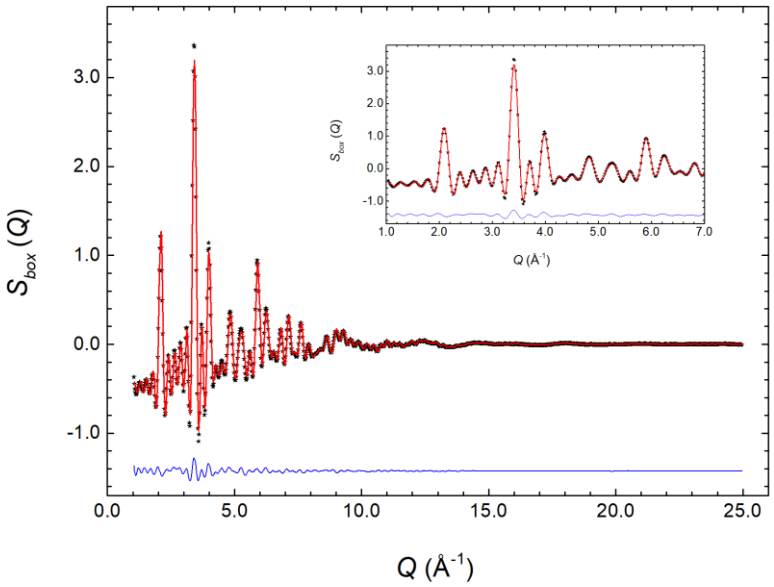

(b)

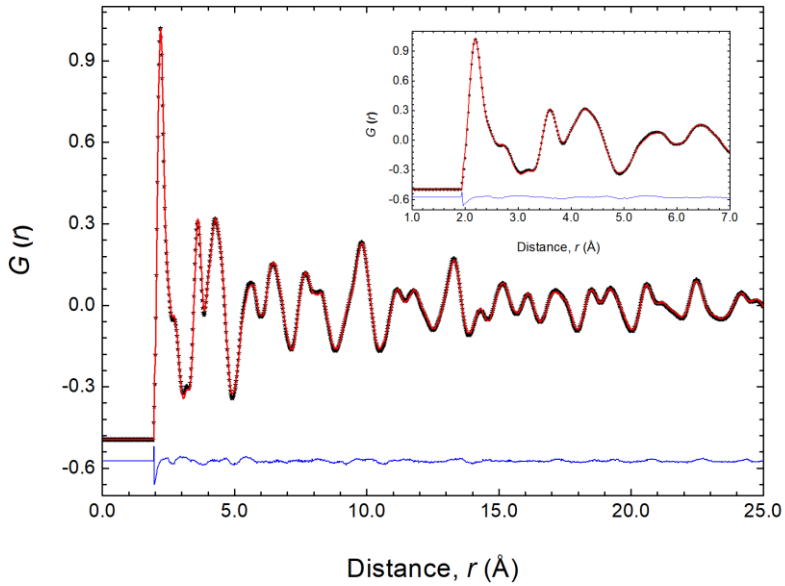

Fig. 7.15. Fits to (a) S(*Q*) and (b) G(*r*) profiles obtained by the RMC modelling of neutron data from the $(Yb_{1-x}Nd_x)_2Zr_2O_7$, x = 0.25. The black dots show the experimental data, the solid red line shows the calculated profile, and the difference profile is shown by the solid blue line.

(a)

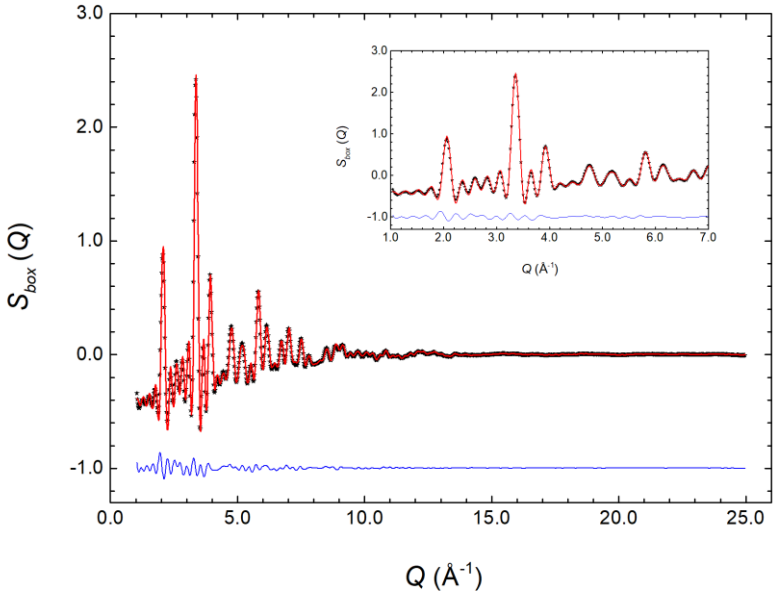

(b)

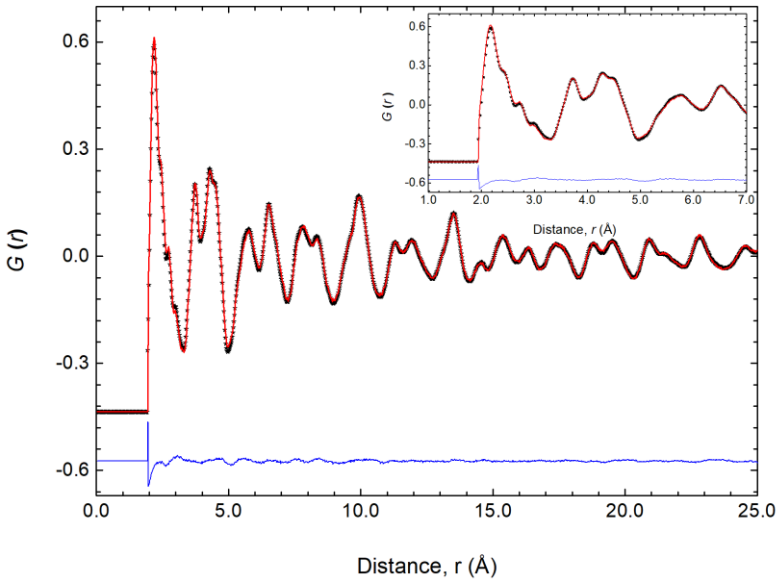

Fig. 7.16. Fits to (a) S(*Q*) and (b) G(*r*) profiles obtained by the RMC modelling of neutron data from the $(Yb_{1-x}Nd_x)_2Zr_2O_7$, x = 0.75, calcined at 950 °C. The black dots show the experimental data, the solid red line shows the calculated profile, and the difference profile is shown by the solid blue line.

(a)

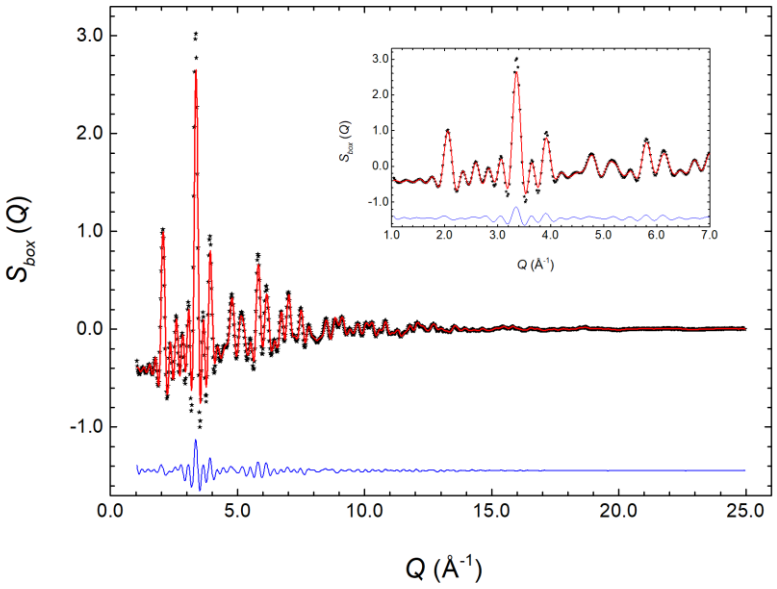

(b)

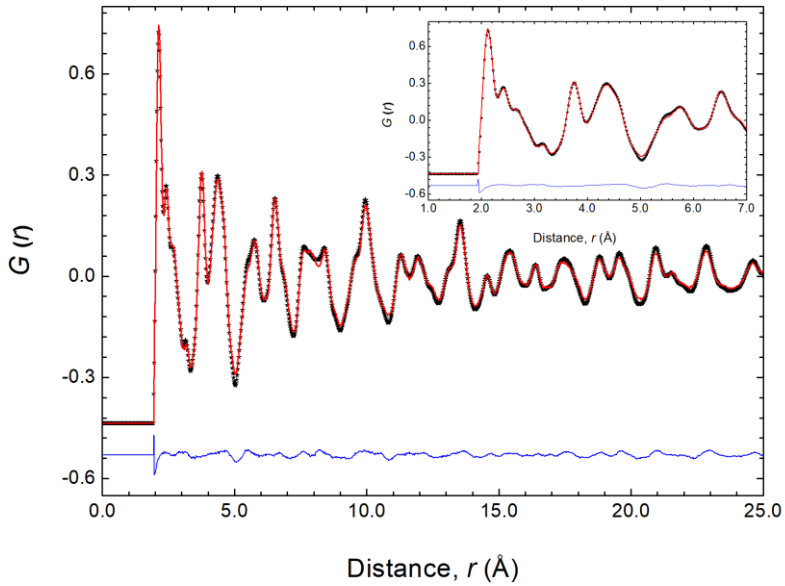

Fig. 7.17. Fits to (a) S(*Q*) and (b) G(*r*) profiles obtained by the RMC modelling of neutron data from the $(Yb_{1-x}Nd_x)_2Zr_2O_7$, x = 0.75, calcined at 1150 °C. The black dots show the experimental data, the solid red line shows the calculated profile, and the difference profile is shown by the solid blue line.

(a)

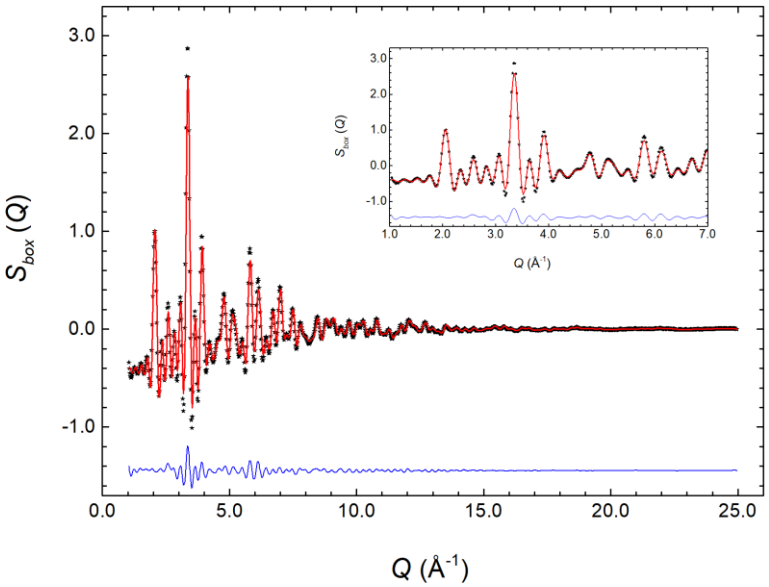

(b)

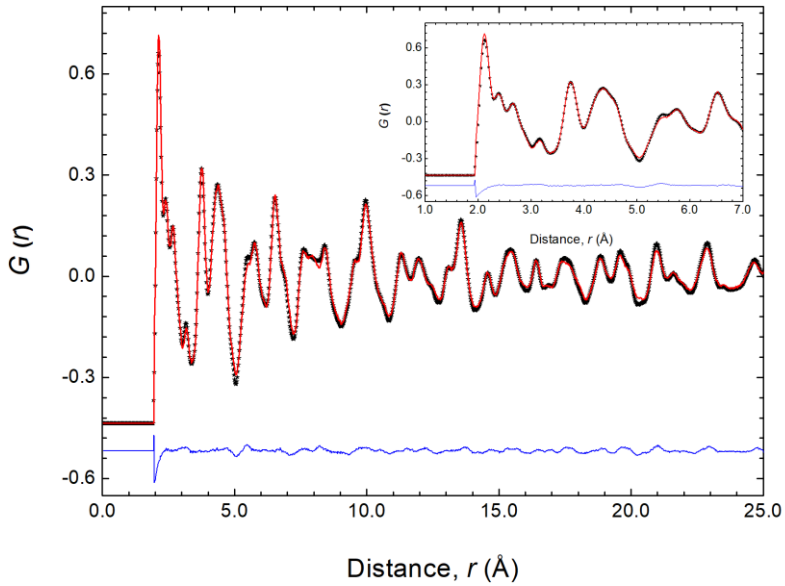

Fig. 7.18. Fits to (a) S(*Q*) and (b) G(*r*) profiles obtained by the RMC modelling of neutron data from the $(Yb_{1-x}Nd_x)_2Zr_2O_7$, x = 0.75, calcined at 1350 °C. The black dots show the experimental data, the solid red line shows the calculated profile, and the difference profile is shown by the solid blue line.

(a)

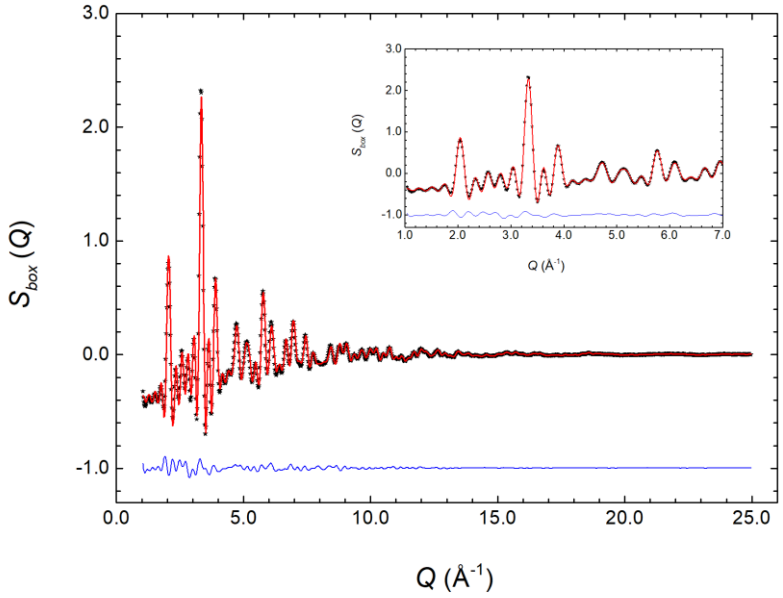

(b)

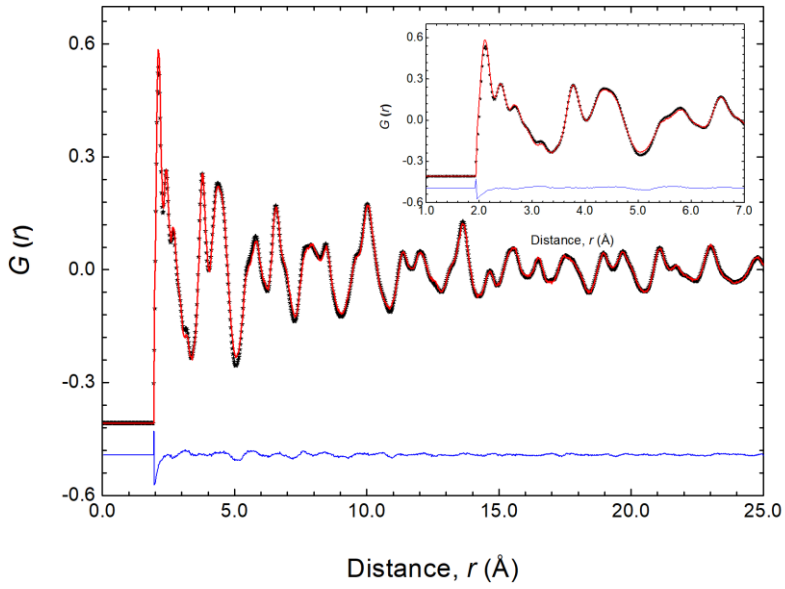

Fig. 7.19. Fits to (a) S(*Q*) and (b) G(*r*) profiles obtained by the RMC modelling of neutron data from the $(Yb_{1-x}Nd_x)_2Zr_2O_7$, x = 1.00, calcined at 950 °C. The black dots show the experimental data, the solid red line shows the calculated profile, and the difference profile is shown by the solid blue line.

(a)

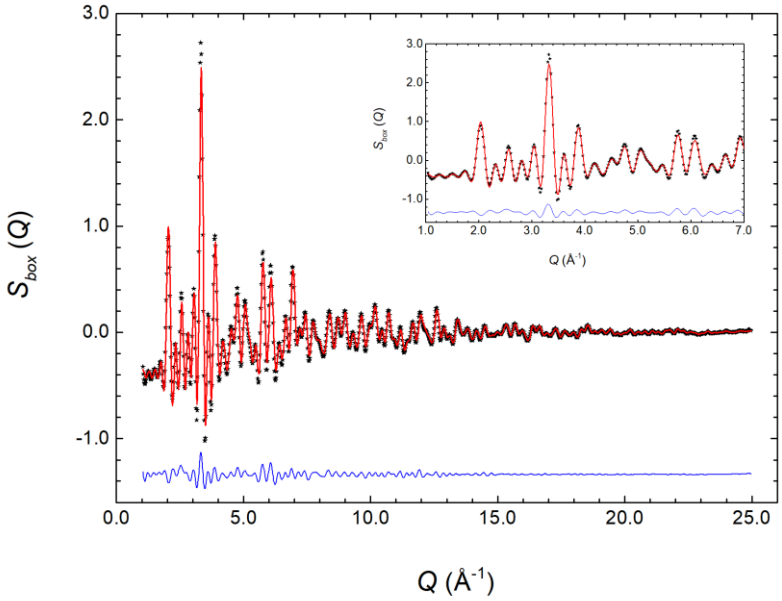

(b)

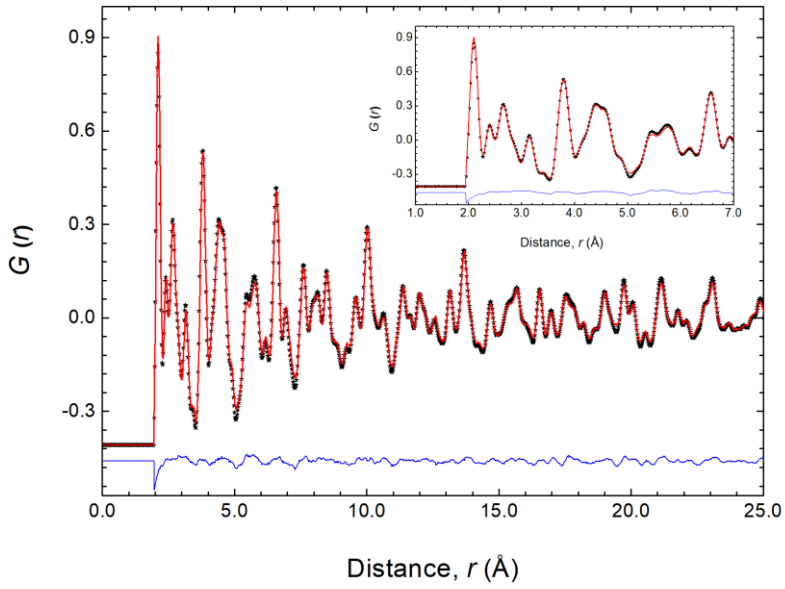

Fig. 7.20. Fits to (a) S(Q) and (b) G(r) profiles obtained by the RMC modelling of neutron data from the $(Yb_{1-x}Nd_x)_2Zr_2O_7$, x = 1.00, calcined at 1350 °C. The black dots show the experimental data, the solid red line shows the calculated profile, and the difference profile is shown by the solid blue line.

(a)

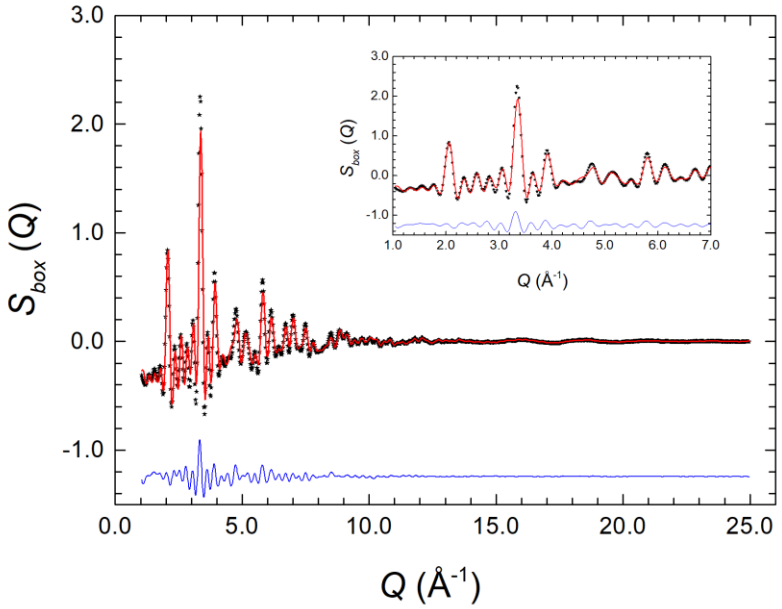

(b)

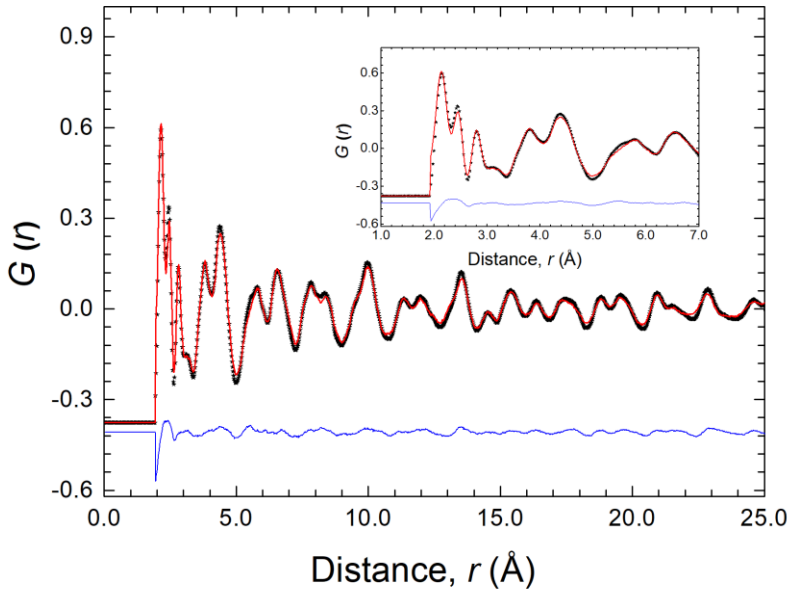

Fig. 7.21. Fitted (a) S(*Q*) and (b) G(*r*) profiles obtained by the RMC modelling of neutron scattering data from $(Nd_{0.5}Ca_{0.5})_2Zr_2O_{6.5}$, at 500 °C. The black dots show the experimental data, the solid red line shows the calculated profile, and the difference profile is shown by the solid blue line.

(a)

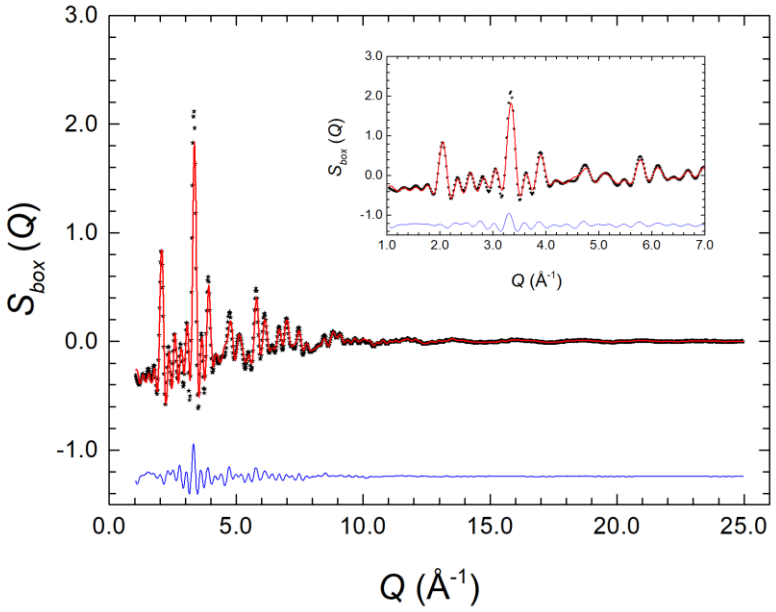

(b)

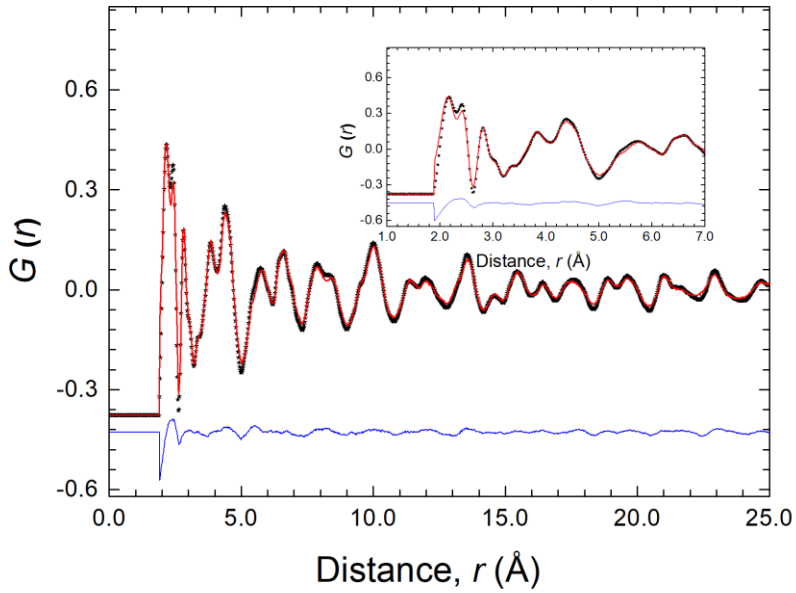

Fig. 7.22. Fitted (a) S(*Q*) and (b) G(*r*) profiles obtained by the RMC modelling of neutron scattering data from $(Nd_{0.5}Ca_{0.5})_2Zr_2O_{6.5}$, at 800 °C. The black dots show the experimental data, the solid red line shows the calculated profile, and the difference profile is shown by the solid blue line.

Appendix D – Conductivity

Table 7.1 Activation energies and total conductivities in the system $(Yb_{1-x}Nd_x)_2Zr_2O_7$ $(0.00 \leq x \leq 1.00)$

x	Ea HT [eV]	Δ_EaHT [eV]	σ at 700°C [Scm-1]	Ea LT [eV]	Δ_EaLT [eV]	σ at 300°C [Scm-1]
0.00	1.5395	0.0034	1.33E-04	1.4245	0.0188	6.96E-10
0.25	1.3747	0.003	1.73E-04	1.3435	0.0065	3.06E-09
0.5	1.2202	0.0027	2.3E-04	1.2415	0.0032	1.23E-08
0.75	1.0436	0.0074	6.82E-04	1.0744	0.0206	2.79E-07
1.00	0.8232	0.0014	9.31E-05	0.7328	0.0039	2.15E-07

Table 7.2 Activation energies and total conductivities in the system $(Nd_{1-x}Ca_x)_2Zr_2O_7$ $(0.10 \leq x \leq 0.50)$

x	Ea HT [eV]	Δ_EaHT [eV]	σ at 700°C [Scm-1]	Ea LT [eV]	Δ_EaLT [eV]	σ at 300°C [Scm-1]
0.1	0.7836	0.0026	0.282E-03	0.9737	0.0097	4.16E-07
0.2	0.8971	0.0056	1.345E-03	1.1181	0.0081	4.75E-07
0.3	0.9564	0.0063	1.728E-03	1.2195	0.0074	2.96E-07
0.4	1.0317	0.0098	1.645E-03	1.2382	0.0032	2.19E-07
0.5	1.1649	0.0035	9.34E-04	1.2817	0.0044	5.64E-08

References

1. A. Rao, *Sustainable Energy Conversion for Electricity and Coproducts - Principles, Technologies, and Equipment*, John Wiley and Sons Inc., New Jersey, 2015.
2. M. Winter and R. J. Brodd, *Chemical Reviews*, 2004, **104**, 4245-4269.
3. L. Carrette, K. A. Friedrich and U. Stimming, *Chemphyschem*, 2000, **1**, 162-193.
4. EG&G Technical Services Inc., *Fuel Cell Handbook*, U.S. Department Of Energy, West Virginia, 2004.
5. N. Q. Minh, *Journal of the American Ceramic Society*, 1993, **76**, 563-588.
6. B. C. H. Steele and A. Heinzel, *Nature*, 2001, **414**, 345-352.
7. A. Lashtabeg and S. J. Skinner, *Journal of Materials Chemistry*, 2006, **16**, 3161-3170.
8. L. Malavasi, C. A. J. Fisher and M. S. Islam, *Chemical Society Reviews*, 2010, **39**, 4370-4387.
9. S. J. Skinner and M. A. Laguna-Bercero, in *Energy Materials*, eds. D. W. Bruce, D. O'Hare and R. I. Walton, John Wiley & Sons, Ltd., United Kingdom, 2011, ch. 2, pp. 33-94.
10. S. J. Skinner, S. Cook and J. A. Kilner, in *Solid Oxide Fuels Cells: Facts and Figures - Past, Present and Future Perspectives for SOFC Technologies*, eds. J. T. S. Irvine and P. Connor, Springer-Verlag, London, 2012, ch. 8, pp. 181-201.
11. O. Yamamoto, *Electrochimica Acta*, 2000, **45**, 2423-2435.
12. D. J. L. Brett, A. Atkinson, N. P. Brandon and S. J. Skinner, *Chemical Society Reviews*, 2008, **37**, 1568-1578.
13. A. Aguadero, L. Fawcett, S. Taub, R. Woolley, K.-T. Wu, N. Xu, J. A. Kilner and S. J. Skinner, *Journal of Materials Science*, 2012, **47**, 3925-3948.
14. N. P. Brandon, S. Skinner and B. C. H. Steele, *Annual Review of Materials Research*, 2003, **33**, 183-213.
15. S. M. Haile, *Acta Materialia*, 2003, **51**, 5981-6000.
16. A. J. Jacobson, *Chemistry of Materials*, 2010, **22**, 660-674.
17. S. J. Skinner and J. A. Kilner, *materialstoday*, 2003.
18. N. Preux, A. Rolle and R. N. Vannier, in *Functional materials for sustainable energy applications*, eds. J. A. Kilner, S. J. Skinner, S. J. C. Irvine and P. P. Edwards, Woodhead Publishing Limited, UK, 2012, ch. 12, pp. 370-401.
19. J. B. Goodenough, *Annual Review of Materials Research*, 2003, **33**, 91-128.
20. F. Abraham, J. C. Boivin, G. Mairesse and G. Nowogrocki, *Solid State Ionics*, 1990, **40-1**, 934-937.
21. H. G. Scott, *Journal of Materials Science*, 1975, **10**, 1527-1535.
22. T. I. Politova and J. T. S. Irvine, *Solid State Ionics*, 2004, **168**, 153-165.
23. S. P. S. Badwal, F. T. Ciacchi and D. Milosevic, *Solid State Ionics*, 2000, **136**, 91-99.
24. K. Nomura, Y. Mizutani, M. Kawai, Y. Nakamura and O. Yamamoto, *Solid State Ionics*, 2000, **132**, 235-239.
25. R. D. Shannon, *Acta Crystallographica Section A*, 1976, **32**, 751-767.
26. H. L. Tuller and A. S. Nowick, *Journal of the Electrochemical Society*, 1975, **122**, 255-259.
27. D. J. Seo, K. O. Ryu, S. B. Park, K. Y. Kim and R. H. Song, *Materials Research Bulletin*, 2006, **41**, 359-366.
28. K. Eguchi, T. Setoguchi, T. Inoue and H. Arai, *Solid State Ionics*, 1992, **52**, 165-172.

29. D. A. Andersson, S. I. Simak, N. V. Skorodumova, I. A. Abrikosov and B. Johansson, *Proceedings of the National Academy of Sciences of the United States of America*, 2006, **103**, 3518-3521.
30. J. W. Fergus, *Journal of Power Sources*, 2006, **162**, 30-40.
31. J. Vanherle, T. Horita, T. Kawada, N. Sakai, H. Yokokawa and M. Dokiya, *Journal of the European Ceramic Society*, 1996, **16**, 961-973.
32. H. Inaba and H. Tagawa, *Solid State Ionics*, 1996, **83**, 1-16.
33. S. Wang, H. Inaba, H. Tagawa and T. Hashimoto, *Journal of the Electrochemical Society*, 1997, **144**, 4076-4080.
34. M. Mogensen, N. M. Sammes and G. A. Tompsett, *Solid State Ionics*, 2000, **129**, 63-94.
35. N. M. Sammes, G. A. Tompsett, H. Nafe and F. Aldinger, *Journal of the European Ceramic Society*, 1999, **19**, 1801-1826.
36. E. D. Wachsman and K. T. Lee, *Science*, 2011, **334**, 935-939.
37. T. Takahashi, H. Iwahara and Y. Nagai, *Journal of Applied Electrochemistry*, 1972, **2**, 97-104.
38. R. Matsuzaki, H. Masumizu and Y. Saeki, *Bulletin of the Chemical Society of Japan*, 1975, **48**, 3397-3398.
39. K. Z. Fung, H. D. Baek and A. V. Virkar, *Solid State Ionics*, 1992, **52**, 199-211.
40. G. Mairesse, in *Fast Ion Transport in Solids*, eds. B. Scrosati, A. Magistris, C. M. Mari and G. Mariotto, Springer Science+Business Media Dordrecht, 1993, ch. 15, pp. 271-290.
41. P. Shuk, H. D. Wiemhofer, U. Guth, W. Gopel and M. Greenblatt, *Solid State Ionics*, 1996, **89**, 179-196.
42. N. X. Jiang, E. D. Wachsman and S. H. Jung, *Solid State Ionics*, 2002, **150**, 347-353.
43. T. Takahashi, T. Esaka and H. Iwahara, *Journal of Applied Electrochemistry*, 1975, **5**, 197-202.
44. M. J. Verkerk and A. J. Burggraaf, *Journal of the Electrochemical Society*, 1981, **128**, 75-82.
45. J. C. Boivin, C. Pirovano, G. Nowogrocki, G. Mairesse, P. Labrune and G. Lagrange, *Solid State Ionics*, 1998, **113**, 639-651.
46. D. W. Jung, J. C. Nino, K. L. Duncan, S. R. Bishop and E. D. Wachsman, *Ionics*, 2010, **16**, 97-103.
47. M. Feng and J. B. Goodenough, *European Journal of Solid State and Inorganic Chemistry*, 1994, **31**, 663-672.
48. T. Ishihara, H. Matsuda and Y. Takita, *Journal of the American Chemical Society*, 1994, **116**, 3801-3803.
49. K. Q. Huang, R. Tichy and J. B. Goodenough, *Journal of the American Ceramic Society*, 1998, **81**, 2581-2585.
50. P. S. Anderson, F. M. B. Marques, D. C. Sinclair and A. R. West, *Solid State Ionics*, 1999, **118**, 229-239.
51. M. S. Khan, M. S. Islam and D. R. Bates, *Journal of Physical Chemistry B*, 1998, **102**, 3099-3104.
52. T. Ishihara, S. Ishikawa, C. Y. Yu, T. Akbay, K. Hosoi, H. Nishiguchi and Y. Takita, *Physical Chemistry Chemical Physics*, 2003, **5**, 2257-2263.
53. T. Ishihara, M. Ando, M. Enoki and Y. Takita, *Journal of Alloys and Compounds*, 2006, **408**, 507-511.

54. K. Q. Huang, M. Feng, J. B. Goodenough and C. Milliken, *Journal of the Electrochemical Society*, 1997, **144**, 3620-3624.
55. J. W. Stevenson, T. R. Armstrong, L. R. Pederson, J. Li, C. A. Lewinsohn and S. Baskaran, *Solid State Ionics*, 1998, **113**, 571-583.
56. A. Matraszek, L. Singheiser, D. Kobertz, K. Hilpert, M. Miller, O. Schulz and M. Martin, *Solid State Ionics*, 2004, **166**, 343-350.
57. G. B. Zhang and D. M. Smyth, *Solid State Ionics*, 1995, **82**, 161-172.
58. S. A. Speakman, J. W. Richardson, B. J. Mitchell and S. T. Misture, *Solid State Ionics*, 2002, **149**, 247-259.
59. A. Manthiram, J. F. Kuo and J. B. Goodenough, *Solid State Ionics*, 1993, **62**, 225-234.
60. P. Berastegui, S. Hull, F. J. Garcia-Garcia and S. G. Eriksson, *Journal of Solid State Chemistry*, 2002, **164**, 119-130.
61. V. Jayaraman, A. Magrez, M. Caldes, O. Joubert, M. Ganne, Y. Piffard and L. Brohan, *Solid State Ionics*, 2004, **170**, 17-24.
62. J. B. Goodenough, J. E. Ruizdiaz and Y. S. Zhen, *Solid State Ionics*, 1990, **44**, 21-31.
63. T. Schober, J. Friedrich and F. Krug, *Solid State Ionics*, 1997, **99**, 9-13.
64. W. Fischer, G. Reck and T. Schober, *Solid State Ionics*, 1999, **116**, 211-215.
65. J. C. Boivin and G. Mairesse, *Chemistry of Materials*, 1998, **10**, 2870-2888.
66. I. Abrahams and F. Krok, *Journal of Materials Chemistry*, 2002, **12**, 3351-3362.
67. P. Lacorre, F. Goutenoire, O. Bohnke, R. Retoux and Y. Laligant, *Nature*, 2000, **404**, 856-858.
68. F. Goutenoire, O. Isnard, R. Retoux and P. Lacorre, *Chemistry of Materials*, 2000, **12**, 2575-2580.
69. S. Georges, F. Goutenoire, F. Altorfer, D. Sheptyakov, F. Fauth, E. Suard and P. Lacorre, *Solid State Ionics*, 2003, **161**, 231-241.
70. S. Georges, S. J. Skinner, P. Lacorre and M. C. Steil, *Dalton Transactions*, 2004, 3101-3105.
71. C. Tealdi, L. Malavasi, C. Ritter, G. Flor and G. Costa, *Journal of Solid State Chemistry*, 2008, **181**, 603-610.
72. E. Kendrick, M. S. Islam and P. R. Slater, *Journal of Materials Chemistry*, 2007, **17**, 3104-3111.
73. J. R. Tolchard, P. R. Slater and M. S. Islam, *Advanced Functional Materials*, 2007, **17**, 2564-2571.
74. L. Leon-Reina, E. R. Losilla, M. Martinez-Lara, S. Bruque and M. A. G. Aranda, *Journal of Materials Chemistry*, 2004, **14**, 1142-1149.
75. P. R. Slater, J. E. H. Sansom and J. R. Tolchard, *Chemical Record*, 2004, **4**, 373-384.
76. V. V. Kharton, F. M. B. Marques and A. Atkinson, *Solid State Ionics*, 2004, **174**, 135-149.
77. A. L. Shaula, V. V. Kharton and F. M. B. Marques, *Solid State Ionics*, 2006, **177**, 1725-1728.
78. A. J. Burggraaf, T. Vandijk and M. J. Verkerk, *Solid State Ionics*, 1981, **5**, 519-522.
79. M. A. Subramanian, G. Aravamudan and G. V. S. Rao, *Progress in Solid State Chemistry*, 1983, **15**, 55-143.
80. B. J. Kennedy, B. A. Hunter and C. J. Howard, *Journal of Solid State Chemistry*, 1997, **130**, 58-65.

81. Z. Zhang, S. C. Middleburgh, M. de los Reyes, G. R. Lumpkin, B. J. Kennedy, P. E. R. Blanchard, E. Reynolds and L.-Y. Jang, *Journal of Physical Chemistry C*, 2013, **117**, 26740-26749.
82. B. C. Chakoumakos, *Journal of Solid State Chemistry*, 1984, **53**, 120-129.
83. K. E. Sickafus, L. Minervini, R. W. Grimes, J. A. Valdez, M. Ishimaru, F. Li, K. J. McClellan and T. Hartmann, *Science*, 2000, **289**, 748-751.
84. L. Minervini, R. W. Grimes and K. E. Sickafus, *Journal of the American Ceramic Society*, 2000, **83**, 1873-1878.
85. A. F. Reid, C. Li and A. E. Ringwood, *Journal of Solid State Chemistry*, 1977, **20**, 219-226.
86. P. J. Wilde and C. R. A. Catlow, *Solid State Ionics*, 1998, **112**, 173-183.
87. B. P. Mandal, A. Banerji, V. Sathe, S. K. Deb and A. K. Tyagi, *Journal of Solid State Chemistry*, 2007, **180**, 2643-2648.
88. C. Heremans, B. J. Wuensch, J. K. Stalick and E. Prince, *Journal of Solid State Chemistry*, 1995, **117**, 108-121.
89. J. Chen, J. Lian, L. M. Wang, R. C. Ewing, R. G. Wang and W. Pan, *Physical Review Letters*, 2002, **88**.
90. G. D. Blundred, C. A. Bridges and M. J. Rosseinsky, *Angewandte Chemie-International Edition*, 2004, **43**, 3562-3565.
91. A. N. Radhakrishnan, P. P. Rao, K. S. Sibi, M. Deepa and P. Koshy, *Journal of Solid State Chemistry*, 2009, **182**, 2312-2318.
92. R. Clements, J. R. Hester, B. J. Kennedy, C. D. Ling and A. P. J. Stampfl, *Journal of Solid State Chemistry*, 2011, **184**, 2108-2113.
93. F. X. Zhang, M. Lang and R. C. Ewing, *Applied Physics Letters*, 2015, **106**, 4.
94. P. K. Moon and H. L. Tuller, *Sensors and Actuators B-Chemical*, 1990, **1**, 199-202.
95. H. L. Tuller, *Solid State Ionics*, 1992, **52**, 135-146.
96. A. V. Shlyakhtina, A. V. Knotko, M. V. Boguslavskii, S. Y. Stefanovich, I. V. Kolbanev, D. V. Peryshkov and L. G. Shcherbakova, *Inorganic Materials*, 2005, **41**, 406-411.
97. M. P. Vandijk, F. C. Mijlhoff and A. J. Burggraaf, *Journal of Solid State Chemistry*, 1986, **62**, 377-385.
98. A. V. Shlyakhtina, S. N. Savvin, A. V. Levchenko, A. V. Knotko, P. Fedtke, A. Busch, T. Barfels, M. Wienecke and L. G. Shcherbakova, *Journal of Electroceramics*, 2010, **24**, 300-307.
99. A. V. Shlyakhtina and L. G. Shcherbakova, *Solid State Ionics*, 2011, **192**, 200-204.
100. D. Michel, Perezyjo.M and Collongu.R, *Materials Research Bulletin*, 1974, **9**, 1457-1468.
101. T. Vandijk, K. J. Devries and A. J. Burggraaf, *Physica Status Solidi a-Applied Research*, 1980, **58**, 115-125.
102. B. J. Wuensch, K. W. Eberman, C. Heremans, E. M. Ku, P. Onnerud, E. M. E. Yeo, S. M. Haile, J. K. Stalick and J. D. Jorgensen, *Solid State Ionics*, 2000, **129**, 111-133.
103. C. Heremans, B. J. Wuensch, J. K. Stalick and E. Prince, in *Solid State Ionics Iii*, eds. G. A. Nazri, J. M. Tarascon and M. Armand, Materials Research Soc, Pittsburgh, 1993, vol. 293, pp. 349-354.
104. S. Kramer, M. Spears and H. L. Tuller, *Solid State Ionics*, 1994, **72**, 59-66.
105. M. R. Diaz-Guillen, K. J. Moreno, J. A. Diaz-Guillen, A. F. Fuentes, K. L. Ngai, J. Garcia-Barriocanal, J. Santamaria and C. Leon, *Physical Review B*, 2008, **78**.

106. M. P. Vandijk, A. J. Burggraaf, A. N. Cormack and C. R. A. Catlow, *Solid State Ionics*, 1985, **17**, 159-167.
107. R. E. Williford, W. J. Weber, R. Devanathan and J. D. Gale, *Journal of Electroceramics*, 1999, **3**, 409-424.
108. M. A. Frechero, J. Dura, M. R. Diaz-Guillen, K. J. Moreno, J. A. Diaz-Guillen, J. Garcia-Barriocanal, A. Rivera-Calzada, A. F. Fuentes and C. Leon, *Journal of Non-Crystalline Solids*, 2015, **407**, 349-354.
109. M. P. Vandijk, K. J. Devries and A. J. Burggraaf, *Solid State Ionics*, 1983, **9-10**, 913-919.
110. M. Pirzada, R. W. Grimes, L. Minervini, J. F. Maguire and K. E. Sickafus, *Solid State Ionics*, 2001, **140**, 201-208.
111. K. V. G. Kutty, C. K. Mathews, T. N. Rao and U. V. Varadaraju, *Solid State Ionics*, 1995, **80**, 99-110.
112. H. Yamamura, H. Nishino, K. Kakinuma and K. Nomura, *Solid State Ionics*, 2003, **158**, 359-365.
113. P. J. Wilde and C. R. A. Catlow, *Solid State Ionics*, 1998, **112**, 185-195.
114. J. Garcia-Barriocanal, K. J. Moreno, G. Mendoza-Suarez, A. F. Fuentes, J. Santamaria and C. Leon, *Journal of Non-Crystalline Solids*, 2005, **351**, 2813-2818.
115. H. Nishino, H. Yamamura, T. Arai, K. Kakinuma and K. Nomura, *Journal of the Ceramic Society of Japan*, 2004, **112**, 541-546.
116. H. Yamamura, H. Nishino, K. Kakinuma and K. Nomura, *Solid State Ionics*, 2007, **178**, 233-238.
117. A. V. Shlyakhtina, *Crystallography Reports*, 2013, **58**, 548-562.
118. T. Uehara, K. Koto, F. Kanamaru and H. Horiuchi, *Solid State Ionics*, 1987, **23**, 137-143.
119. A. V. Shlyakhtina, S. N. Savvin, A. V. Levchenko, M. V. Boguslavskii and L. G. Shcherbakova, *Solid State Ionics*, 2008, **179**, 985-990.
120. V. V. Kharton, E. V. Tsipis, A. A. Yaremchenko, N. P. Vyshatko, A. L. Shaula, E. N. Naumovich and J. R. Frade, *Journal of Solid State Electrochemistry*, 2003, **7**, 468-476.
121. J. A. Diaz-Guillen, M. R. Diaz-Guillen, K. P. Padmasree, A. F. Fuentes, J. Santamaria and C. Leon, *Solid State Ionics*, 2008, **179**, 2160-2164.
122. X. L. Xia, J. H. Ouyang, Z. G. Liu, S. A. Gao and S. Li, *Journal of the Electrochemical Society*, 2010, **157**, B470-B476.
123. X.-L. Xia, Z.-G. Liu, J.-H. Ouyang, S. Gao and X.-M. Liu, *Solid State Sciences*, 2011, **13**, 1328-1333.
124. M. Shafique, B. J. Kennedy, Y. Iqbal and R. Ubic, *Journal of Alloys and Compounds*, 2016, **671**, 226-233.
125. Z. G. Liu, J. H. Ouyang, Y. Zhou and X. L. Xia, *Philosophical Magazine Letters*, 2010, **90**, 753-761.
126. K. Zakharchuk, E. Kravchenko, D. P. Fagg, J. R. Frade and A. A. Yaremchenko, *Rsc Advances*, 2016, **6**, 70186-70196.
127. S. A. Kramers and H. L. Tuller, *Solid State Ionics*, 1995, **82**, 15-23.
128. A. V. Shlyakhtina, J. C. C. Abrantes, A. V. Levchenko, S. Y. Stefanovich, A. V. Knot'ko, L. L. Larina and L. G. Shcherbakova, in *Advanced Materials Forum Iii, Pts 1 and 2*, ed. P. M. Vilarinho, Trans Tech Publications Ltd, Zurich-Uetikon, 2006, vol. 514-516, pp. 422-426.
129. A. V. Shlyakhtina, J. C. C. Abrantes, A. V. Levchenko, A. V. Knot'ko, O. K. Karyagina and L. G. Shcherbakova, *Solid State Ionics*, 2006, **177**, 1149-1155.

130. J. C. C. Abrantes, A. Levchenko, A. V. Shlyakhtina, L. G. Shcherbakova, A. L. Horovistiz, D. P. Fagg and J. R. Frade, *Solid State Ionics*, 2006, **177**, 1785-1788.
131. P. K. Moon and H. L. Tuller, in *Science and Technology of Fast Ion Conductors*, eds. H. L. Tuller and M. Balkanski, Plenum Press, New York, 1989, pp. 307-312.
132. D. A. Belov, A. V. Shlyakhtina, S. Y. Stefanovich, I. V. Kolbanev, Y. A. Belousov, O. K. Karyagina and L. G. Shcherbakova, *Materials Research Bulletin*, 2009, **44**, 1613-1620.
133. O. Porat, C. Heremans and H. L. Tuller, *Solid State Ionics*, 1997, **94**, 75-83.
134. A. V. Shlyakhtina, A. E. Sokolov, V. A. Ul'yanov, V. A. Trunov, M. V. Boguslavskii, A. V. Levchenko and L. G. Shcherbakova, *Crystallography Reports*, 2009, **54**, 25-30.
135. A. V. Shlyakhtina, D. A. Belov, S. Y. Stefanovich, O. K. Karyagina and L. G. Shcherbakova, *Inorganic Materials*, 2012, **48**, 1126-1130.
136. A. V. Shlyakhtina, A. V. Mosunov, S. Y. Stefanovich, O. K. Karyagina and L. G. Shcherbakova, *Inorganic Materials*, 2004, **40**, 1317-1320.
137. P. K. Moon and H. L. Tuller, *Solid State Ionics*, 1988, **28**, 470-474.
138. B. P. Mandal, S. K. Deshpande and A. K. Tyagi, *Journal of Materials Research*, 2008, **23**, 911-916.
139. J. A. Diaz-Guillen, A. F. Fuentes, M. R. Diaz-Guillen, J. M. Almanza, J. Santamaria and C. Leon, *Journal of Power Sources*, 2009, **186**, 349-352.
140. F. N. Sayed, B. P. Mandal, D. Jain, C. G. N. S. Pillai and A. K. Tyagi, *Journal of the European Ceramic Society*, 2012, **32**, 3221-3228.
141. T. H. Yu and H. L. Tuller, *Solid State Ionics*, 1996, **86-8**, 177-182.
142. G. Ou, W. Liu, L. Yao, H. Wu and W. Pan, *Journal of Materials Chemistry A*, 2014, **2**, 1855-1861.
143. F. Yang, Y. F. Wang, X. F. Zhao and P. Xiao, *Journal of Power Sources*, 2015, **273**, 290-297.
144. G. V. M. Kiruthika, K. V. G. Kutty and U. V. Varadarju, *Solid State Ionics*, 1998, **110**, 335-340.
145. R. E. Carbonio, J. A. Alonso and J. L. Martinez, *Journal of Physics-Condensed Matter*, 1999, **11**, 361-369.
146. R. Martinez-Coronado, J. A. Alonso, V. Cascos and M. T. Fernandez-Diaz, *Journal of Power Sources*, 2014, **247**, 876-882.
147. R. Martinez-Coronado, A. Aguadero, C. de la Calle, M. T. Fernandez and J. A. Alonso, *Journal of Power Sources*, 2011, **196**, 4181-4186.
148. Z. G. Liu, J. H. Ouyang, Y. Zhou, Q. C. Meng and X. L. Xia, *Philosophical Magazine*, 2009, **89**, 553-564.
149. Z. P. Shao, W. Zhou and Z. H. Zhu, *Progress in Materials Science*, 2012, **57**, 804-874.
150. M. J. Buerger, *Elementary Crystallography - An Introduction to the fundamental geometrical features of crystals*, John Wiley and Sons, Inc., New York, 1956.
151. S. R. Elliott, *The Physics and Chemistry of Solids*, John Wiley and Sons Ltd., England, 1998.
152. A. R. West, *Solid State Chemistry and its Applications*, John Wiley and Sons Ltd., United Kingdom, 2014.
153. A. K. Cheetham, in *Solid State Chemistry - Techniques*, eds. A. K. Cheetham and P. Day, Oxford University Press Inc., New York, 1987, ch. 2, pp. 39-83.
154. C. Giacovazzo, H. L. Monaco, D. Viterbo, F. Scordari, G. Gilli, G. Zanotti and M. Catti, *Fundamentals of Crystallography*, Oxford University Press, New York, 1992.

155. U. Shmueli, *Theories and Techniques of Crystal Structure Determination*, Oxford University Press Inc., New York, 2007.
156. J. P. Glusker, M. Lewis and M. Rossi, *Crystal Structure Analysis for Chemists and Biologists*, VCH Publishers, New York, 1994.
157. B. D. Cullity and S. R. Stock, *Elements of X-Ray Diffraction*, Pearson Education Limited, England, 2014.
158. V. K. Pecharsky and P. Y. Zavalij, *Fundamentals of Powder Diffraction and Structural Characterization of Materials*, Springer Science+Business Media, New York, 2009.
159. G. E. Bacon, *Neutron Diffraction*, Oxford University Press, London, 1962.
160. J. A. Alonso, M. J. Martinez-Lope, A. Aguadero and L. Daza, *Progress in Solid State Chemistry*, 2008, **36**, 134-150.
161. G. L. Squires, *Introduction to the Theory of Thermal Neutron Scattering*, Dover Publications, Inc., New York, 1978.
162. J. P. Glusker and K. N. Trueblood, *Crystal Structure Analysis A primer*, Oxford University Press, Oxford, 2010.
163. K. D. M. Harris and M. Tremayne, *Chemistry of Materials*, 1996, **8**, 2554-2570.
164. G. E. Bacon, *X-ray and Neutron Diffraction*, Pergamon Press Ltd., Oxford, 1966.
165. V. Sears, *Neutron News*, 1992, **3**.
166. P. E. R. Blanchard, R. Clements, B. J. Kennedy, C. D. Ling, E. Reynolds, M. Avdeev, A. P. J. Stampfl, Z. M. Zhang and L. Y. Jang, *Inorganic Chemistry*, 2012, **51**, 13237-13244.
167. V. K. Peterson and G. J. Kearley, in *Neutron Applications in Materials for Energy*, eds. G. J. Kearley and V. K. Peterson, Springer International Publishing, Switzerland, 2015, ch. 1, pp. 1-16.
168. R. L. McGreevy, *International Journal of Modern Physics B*, 1993, **7**, 2965-2980.
169. T. Egami and S. J. L. Billinge, *Underneath the Bragg peaks - Structural Analysis of Complex Materials*, Elsevier Ltd., UK, 2003.
170. R. Pynn, in *Neutron Applications in Earth, Energy and Environmental Sciences*, eds. L. Liang, R. Rinaldi and H. Schober, Springer Science+Business Media, New York, 2009, ch. 2, pp. 15-36.
171. K. Cockcroft and A. N. Fitch, in *Powder Diffraction Theory and Practice*, eds. R. E. Dinnebier and S. J. L. Billinge, The Royal Society of Chemistry, UK, 2008, ch. 2, pp. 20-57.
172. M. Arai, in *Neutron Scattering - Fundamentals*, eds. F. Fernandez-Alonso and D. L. Price, Elsevier Inc., United Kingdom, 2013, ch. 3, pp. 245-320.
173. P. J. Chupas and K. W. Chapman, in *Principles and Applications of Powder Diffraction*, eds. A. Clearfield, J. H. Reibenspies and N. Bhuvanesh, John Wiley and Sons, United Kingdom, 2008, ch. 5, pp. 199-225.
174. W. Knop, P. K. Pranzas and P. Schreiner, in *Neutrons and Synchrotron Radiation in Engineering Materials Science*, eds. W. Reimers, A. R. Pyzalla, A. Schreyer and H. Clemens, Wiley-VCH, Weinheim, 2008, ch. 5, pp. 91-112.
175. S. Hull, R. I. Smith, W. I. F. David, A. C. Hannon, J. Mayers and R. Cywinski, *Physica B*, 1992, **180**, 1000-1002.
176. R. I. Smith and S. Hull, *User Guide for the Polaris Powder Diffractometer at ISIS*, Rutherford Appleton Laboratory Report RAL-TR-97-038, Oxford, 1997.
177. S. T. Norberg, I. Ahmed, R. I. Smith, S. G. Eriksson, L. C. Chapon and S. Hull, *The Polaris Diffractometer at ISIS: Planned Upgrade and New Facilities*, Poster, Rutherford Appleton Laboratory, Oxford, 2009.

178. A. K. Soper, *GudrunN and GudrunX : programs for correcting raw neutron and X-ray diffraction data to differential scattering cross section*, Rutherford Appleton Laboratory Report RAL-TR-2011-013, Oxford, 2012.
179. D. A. Keen and R. L. McGreevy, *Journal of Physics-Condensed Matter*, 1991, **3**, 7383-7394.
180. V. M. Nield and D. A. Keen, *Diffuse Neutron Scattering from Crystalline Materials*, Clarendon Press, Oxford, 2001.
181. R. L. McGreevy and M. A. Howe, *Annual Review of Materials Science*, 1992, **22**, 217-242.
182. T. Proffen and H. Kim, *Journal of Materials Chemistry*, 2009, **19**, 5078-5088.
183. L. Malavasi, *Dalton Transactions*, 2011, **40**, 3777-3788.
184. M. T. Dove, *Structure and Dynamics: An Atomic View of Materials*, Oxford University Press, Oxford, 2002.
185. S. J. L. Billinge and M. G. Kanatzidis, *Chemical Communications*, 2004, 749-760.
186. D. A. Keen, *Journal of Applied Crystallography*, 2001, **34**, 172-177.
187. R. B. Neder, in *Structure from Diffraction Methods*, eds. D. W. Bruce, D. O'Hare and R. I. Walton, John Wiley and Sons Ltd., United Kingdom, 2014, ch. 3, pp. 155-200.
188. I. K. Jeong, R. H. Heffner, M. J. Graf and S. J. L. Billinge, *Physical Review B*, 2003, **67**, 9.
189. M. G. Tucker, D. A. Keen, M. T. Dove, A. L. Goodwin and Q. Hui, *Journal of Physics-Condensed Matter*, 2007, **19**, 16.
190. M. G. Tucker, M. T. Dove, A. L. Goodwin, D. A. Keen and H. Playford, *RMCProfile User Manual: Code Version 6.5.2*, 2014.
191. C. L. Farrow, P. Juhas, J. W. Liu, D. Bryndin, E. S. Bozin, J. Bloch, T. Proffen and S. J. L. Billinge, *Journal of Physics-Condensed Matter*, 2007, **19**, 7.
192. T. Proffen and R. B. Neder, *Journal of Applied Crystallography*, 1997, **30**, 171-175.
193. R. A. Young, in *The Rietveld Method*, ed. R. A. Young, Oxford University Press, New York, 1993, ch. 1, pp. 1-38.
194. R. B. Von Dreele, in *Neutron Scattering in Earth Sciences*, ed. H. R. Wenk, Mineralogical Society of America, United States of America, 2006, ch. 4, pp. 81-98.
195. H. M. Rietveld, *Journal of Applied Crystallography*, 1969, **2**.
196. W. Clegg, in *Structure from Diffraction Methods*, eds. D. W. Bruce, D. O'Hare and R. I. Walton, John Wiley and Sons Ltd., United Kingdom, 2014, ch. 2, pp. 83-154.
197. L. B. McCusker, R. B. Von Dreele, D. E. Cox, D. Louer and P. Scardi, *Journal of Applied Crystallography*, 1999, **32**, 36-50.
198. B. H. Toby, *Journal of Applied Crystallography*, 2001, **34**, 210-213.
199. A. C. Larson and R. B. Von Dreele, *General Structure Analysis System (GSAS)*, Los Alamos National Laboratory Report LAUR 86-748, United States of America, 2004.
200. R. L. McGreevy, M. A. Howe, V. M. Nield, J. D. Wicks and D. A. Keen, *Physica B*, 1992, **180**, 801-804.
201. A. Mellergard and R. L. McGreevy, *Acta Crystallographica Section A*, 1999, **55**, 783-789.
202. M. G. Tucker, M. T. Dove and D. A. Keen, *Journal of Applied Crystallography*, 2001, **34**, 630-638.
203. R. L. McGreevy, *Journal of Physics-Condensed Matter*, 2001, **13**, R877-R913.
204. R. L. McGreevy and L. Pusztai, *Molecular Simulation*, 1988, **1**, 359-367.
205. G. Evrard and L. Pusztai, *Journal of Physics-Condensed Matter*, 2005, **17**, S37-S46.

206. D. A. Keen and R. L. McGreevy, *Nature*, 1990, **344**, 423-425.
207. S. J. Gurman and R. L. McGreevy, *Journal of Physics-Condensed Matter*, 1990, **2**, 9463-9473.
208. D. A. Keen, M. G. Tucker and M. T. Dove, *Journal of Physics-Condensed Matter*, 2005, **17**, S15-S22.
209. S. T. Norberg, M. G. Tucker and S. Hull, *Journal of Applied Crystallography*, 2009, **42**, 179-184.
210. J. Li, *Modelling and Simulation in Materials Science and Engineering*, 2003, **11**, 173-177.
211. J. T. S. Irvine, D. C. Sinclair and A. R. West, *Advanced Materials*, 1990, **2**.
212. J. R. Macdonald, *Annals of Biomedical Engineering*, 1992, **20**, 289-305.
213. D. C. Sinclair, *Boletín de la Sociedad Española de Cerámica y Vidrio*, 1995, **34**, 55-65.
214. E. J. Abram, D. C. Sinclair and A. R. West, *Journal of Electroceramics*, 2003, **10**, 165-177.
215. J. R. Dygas and M. W. Breiter, *Electrochimica Acta*, 1996, **41**, 993-1001.
216. J. R. Dygas, P. Kurek and M. W. Breiter, *Electrochimica Acta*, 1995, **40**, 1545-1550.
217. X. Q. Cao, R. Vassen and D. Stoever, *Journal of the European Ceramic Society*, 2004, **24**, 1-10.
218. Q. Xu, W. Pan, J. D. Wang, C. L. Wan, L. H. Qi, H. Z. Miao, K. Mori and T. Torigoe, *Journal of the American Ceramic Society*, 2006, **89**, 340-342.
219. R. C. Ewing, W. J. Weber and J. Lian, *Journal of Applied Physics*, 2004, **95**, 5949-5971.
220. L. Kong, Y. Zhang, J. Karatchevtseva, M. G. Blackford, G. R. Lumpkin and G. Triani, *Ceramics International*, 2014, **40**, 651-657.
221. M. Uno, A. Kosuga, M. Okui, K. Horisaka, H. Muta, K. Kurosaki and S. Yamanaka, *Journal of Alloys and Compounds*, 2006, **420**, 291-297.
222. Y. Tong, J. Zhu, L. Lu, X. Wang and X. Yang, *Journal of Alloys and Compounds*, 2008, **465**, 280-284.
223. Z.-G. Liu, J.-H. Ouyang, K.-N. Sun and X.-L. Xia, *Electrochimica Acta*, 2010, **55**, 8466-8470.
224. Z.-G. Liu, J.-H. Ouyang, Y. Zhou, J. Xiang and X.-M. Liu, *Materials & Design*, 2011, **32**, 4201-4206.
225. A. V. Shlyakhtina, A. V. Knotko, M. V. Boguslavskii, S. Y. Stefanovich, D. V. Peryshkov, I. V. Kolbanev and L. G. Shcherbakova, *Solid State Ionics*, 2005, **176**, 2297-2304.
226. Y. Matsukawa and S. J. Zinkle, *Science*, 2007, **318**, 959-962.
227. H. L. Tuller, *Journal of Physics and Chemistry of Solids*, 1994, **55**, 1393-1404.
228. Z. G. Liu, J. H. Ouyang and K. N. Sun, *Fuel Cells*, 2010, **10**, 1050-1056.
229. O. Fabrichnaya, G. Savinykh, G. Schreiber and H. J. Seifert, *Journal of Phase Equilibria and Diffusion*, 2011, **32**, 284-297.
230. V. L. Stolyarova, S. I. Lopatin, O. B. Fabrichnaya and S. M. Shugurov, *Rapid Communications in Mass Spectrometry*, 2014, **28**, 109-114.
231. Z.-G. Liu, J.-H. Ouyang, Y. Zhou and X.-L. Xia, *Journal of Power Sources*, 2010, **195**, 3261-3265.
232. M. G. Tucker, D. A. Keen, M. T. Dove, A. L. Goodwin and Q. Hui, *Journal of Physics-Condensed Matter*, 2007, **19**.
233. Z. G. Liu, J. H. Ouyang, Y. Zhou and X. L. Xia, *Advances in Applied Ceramics*, 2010, **109**, 12-17.

234. J. L. Payne, M. G. Tucker and I. R. Evans, *Journal of Solid State Chemistry*, 2013, **205**, 29-34.
235. L. G. Kong, I. Karatchevtseva, D. J. Gregg, M. G. Blackford, R. Holmes and G. Triani, *Journal of the European Ceramic Society*, 2013, **33**, 3273-3285.
236. B. P. Mandal, P. S. R. Krishna and A. K. Tyagi, *Journal of Solid State Chemistry*, 2010, **183**, 41-45.
237. E. Reynolds, P. E. R. Blanchard, B. J. Kennedy, C. D. Ling, S. Liu, M. Avdeev, Z. Zhang, G. J. Cuello, A. Tadich and L.-Y. Jang, *Inorganic Chemistry*, 2013, **52**, 8409-8415.
238. A. V. Shlyakhtina, O. K. Karyagina and L. G. Shcherbakova, *Inorganic Materials*, 2004, **40**, 59-65.
239. V. V. Popov, A. P. Menushenkov, A. A. Yaroslavtsev, Y. V. Zubavichus, B. R. Gaynanov, A. A. Yastrebtsev, D. S. Leshchev and R. V. Chernikov, *Journal of Alloys and Compounds*, 2016, **689**, 669-679.
240. W. C. Hamilton, *Acta Crystallographica*, 1965, **18**, 502-510.
241. M. Leszczynska, X. Liu, W. Wrobel, M. Malys, S. T. Norberg, S. Hull, F. Krok and I. Abrahams, *Journal of Physics-Condensed Matter*, 2013, **25**, 8.
242. S. T. Norberg, S. Hull, S. G. Eriksson, I. Ahmed, F. Kinyanjui and J. J. Biendicho, *Chemistry of Materials*, 2012, **24**, 4294-4300.
243. J. R. Dygas, M. Malys, F. Krok, W. Wrobel, A. Kozanecka and I. Abrahams, *Solid State Ionics*, 2005, **176**, 2085-2093.
244. S. K. Cole and H. R. Cole *The Journal of Chemical Physics*, 1941, **9**.
245. M. Pirzada, R. W. Grimes and J. F. Maguire, *Solid State Ionics*, 2003, **161**, 81-91.
246. T. H. Yu and H. L. Tuller, *Journal of Electroceramics*, 1998, **2**, 49-55.
247. A. V. Shlyakhtina, P. Fedtke, A. Busch, I. V. Kolbanev, T. Barfels, M. Wienecke, A. E. Sokolov, V. A. Ulianov, V. A. Trounov and L. G. Shcherbakova, *Solid State Ionics*, 2008, **179**, 1004-1008.
248. I. Abrahams, X. Liu, S. Hull, S. T. Norberg, F. Krok, A. Kozanecka-Szmigiel, M. S. Islam and S. J. Stokes, *Chemistry of Materials*, 2010, **22**, 4435-4445.
249. X. Liu, I. Abrahams, S. Hull, S. T. Norberg, M. Holdynski and F. Krok, *Solid State Ionics*, 2011, **192**, 176-180.
250. B. P. Mandal, N. Garg, S. M. Sharma and A. K. Tyagi, *Journal of Solid State Chemistry*, 2006, **179**, 1990-1994.
251. K. Shimamura, T. Arima, K. Idemitsu and Y. Inagaki, *International Journal of Thermophysics*, 2007, **28**, 1074-1084.
252. B. J. Wuensch and K. W. Eberman, *Jom-Journal of the Minerals Metals & Materials Society*, 2000, **52**, 19-21.
253. P. Nachimuthu, S. Thevuthasan, E. M. Adams, W. J. Weber, B. D. Begg, B. S. Mun, D. K. Shuh, D. W. Lindle, E. M. Gullikson and R. C. C. Perera, *Journal of Physical Chemistry B*, 2005, **109**, 1337-1339.
254. M. Burbano, S. T. Norberg, S. Hull, S. G. Eriksson, D. Marrocchelli, P. A. Madden and G. W. Watson, *Chemistry of Materials*, 2012, **24**, 222-229.
255. H. C. Yao and Y. F. Y. Yao, *Journal of Catalysis*, 1984, **86**, 254-265.
256. T. Sasaki, Y. Ukyo, A. Suda, M. Sugiura, K. Kuroda and H. Saka, *Journal of the Ceramic Society of Japan*, 2002, **110**, 899-903.
257. M. Sugiura, *Catalysis Surveys from Asia*, 2003, **7**, 77-87.

258. F. Esch, S. Fabris, L. Zhou, T. Montini, C. Africh, P. Fornasiero, G. Comelli and R. Rosei, *Science*, 2005, **309**, 752-755.
259. C. T. Campbell and C. H. F. Peden, *Science*, 2005, **309**, 713-714.
260. J. B. Thomson, A. R. Armstrong and P. G. Bruce, *Chemical Communications*, 1996, 1165-1166.
261. M. S. Whittingham, in *Intercalation Chemistry*, eds. M. S. Whittingham and A. J. Jacobson, Academic Press, New York, 1982, ch. 1, pp. 1-18.
262. J. B. Thomson, A. R. Armstrong and P. G. Bruce, *Journal of Solid State Chemistry*, 1999, **148**, 56-62.
263. A. R. Armstrong and P. G. Bruce, *Nature*, 1996, **381**, 499-500.
264. G. Vlaic, R. Di Monte, P. Fornasiero, E. Fonda, J. Kaspar and M. Graziani, *Journal of Catalysis*, 1999, **182**, 378-389.
265. J. B. Thomson, A. R. Armstrong and P. G. Bruce, *Journal of the American Chemical Society*, 1996, **118**, 11129-11133.
266. T. Sasaki, Y. Ukyo, A. Suda, M. Sugiura, K. Kuroda, S. Arai and H. Saka, *Journal of the Ceramic Society of Japan*, 2003, **111**, 382-385.
267. M. Yashima, M. Kakihana and M. Yoshimura, *Solid State Ionics*, 1996, **86-8**, 1131-1149.
268. S. Meriani, *Journal De Physique*, 1986, **47**, 485-489.
269. M. Yashima, H. Arashi, M. Kakihana and M. Yoshimura, *Journal of the American Ceramic Society*, 1994, **77**, 1067-1071.
270. M. Yashima, S. Sasaki, Y. Yamaguchi, M. Kakihana, M. Yoshimura and T. Mori, *Applied Physics Letters*, 1998, **72**, 182-184.
271. Y. M. and S. T., *Bull. Tokyo Inst. Technol.*, 1972, **108**.
272. T. Sasaki, Y. Ukyo, K. Kuroda, S. Arai, S. Muto and H. Saka, *Journal of the Ceramic Society of Japan*, 2004, **112**, 440-444.
273. S. Otsuka-Yao-Matsuo, T. Omata, N. Izu and H. Kishimoto, *Journal of Solid State Chemistry*, 1998, **138**, 47-54.
274. E. Tani, M. Yoshimura and S. Somiya, *Journal of the American Ceramic Society*, 1983, **66**, 506-510.
275. S. N. Achary, S. K. Sali, N. K. Kulkarni, P. S. R. Krishna, A. B. Shinde and A. K. Tyagi, *Chemistry of Materials*, 2009, **21**, 5848-5859.
276. H. Kishimoto, T. Omata, S. Otsuka-Yao-Matsuo, K. Ueda, H. Hosono and H. Kawazoe, *Journal of Alloys and Compounds*, 2000, **312**, 94-103.
277. P. E. Raison, C. C. Pavel, R. Jardin, E. Suard, R. G. Haire and K. Popa, *Physics and Chemistry of Minerals*, 2010, **37**, 555-559.
278. V. P. Kol'ko, D. A. Zyuzin, V. A. Sadykov, V. V. Kriventsov and E. M. Moroz, *Glass Physics and Chemistry*, 2007, **33**, 335-339.